Max-Planck-Institut für Metallforschung
Stuttgart

HRTEM Investigations of Structure and Composition of Polar Pd/ZnO Heterophase Interfaces

Mitsuhiro Saito

Dissertation
an der
Universität Stuttgart

Bericht Nr. 179
Dezember 2005

HRTEM Investigations of Structure and Composition of Polar Pd/ZnO Heterophase Interfaces

Von der Fakulät Chemie der Universität Stuttgart
Zur Erlangung der Würde eines
Doktors der Naturwissenschaften (Dr. rer. nat.)
genehmigte Abhandlung

Vorgelegt von
MITSUHIRO SAITO
aus Tokyo

Hauptberichter: Prof. Dr. Dr. h.c. M. Rühle
Mitberichter: Prof. Dr. F. Aldinger
Tag der Einreichung: 03. November 2005
Tag der Prüfung: 19. Dezember 2005

MAX-PLANCK-INSTITUT FÜR METALLFORSCHUNG STUTTGART
2005

Contents

Zusammenfassung

In der vorliegenden Arbeit wurde die Struktur und Bindung an Pd/{0001}ZnO Grenzflächen unter Einsatz der hochauflösenden Transmissionselektronenmikroskopie (HRTEM) sowie Röntgenbeugung erstmals systematisch quantitativ analysiert. Ein Vergleich der Resultate aus den experimentellen Untersuchungen erfolgte mit semi-quantitativen *first principle* Rechnungen und *crystal truncation rod* Rechnungen.

In einem ersten Schritt erfolgte eine definierte Präparation der ZnO Oberflächen in Sauerstoff und im Ultrachochvakuum (UHV). Die Wärmebehandlung in Sauerstoff mit nachfolgender Wärmebehandlung in UHV bei 600 °C führte zu einer flachen, gestuften und kontaminationsfreien Oberfläche mit einer (1 × 1) Rekonstruktion. Auf der Oberfläche wurden Stufen mit einer Höhe einer halben Einheitszelle bestimmt, was zur Bildung von 2 unterschiedlichen Oberflächendomänen führt. Beide polaren ZnO Oberflächen, die (0001) ZnO ($^{+}$**ZnO**) und die $(000\bar{1})$ ZnO ($^{-}$**ZnO**) Oberfläche, wurden mittels Röntgenbeugung eingehend charakterisiert. Diese Messungen zeigen, dass der Bedeckungsgrad der Oberflächen von der Präparationsmethode abhängt. Die in Sauerstoff präparierte $^{+}$**ZnO**-Oberfläche ist Zn terminiert ist und weist, in sehr guter Übereinstimmung mit Rechnungen von Noguera [Noguera 2000], einen reduzierten Bedeckungsgrad von 77 % auf. Dieser Bedeckungsgrad führt zu einer elektrostatischen Aufladung der Oberfläche, die das durch die Zn-O-Dipole verursachte elektrostatische Feld kompensiert und somit die Oberfläche stabilisiert. Der von Noguera theoretisch berechnete optimale Bedeckungsgrad liegt bei 75 %, die Abweichungen zu den experimentellen Werten liegen im Rahmen der Messgenauigkeit (±5 %).

Beide ZnO-Oberflächen wurden in einer Molekularstrahlepitaxieanlage mit Pd bedampft. Pd bildet Inseln auf beiden ZnO-Oberflächen. Durch XRD-, RHEED- und TEM-Untersuchungen konnte nachgewiesen werden, dass Pd auf ZnO bei 600 °C mit folgender

Orientierungsbeziehung epitaktisch wächst:

$$(111)_{Pd} \,//(0001)_{ZnO} \text{ und } [\bar{1}10]_{Pd} \,//[11\bar{2}0]_{ZnO}$$

Diese epitaktische Orientierung wird im Vergleich zu anderen Orientierungen auf Grund der relativ geringen Fehlpassung von 18 % zwischen Pd und ZnO sowie der relativ geringen Energie der $\{111\}_{Pd}$ Oberfläche energetisch begünstigt. XRD-Messungen zeigten, dass die optimale Wachstumstemperatur bei 600 °C liegt. Diese Temperatur ist hoch genug, um einerseits eine gute Ausrichtung der Pd-Inseln zu gewährleisten (ausreichende Mobilität der Pd-Adatome auf der ZnO-Oberfläche) und andererseits noch ausreichend tief, um eine Segregation von S, K, und In an die Oberflächen der ZnO-Einkristalle zu verhindern.

Mittels HRTEM Untersuchungen konnte gezeigt werden, dass sich zwischen Pd und ZnO keine Reaktionsphase gebildet hat und ein atomar abrupter Übergang an den Pd/ZnO Grenzflächen besteht. Die Grenzflächen sind über Bereiche von über 100 nm atomar eben. An der **Pd/$^{+}$ZnO** Grenzfläche und der **Pd/$^{-}$ZnO** Grenzfläche wurden Gitterrelaxationen detektiert, die auf eine Anpassung der Fehlpassung zurückzuführen sind. Der experimentell bestimmte Abstand zwischen den relaxierten Bereichen beträgt 1.5 nm und entspricht dem Abstand, der auf Grund der 18 % Fehlpassung zu erwarten ist, überein. Zwischen diesen relaxierten Bereichen existieren strukturell annähernd perfekte Bereiche, die zur Bestimmung der Terminierung der Grenzflächen und der Translationszustände mittels quantitativer Bildverarbeitung herangezogen wurden.

Mittels Bildverarbeitung konnte gezeigt werden, dass die **Pd/$^{+}$ZnO** Grenzfläche Zn-terminiert ist, die Zn-Atome der Grenzflächenlage auf Pd-Gitterplätzen sitzen und der Abstand zwischen der ersten Pd- und der letzten Zn-Lage im Vergleich zum Pd-Gitter um 0.02 nm vergrößert ist. Im Gegensatz zu der gereinigten nicht bedampften Oberfläche beträgt die Besetzung der teminierenden Zn-Lage, nach dem Bedampfen mit Pd, 100 %. Das heißt es findet eine Segregation von Zn aus ZnO an die Grenzfläche statt. An der **Pd/$^{+}$ZnO** Grenzfläche wurden periodische Relaxationen nur in der Zn-Grenzflächenlage im ZnO beobachtet. Dies lässt auf eine relativ starke Bindung zwischen der ersten Zn-Lage ($^{1.}$Zn) und Pd schließen (starke $^{1.}$Pd -$^{1.}$Zn Bindung; Grenzflächenlagen Pd, Zn: „1.“ bedeutet 1. Lage and der Grenzfläche).

Für die **Pd/$^{-}$ZnO** Grenzfläche ergab eine quantitative Bildanalyse eine O-Terminierung des **$^{-}$ZnO**. Die Pd-Atome der letzten Lage sitzen über den Zn-Atomen der ersten ZnO-Lage.

Der Abstand zwischen der letzten O-Lage und der ersten Pd-Lage ist im Vergleich zu den Abständen im Pd-Gitter um 0.01 nm verkleinert. Die Besetzung der terminierenden O-Lage beträgt 100 %. Im Vergleich zur **Pd/$^{+}$ZnO** Grenzfläche wurden an der **Pd/$^{-}$ZnO** Grenzfläche ausgedehnte Relaxationen im Pd-Gitter detektiert, die sich auf mehrere Pd-Lagen auswirken. Folglich ist die Bindung an der **Pd/$^{-}$ZnO** Grenzfläche schwächer (kleinere Adhäsionsenergie) als die an der **Pd/$^{+}$ZnO** Grenzfläche, was auf eine relativ schwache $^{1.}$Pd-$^{1.}$O Bindung hinweist.

Die Bindungs- und Ladungsverhältnisse der verschiedenen Pd/ZnO Grenzflächen wurden mit semi-quantitativen *first principle* DVXα Rechnungen ermittelt.

Es konnte gezeigt werden, dass die terminierende Zn-Lage an der **Pd/$^{+}$ZnO**-Grenzfläche negativ und die terminierende O-Lage an der **Pd/$^{-}$ZnO**-Grenzfläche positiv geladen ist. Diese Veränderung des Ladungszustandes an der Grenzfläche im Vergleich zur Oberfläche führt zu einer Segregation von Zn an die **Pd/$^{+}$ZnO**-Grenzfläche. Elektronen werden vom Pd zum Zn transferiert. Das durch die Zn-O-Dipole verursachte elektrostatische Feld wird durch die geladene Zn-Schicht kompensiert. Im Falle der O-terminierten **Pd/$^{-}$ZnO**-Grenzfläche erfolgt ein Elektronentransfer vom Pd zum O, was zur Segregation von O an die Grenzfläche führt. Dies bedeutet, dass die an den O- und Zn-terminierten Oberflächen vorhandenen strukturellen Defekte (Leerstellen) zur Kompensation des elektrostatischen Feldes der Zn-O-Dipole an den Pd/ZnO Grenzflächen nicht mehr benötigt werden.

Die relativen Bindungsverhältnisse der Grenzflächen wurden wie folgt bestimmt:

$^{1.}$Pd-$^{1.}$Zn (Zn-terminierte Oberfläche) > $^{1.}$Pd-$^{1.}$O (O-terminierte Oberfläche)
(Grenzflächenlagen Pd, Zn: „1.“ bedeutet 1. Lage and der Grenzfläche)

Dieses Resultat ist in Übereinstimmung mit der HRTEM-Beobachtung, aus denen aus dem Relaxationsverhalten an der Grenzfläche auf die Bindungsstärke geschlossen werden konnte. Die unterschiedlichen Bindungsverhältnisse führen auch zu einem unterschiedlichen Wachstumsverhalten. Bei gleicher Schichtdicke bilden sich im Fall der O-terminierten Oberfläche größere zusammenhängende Inseln, was auf ein früheres Koaleszenzverhalten im Vergleich zur Zn-terminierten Oberfläche hinweist und folglich auf eine größere Mobilität der Pd-Adatome. Das heißt, dass das Wachstumsverhalten durch die Wahl der Oberflächenterminierung gezielt gesteuert werden kann. Auf der Zn-terminierten Oberfläche

lassen sich bei gleichen nominellen Schichtdicken schneller geschlossene Schichten herstellen.

Vergleicht man die *first principle* Rechnungen mit Resultaten der quantitativen HRTEM, mittels der die Terminierung und das Relaxationsverhalten der Grenzflächen ermittelt wurden, so lässt sich folgender qualitativer Vergleich der Bindungsstärken für die Zn- und die O-terminierten Grenzflächen aufstellen:

$$[{}^{1.}\text{O-Zn} \; ; \; {}^{1.}\text{Pd-}{}^{1.}\text{Zn}] > {}^{1.}\text{Pd-}{}^{1.}\text{O} > {}^{1.}\text{Pd-Pd} > {}^{1.}\text{Zn-O}$$

oder

$${}^{1.}\text{Pd-}{}^{1.}\text{Zn} > {}^{1.}\text{Pd-}{}^{1.}\text{O} > {}^{1.}\text{O-Zn} > {}^{1.}\text{Pd-Pd} > {}^{1.}\text{Zn-O}$$

Aus den obigen Vergleichen folgt, dass die ${}^{1.}$Zn-O-Bindung die schwächste der Bindungen im Bereich der Grenzfläche ist. Die Ungleichung ${}^{1.}$O-Zn > ${}^{1.}$Zn-O in ein Hinweis darauf, warum sich die Zn-terminierte ZnO-Oberfläche auch mechanisch leichter bearbeiten lässt.

Das unterschiedliche Verhalten der Pd/ZnO Grenzflächen ist ein schönes Beispiel dafür, wie eine unterschiedlich terminierte Oxidoberfläche sich stark auf die Entstehung der Struktur einer Metall/Oxidgrenzfläche auswirken kann. Aufgrund des unterschiedlichen Relaxationsverhaltens ist auch mit unterschiedlichen physikalischen Eigenschaften der Zn- und O-terminierten Grenzflächen zu rechnen. Im Fall der stärkeren **Pd/$^{+}$ZnO** Grenzfläche werden die Epitaxie-Spannungen auf den ZnO-Kristall übertragen und können aufgrund der schwachen ${}^{1.}$Zn-O-Bindung zu Relaxationen im ZnO-Kristall führen. Für die **Pd/$^{-}$ZnO** Grenzfläche ist es genau umgekehrt. Die schwächere ${}^{1.}$Pd-${}^{1.}$O-Bindung ermöglicht Relaxationen im Pd.

Abschließend lässt sich sagen, dass sich in Abhängigkeit der Oberflächenterminierung eine Grenzflächenterminierung einstellt, die zur Minimierung der Grenzflächenenergie beiträgt. Dies führt letztendlich zur Ausbildung einer lokalen Grenzflächenstruktur mit hoher geometrischer Kohärenz bzw. Epitaxie.

Summary

The present work is a fundamental, quantitative and systematic study of the structure and bonding of Pd/{0001}ZnO interfaces. The interface was studied experimentally via high-resolution transmission electron microscopy (HRTEM). These studies were completed by semi-quantitative *first principle* calculations and crystal truncation rod measurements.

The ZnO substrate surfaces were prepared under well-defined oxygen atmospheres and in ultra-high vacuum (UHV). Flat, stepped, contamination free, and unreconstructed surfaces were obtained during heat treatment at 600 °C. The steps on the surfaces were half a unit cell in height, resulting in uniform terminating atomic species. Both polar ZnO surfaces, the (0001) ZnO ($^{+}$**ZnO**) and the $(000\bar{1})$ ZnO ($^{-}$**ZnO**) surface, were analyzed in detail with surface XRD. These investigations showed that the coverage of the surface depends very sensitively on the surface preparation process. The oxygen prepared $^{+}$**ZnO** surface was Zn-terminated with a mean reduced coverage of 77 % (±5 %). This coverage is in good agreement with that calculated by Noguera [Noguera 2000] as 75 %. Following the explanation of Noguera, a partial coverage of the surface leads to an electrostatic charging of the surface which compensates the electrostatic field caused by the Zn-O dipoles, stabilizing the surface structure.

Single crystalline Pd films were grown on both ZnO surfaces via molecular-beam-epitaxy. Pd forms three-dimensional clusters (islands) on the ZnO surfaces. With XRD, RHEED, and TEM investigations the following well-defined epitaxial orientation relationship between Pd islands and ZnO crystal was observed (deposition temperature 600 °C):

$$(111)_{Pd}\ //(0001)_{ZnO} \text{ and } [\bar{1}10]_{Pd}\ //[11\bar{2}0]_{ZnO}$$

This epitaxial orientation relationship is favored by a lower lattice mismatch of 18 %

between Pd and ZnO and the relatively low energy of the $\{111\}_{Pd}$ surface. The optimum growth temperature for this epitaxial orientation relationship is 600 °C. This temperature was sufficiently high to promote a well alignment of the islands (high enough Pd atom mobility) and low enough to suppress the segregation of S, K, and In to the ZnO surfaces.

HRTEM investigations revealed that the Pd/ZnO interfaces are atomically abrupt and, as expected due to the low reactivity of Pd, free of reaction phases. The interfaces are atomically flat over regions of more than 100 nm. Structural defects were detected in the **Pd/$^{+}$ZnO** and the **Pd/$^{-}$ZnO** interfaces. These defects are misfit dislocations which are formed by the relaxation of the lattice misfit between Pd and ZnO. The experimentally determined distance between the cores of the dislocations is 1.5 nm and corresponds to the theoretical misfit dislocation distance. The structurally matching regions between the dislocations were used to perform a quantitative analysis of the interfacial translation state via quantitative image processing.

It could be shown that the **Pd/$^{+}$ZnO** interface is Zn-terminated and the Pd atoms are positioned on Zn lattice sites. The distance between the interfacial Pd layer and the terminating Zn layer increased by 0.02 nm compared to the theoretically expected distance between the $\{111\}_{Pd}$ lattice planes. Pd coverage resulted in a segregation of Zn atoms to the interface until 100 % coverage was reached. The periodic relaxations at the **Pd/$^{+}$ZnO** interface were located only in the terminating Zn layer.

Quantitative image analysis of the HRTEM micrographs from the **Pd/$^{-}$ZnO** interface shows O termination of this interface. The interfacial Pd and O atoms are located top-on-top and the distance between them is about 0.01 nm smaller than the distances in the Pd lattice. The coverage of the interfacial O layer is 100 %. In contrast to the **Pd/$^{+}$ZnO** interface the lattice relaxations at the **Pd/$^{-}$ZnO** interface were located in the Pd.

The charge distribution and bonding at both Pd/ZnO interfaces were investigated by semi-quantitative *first principle* DVXα calculations. The calculations revealed that the terminating Zn layer at the **Pd/$^{+}$ZnO** interface was charged negative and the terminating O layer at the **Pd/$^{-}$ZnO** positive. This is a change in interfacial charge distribution compared to the clean ZnO surfaces. In the case of the Zn-terminated **Pd/$^{+}$ZnO** interface, the structural defects (e.g. Zn vacancies at the interface) which are compensating the electrostatic field of the Zn-O dipoles are now not necessary because electrons are supplied from Pd to Zn. The electrostatic field of the Zn-O dipoles is now compensated via the

charged interfacial Zn layer. Thus, segregation of Zn to the **Pd/$^{+}$ZnO** interface takes places. In the case of the O-terminated **Pd/$^{-}$ZnO** interface, electrons are supplied from O to Pd leading to a segregation of O to the interface.

The following inequalities could be deduced from the calculations of the bonding at the different interfaces:

$^{1.}$Pd-$^{1.}$Zn (Zn-terminated surface)> $^{1.}$Pd-$^{1.}$O (O-terminated surface)

(„1.“ means 1. layer at the interface or interfacial layer).

These differences in interfacial bonding result also in a different growth behavior of the Pd islands. In the case of the O-terminated interface large islands are formed, liquid like coalescence is observed more early which indicates that the Pd atoms on this surface are more mobile (less strongly bonded).

Furthermore, a qualitative comparison of the *first principle* calculations with HRTEM results (relaxation behavior, termination) allows deducing the following inequalities for the interatomic bonding near the differently terminated interfaces:

$$[^{1.}\text{O-Zn} ; {}^{1.}\text{Pd-}^{1.}\text{Zn}] > {}^{1.}\text{Pd-}^{1.}\text{O} > {}^{1.}\text{Pd-Pd} > {}^{1.}\text{Zn-O}$$

or

$$^{1.}\text{Pd-}^{1.}\text{Zn} > {}^{1.}\text{Pd-}^{1.}\text{O} > {}^{1.}\text{O-Zn} > {}^{1.}\text{Pd-Pd} > {}^{1.}\text{Zn-O}$$

From these inequalities one obtains that the $^{1.}$Zn-O bond is the weakest bond in the region near the interface. The inequality $^{1.}$O-Zn > $^{1.}$Zn-O indicates why the Zn terminated surface is mechanically softer than the O terminated surface.

This result is an impressive example demonstrating how different terminated oxide surfaces strongly influence the formation of interfacial defects. These differences will also be reflected in different physical properties of the interfaces. In the case of the more strongly bonded **Pd/$^{+}$ZnO** interface, epitaxial strain is transferred into the ZnO crystal. This is due to the relatively weak $^{1.}$Zn-O bond in ZnO. The more weekly bonded **Pd/$^{-}$ZnO** interface behaves different. The relatively weak $^{1.}$Pd-Pd bond favors relaxations in the Pd. This shows how the growth behavior can be tuned by selecting the termination of the ZnO surface.

Depending on surface polarity the terminating atomic species are adjusted in such a manner that the total energy of the system is minimized. This also results in the establishment of an interfacial local structure that preserves high geometrical coherency and a chemically interactive geometry as a function of interfacial termination.

1 Introduction

Metal/oxide hybrid systems are used in a variety of different applications, e.g. microelectronics, oxide-strengthened alloys, catalysis, sensors, etc. In these applications, the interface plays a key role. To gain understanding of the correlation between the macroscopic properties and the microscopic interfacial behavior, it is of great importance to perform precise examinations of the local atomic structure and the local bonding at the metal/oxide interface.

It is not easy to determine the local atomic structure at metal/oxide interfaces with direct imaging methods. In HRTEM observation, it is difficult to distinguish simultaneously a light element like oxygen and a heavy element like a metal. In addition, oxides have quite small lattice spacings. Furthermore, the real atomic centers often shift from the contrast centers near an interface on an image. These points make it difficult to determine the exact interfacial local atomic structure.

Fortunately, such problems could be solved employing ultra high resolution microscopes and quantitative high resolution image analysis techniques [Möbus, 1996]. Several experimental and theoretical studies for the 'ideal' model systems with a coherent interface, e.g., Al/$MgAl_2O_4$ [Schweinfest, 1998] and Pd/$SrTiO_3$ [Tchernychova, 2004], contributed to understand quantitatively the behavior of metal/oxide interfaces.

In actual applications, however, we may encounter more complex situations. Therefore, it is also essential to examine the heterophase interface of more general model systems including lattice mismatch or polarity of the oxide. In this work, the Pd/ZnO system was used as such a model system. As oxide, ZnO was adopted, because it has been widely used in electronics. As metal, Pd was used, because it was already qualitatively observed by HRTEM in many other systems [Ichimori, 1996a], [Ichimori, 1996b], [Groen, 1998], [Chen, 1994], [Lu, 1992], [Ichinose, 1994], [Ichinose, 1994b], [Merkle, 1990], [Dehm, 1996]. ZnO has wurzite structure and Pd has fcc structure. The system has a large lattice mismatch. {0001}ZnO possesses a polar plane terminated by either Zn or O.

Pd/ZnO interfaces for this work are produced by Molecular Beam Epitaxy (MBE). The local atomic structures at the interfaces will be investigated with HRTEM JEM-ARM1250 and the local electronic structures at the interfaces will be determined with electron energy loss spectroscopy. In order to examine the structural difference of the ZnO before/after Pd deposition, the local atomic structures of the ZnO surfaces also are examined by surface X-ray diffraction. Furthermore, all experimental results are quantitatively verified by comparing them with simulated results (EMS Image calculations, semi-quantitative *first-principle* DVXα calculations, and crystal truncation rod simulations).

The work is structured as follows: After the introduction, chapter 2 outlines fundamental aspects of crystal interfaces, metal/oxide interfaces, ZnO surfaces, and Pd/ZnO interfaces. Furthermore, the aim of this thesis will be described in detail. In chapter 3 essential experimental and computational techniques are summarized. Chapter 4 covers the surface treatments, the experimental procedures of MBE Pd film growth, and TEM specimen preparation. In chapter 5 and 6, the obtained results for the ZnO surface and the Pd/ZnO interface are described, quantitatively evaluated, and finally discussed. In chapter 7, *first principle* DVXα calculation results for the bulk ZnO and Pd/ZnO interfaces are described and discussed. In the final chapter 8, all results are summarized and the thesis finishes with a conclusion.

2 Literature study

In this chapter, studies related to metal/oxide (or metal/ceramic) interfaces are reviewed. Atomically abrupt metal/oxide interfaces with reasonably good lattice matching, and thus a large spacing between misfit dislocations, were very interesting for fundamental studies in material science research.

Over the past 10 years, there has been considerable progress in the understanding of metal/oxide interfaces. In particular, improvements in experimental characterization have provided a lot of new experimental insight into the structure and chemistry of metal/oxide interfaces, mainly, through high symmetric 'model' studies. Furthermore, advancements in computer capabilities have led to also more reliable computational modeling than were previously possible. Up to 200 atoms can be treated by *first principle* calculation. The studies obtained so far for metal/oxide interfaces are summarized in section 2.1.

In this work, the heterophase Pd/ZnO interface which includes a large lattice mismatch and oxide polarity was used as a more general model system. The study for such a low symmetric 'model' system at the atomic level may allow understanding the nature of general metal/oxide interfaces.

The results obtained so far for the Pd/ZnO system are summarized in section 2.2. Finally, the goal of this thesis is described in section 2.3.

2.1 Metal/Oxide Interfaces

Metal/oxide interfaces are employed in a variety of industrial applications, e.g., as, oxide strengthened alloy, as catalysts, in microelectronics, or as coating, etc., and the interfaces play a key role for the macroscopic properties of the material. As pointed out by many authors [Rühle, 1989b], [Rühle, 1996], [Finnis, 1996], [Ohuchi, 1991], [Ernst, 1995], [Sinnott, 2003], a detailed analysis of the local atomic structure of metal/ceramic interfaces is essential for the understanding and improvement of their performance and functionality.

The interfacial atomic structure can be experimentally studied via cross sectional HRTEM observations. However, this technique implies some experimental restrictions. The following two conditions should be satisfied for a successful observation of an accurate projected image of atomic columns along the e-beam on the screen of the transmission electron microscope.

The most important restrictions are:
(1) Low index zone axes of both crystals should be aligned parallel and they should also be parallel to the incoming electron beam.
(2) The interfacial normal should be perpendicular to the zone axis and the interface plane should be parallel to the incoming beam.

Condition (1) and (2) limit the number of orientations which can be successfully analyzed by HRTEM.

HRTEM observations were performed for a variety of metal/oxide systems: Nb/Al_2O_3 [Ishida, 1990], [Ishida, 1990b], [Ishida, 1992], [Rühle, 1989], [Mayer, 1990], [Ishida, 1987], [Fischmeister, 1988], [Mader, 1987], [Evans, 1990], [Guterkunst, 1994], [Tricker, 1995a, b], V/Al_2O_3 [Ikuhara, 1994], Cu/Al_2O_3 [Ernst, 1991], [Scheu, 2000], Fe/Al_2O_3 [Trumble, 1989], Ni/Al_2O_3 [Muschik, 1992] Pd/Al_2O_3 [Dehm, 1996], Mo/Al_2O_3 [Tricker, 1995a, b], Mo/$SrTiO_3$ [Tchernychova, 2003], Al/$MgAl_2O_4$ [Schweinfest, 1998], Ag/CdO [Necker, 1988], Pd/NiO [Merkle, 1990], Cu/NiO [Gao, 1990], Ag/NiO, Au/NiO, Au/MgO [Merkle, 1992], Cu/MgO [Chen, 1994], V/MgO [Ikuhara, 1995], Ag/MgO [Trampert, 1992], Pd/MgO [Chen, 1994], [Lu, 1992], [Ichinose, 1994], Pd/$SrTiO_3$ [Tchernychova, 2004], and Pd/ZnO [Ichinose, 1994b], [Ichimori, 1996a, b], [Saito, 2001], [Groen, 1998], [Murakami, 2003].

Experimental and theoretical details are summarized in this section for the interface

synthesis, geometrical theories for the interface (grain boundary), the orientation relationships between oxide and metal, terminating atomic species of the oxide, interfacial local structure, and geometry for interfacial structure.

2.1.1 Methods for Synthesizing Well-Defined Interfaces

Successful methods for a synthesis of well-defined metal/oxide model interfaces are diffusion bonding, internal oxidation of a binary metal alloy, and deposition of a metal layer on an oxide substrate.

In thermodynamic equilibrium, atoms will occupy the energetically most favorable interfacial sites. However, the formation of interfaces is possible under non-equilibrium condition depending on the synthesis process. In fact, the local atomic structures were strongly affected by the synthesis process. This has been shown by different authors [Rühle, 1989], [Florjancic, 1985], [Knauss, 1991], [Mayer, 1990]. In the following, 3 synthesis methods are shortly explained.

A) Diffusion Bonding

Pressing a metal and an oxide together at a high temperature results in the formation of an interface. In principle, one can produce well-defined interfaces with various preselected orientation relationships [Ishida, 1987]. In this method, the interfacial atomic structure is strongly affected by the crystal surfaces prior to the bonding. The specimen surfaces should be cleaned and flattened via heat treatment in UHV environment before bonding [Fischmeister, 1988]. During bonding at high temperature and at a sufficient high pressure, atomic concentration gradients are developed and plastic deformation of the metal can occur. The recovery processes may influence the structure of the interface. On the other hand, during cooling, different thermal expansion coefficients of the metal and the oxide cause interfacial thermal strain which often lead to interfacial fracture.

B) Internal Oxidation

This method leads to the formation of an interface between a precipitated oxide and a metal matrix by heating a thin film of a metallic alloy in oxidizing atmosphere and by selectively oxidizing either metal within the binary alloy [Mader, 1987]. Well defined interfaces were obtained by internal oxidation for the following systems: Nb/Al_2O_3, Ag/CdO, Ag/MgO, Ag/ZnO, Pd/Al_2O_3, Pd/ZnO, and Cu/Al_2O_3 [Ashby, 1963], [Merkle, 1990], [Ernst, 1996], [Ichinose, 1994b], [Ichimori, 1996a, b], [Saito, 2001], [Groen, 1998], [Murakami,

2003]. The following prerequisites have to be fulfilled for internal oxidation: (i) oxygen can diffuse into the alloy, (ii) the metal matrix element should have a lower oxygen affinity than the oxidized metal element, and (iii) the matrix surface should not be oxidized during internal oxidation conditions. Therefore, a noble metal has been often used as matrix material. Since internal oxidation can proceed near equilibrium conditions, the precipitate has a shape which is dictated most likely by the lowest total energy for a given oxidation temperature. During the internal oxidation of an alloy, the system will undergo a very large change of chemical energy. On the other hand, the interfacial atomic structure and the shape of the precipitate depend not only on the interfacial energy but also on the strain energy generated by the precipitation. The crystal orientation relationship can be determined by the difference between two lattice constants and the stable crystal phases [Eastman, 1989]. There also exist experimental observations that close packed planes and close packed directions of the systems are parallel. Another method to produce metal/oxide interfaces is the internal reduction of a ternary oxide [Merkle, 1996], [M. Backhaus-Ricoult, 1992].

C) Molecular Beam Epitaxy

C-1) Basics of Epitaxial Growth

During MBE (Molecular Beam Epitaxy) deposition the metallic film is grown on a preselected plane of the oxide substrate. An epitaxial thin film can be grown with a specific orientation relationship to the substrate. The typical MBE growth rate is ≤ 1 ML/s (1 mono layers per second) under UHV (Ultra High Vacuum) environment which prevents the surface from contaminating. Typical variable parameters are growth rate (beam flux), growth temperature, crystal type, and surface roughness.

A high quality thin film can also be produced by a ledge growth mechanism [Seifert, 1996]. An adsorbed atom continues to move on the flat surface until it contacts with the ledge. The growth process occurs by translating a ledge along a surface. The ledge growth can easily happen when the growth surface is parallel to the close packed plane of the crystal. Easy surface atomic diffusion allows the adatom to reach a ledge before surface roughening occurs. A typical growth temperature of $3/8T_m$ (T_m: Melting point) is required for ledge growth of a metal. On the other hand, the temperature of $1/10T_m$ is required for ledge growth of an oxide. Generally, high temperature is better for epitaxial growth in most materials than low temperature. However, too high temperatures cause a strong interdiffusion between the metal and oxide without forming an atomically abrupt interface. Therefore, the appropriate temperature range for epitaxial metal film growth on an oxide

substrate is not usually so wide. Another problem for applying too high temperatures for metal/oxide interfaces produced by heteroepitaxial growth is internal strains after cooling due to the lattice mismatch and/or difference in thermal expansion coefficients between film and substrate. The strain strongly affects the growth behavior and the mechanical stabilities at the metal/oxide interfaces.

The MBE technique generates usually thin films with higher quality than internal oxidation, internal reduction, and diffusion bonding. Furthermore, the chemical purity at the interface is much higher and the surface orientation of the substrate can be chosen. The oxide substrate provides good mechanical stability of the TEM specimen. Thus, MBE specimens are quite appropriate for studying metal/oxide interfaces.

C-2) Hetero-Epitaxial Growth

In hetero-epitaxial growth, one of the most important factors which dominate the quality of the epitaxy is the lattice mismatch between the substrate and the epitaxial film. The lattice mismatch is given by the difference between the lattice constant a_e of the epitaxial film and the lattice constant a_s of the substrate as follows.

$$\Delta a / a = \frac{a_e - a_s}{a_e} . \tag{2-1}$$

When this value $\Delta a / a$ is positive, a compressive stress will be applied to the epitaxial layer. Conversely, negative value of $\Delta a / a$ results in a tensile stress to the substrate.

A hetero interface can be classified into three type interfaces as shown in Fig. 2.1: (i) coherent interface, (ii) semi-coherent interface, and (iii) incoherent interface. If a film grows epitaxially on the substrate without forming any defects, the interface is called a coherent interface. If the system has small lattice mismatch, homogeneous strains can be introduced into the thin film to compensate for the mismatch. The elastic strain energy will be increased with increasing mismatch. For large lattice mismatch, it is energetically favorable to introduce misfit dislocations to compensate for high elastic stress fields. This interface is called semi-coherent interface. In the case that no strain appears, the interfacial structure is called incoherent interface. The difference between (ii) semi coherent interface and (iii) incoherent interface can be described by degree of a delocalization of a dislocation core [Romanov, 1998].

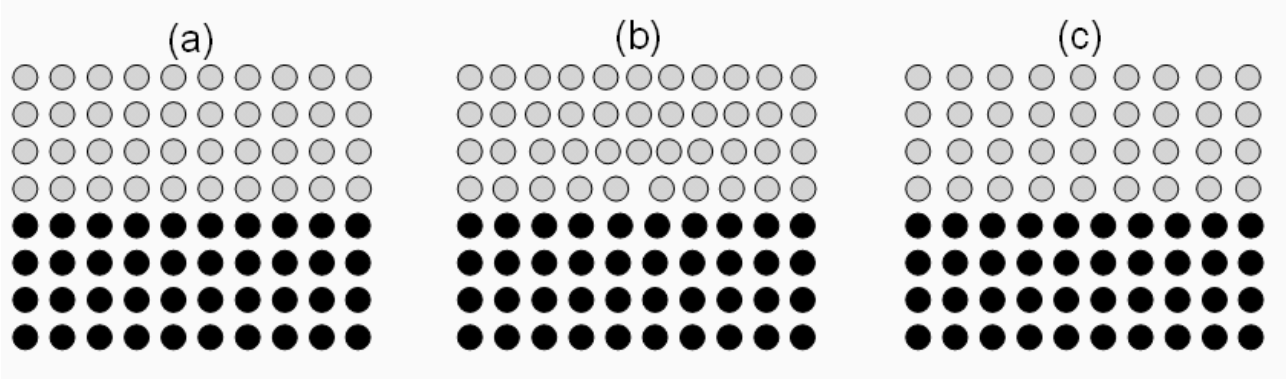

Fig. 2.1 A hetero interface can be classified into three type interfaces. Schematic drawing of (a) a coherent, (b) a semi-coherent, and (c) an incoherent interface structure.

Furthermore, misfit dislocations are introduced in the film thickness surpassing a critical value. Since the high film thickness causes to increase the elastic strain energy, the misfit dislocation would be easily introduced to compensate for high elastic strain fields [Nakajima, 1980]. The critical film thickness at where the misfit dislocation can start to be formed was given by Matthews, Blakeslee [Matthews, 1974], People and Bean [People, 1985]. Since the critical thickness is inversely proportion to the lattice mismatch, it will be largest in the case of best coherence between the film and the substrate.

The mismatch often causes the generation of a misfit dislocation or a bending of an epitaxial layer, suggesting that it largely affects growth mode.

C-3) Growth Modes

The growth mode of an epitaxial crystal can be classified into three typical modes as shown in Fig. 2.2 [Bauer, 1958], [Seifert, 1996]. FM (Frank-Van der Merwe) type starts with the formation of a 2-dimensional nucleus on the substrate surface and it continues to grow onto overall surface and then it repeats layer by layer. The homo-epitaxial growth or the hetero-epitaxial growth with small mismatch shows this FM mode [Van der Merwe, 1962]. From the energetic point of view, the formation of a heterophase interface is energetically favored compared to the formation of islands with large surface area.

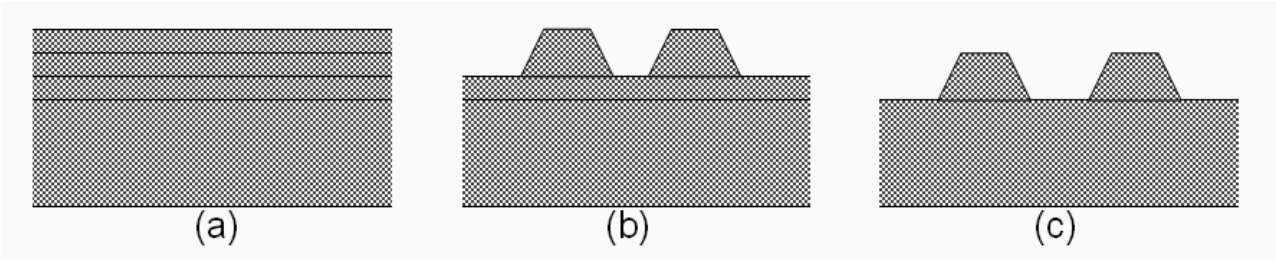

Fig. 2.2 The growth mode of an epitaxial crystal can be classified into three typical modes. Growth modes of (a) Frank-van der Merve, (b) Stranski-Krastanov, and (c) Volmer-Weber.

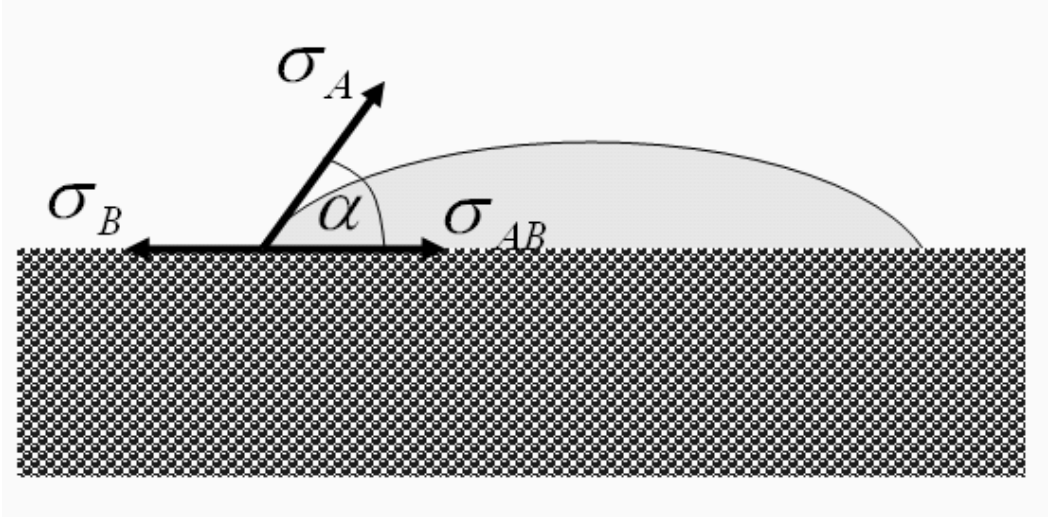

Fig. 2.3 A drop of a liquid metal film on a solid substrate. Growth modes can be determined by an energy balance between surface energies and an interfacial energy. In thermodynamic equilibrium the contact angle α is given by the surface energies σ_A, σ_B, and by the interface energy σ_{AB}.

SK (Stranski-Krastanov) type is that at the initial growth stage a 2-dimensional film is grown and then at a critical thickness 3-dimensional islands are formed on the surface. This mode appears for the case of the material system with comparatively large mismatch and small surface energy and interfacial energy. The reason for a combination of layer growth and island growth can be explained by a change of the interface energy after the coverage of film on the substrate surface. For the VW (Volmer-Weber) type, the 3-dimensional island is already formed in an initial growth stage. This mode appears in the case of hetero epitaxial growth with large mismatch. In this case, new layers of the deposit material are formed before the previous layer is completed, leading to island formation on the substrate surface.

In a very simplified picture, these growth modes can be also determined by an energy balance between surface energies and an interfacial energy. When a contacting angle between a liquid metal and a substrate is defined as α (see Fig. 2.3), then the relationship between these energies are given by the so-called Young-Dupré equation (2-2).

$$\sigma_A \cos\alpha + \sigma_{AB} = \sigma_B \tag{2-2}$$

σ_A and σ_B are defined as the surface energies of a liquid metal and of a solid substrate, respectively. The σ_{AB} is the interfacial energy. For perfect 2-dimensional growth ($\alpha \approx 0^\circ$), one obtains $\cos 0^\circ = 1$. A contact angle of $90^\circ \geq \alpha > 0^\circ$ denotes partial wetting of the substrate surface in which formation of interface is favored [Sutton, 1995]. The corresponding interface energy behaves like

$$\sigma_A + \sigma_{AB} \leq \sigma_B . \tag{2-3}$$

For the 3-dimensional growth mode, denoted by $90^\circ < \alpha \leq 180^\circ$, formation of interface is energetically unfavorable compared to formation of free surface of the wetting film and the interface energy fulfills the condition

$$\sigma_A + \sigma_{AB} > \sigma_B . \tag{2-4}$$

The Young-Dupré equation is valid for liquid drops on solid substrates where surface energies are isotropic. The model has to be modified for solid-solid interfaces. In general, surface energies for a solid are anisotropic. The crystallographic structure of the solid particle is given by the Wulff-construction [Wulff, 1901]. Crystals will create facets along low-index crystallographic planes to decrease the total surface energy.

C-4) Deposition Rate and Growth Temperature

Usually, MBE involves non-equilibrium growth conditions. This will affect nucleation behavior. Therefore, the criterion of Bauer [Bauer, 1958] and also the Young-Dupré equation have to be modified with respect to the substrate temperature and the deposition rate (beam flux). For high temperature and low beam flux, an adatom can easily reach a site which is energetically favored. Therefore, the growth process will occur near thermodynamic equilibrium and the film will grow with an epitaxial orientation relationship to the substrate. For the low temperature and high beam flux, the diffusion length of the adatoms on the surface is short, which can lead to polycrystalline growth far away from thermodynamic equilibrium.

D) Dependency of Interfacial Structure on Synthesizing Process

It was reported that the interfacial atomic structure depends on the synthesis method [Rühle, 1989], [Florjancic, 1985], [Knauss, 1991], [Shashkov, 1996]. Mayer examined the structural difference due to a variety of specimen synthesizing methods for the Nb/Al_2O_3 system as shown in Table 2.1 [Mayer, 1990].

Table 2.1 Dependency of interfacial structure on fabrication process [Mayer, 1990]. Processes for generating the Nb/Al_2O_3 system: (a) Diffusion bonding: Bonding temperature 1973 K, pressure 10 MPa, annealing time 2 hours, and vacuum 1.3×10^{-3} Pa, (b) internal oxidation of Nb-3 at%Al alloy: oxidizing temperature 1773 K, annealing time 45 min, and vacuum 5×10^{-3} Pa, (c) MBE: growth temperature 1123 K, growth rate 1 ML/s, and vacuum 1×10^{-6} Pa.

Proc.	Orientation relationship	Reaction layer	Misfit dislocation	Stand off
(a)	$(0001)_S//(110)_{Nb}$ $[01\bar{1}0]_S//[001]_{Nb}$	-	+	+
(b)	$(0001)_S//(110)_{Nb}$ $[01\bar{1}0]_S//[001]_{Nb}$	-	+	+
(c)	$(0001)_S//(111)_{Nb}$ $[2\bar{1}\bar{1}0]_S//[\bar{1}\bar{1}0]_{Nb}$	-	+	-

Table 2.1 shows the different atomic structures for the Nb/Al_2O_3 interfaces obtained for the different processing conditions. In the case of the process (c), the interface is parallel to both close-packed planes and the misfit dislocation core was located at the interface. It seems that at the low growth temperature the dislocation did not climb in the true equilibrium positions. On the other hand, the process (a) and (b) resulted in different orientation relationship and the high temperature processes allowed the core the misfit dislocation to climb to the true equilibrium positions. Thus the fabrication process seems to affect a local interfacial structure.

2.1.2 Geometrical Theories for Interfacial Structures

Many geometrical models which describe a stable structure have been suggested for grain boundaries or interfaces. In many cases, stable interfacial atomic structures can be described by the following (major) geometrical models.

The CSL Model for the Grain Boundary

The CSL (Coincidence Site Lattice) theory developed by Kronberg [Kronberg, 1964], [Smith, 1976] provides a geometrical model for a general grain boundary which can describe the possible orientation relationships between two crystals. When the two crystals were virtually overlapping, the number of coincident sites depends on the orientation relationship. It indicates that specific orientation relationship which provides many good

coincident sites can be easily formed.

Brandon suggested that interfaces including a highest CSL point density should be formed [Brandon, 1964]. Experimentally, for the first time, such a grain boundary in a metal was observed by HRTEM: Au (112) Σ11 grain boundary [Ichinose, 1981].

O-Lattice Theory

The CSL model represents a geometrical description on possible orientation relationships and a possible local atomic structure between two crystals of same material (at a grain boundary). However, only some discrete special angles result in high CSL point densities. Tilting away from such special angles, the CSL point density would be rapidly decreased, resulting in a poor coincidence. Furthermore, the lattice constants between the crystals forming a heterophase interface generally do not have fractional ratios, suggesting that a precise CSL point cannot exist mathematically. Therefore, a CSL theory has to be expanded allowing small deviation from the exact CSL condition.

For this, Bollmann introduced the O-lattice theory [Bollmann, 1980] which embodies Frank's formula in a small tilt grain boundary or CSL theory [Brandon, 1966]. In the O-lattice theory, not only a lattice point but also an internal point within an original unit cell is considered. Therefore, this model can be adapted to heterophase interfaces.

When two crystals were virtually perfectly overlapping and one of the crystals was rotated around one atomic column, there exist the coincident internal coordinates in the unit cells of both crystals. The coincident sites periodically exist and then can form a supercell which is defined as an O-lattice. The minimum O-lattice formed at specific orientation relationship is called the O-unit-cell [Bollmann, 1980].

In a heterophase interface, there are both better coincident sites and worse coincident sites. A shift of atoms can be expected near the worst coincident sites to fit two lattices as shown in Fig. 6.51. According to the O-lattice model, a Wigner-Seitz cell can be formed by enclosing these good coincident sites, resulting in a dislocation network in the interface by introducing linear defects on the cell boundary.

2.1.3 Orientation Relationships in Metal/Oxide Systems

In order to explain orientation relationships of the interfaces between ionic crystals and metals, Fecht and Gleiter introduced the so-called 'Lock-in' model [Fecht, 1985], [Fecht, 1989].

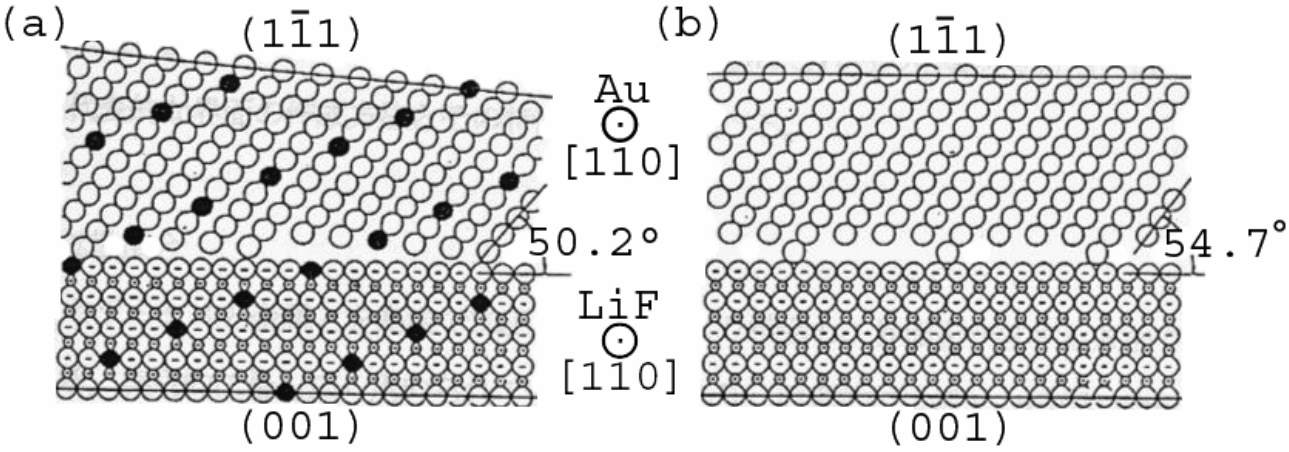

Fig. 2.4 Schematic diagram of atomic structures of the interface area in an Au particle sintered to LiF(001) substrate. Lock-in model: (a) theoretical CSL orientation relationship, (b) experimentally observed orientation relationship [Fecht, 1985].

They observed the crystal orientation relationships between sintered small particles of Au, Cu, or Ag and LiF, KCl, NaCl, MgO, or Al_2O_3 substrates, and showed that the equilibrium crystal orientation relationships depend on the degree of coincidence at the interface rather than the CSL relationship.

Fig. 2.4 shows schematically atomic structures of the interface area in an Au particle sintered to LiF(001) substrate. A Σ11 CSL boundary formed by 50.2° rotation around the [110] axis (see in Fig. 2.4 (a)) was not observed. However the crystal orientation relationship formed by a 54.7° rotation was observed (see Fig. 2.4 (b)). Although this actual orientation relationship has a low CSL point density, the interface is parallel to both close packed planes. In this case, it can be seen that interfacial atoms of the metal crystal are locked in hollow sites of the interfacial atoms of the ionic crystal. This case is described by the so called 'Lock-in' model. Observed orientation relationships in this kind of systems (metal/ionic crystals) can be explained by this 'Lock-in' model.

It was observed that the (111)Cu//(111)MgO interface and the (111)Pd//(111)MgO interface produced by internal oxidation can form a pseudo coincidence site lattice which includes the distorted Cu_2O or PdO unit cell at the interfaces. Chen suggested a local phase transformation that at the Cu/MgO interface the occupancy of the interfacial oxygen would be 1/2 of the occupancy of bulk MgO [Chen, 1994]. This means that the interface is relaxed to geometrically coincide by transforming into a different phase at the interface.

For the Nb//(0001)Al_2O_3 interface produced by MBE, the Nb atoms at the interface sit on sites of the Al sublattice in the α-Al_2O_3 [Mayer, 1992]. Since the interfacial O^{2-} ion approach to the interfacial Nb ion, then the Nb should be charged to Nb^{3+} in order to compensate local

ionic charges. This indicates that the Nb ionic radius was getting smaller and then the continuity of the Al sublattice can be kept over the interface. Even if a substrate surface orientation was changed, the interface can be constructed by this sub lattice [Gutekunst, 1994]. This principle seems to be also valid for the V/Al_2O_3 system [Ikuhara, 1994]. Those results suggest that the charge transfer across the interface provides a geometrical fit.

Since a {111} plane on an ionic crystal surface of NaCl type like CdO or MgO has energetically unfavorable dipole moments, typically {100} planes can be exposed as an electrostatically stable surface which neutralize charge. However, {111} interfaces rather than {100} interfaces were observed in specific metal/oxide systems [Merkle, 1990]. Finnis [Finnis, 1990] explained that the {111} plane with a higher atomic density can supply many more bonds and then the interfacial bonds cause a polarization in a metal. This results in a reduction of the unfavorable electrostatic field due to the dipole moments. This means that an orientation relationship in some oxide/metal system can be explained not by the geometrical theory but by the electrostatic model.

2.1.4 Terminating Atomic Species at Metal/Oxide Interfaces

Oxide ceramics have nonpolar planes, which terminate by mixture of metal ions and oxygen ions, and polar planes, which terminate either by a metal layer or by an oxygen layer. When the interface is formed along the polar plane, the terminating atomic species strongly affects the interfacial atomic structure or bonding.

Most of interfaces produced by internal oxidation are polar interfaces. A HRTEM observations and a quantitative analysis with simulation revealed that the oxides at the Ag/CdO [Necker, 1988], Cu/Al_2O_3 [Epicier, 1992], Cu/MgO, and Pd/MgO [Chen, 1994] interfaces produced by internal oxidation are terminated by an oxygen layer. It was explained that the O-termination can be attributed to an excess oxygen concentration in the matrix, because the specimen was subjected to high temperature and an oxidizing environment for a long time during the internal oxidation process.

Pd/Al_2O_3 interfaces were produced by internal oxidation (interface (1)). The structure was compared to the interfaces annealed in Al vapor (interface (2)) [Dehm, 1996]. A quantitative analysis revealed that the interface (1) was terminated by O while the interface (2) was terminated by Al. For the same system, one obtained different terminations.

Kirchheim [Kirchheim, 1980] indirectly reconfirmed the terminating atomic species by performing specific segregation experiments of hydrogen to the interface. The change of the chemical potential, the diffusivity, the volume, and the resistivity were measured. For interface (1), all properties were changed by the hydrogen segregation. However, no change was observed for interface (2). Since the changes were independent on thermal changes, Kirchheim concluded that strong O-H bonds were formed at the interface (1), meeting the suggestions that interface (1) is O-terminated [Dehm, 1996], [Gao, 1990], [Rodrigues, 1983], [Huang, 1988]. These observations suggest that the terminating atomic species at the interface depends on the synthesis and on the activity of O or Al in the Pd matrix.

Since the diffusion bonding occurs under UHV conditions, one would expect that the oxygen concentration should be much different from that of an interface formed under internal oxidation condition. Knauss and Mader [Knauss et al., 1991] produced the Nb/Al_2O_3 interface by diffusion bonding with the orientation relationship:

$$(110)Nb//(0001)Al_2O_3 \text{ and } [001]Nb//[01\bar{1}0]Al_2O_3.$$

An analysis of the HRTEM image revealed that the interface was terminated by Al with a 1.5 times higher concentration compared to the bulk. They explained the high Al concentration as follows. Since O, dissolved from Al_2O_3, diffuses much faster in Nb than Al, the O concentration in Nb is quite homogeneous while metallic Al precipitates at the interface owing to the high supersaturation during cooling. Furthermore, the excess Al in Nb, which could not reach the interface, may precipitate as a metastable Al_2O_3 phase in Nb far away from the interface. Then there should be a region with low oxygen concentration between the interface and the precipitates suggesting that the concentration of Al should be higher than that of O at the interface. This results in Al-termination. This case is also similar to the internal oxidation mechanism, e.g., the activity of O and Al in the metal strongly affects the terminating atomic species at the interface.

Backhaus-Ricoult [Backhaus-Ricoult, 2003] examined the dependency of the interfacial atomic and electronic structure on various oxygen environments. Cu/Mg alloys are internally oxidized in different oxygen chemical potential at 900°C.

For most oxidation conditions, $(111)_{MgO}//(111)_{Cu}$ interfacial planes were formed with long length. All MgO-Cu interfaces were semi-coherent, almost incoherent. The large lattice mismatch of 14% between the two phases leads to the formation of dislocations every seventh plane in copper (six planes in MgO). The misfit dislocation can be seen by a HRTEM image of the interface. These interfaces were studied in detail by CTEM, HREM and EELS.

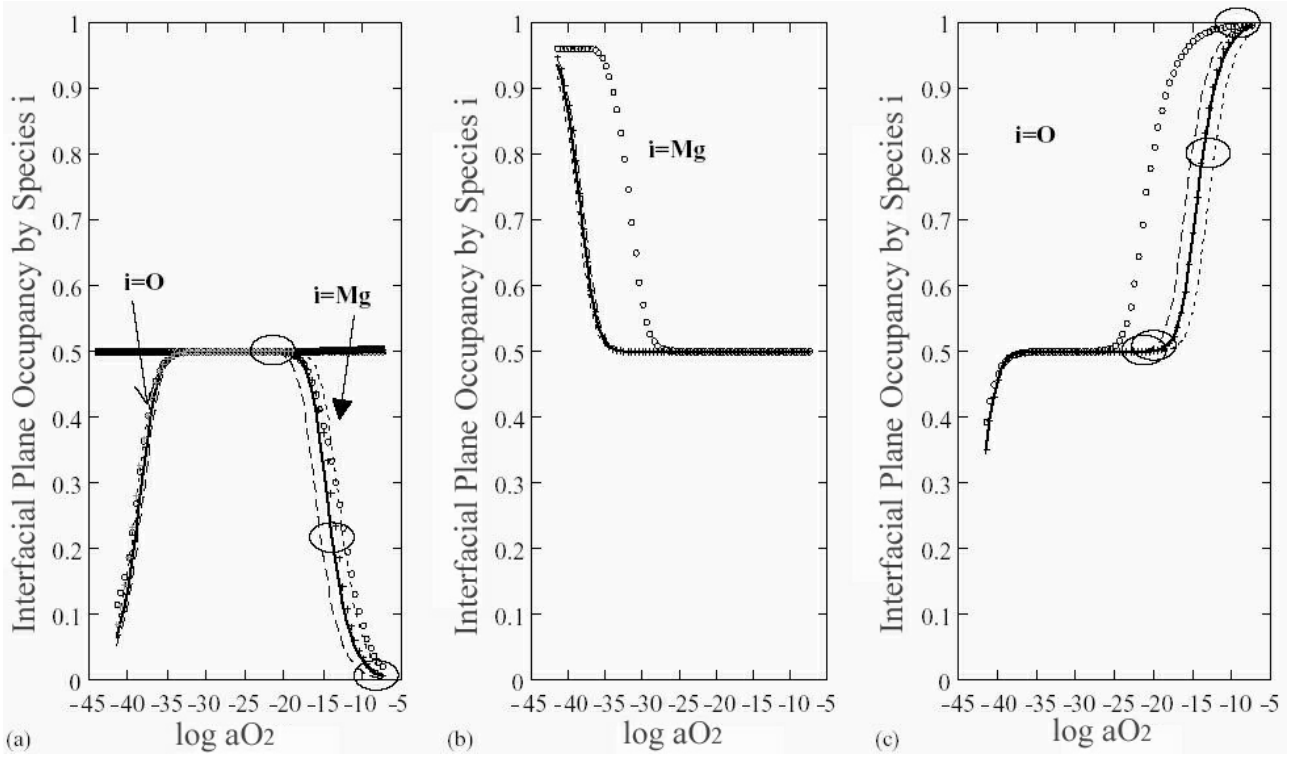

Fig. 2.5 Occupancies of the terminating oxide plane as function of oxygen activity for (a) mixed $(001)_{MgO}//(001)_{Cu}$, (b) polar O-terminated $(111)_{MgO}//(111)_{Cu}$ and (c) polar Mg-terminated $(111)_{MgO}//(111)_{Cu}$ interfaces. The curves represented computed model predictions for different values of the adsorption energies; the continuous line corresponds to the volume formation enthalpy of the corresponding bulk phases Cu_2O and Cu_2Mg, the dotted line to 90 % of these values, the dashed line to 110 % of these values, circles represent a computation, which includes in addition to the enthalpies a reaction volume-related strain energy term and the crosses show the shift of the adsorption behavior, when not only the enthalpy, but also a configurational adsorption entropy is considered. The large open dots show experimental ELNES results. [Backhaus-Ricoult, 2003]

From the experimental observations of the atomic and electronic structure of the polar $(111)_{MgO}//(111)_{Cu}$ and mixed $(001)_{MgO}//(001)_{Cu}$ (terminated by Mg and O) interfaces at different oxygen activities, one can determine the local atomic model of the interfaces for different oxygen activity domains.

While the mixed MgO-Cu interface is made of a (001)MgO and a (001)Cu plane with their regular bulk occupancies 0.5 in the intermediate oxygen pressure, the polar interface is composed of a regular (111) copper plane and an only half occupied (111) oxygen plane in the intermediate oxygen pressure. The half occupancy corresponds to the electroneutrality of the magnesia half-crystal. At high oxygen activity, a relative oxygen excess is established by adsorption of excess oxygen to the structural vacancies of the half-occupied (111) O-terminating oxide plane in case of the polar interface or by desorption of magnesium from the regular terminating (001) oxide plane.

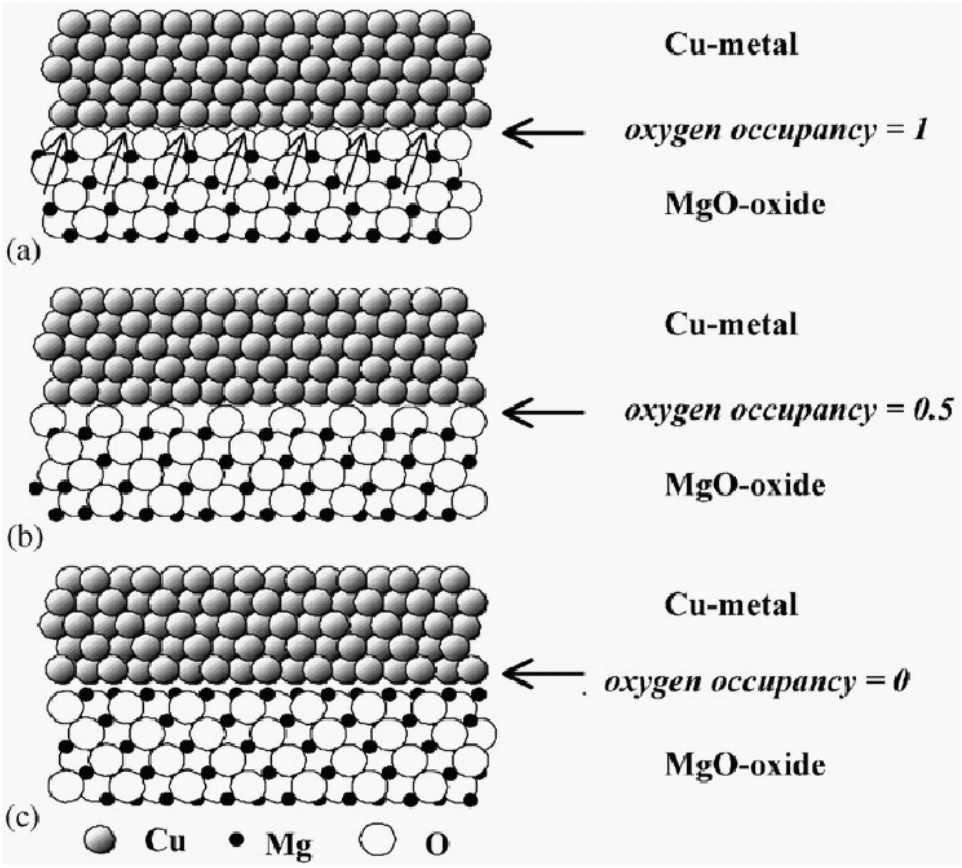

Fig. 2.6 Schematic presentation of the unrelaxed structure of the polar $(111)_{MgO}//(111)_{Cu}$ interface in the different oxygen potential domains. interface (a) with oxygen excess in the high oxygen activity range, (b) in its adsorption-free state in the intermediate oxygen activity range and (c) with relative magnesium excess in the low oxygen activity range. Possible atomic relaxation is indicated by arrows. [Backhaus-Ricoult, 2003]

At the highest oxygen activity, the O-terminating (111) oxide plane is completely occupied, see Fig. 2.6(a) and 2.5, providing then an atomically flat interface with a minimal relaxation in the interfacial area. Mixed interfaces at the same highest oxygen activity should show a high number of missing cations, see Fig. 2.7(a) and 2.5.

For not fully occupied oxygen terminating planes, more or less important structural relaxations are expected for polar interfaces, see Fig. 2.6(b) and 2.5, which conducts important perturbations of the copper lattice in proximity of the interface.

At very low oxygen activities, according to the modeling at 900 °C, relative oxygen deficiency establishes at the interface. For polar interfaces, the terminating oxide plane will then be made of Mg and will be more than half occupied, see Fig. 2.6(c) and 2.5. Mixed interfaces become Mg-rich by desorption of oxygen from the terminating mixed oxide plane, creating thereby oxygen vacancies, which induce major structural relaxation in the adjacent copper lattice, Fig. 2.7(c) and 2.5.

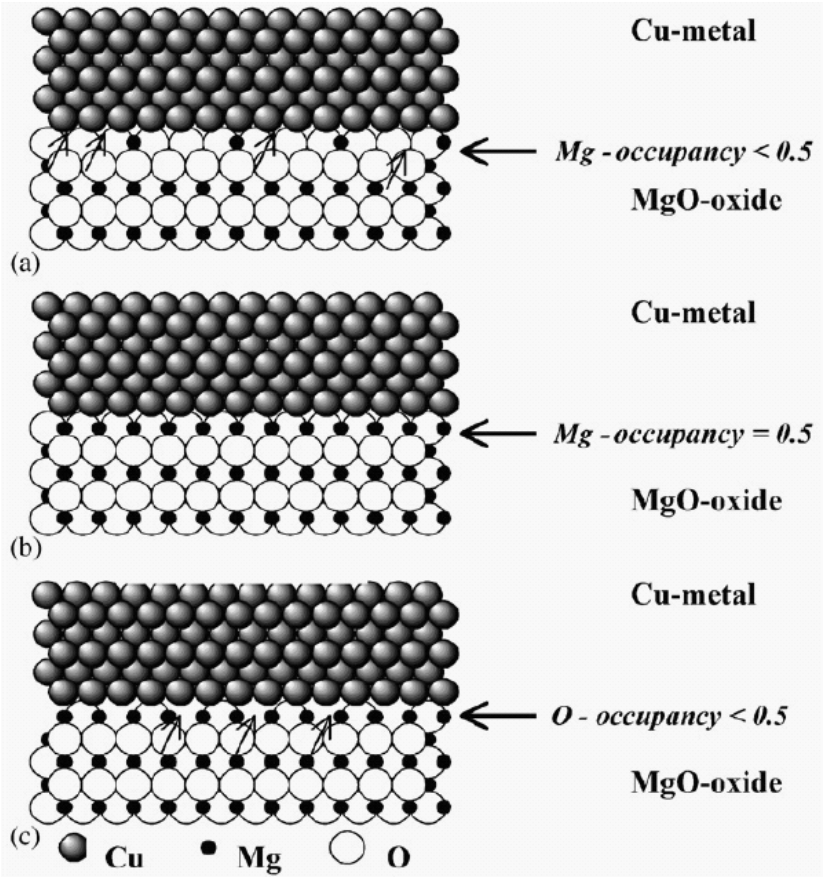

Fig. 2.7 Schematic presentation of the unrelaxed structure of the mixed $(001)_{MgO}/(001)_{Cu}$ interface in the different oxygen potential domains: (a) with oxygen excess in the high oxygen activity range. (b) in its adsorption-free state in the intermediate oxygen activity range and (c) with relative magnesium excess in the low oxygen activity range. Possible atomic relaxation is indicated by arrows. [Backhaus-Ricoult, 2003]

The interfacial specific ELNES supported the changes of terminations. At the highest oxygen activity, important rigid-body contraction/expansion across the interface is found together with a strong modification of the interfacial electronic structure (compared to the adjacent bulk phases) indicating important hybridization of O 2*p* and Cu 3*d* states. The experiments suggest local bonding between O and Cu. At lower oxygen activity, the intensity of interfacial ELNES features associated to the O 2*p* and Cu 3*d* hybridization diminishes and finally disappears with decreasing oxygen activity.

The results suggest that the terminating atomic species and the occupancy at an interface depend on the synthesizing process, especially, on oxygen activity.

2.1.5 Interfacial Local Atomic Structures

A) Formation of Misfit Dislocations

It is known that misfit dislocations are delocalized for a system with large mismatch. However, misfit dislocations with clearly visible dislocation core could be observed in the Cu/MgO system which has a large mismatch of 14 % [Chen, 1994], [Lu, 1992]. Table 2.2 gives an overview of Pd/ZnO system observed by HRTEM. At the Pd/ZnO interface $[(0001)_{ZnO}//(111)_{Pd} \cap [1\bar{1}00]_{ZnO}//[\bar{1}10]_{Pd}]$ which has a low lattice mismatch of 2 %, misfit dislocations could not be observed [Ichimori, 1996a, b]. It seems that the existence of misfit dislocations does not necessarily result from a degree of a geometrical mismatch at the interface.

The interfacial bonding also seems to be strongly related to the formation of misfit dislocation. It was suggested that an interfacial bonding between a noble metal and an oxide is induced due to an image potential (Coulomb forces (see Fig. 2.8)) caused by the charge of an ion and by the imaging charge in the metal [Stoneham, 1985], [Stoneham, 1987]. It was pointed out that a symmetric arrangement of Coulomb force vector which is often expected in such a system prevents the formation of misfit dislocations at the interface, because an electrostatic matching (stability) is already obtained [Mader, 1989].

It was reported that specific interfacial bonding type results in special orientations of misfit dislocations. A {100} surface of a NaCl type crystal possesses a neutrality of a surface charge. In such a case, the direction of the misfit dislocation in a {100}oxide/fcc metal interface can reveal whether the bonding strength of the metal-cation bond or the metal-anion bond is higher [Mader, 1992]. When a metal forms a bond with only one kind of ion of the oxide, the direction of the misfit dislocation should be along the $<110>_{NaCl}$. Then the Burgers vector should be $a/2<110>$. The Pt/NiO interface forms a bond with only one kind of ion of the oxide, because the direction of the misfit dislocation was along the $<110>_{NiO}$ [Shieu, 1990]. On the other hand, when the strengths of two kinds of bonds are the same, it can be expected that the direction should be along the <100> and then the burgers vector should be $a/2<100>$. This was experimentally observed at the Ag/MgO interface produced by MBE [Trampert, 1992]. Therefore, it seems that the existence of a misfit dislocation depends on mismatch, interfacial bonding type, and interfacial bonding strength.

Table 2.2 The interfacial misfit dislocation at Pd/ZnO interfaces observed with HRTEM. At the Pd/ZnO interface [$(0001)_{ZnO}//(111)_{Pd} \cap [1\bar{1}00]_{ZnO}//[\bar{1}10]_{Pd}$] which has a low lattice mismatch of 2 %, misfit dislocations could not be observed [Ichimori, 1996a, b], [Saito, 2001], [Murakami, 2002], [Hosson, 1998].

System	Interfacial ORs	Preparation	Mismatch	Misfit Dislocation
Pd/ZnO	$[\bar{1}10]//[11\bar{2}0] \cap$ $(0001)//(111)$	Internal Oxidation	18 %	+
Pd/ZnO	$[\bar{1}10]//[11\bar{2}0] \cap$ $(\bar{1}101)//(002)$	Internal Oxidation	16 %	+
Pd/ZnO	$[\bar{1}10]//[1\bar{1}00] \cap$ $(0001)//(111)$	Internal Oxidation	2 %	-

B) Detailed Structure of Misfit Dislocation

Two formation mechanisms of misfit dislocation during diffusion bonding were suggested [Knauss, 1991].

(1) After a lattice dislocation in a metal is translated to an interface via a climbing or a slipping process, a misfit dislocation is formed by arranging to lowest energy sites [Matthews, 1970].
(2) A misfit dislocation can be generated as a dislocation of Van-der-Merwe type at an interface and then via a climbing process a ‘stand-off’ position can be obtained.

The mechanism depends strongly on the supply of vacancies [Mader, 1989]. Most likely, the formation of a misfit dislocation seems to be due to the mechanism (1) for MBE growth or due to the mechanism (2) for internal oxidation.

It was also reported that the position of the core of a misfit dislocation can be determined by a balance between a repulsive forces due to elastic strain fields and an attractive force across the interface [Kamet, 1988]. The Mo/Al_2O_3 interface showed that a misfit dislocation was located at the interface while at the Nb/Al_2O_3 interface a misfit dislocation with stand-off position was observed. This was caused by the higher elasticity of Mo compared to Nb [Tricker, 1995a, b].

In order to examine a relationship between misfit dislocation core structure and an

interfacial bonding strength, the relaxed structure of the Nb/Al_2O_3 interface was calculated by assuming a simple potential [Klomp, 1987]. Klomp and coworkers concluded that (1) a large interfacial bonding forms a stand-off structure and (2) a large misfit does not show a relaxed structure.

The detailed structure near a misfit dislocation seems to be affected by process temperature, elastic constants of crystals, interfacial bonding strength, and mismatch.

2.1.6 Theoretical Calculations for Metal/Oxide Interfaces

A) Image Charge Theory

First principle calculations by Kohyama [Kohyama, 1999] suggested that an interfacial bonding strongly depends on (i) each bonding type in the bulk components, (ii) their combination, (iii) the interfacial orientation, (iv) the stoichiometry, and (v) the terminating atomic species. An interface can be largely classified into two categories.

No reaction layer is usually formed at noble-metal/oxide interfaces while at a transition-metal/covalent ceramic interface most likely a reaction layer is being formed. The latter behavior is a consequence that it is attributed to a strong chemical bonding. Although a nonreative interface also forms weak bonds, the formation mechanism of the interface remained unclear.

As an example for the formation mechanism in the non-reactive interface, an imaging potential model was suggested to explain the interfacial bonding [Tasker, 1987]. In such a nonreactive interface, an orbital hybridization or a charge transfer is not remarkable. The main interactions are an electrostatic interaction across the interface, which is completely different from that in a reactive interface.

Stoneham and Tasker provided the ‘imaging charge theory’ which is a simple physical concept to understand quantitatively the adhesion of metals to ionic crystals [Stoneham, 1987]. Based on classical electrostatics, this ‘image charge theory’ can describe the interaction between a polarizable metal and an ionic crystal due to Coulomb forces. Positioning a charge in front of a metal surface causes quasi-free charges in the metal surface to rearrange and create a charge distribution as shown in Fig. 2.8. The electric field across the interface is the same as if an image charge with opposite sign also was placed in the metal. As a consequence, the charge of the ion can be attracted due to Coulomb force towards the interface.

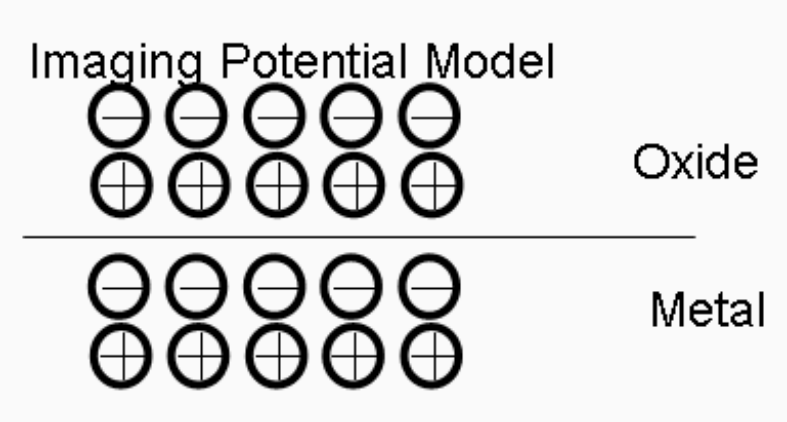

Fig. 2.8 Imaging potential model [Stoneham, 1985], [Stoneham, 1987], [Kohyama, 1999]. Positioning a charge in front of a metal surface causes quasi-free charges in the metal surface to rearrange and create a charge distribution.

Many experimental observations supported the image charge theory. The wetting behaviors of non-reactive metals on oxide substrates mainly depends on the ionic behavior of the oxide, as expected by the image charge theory. Moreover, wetting data revealed that metals most probably wet oxides with defect structure. The image charge theory explains this trend by the interaction of point defects with metal-oxide interfaces. Disorder in the oxide implies charged point defects, which create further image charges in the metal, and the attractive interaction between the charged defects and their image charges increase the adhesion of the metal to the oxide.

First principle calculations for the (001)MgO/Al and the (001)MgO/Ag interfaces without a mismatch supported the model [Smith, 1994], [Hong, 1994]. The (001)MgO surface is a non-polar plane consisting of both O and Mg. The geometry of Al or Ag atom on top of O atom results in an energy minimum. The local density of states indicates only little change of the band structure near the Fermi level and little orbital hybridization. Furthermore, the charge density in the metal increased in front of the Mg atoms while it decreased in front of the O atoms. This agrees with the expectation of the image charge theory as shown in Fig. 2.8.

B) Species of Terminating Plane

The polarity of the oxide ceramic, its stoichiometry, and the terminating atomic species strongly affect the interfacial behavior. Atomic geometries and adhesive energetics as computed from first principles were presented by Smith et al. [Smith, 2000] for stoichiometric (111)Al/(0001)Al_2O_3 and (111)Ag/(0001)Al_2O_3 interfaces and for the

(0001)Al_2O_3 surface. Smith et al. found the (0001)Al_2O_3 surface energy to be 2.150 J/m^2, in reasonable agreement with earlier results. For Al/Al_2O_3, they found the metal equilibrium configuration to be on top of Al atoms of the alumina, with a work of adhesion of 1.078 J/m^2. For Ag/Al_2O_3, the work of adhesion is determined to be 0.672 J/m^2, and they found the Ag atoms to be in the (3-fold oxygen) hollow sites. These works of adhesion appear to be reasonably consistent with experimental data for solid Al or Ag on Al_2O_3. Benedek [Benedek, 1996] calculated that the interfacial energy of the O-terminated (111)MgO/Cu interface is larger than that of the (001)MgO/Cu interface which terminates by both atomic species. Actually the HRTEM image showed occurrence of the O-terminated (111)MgO/Cu interface [Jang, 1993], [Shashkov, 1995]. This means that a polar interface and the specific terminating atomic species provide stable interfaces .

The *first principle* calculation for the (0001)Al_2O_3/Nb interface revealed also the importance of the terminating layer [Kruse, 1996]. The interaction across Al-terminated (0001)Al_2O_3/Nb interface had non-reactive character. On the contrary, the O-terminated (0001)Al_2O_3/Nb interface possesses a strong mixed ionic and covalent bonding.

Even for non-oxide ionic crystals, the weak polarity strongly affects the interfacial behavior. Hoekstra calculated the electronic structures of the (001)SiC/Al interfaces [Hoekstra, 1998]. The Si-terminated (001)SiC/Al interface possesses the most stable structure. The interfacial Si atoms contact two Al atoms originating in 4-fold coordinations. The C-terminated (001)SiC/Al interface possesses also a stable atomic structure. The interfacial C atoms sit on top of Al atoms and are 3-fold coordinated. The charge density between C-Al was similar to the backbond of Si-C, indicating a strong mixed covalency and ionicity between C-Al. Furthermore, the electrons around the Al atom are attracted towards the C atom resulting in a remarkable decrease of the electron distribution around the Al atom.

The local density of states between Si-Al indicates the similarity to the LDOS of Al, indicating metallic character. The leaking of the metallic states into the semiconductor side forms a continuous state within the band gap. This has been known as MIGS (Metal-induced Gap State). It can be considered that the MIGS in the semi conductor can be occupied until the boundary area is locally neutralized. On the other hand, the LDOS between the C-Al bond is similar to the Si-C backbond. However, the LDOS between Si-C bond is not similar to the bulk C-Si bond. It seems that the chemical environment around the interfacial C atom was largely changed due to interfacial specific 3-fold coordinates and that then formed interface specific electronic states.

The interfacial energy for the Si-terminated SiC/Al interface is 3.74 J/m^2 while the interfacial energy for the C-terminated SiC/Al interface is 6.42 J/m^2, indicating that the C-terminated surface can be more easily bonded with an Al layer. Since the interfacial energy between bulk (0001)Al layers is 2.04 J/m^2, the interfacial bonding strength is stronger than that in the bulk [Smith, 1994]. Since the energy for the (001)MgO/Al interface is 1.10 J/m^2 [Smith, 1994], the reactive SiC/Al interface clearly is stronger than a non-reactive interface.

2.1.7 Summary

Interfacial orientation relationships between metal and oxide are influenced by terminating atomic species of the oxide, local atomic structure, local chemical bonding, combination in the system, polarity of the oxide, degree of mismatch, stiffness or elasticity of the oxide, synthesizing method, and synthesizing temperature. Many experimental and theoretical results provide much new insight into the structure and chemistry of the interfaces. The polarity of the oxide plays an important role for interfacial local behaviors in polar metal/oxide interfaces.

So far many TEM studies for metal/oxide interfaces were performed without quantitative analysis. This may cause a problem for an accuracy to determine the interfacial local atomic structure. Therefore, it is not so easy to conclude the interfacial behaviors at atomic level only by the results obtained without quantitative analysis. Furthermore, dependency of local atomic/electronic structures at the polar interface on polarity of oxide has not yet analyzed in detail.

2.2 Pd/ZnO System

Several quantitative analyses of HRTEM images for the 'ideal' model systems with reasonably good lattice matching, e.g., $Al/MgAl_2O_4$ [Schweinfest, 1998] and $Pd/SrTiO_3$ [van Benthem, 2002], [Tchernychova, 2004], contributed to understand the behavior of metal/oxide interfaces. For actual applications, a more complex situation may be encountered. Therefore, it is also essential to examine the interfacial behaviors of the more general model system which includes a lattice mismatch, a polarity of oxide, and a heterophase boundary. In this thesis, the Pd/ZnO system will be investigated.

The noble metal Pd is important for electrode material. Preliminary studies, although without quantitative analysis, also exist for a variety of Pd/oxide systems: Pd/Al_2O_3 [Dehm, 1996], Pd/MgO [Chen, 1994], [Lu, 1992], Pd/NiO [Merkle, 1990], Pd/ZnO [Ichinose, 1994], [Ichinose, 1994b], [Ichimori, 1996a], [Ichimori, 1996b], [Groen, 1998], [Saito, 2001], [Murakami, 2002]. ZnO is widely used due to its applications in electronics.

In this section, the experimental and theoretical results for the Pd/{0001}ZnO interfaces are summarized. Furthermore, in this work, the atomic structure near the Pd/ZnO interface produced by MBE will be compared with that near the ZnO surface prior to Pd deposition. For this reason, literature studies on {0001}ZnO surfaces are also summarized.

2.2.1 Nomenclature

To simplify the description of the ZnO surfaces and the Pd/ZnO interfaces, we will use the following nomenclature for the different possible ZnO surfaces and Pd/ZnO interfaces.

ZnO crystallizes in the wurzite structure with lattice parameters of $a = 0.325$ nm and $c = 0.521$ nm. When either kind of atom of the ZnO is located at the center of the tetrahedron, then the other type of atom occupy the four apexes of the tetrahedron. The center atom is 4-fold bonded with the 4 other kinds of atoms. The angle between these bonds is 109.471°. The projected structure of the ZnO along the $<11\bar{2}0>$ zone axis is shown in Fig. 2.9. The longer Zn-O projected bonding distance represents the real bonding length of 0.198 nm while the short Zn-O projected distance which corresponds to the so-called dumbbell is 0.114 nm in Fig. 2.9. The short dumbbell hides two bonds. The terminating atom possesses 1 or 3 dangling bonds (3 or 1 back bonds) as shown in Fig. 2.9. The $^{+}$**ZnO** and $^{-}$**ZnO** surfaces are polar planes which can be O- or Zn-terminated. This means that the {0001}ZnO surfaces can be classified into 4 kinds of surfaces.

(0001)ZnO surface → $^{+}$**ZnO** surface $(000\bar{1})$ZnO surface → $^{-}$**ZnO** surface

Zn-terminated (0001)ZnO surface → $^{+Zn}$**ZnO** surface

O-terminated (0001)ZnO surface → $^{+O}$**ZnO** surface

Zn-terminated $(000\bar{1})$ZnO surface → $^{-Zn}$**ZnO** surface

O-terminated $(000\bar{1})$ZnO surface → $^{-O}$**ZnO** surface

Pd/(0001)ZnO interface → **Pd/**$^{+}$**ZnO** interface

Pd/$(000\bar{1})$ZnO interface → **Pd/**$^{-}$**ZnO** interface

Pd/Zn-terminated (0001)ZnO interface→ **Pd/**$^{+Zn}$**ZnO** interface

Pd/O-terminated (0001)ZnO interface→ **Pd/**$^{+O}$**ZnO** interface

Pd/Zn-terminated $(000\bar{1})$ZnO interface→ **Pd/**$^{-Zn}$**ZnO** interface

Pd/O-terminated $(000\bar{1})$ZnO interface→ **Pd/**$^{-O}$**ZnO** interface

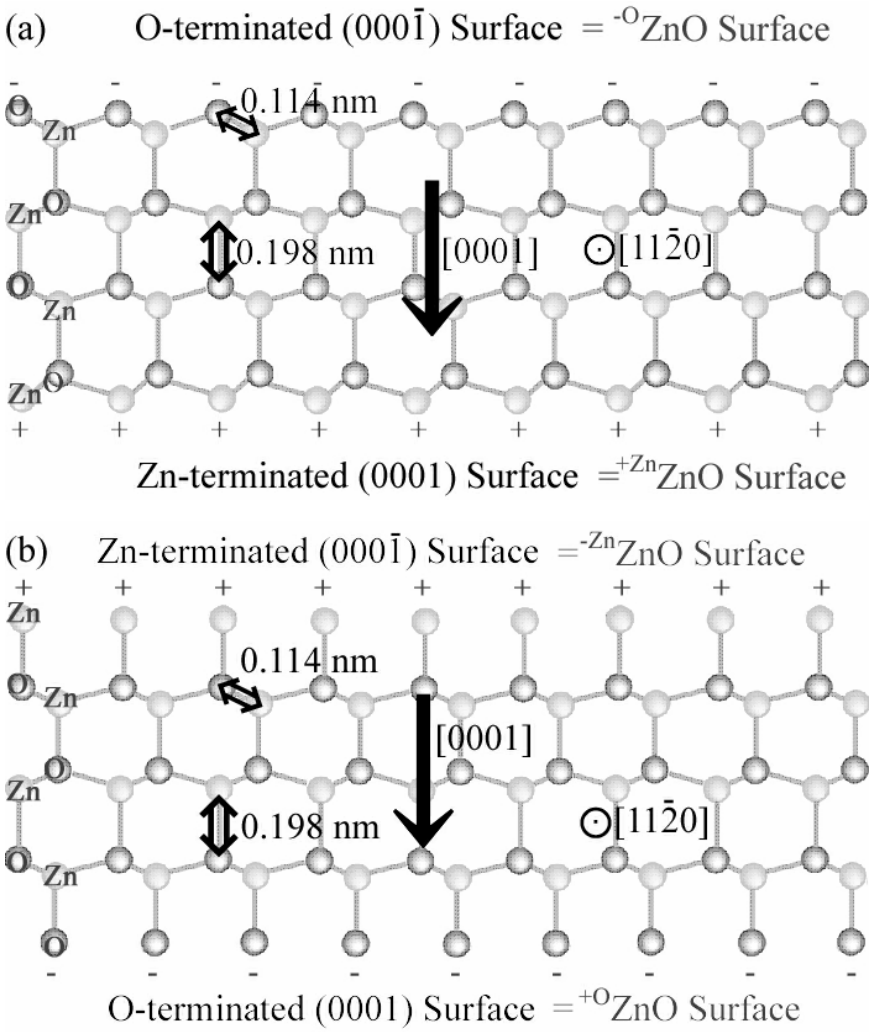

Fig. 2.9(a)(b) Projected structure of the ZnO crystal along the $<11\bar{2}0>_{ZnO}$ zone axis. ZnO has dipole moments caused by Zn-O dimmers. It cannot be cancelled along the *c*-axis. For this reason, $[0001]_{ZnO}$ direction should be distinguished with $[000\bar{1}]_{ZnO}$ direction. (a) Individual terminating atom possesses 1 dangling bond. (b) Individual terminating atom possesses 3 dangling bonds. There exist 4 possible $\{0001\}$ZnO surfaces.

2.2.2 Surfaces of ZnO

Topmost Atomic Occupancy on ZnO Surface

Jedrecy quantified the local atomic structures of a $^{+}$**ZnO** surface by X-ray diffraction studies by using the CTR (Crystal Truncation Rod) measurements [Jedrecy, 2000]. Jedrecy prepared the surfaces very carefully by iteration of annealing in oxygen radicals and in UHV in order to flatten the surface and to remove surface impurities. After final annealing in UHV, the CTR measurements revealed that the topmost atomic species is Zn and the Zn toplayer of the surface has the spatial occupancy (coverage) of 75 at%. Furthermore, Dulub cleaned [Dulub, 2003] a $^{+}$**ZnO** surface by cycles of 1 ~ 2 keV Ar^{+} sputtering and annealing in UHV at 600 ~ 750 °C for 5 ~ 30 min. His STM images showed many triangular hollows and islands on the $^{+}$**ZnO** surface which has several specific sizes and a step height of $c/2$ (c: lattice constant). For example of the island, all islands locally have a stoichiometry of ratio of 75: 100 = Zn: O.

Although Jedrecy and Dulub treated to the ZnO surface via different ways, the results concerning stoichiometry of the surfaces were identical. This value can be explained by considering an instability of atomically flat {0001}ZnO surfaces.

Instability of Flat {0001}ZnO Surfaces

ZnO has dipole moments formed by Zn-O dimers [Noguera, 2000], corresponding to dumbbell in Fig. 2.10. These dipole moments generate an electrostatic field which can be annihilated along all in-plane directions on the {0001} plane. However, the electrostatic field cannot be annihilated along the c-axis of ZnO if the surface is atomically flat, suggesting that a linear sum of electrostatic fields will diverge to infinity along the c-axis. Then, the surface energy can also be diverged to infinity. The instability of an atomically flat {0001}ZnO surface is theoretically predicted. An open question is how can the electrostatic field be annihilated? This question will be considered in following.

Stabilizing Mechanism of Flat {0001}ZnO Surface

Noguera [Noguera, 2000] explained three stabilizing mechanisms of the flat {0001}ZnO surface owing to cancellation of the unpreferable electrostatic field caused by dipole moments of the ZnO. The electronic field should be annihilated by a surface charging. The surface charging can be supplied by (i) real surface charges, (ii) surface impurities, or (iii) virtual charging due to the partial absence (coverage) of the topmost ions.

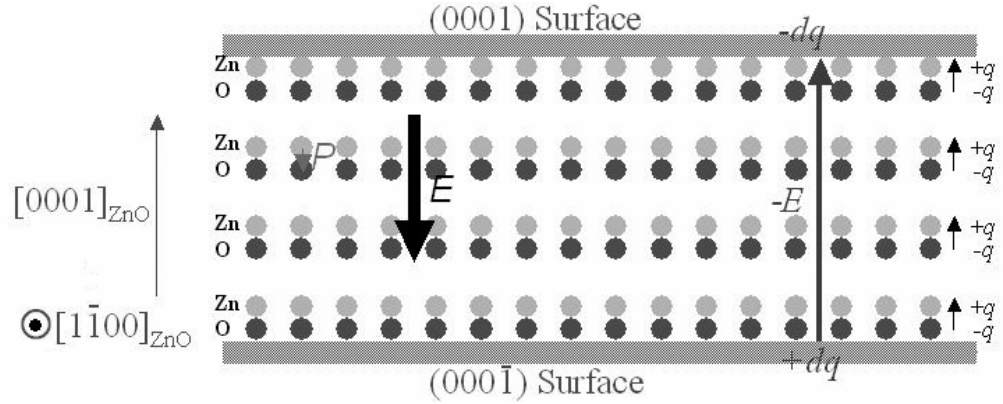

Fig. 2.10 Explanation for electrostatic self-stabilization mechanism. If the number of bi-layers which are consisted of Zn and O layer along the *c*-axis is infinite or very large, then the surface charge would be $dq = \mp q/4$, where q $(= \pm 2e)$ is the ionic charge of the ZnO and dq is the required surface charge which should be of opposite sign for the ionic charge q. [Noguera, 2000]

Noguera calculated also the required surface charge value to cancel the unpreferable electrostatic field from the ZnO. Since the electrostatic field caused by the dipole moments P should be cancelled due to an electrostatic field caused by the surface charge dq. P should be satisfied by equation (2-5), where c is lattice constant of ZnO along the *c*-axis.

$$P = q\left(\frac{3c}{8}\right) - dq\left[(N-1)\frac{c}{2} + \left(\frac{3c}{8}\right)\right] = 0\,. \tag{2-5}$$

If the number N of bi-layers which are consisted of Zn and O layer along the *c*-axis is infinite or very large, then the surface charge dq is given by equation (2-6).

$$|dq| = \frac{q}{4 - \frac{1}{N}} \rightarrow \frac{q}{4}\,. \tag{2-6}$$

Then, the surface charge would be $dq = \mp q/4$, where q $(= \pm 2e)$ is the ionic charge of the Zn and O and dq is the required surface charge which should be of opposite sign of the ionic charge q (see Fig. 2.10). The expected surface charge can be obtained by (ii) a 'real' surface charging or (iii) 'virtual' surface charging in the case of an impurity free surface. Surprisingly, this situation can be fulfilled, if 25 % of the topmost Zn atoms are missing (surface coverage of 75 % of the Zn layer). This theoretical expectation completely agrees with the experimental results by Jedrecy [Jedrecy, 2000] and Dulub [Dulub, 2003]. It can be concluded that the atomically flat $^{+}$**ZnO** surfaces is self-stabilized due to vacancies of ions in the toplayer. STM images taken by T. M. Parker [Parker, 1998] showed many triangular hollows and islands on the $^{-}$**ZnO** surface as well as on the $^{+}$**ZnO** surface. The both surfaces seem to be stabilized by the same mechanism.

2.2.3 Pd/ZnO Interfaces

So far, the Pd/ZnO interfaces produced by internal oxidation were investigated [Saito, 2001], [Murakami, 2003], [Ichimori, 1996a, b], [Groen, 1998].

A) Shape of Precipitates [Saito, 2001]

Small ZnO crystals were precipitated in a Pd matrix by internal oxidation of a Zn-Pd alloy. A bright field image taken along the $[11\bar{2}0]_{ZnO}$ zone axis [Fig. 2.11 (left)] shows that ZnO precipitates have rod-like (plate) shapes. TEM observations revealed that there exist four kinds of precipitates (four crystal orientation relationships). The diffraction pattern in Fig. 2.11 (right) suggested that the ZnO precipitates are mainly the wurtzite structure with a lattice parameters of $a = 0.325$ nm and $c = 0.521$ nm, rarely zincblende structure. The Pd matrix (fcc) has a lattice parameter of $a = 0.389$ nm.

B) Interfacial Orientation Relationships [Saito, 2001]

Table 2.3 and 2.4 show the observed interfacial orientation relationships. The large grown interfaces are marked as A, E, F, I, and J for each precipitate. The short interfaces are marked as B, C, D, G, and H. Since the larger interfaces A, E, F, I, and J are parallel to polar plane of the ZnO, the polar interfaces seem to contribute to the stability of the Pd/ZnO system. The largest interface corresponds to the interface A (OR1: $(0001)_{ZnO}//(111)_{Pd} \cap [11\bar{2}0]_{ZnO}//[\bar{1}10]_{Pd}$). This orientation relationship has a lattice mismatch of 18 % at the interface (between Pd and ZnO).

C) Interfaces of Main Precipitate (Crystal OR1) [Saito, 2001]

Almost all precipitates possess an orientation relation OR1, which have a thickness of 0.01 ~ 1 μm and a length of 0.1 ~ 5 μm, resulting in a relatively large interface A, and short subsidiary interfaces B and C (see Fig. 2.12). Since these interfaces B, C are not exactly parallel to the low index facets of Pd but parallel to $[\bar{1}101]_{ZnO}$, $[1\bar{1}01]_{ZnO}$, respectively, such interfaces B and C must include steps which involve energetically unstable. Nevertheless, almost all precipitates belong to OR1 which includes such steps. This also suggests that a polar interface (A) strongly contributes the energetical stability for the system.

D) Local Atomic Structures of Main Interfaces [Saito, 2001]

Furthermore, the polar interface A was examined in detail. The interface A has two equivalent interfacial orientation relationships: the **Pd/$^{-}$ZnO** and **Pd/$^{+}$ZnO** interfaces.

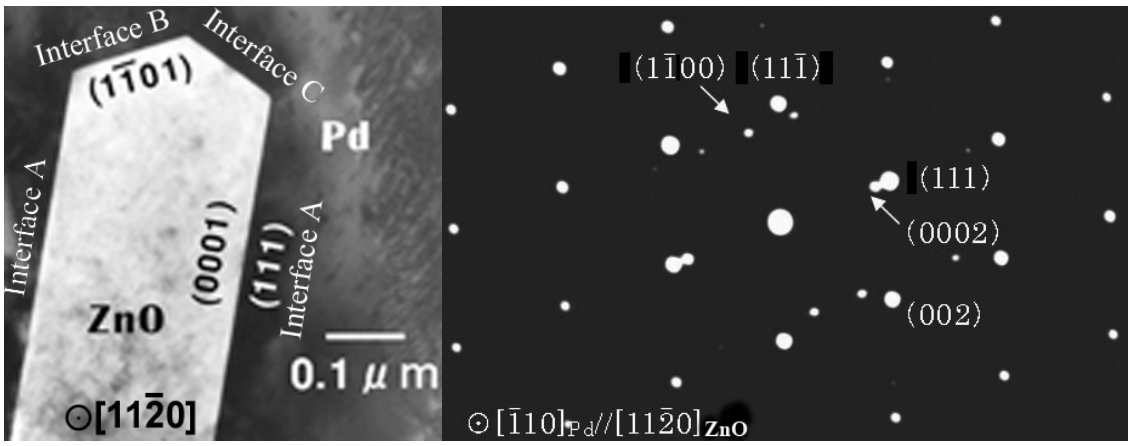

Fig. 2.11 A bright field image [left] taken along the $[11\bar{2}0]_{ZnO}$ zone axis shows ZnO precipitates have rod-like (plate) shapes in a Pd matrix. Right image is the diffraction pattern [Saito, 2001].

Table 2.3 Interfacial orientation relationships between Pd and ZnO precipitates with wurtzite structure [Saito, 2001]. *) frequently observed.

Crystal OR1* $(0001)_{ZnO}//(111)_{Pd} \cap [11\bar{2}0]_{ZnO}//[\bar{1}10]_{Pd}$

Interface	Interfacial OR	Polarity
A**	$(0001)_{ZnO}//(111)_{Pd} \cap (000\bar{1})_{ZnO}//(\bar{1}\bar{1}\bar{1})_{Pd}$	Polar
B	$(1\bar{1}01)_{ZnO}//(002)_{Pd\ with\ step}$	Polar
C	$(\bar{1}101)_{ZnO}//(11\bar{1})_{Pd\ with\ step}$	Polar
D	$(1\bar{1}00)_{ZnO}//(11\bar{2})_{Pd}$	Nonpolar

Crystal OR2 $(0001)_{ZnO}//(111)_{Pd} \cap [1\bar{1}00]_{ZnO}//[\bar{1}10]_{Pd}$

Interface	Interfacial OR	Polarity
E*	$(0001)_{ZnO}//(111)_{Pd}$	Polar

Crystal OR3 $(0001)_{ZnO}//(002)_{Pd} \cap [11\bar{2}0]_{ZnO}//[\bar{1}10]_{Pd}$

Interface	Interfacial OR	Polarity
F*	$(0001)_{ZnO}//(002)_{Pd}$	Polar
G	$(1\bar{1}00)_{ZnO}//(220)_{Pd}$	Nonpolar
H	$(\bar{1}101)_{ZnO}//(111)_{Pd\ with\ step}$	Polar

Table 2.4 Interfacial orientation relationships between Pd and ZnO precipitates with zincblende structure [Saito, 2001]. *) frequently observed.

Crystal OR4 $(111)_{ZnO}//(111)_{Pd} \cap [\bar{1}10]_{ZnO}//[\bar{1}10]_{Pd}$

Interface	Interfacial OR	Polarity
I*	$(111)_{ZnO}//(111)_{Pd}$	Polar
J*	$(002)_{ZnO}//(002)_{Pd}$	Polar

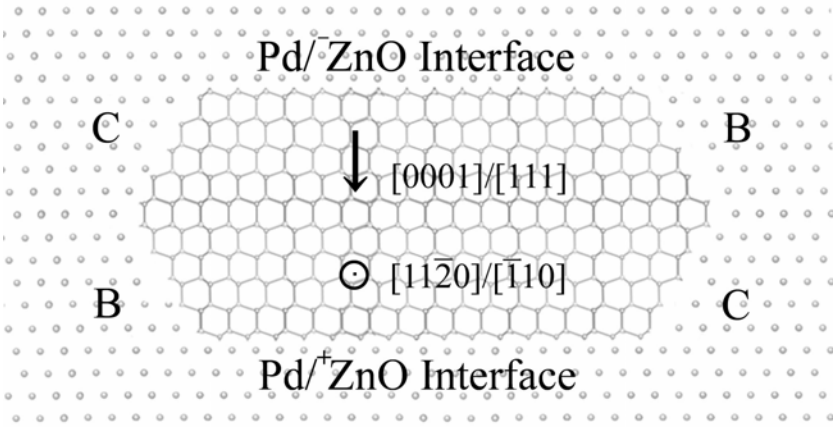

Fig. 2.12 Schematic diagram of the main ZnO precipitate in Pd matrix. Almost all precipitates possess an orientation relation OR1, which have a thickness of 0.01 ~ 1 μm and a length of 0.1 ~ 5 μm, resulting in a relatively large interface A, and short subsidiary interfaces B and C [Saito, 2001].

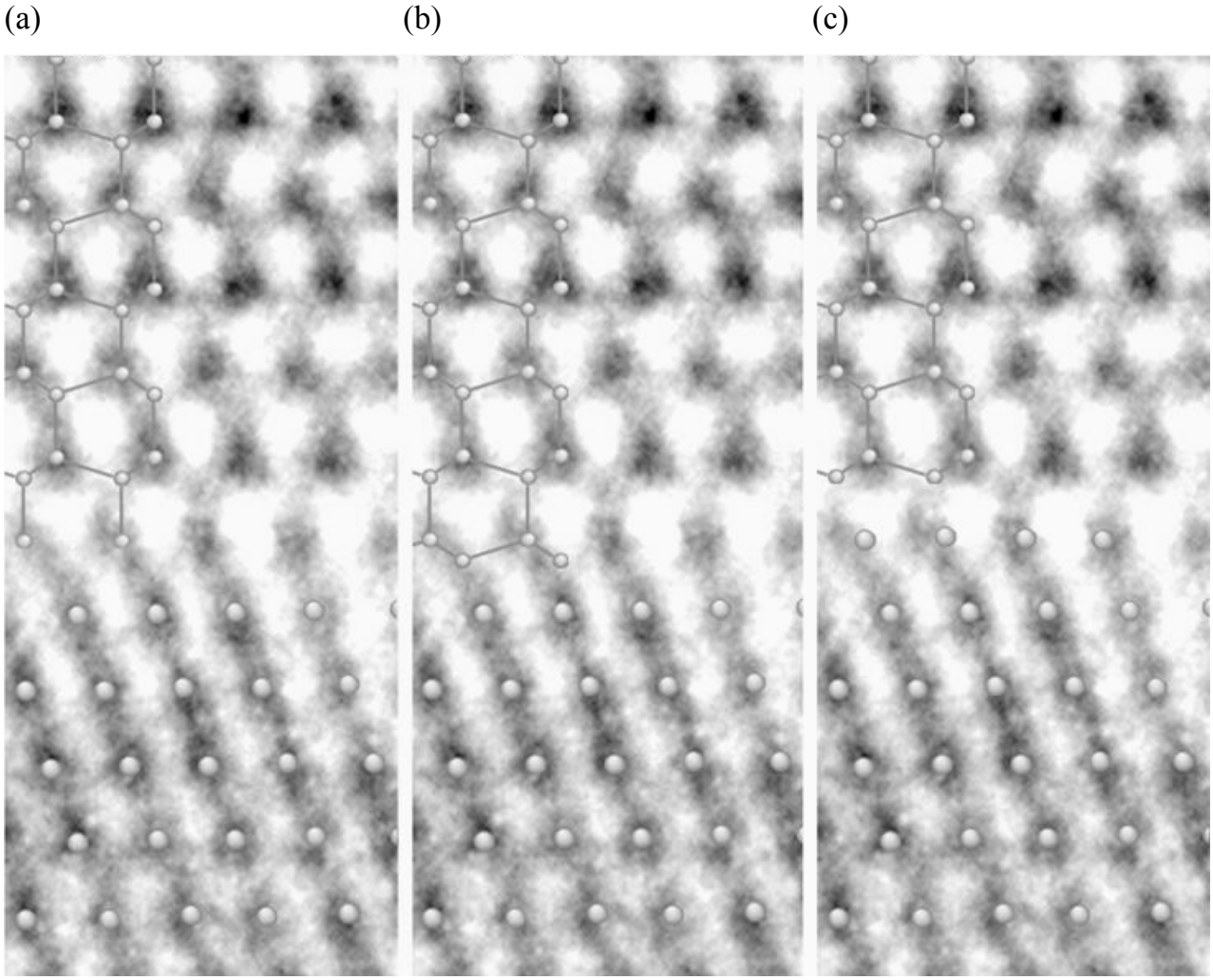

Fig. 2.13 ARM images of the **Pd/$^{-}$ZnO** interfaces with model: (a) Case1: Zn-terminated, (b) Case2: O-terminated, (c) Case3: O-terminated [Saito, 2001]. The simulation for ZnO revealed that columns of Zn ions are imaged as a black spot with lower intensity while O atomic columns are imaged with light gray color (higher intensity).

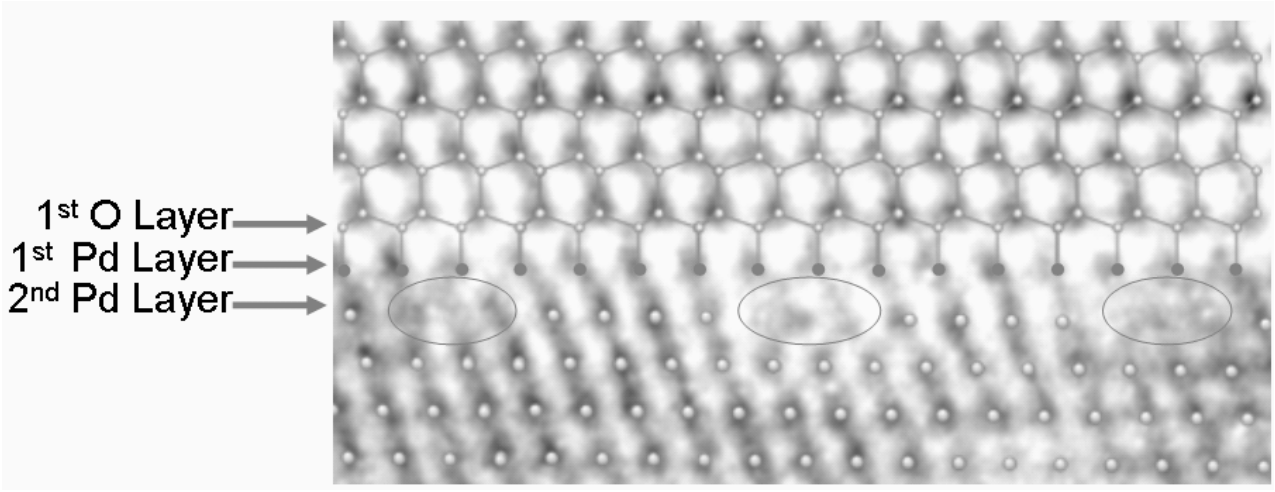

Fig. 2.14 ARM image of the **Pd/ZnO** interface with the model of case 3. It can be seen that the atom positions of ZnO matches perfectly to contrasts while the positions of almost all Pd atoms are also the same as that in bulk Pd except the first and second Pd layer. [Saito, 2001]

Analysis of local atomic structures at these interfaces was performed with a JEOL JEM-ARM1250 (Tokyo ARM) at the University of Tokyo.

D-1) **Pd/ZnO** Interface

ARM images of the **Pd/ZnO** Interfaces were taken along the $[11\bar{2}0]_{ZnO}//[\bar{1}10]_{Pd}$ zone axes as shown in Fig. 2.14. ZnO forms the upper crystal while Pd forms the lower crystal. It can be seen that there are misfit dislocations near the interface in the lower crystal (Pd). The periodicity is ~1.5 nm. The ARM image shows both coherent interface areas ('CIA' in where the image of the interfacial atomic columns are clearly resolved) and diffuse interface areas ('DIA' in where the image of the interfacial atomic columns are not clear) in ZnO layer at the interface. Those contrasts alternate and are periodically repeated. DIA were not analyzed, because it is most likely that the simulation for DIA is not possible. Therefore, the region including only CIA was defined and the local atomic geometry near the CIA was analyzed by simple inspection only.

The simulation for bulk ZnO revealed that columns of Zn ions are imaged as a black spot with lower intensity while O atomic columns are imaged with light gray color (higher intensity). According to the simulation, the position of each atomic column was simply plotted by continuating the bulk region into the interfacial region and extended to the interface. However, the plots close to the interface must be discussed in detail. Three cases are considered as shown in Fig. 2.13.

Case 1 shows that the assumed interfacial Zn atoms sit at the centers of black columns on

the image, however, the projections of the columns on the assumed interfacial Zn atoms are less wide than that in bulk ZnO. This indicates that this model is not possible.

Case 2 shows that the columns on the assumed interfacial O have higher intensities (brighter) than that in bulk ZnO. For this situation, the interfacial distance is below 0.15 nm, indicating that this is also not an appropriate case.

Case 3 shows that the positions of the assumed interfacial O atoms coincide on the contrasts corresponding to O ions. However, this assumption gives rise to incoherency between the positions of the assumed interfacial Pd atoms and the black spots on the image as shown in Fig. 2.13. If the assumed interfacial Pd atoms relax to fit the juxtaposing ZnO lattice, the coincidence between both lattices would be better. Furthermore, the size of the column is quite similar to that in bulk Pd. Therefore, it seems that case 3 is close to a realistic situation and Pd lattice seems to accommodate.

Fig. 2.14 shows the ARM image with the model of case 3. It can be seen that the atom positions of ZnO matches perfectly to contrasts while the positions of almost all Pd atoms are also the same as that in bulk Pd except the first and second Pd layer. The atomic positions of the first Pd layer next to ZnO are shifted so that they coincide with the unrelaxed ZnO lattice. The second Pd layer includes diffuse interface areas (DIA) marked by ellipsis in Fig. 2.14, where atomic columns cannot be recognized, and also coherent interface areas (CIA). It can be seen that the half planes of $(11\bar{1})_{Pd}$ at the CIA can be contacted to ZnO without any strong relaxations while the other half planes must involve DIA at the interface. They cannot be connected with the ZnO lattice. Nevertheless, all interfacial Pd atomic positions nearly fit to the ZnO lattice. The observations suggest that the edge dislocation is positive near the region including the DIA and stand-off which has a distance to the interface. The ‘stand-off’ of dislocation may be attributed to high a diffuse activity due to the specimen preparation at high temperature (1000 °C) and stresses due to large lattice mismatch. Mader also observed stand-off dislocation in the Nb/Al_2O_3 system [Mader, 1989].

The studies done so far revealed that the periodicity of the relaxation can perfectly explain the mismatch, the **$\bar{}$ZnO** is terminated by O, the Pd crystal relaxes, the edge dislocation core has a stand-off. However, the detailed atomic structure of these defects can only be understood with quantitative image analysis.

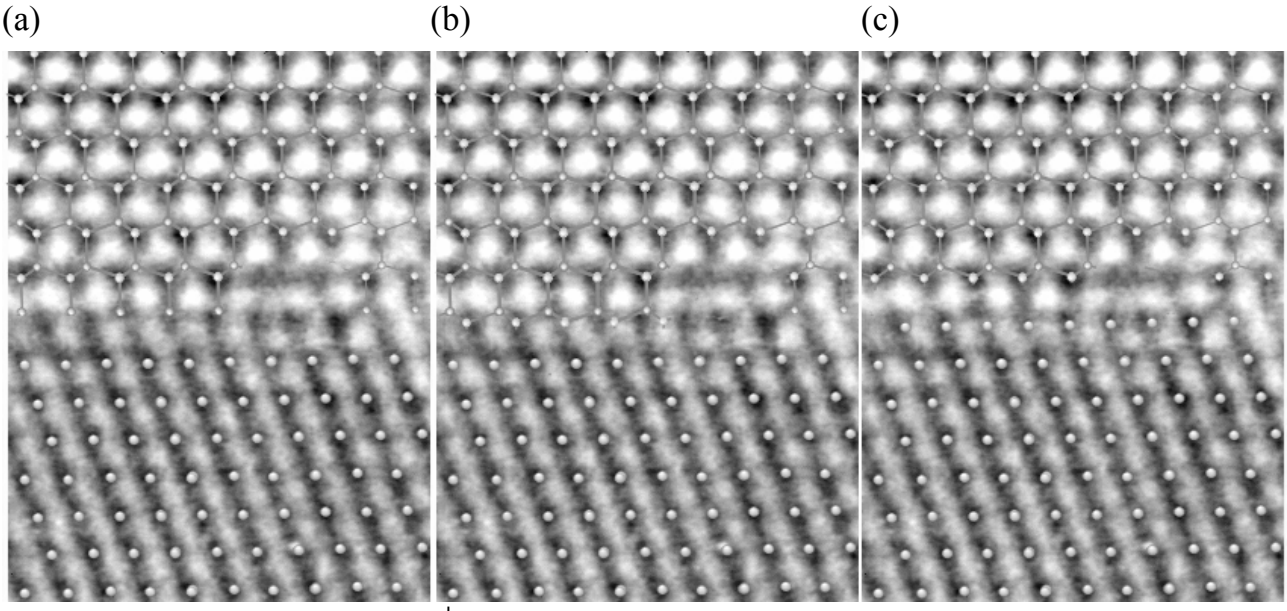

Fig. 2.15 ARM images of the **Pd/$^{+}$ZnO** interfaces with model taken under specific condition along the $[11\bar{2}0]_{ZnO}//[\bar{1}10]_{Pd}$ zone axes.: (a) Case4: O-terminated, (b) Case5: Zn-terminated, (c) Case6: Zn-terminated. This interface is also relaxed. [Saito, 2001].

D-2) **Pd/$^{+}$ZnO** Interface

Fig. 2.15 shows the HRTEM image of the **Pd/$^{+}$ZnO** interface taken under specific condition along the $[11\bar{2}0]_{ZnO}//[\bar{1}10]_{Pd}$ zone axes. This interface is also relaxed. Two regions of DIA and CIA alternate and are periodically repeated at the interface. The picture was evaluated as in the section D-1. The HRTEM micrographs in Fig. 2.15 were compared to structural models (Case 4 to Case 6) by simple inspection.

Case 4 shows that all interfacial O atoms are not positioned at the centers of columns on the image. Even if the assumed O atoms were shifted to fit on the half planes of the Pd lattices, the intensity of the column is too low (dark) compared to that of O atoms in bulk ZnO, indicating that this model cannot be correct.

Case 5 shows that the coincidence between the positions of the assumed interfacial Zn atom and the contrast centers is worse than in the bulk region, indicating that this is also not a possible structure. If the assumed interfacial Zn atoms were relaxed, then the interfacial distance would be extremely short which is not likely.

Case 6 shows that a coincidence between the assumed interfacial Zn atomic position and the column is much better. Furthermore, the coherency between the half planes of the interfacial Pd and the Zn is much better. Moreover, the contrasts of columns on the assumed interfacial Pd atoms are quite similar to that in bulk Pd region. Therefore, it seems that Case 6 seems to be near real case.

It can be seen that the positions of all ions are the same as that in bulk region except DIA in the first Zn layer. The positions of the interfacial Pd atoms also are the same as that in bulk Pd. Pd does not relax. The interfacial Zn layer accommodates the misfit. This is an unusual relaxation in a metal/ceramic system. If we distinguish an atom at an interface with an atom in a bulk, the relaxation of the interfacial atoms of ZnO might be explained. We should notice a specific environment around an atom, especially at an interface. However, so far these phenomena cannot be explained.

The studies done so far revealed different behaviors between the **Pd/$^{-}$ZnO** interface and the **Pd/$^{+}$ZnO** interface. In spite of the same system, the relaxed crystal depends on the sign of polarity.

However, it is dangerous to assure these results determined by simple inspection. Complicated image contrast within Zn-O dumbbell and similar contrasts between Zn and Pd makes it difficult to determine the local interfacial atomic structure. A quantitative analysis is essential for conclusive results for the **Pd/$^{+}$ZnO** interface as well as the **Pd/$^{-}$ZnO** interface.

The results produced here should be compared to the results obtained by a quantitative analysis for the Pd/ZnO interfaces produced by MBE.

2.2.4 *First Principle* Calculations of Pd/ZnO Interfaces

Ab-initio (*first principle*) calculations based on local density approximation of the density functional theory were performed for the Pd/ZnO interfaces by Zaoui [Zaoui, 2004]. The results are summarized in this subsection.

A) Stable Terminating Atomic Species [Zaoui, 2004]

The work of separation between Pd and ZnO was calculated for the **Pd/$^{+}$ZnO** interface and the **Pd/$^{-}$ZnO** interface as shown in Table 2.5. Higher work of separation denotes strong interfacial bonding. The calculation required a super cell which does not include a lattice mismatch of 18 % of the Pd/ZnO interface in order to avoid a huge super cell. This means both lattice constants are identical.

Possible atomic geometries can be considered as shown in Fig. 2.16. [(a): '**fcc hollow**' geometry] The Pd stacks on the lattice site of the ZnO and the Pd atom in the 3rd layer sits on top of the interfacial atom of the ZnO. [(b): '**hcp hollow**' geometry] The Pd stacks on the lattice site of the ZnO and the Pd atom in the 2nd layer sits on top of the interfacial atom of the ZnO. [(c): '**on top**' geometry] The interfacial Pd atom sits on top of the interfacial atom of the ZnO. [(d): '**on bridge**' geometry] The Pd stacks on in-between hollow site of the two terminating atoms of the ZnO.

It can be seen that, for almost all geometries, the separation energies of the **Pd/$^{\pm Zn}$ZnO** interfaces are much higher than that of the **Pd/$^{\pm O}$ZnO** interfaces, indicating Zn-terminations are the most stable one. The interfacial bonding strength strongly depends on the terminating atomic species. The critical results indicate that O-termination should not be likely at the **Pd/$^{-}$ZnO** interface. However, O-termination was actually observed as shown in subsection 2.2.3.

B) Most Stable Adhesion Geometries of Pd on ZnO [Zaoui, 2004]

The largest energy of separation appears for the 'fcc-hollow' geometry in case of the **Pd/$^{+}$ZnO** interface and for the 'on top' geometry in case of the **Pd/$^{-}$ZnO** interface as shown in Table. 2.5, indicating that these adhesion geometries result in the strongest interfacial bonding.

Table 2.5 Energy of interface separation in J/m^2 of Pd/ZnO for different adhesion geometries [Zaoui, 2004]. [(a): '**fcc hollow**' geometry] The Pd stacks on the lattice site of the ZnO and the Pd atom in the 3rd layer sits on top of the interfacial atom of the ZnO. [(b): '**hcp hollow**' geometry] The Pd stacks on the lattice site of the ZnO and the Pd atom in the 2nd layer sits on top of the interfacial atom of the ZnO. [(c): '**on top**' geometry] The interfacial Pd atom sits on top of the interfacial atom of the ZnO. [(d): '**on bridge**' geometry] The Pd stacks on in-between hollow site of the two terminating atoms of the ZnO.

Adsorbed site	(a) fcc hollow	(b) hcp hollow	(c) on top	(d) on bridge
Pd/$^{+Zn}$ZnO	**1.320**	**1.315**	**1.288**	**1.094**
Pd/$^{+O}$ZnO	1.092	1.098	1.169	1.112
Pd/$^{-Zn}$ZnO	1.266	1.270	1.232	0.909
Pd/$^{-O}$ZnO	**0.368**	**0.271**	**0.508**	**0.229**

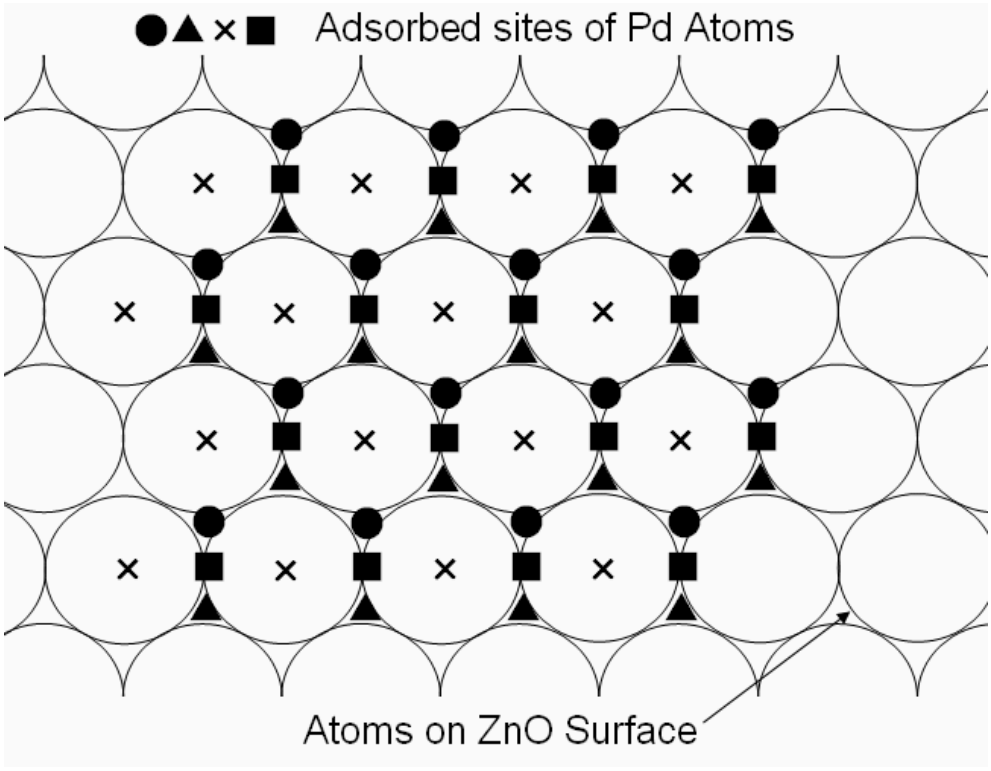

Fig. 2.16 Possible adsorbed sites of Pd atoms on ZnO surfaces. ●: fcc hollow sites, ▲: hcp hollow sites, ■: on top of the surface atoms of ZnO, ×: on bridge of the surface atoms of ZnO.

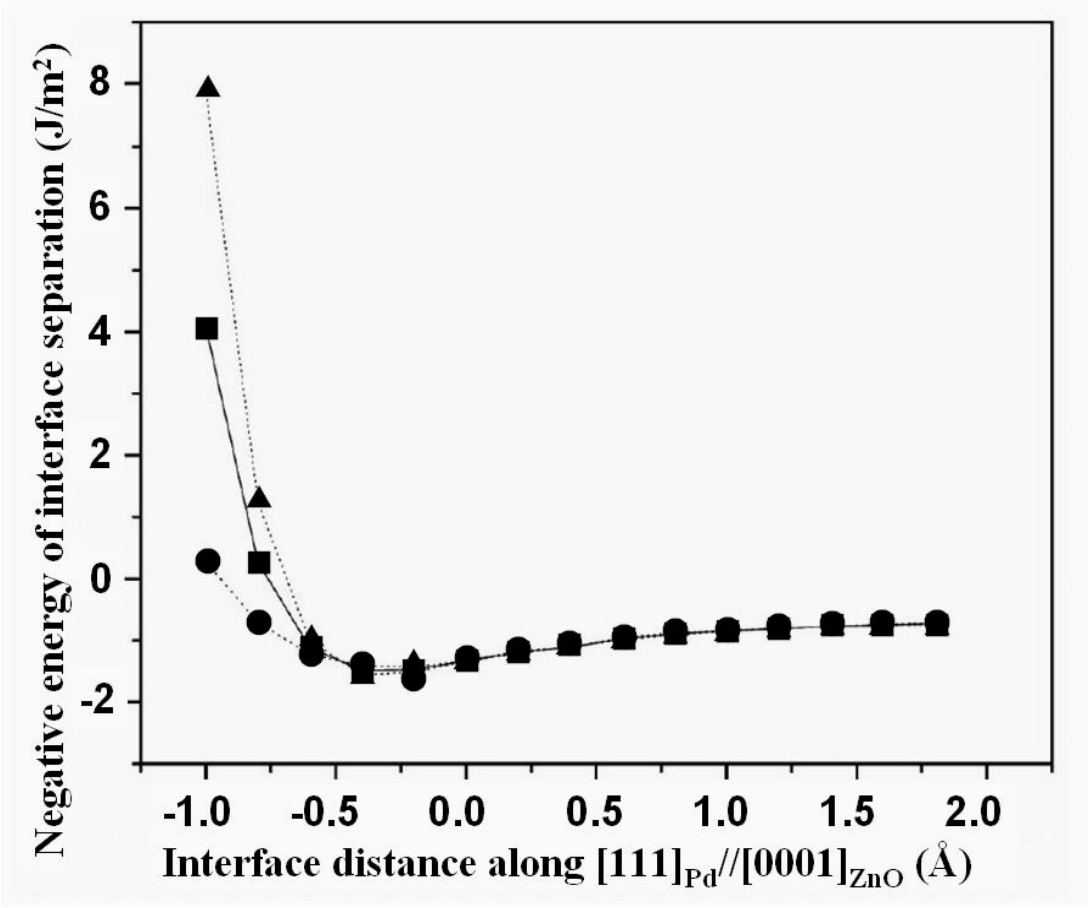

Fig. 2.17 Negative energy of interface separation, $-W_{sep}$, as function of **Pd/$^{+Zn}$ZnO** interface distance (●), **Pd/$^{-O}$ZnO** interface distance (▲), and mixed **Pd/$^{+Zn}$ZnO** and **Pd/$^{-O}$ZnO** interfaces distance (■) [Zaoui, 2004].

C) Stable Interfacial Distance [Zaoui, 2004]

The work of separation was calculated for different initial interfacial distances between Pd and ZnO. Fig. 2.17 shows a negative energy of interface separation, $-W_{sep}$, as function of interfacial distance of **Pd/$^{+Zn}$ZnO** interface (● with dotted line) and **Pd/$^{-O}$ZnO** interface (▲ with dotted line). The interfacial distance was based on the interlayer distance d_{111} (= 0.225 nm) of a bulk Pd. It can be seen that the specific interfacial distances of 0.185 nm (-0.04 nm) possess the highest interfacial separation energy for both interfaces.

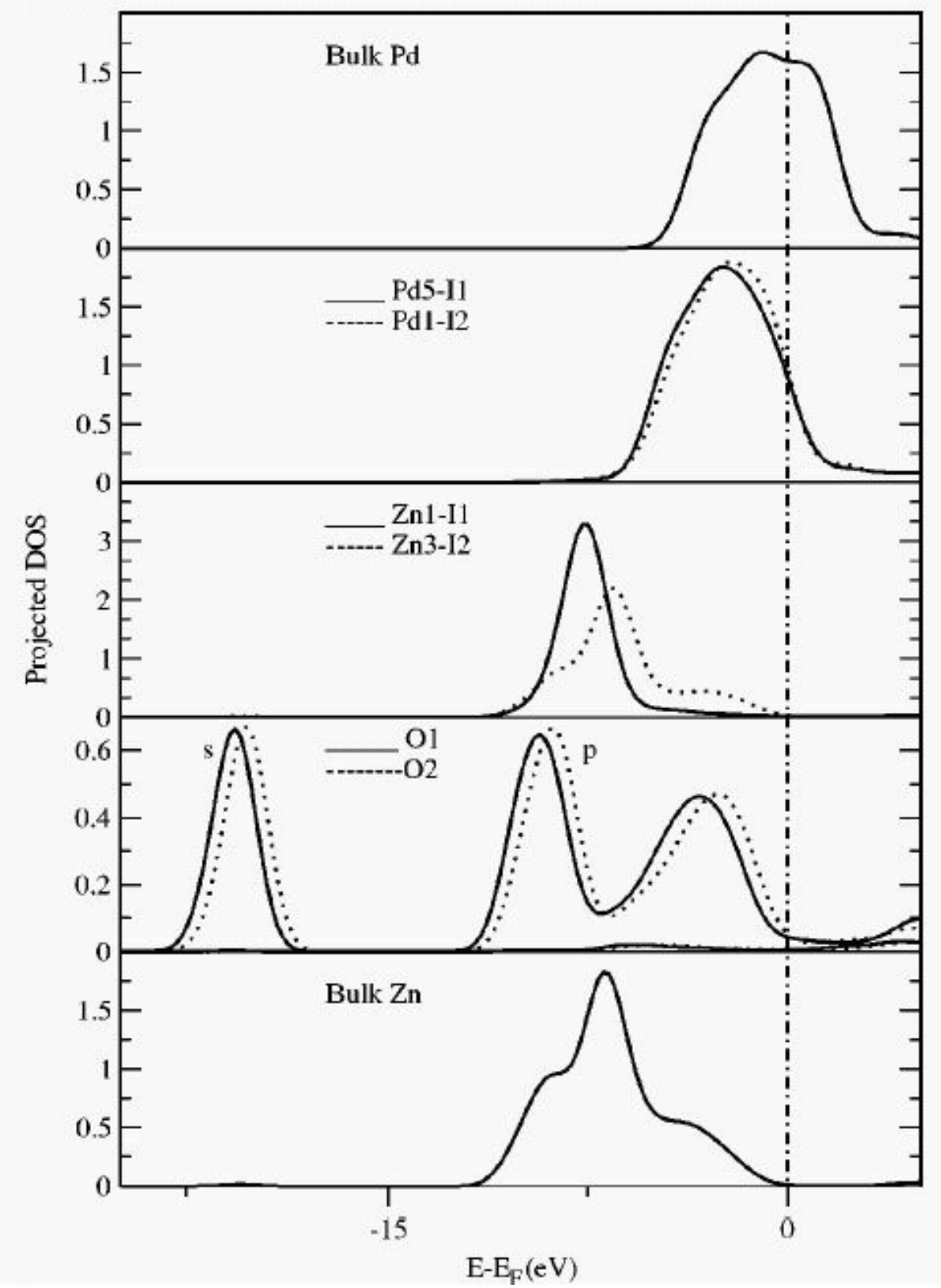

Fig. 2.18 Projected local density of states on a Pd/ZnO slab. From the top to the bottom: the *d* states of bulk DOS of Pd; the *d* states of Pd (solid line) and Pd (dashed line) at interface I1 (**Pd/$^{-Zn}$ZnO** interface) and I2 (**Pd/$^{+Zn}$ZnO** interface), respectively; the d states of Zn (solid line) and Zn (dashed line) at the interface I1 and I2, respectively; the *s* and *p* states of two oxygen atoms O1 (solid line) and O2 (dashed line) closer to I1 and I2; the *d* states of bulk Zn [Zaoui, 2004].

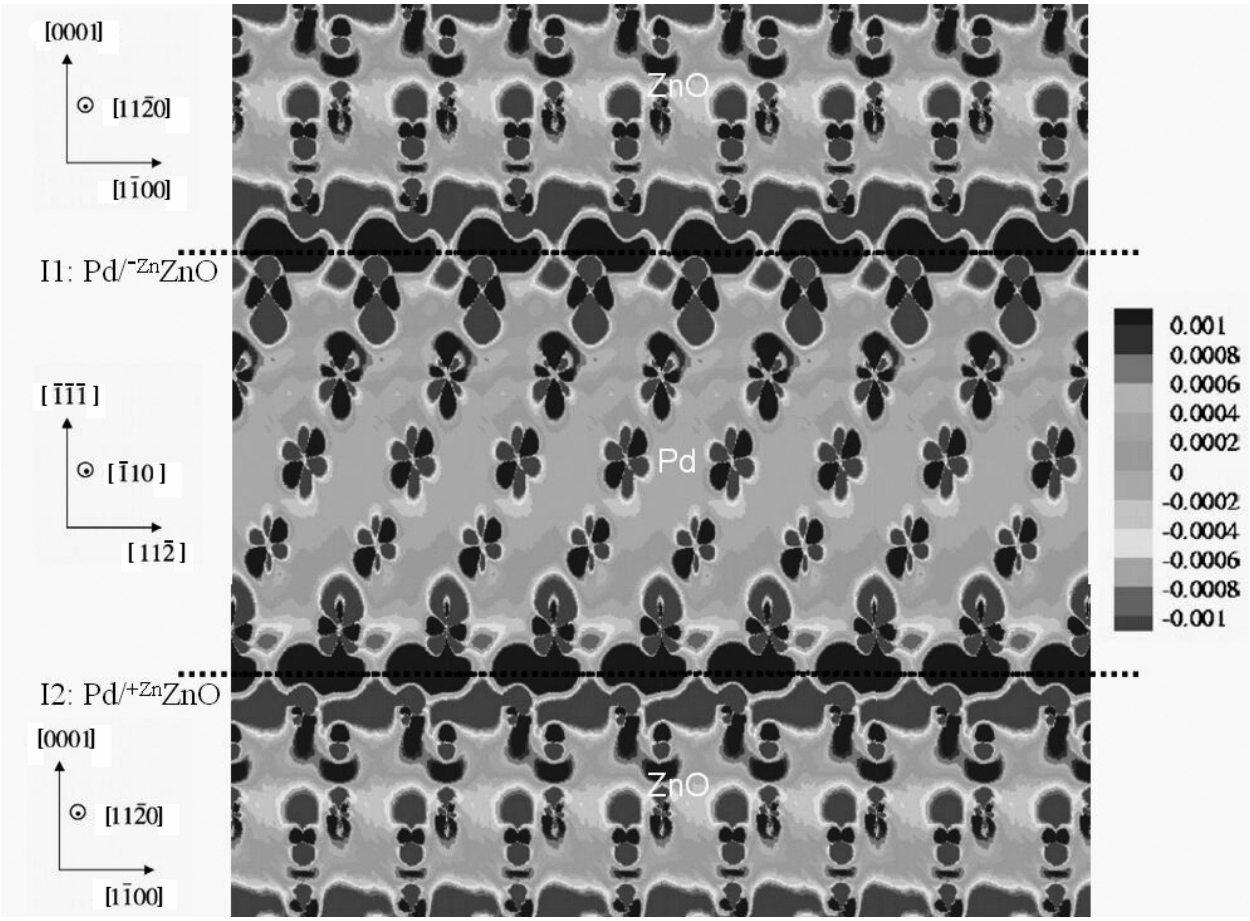

Fig. 2.19 The difference charge distribution maps of the total electron density for the Pd/ZnO slab minus the same densities for the Pd/vacuum and ZnO/vacuum slabs, indicating wider distribution and higher charge density near the interface than bulk. It suggests also metallic and covalent character. [Zaoui, 2004].

D) Local Density of State and Charge Density Distribution [Zaoui, 2004]

Fig. 2.18 shows the local densities of states for the **Pd/^{Zn}ZnO** interfaces. The interface I2 corresponds to an experimentally observed **Pd/$^{+Zn}$ZnO** interface (see subsection 2.2.3) while the other interface I1 corresponds to the **Pd/$^{-Zn}$ZnO** interface which was not identified by an experiment. It can be seen that for the interface I2 the peak position of LDOS of the interfacial Pd *d* state is shifted to a deeper level compared to bulk while that of the interfacial Zn *d* state is slightly shifted to higher energy side than bulk, indicating a slight ionic charge transfer. Furthermore, it seems that Pd *d* state is emphasized by hybridizing with Zn *d* state within the same energy region. Therefore, Zaoui [Zaoui, 2004] concluded that the bonding across the **Pd/$^{+Zn}$ZnO** interface consists of a mixed ionic and covalent bond. Fig. 2.19 shows a difference charge density distribution. It can be seen that it has wider distribution and higher charge density near the interface than bulk suggesting also metallic and covalent character.

2.3 Goal of the Thesis

Pd/ZnO system gives rise to questions of scientific and technological problems. The scientific questions are (i) orientation relationships between Pd and ZnO depending on synthesis process, (ii) local atomic structure, (iii) terminating atomic species of ZnO, (iv) spatial occupancy of each column of the terminater, (v) the number of back bond (dangling bond) of the terminater, (vi) nature of interfacial bonding, (vii) structural difference for different polar plane, (viii) structural change of ZnO due to Pd deposition, and (ix) what dominates the Pd/ZnO polar interfaces. The technical problems related to HRTEM observation are (I) image analysis for ZnO with extremely small lattice spacings, (II) differentiation of atomic species including simultaneously light (O) and heavy (Zn, Pd) elements, (III) interpretation of image contrast near the interface where periodicities of crystals can be broken, and (IV) understandings of the 3-dimensional structure.

Previous work for the Pd/ZnO interface [Saito, 2001] was performed with atomic resolution microscope (JEM ARM-1250) for the first time. The interfaces were produced by internal oxidation of Pd-Zn alloy. However, the quality of the HRTEM images was not sufficiently good, in particular, for a determination of the interfacial local atomic structure. The scientific question or the technical problems as mentioned above could not completely solved except (i), (I), and (II).

The low quality image in the previous work [Saito, 2001] was due to the bad quality of the TEM specimen, e.g., (i) thick specimen caused by selective ion-milling, (ii) strong specimen bending of the metal matrix caused by irradiation damage, (iii) possibility of diffusion across the interface resulting due to the high internal oxidation temperature. Therefore, excellent specimens for HRTEM observation are a prerequisite for a quantitative analysis. MBE is an appropriate technique for specimen preparation. Usually the temperature during film growth is lower than internal oxidation. The ZnO substrate will prevent a TEM specimen from bending due to irradiation damage.

So far, it was not so easy to determine the local atomic structure and the terminating atomic species at the Pd/ZnO interfaces by HRTEM. The real atomic center is often shifted from the contrast center on the image near the interface. Such problems will be solved employing quantitative high resolution image analysis technique [Möbus, 1996].

EELS (Electron Energy Loss Spectroscopy) provides information about the interfacial

electronic structure with high spatial resolution. Since the probe size of incident e-beam of HRTEM is larger than atomic scale, the fine structure will be generated from the interface and bulk region. Therefore, the pure interfacial specific peaks have to be extracted. This is done by the Spatial Difference Technique [Scheu, 2002]. Furthermore, the interfacial local electronic structure will be simulated by DVXα *first principle* calculation (cluster calculation).

Pd films were grown on the $^{+}$**ZnO** and $^{-}$**ZnO** surfaces by MBE, respectively, in order to examine the difference in the polarity. The results from both interfaces are compared.

Prior Pd deposition, the structures of both {0001}ZnO surfaces are analyzed by surface X-ray diffraction and then the surface atomic structure also is quantitatively determined. The structural comparison of ZnO before and after Pd depositions will reveal the interaction between ZnO and Pd, the effect on ZnO due to Pd deposition, and stabilization mechanism of the ZnO.

In order to extract the 3-dimensional atomic structure from TEM images, the interface will be observed along the different zone axes which are different by 90°.

The final purpose of this work is to get a deep scientific insight into the local atomic/electronic structure and the nature of Pd/ZnO polar interface, as a first step to elucidate a correlation between microscopic behaviors and macroscopic material properties in such a hybrid metal/oxide system and to obtain a guideline to improve, to design, and to create new materials properties with hybrid metal/oxide systems.

3 Experimental and Computational Details

In this chapter, the principles will be introduced for those experimental and theoretical techniques which are employed within this thesis. This chapter allows the reader to follow the explanations in Chapter 4 ~ 7 which cover the results and the discussions of the results.

3.1 Anomalous X-Ray Diffraction

The different polar surfaces, $^{+}$**ZnO** and $^{-}$**ZnO** (see subsection 2.2.1), can be distinguished by anomalous X-ray diffraction. Although the orientations of the surfaces were claimed by the commercial vendors, they were reconfirmed. In this section, the principles of anomalous X-ray diffraction are described and applied to the ZnO surfaces.

The $^{+}$**ZnO** and $^{-}$**ZnO** surfaces are structurally equivalent and cannot be distinguished by conventional XRD. However, if one considers imaginary terms of the ASF (Atomic Scattering Factor), the surfaces can be distinguished by XRD when special wavelengths of the X-rays are used [Heiland, 1963]. Both real term f' and imaginary term $\Delta f''$ of the ASF f tend to show anomalous behavior near the absorption edge of X-ray, see Fig. 3.1 and Fig. 3.2 [Henke, 1993]. If these anomalous terms are included in the calculations of the reflection intensities, then the intensities depend on the surface orientation. The imaginary term $\Delta f''$ of Zn is 1.47527 (See Fig. 3.1) near the electron energy (17.386 keV) of MoKα X-rays. The imaginary term plays an important role for the discrimination of a different surface orientation.

For MoKα X-rays or CuKα X-rays, the intensities from the $^{+}$**ZnO** or $^{-}$**ZnO** surface can be calculated as follows. ZnO crystallized in the wurtzite structure and the atomic coordinates of the unit cell are Zn(0, 0, 0), Zn(1/3, 2/3, 1/2), O(0, 0, 3/8), and O(1/3, 2/3, 7/8). If only one kind of atoms, Zn or O, is considered, then the sublattices would form an hcp structure. Since the translation vector between the Zn sublattice and the O sublattice is (0, 0, 3*c*/8), the crystal structure factor of the wurtzite structure can be easily estimated from the crystal structure factor of the hcp structure.

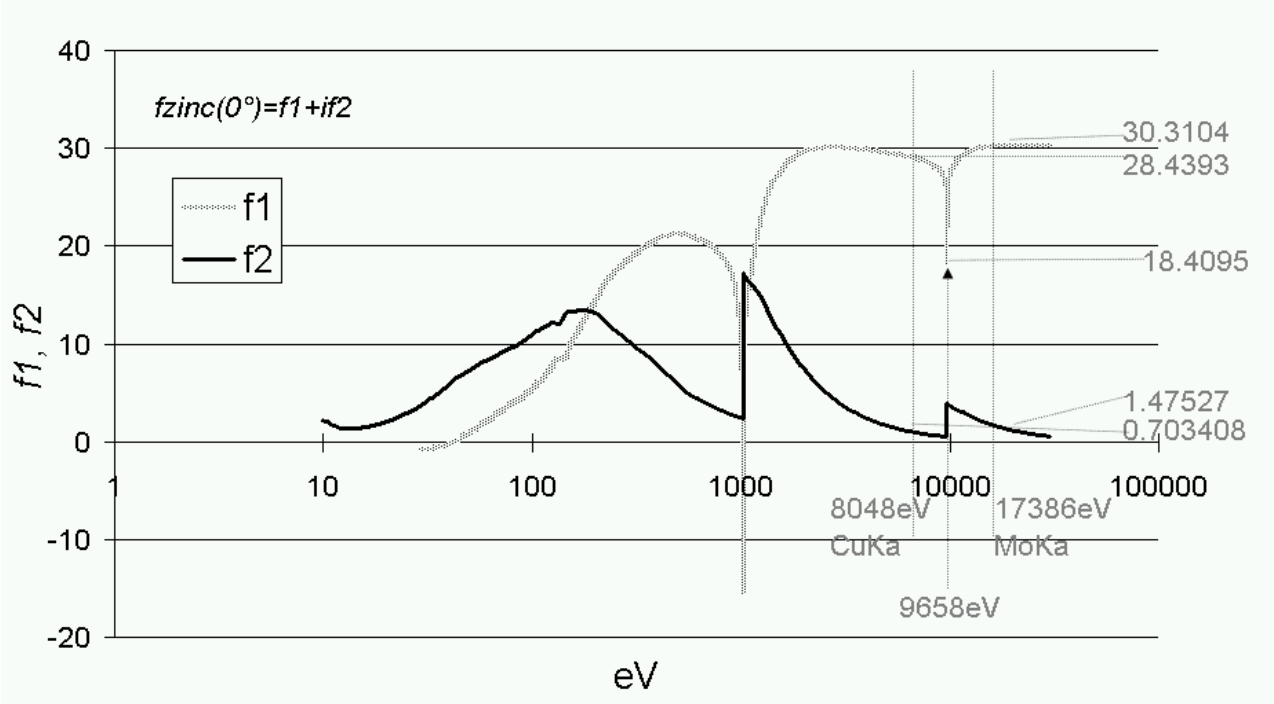

Fig. 3.1 Atomic scattering factor of Zn atom depending on the wavelength of the X-rays: $f1$ corresponds to the real part f' and $f2$ corresponds to the imaginary part $\Delta f''$ of the atomic scattering factor $f(0^\circ)$ [Henke, 1993].

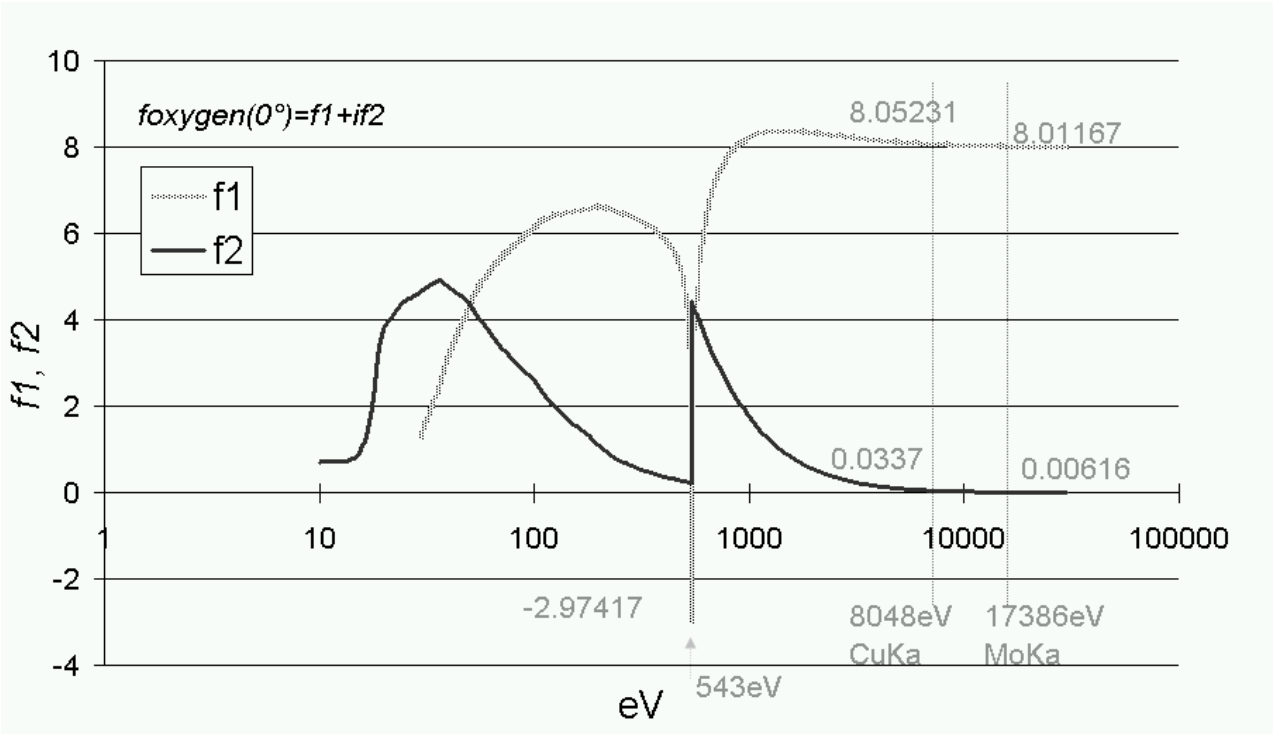

Fig. 3.2 Atomic scattering factor of O atom depending on the wavelength of the X-rays: $f1$ corresponds to the real part f' and $f2$ corresponds to the imaginary part $\Delta f''$ of the atomic scattering factor $f(0^\circ)$ [Henke, 1993].

The crystal structure factor of an hcp crystal S_{hcp} is given by equation (3-1):

$$S_{hcp} = \sum_j f_j \exp[iK \cdot r_j] = 1 + \exp 2\pi i(\frac{1}{3}h + \frac{2}{3}k + \frac{1}{2}l), \tag{3-1}$$

where f_j is atomic scattering factor of j^{th} atom, r_j is internal coordinate in the unitcell of j^{th} atom, (hkl) is mirror index, and K is reciprocal lattice vector. The crystal structure factor of the wurtzite structure $S_{wurtzite}$ is given by equation (3-2a). Furthermore, the intensity for $\{00l\}$ reflections is also included in equation (3-2a).

$$\begin{aligned} S_{wurtzite} &= S_{hcp}(f_Z + f_O \exp 2\pi i \cdot \frac{3}{8}l) \\ F_{hkl} \equiv S_{wurtzite} &= \left(1 + e^{2\pi i(\frac{h+2k}{3} + \frac{l}{2})}\right)\left(f_Z + f_O e^{2\pi i \cdot \frac{3}{8}l}\right) \\ F_{00l} &= \left(1 + e^{l\pi i}\right)\left(f_Z + f_O e^{\frac{3}{4}l\pi i}\right) \end{aligned} \tag{3-2a}$$

F_{00l} is identical for the $(00l)$ and $(00\bar{l})$ reflections. This means that both surfaces cannot be distinguished without considering the anomalous scattering. Therefore, the ASF has to be extended as follows: $f \to f = f' + i\Delta f''$.

If $f_Z = f_Z' + i\Delta f_Z''$ for Zn and $f_O = f_O' + i\Delta f_O''$ for O are inserted into equation (3-2a), then the scattering factors F_{00l} and intensity $|F_{00l}|^2$ are given by:

$$\begin{gathered} \text{for } l = \text{odd},\ F_{00l} = 0, \\ F_{002} = F_{00\bar{6}} = F_{0010} = 2\{(f_Z' + \Delta f_O'') + i(\Delta f_Z'' - f_O')\}, \\ F_{00\bar{2}} = F_{006} = F_{00\bar{1}\bar{0}} = 2\{(f_Z' - \Delta f_O'') + i(\Delta f_Z'' + f_O')\}, \\ F_{004} = F_{00\bar{4}} = F_{0012} = F_{00\bar{1}\bar{2}} = 2\{(f_Z' - f_O') + i(\Delta f_Z'' - \Delta f_O'')\}, \\ F_{000} = F_{008} = F_{00\bar{8}} = 2\{(f_Z' + f_O') + i(\Delta f_Z'' + \Delta f_O'')\}, \\ \text{for } l = \text{odd},\ |F_{00l}|^2 = 0, \\ |F_{002}|^2 = |F_{00\bar{6}}|^2 = |F_{0010}|^2 = 4\{(f_Z' + \Delta f_O'')^2 + (\Delta f_Z'' - f_O')^2\}, \\ |F_{00\bar{2}}|^2 = |F_{006}|^2 = |F_{00\bar{1}\bar{0}}|^2 = 4\{(f_Z' - \Delta f_O'')^2 + (\Delta f_Z'' + f_O')^2\}, \\ |F_{004}|^2 = |F_{00\bar{4}}|^2 = |F_{0012}|^2 = |F_{00\bar{1}\bar{2}}|^2 = 4\{(f_Z' - f_O')^2 + (\Delta f_Z'' - \Delta f_O'')^2\}, \text{ and} \\ |F_{000}|^2 = |F_{008}|^2 = |F_{00\bar{8}}|^2 = 4\{(f_Z' + f_O')^2 + (\Delta f_Z'' + \Delta f_O'')^2\}. \end{gathered} \tag{3-2b}$$

Table 3.1 Theoretical reflection intensity ratio from {0001}ZnO surfaces for CuKα and for MoKα X-rays. The calculated values strongly depend on the polarity and the Bragg peak.

$00l$	000	002	004	006	008	00 10
$\lvert F_{00l}\rvert^2 / \lvert F_{00\bar{l}}\rvert^2$ for CuKα	1.000	0.977	1.000	1.033	1.000	0.918
$\lvert F_{00l}\rvert^2 / \lvert F_{00\bar{l}}\rvert^2$ for MoKα	1.000	0.951	1.000	1.174	1.000	0.884

Table 3.1 summarizes the intensity ratio $\lvert F_{00l}\rvert^2 / \lvert F_{00\bar{l}}\rvert^2$ for specific Bragg peaks. It can be seen that the calculated values strongly depend on the Bragg peak, in particular, if MoKα X-rays are used. Therefore, the surface orientations of {0001}ZnO can be quantitatively distinguished by anomalous XRD.

Thus a calibration of the imaginary terms, $\Delta f_O''$ and $\Delta f_{Zn}''$ is essential to distinguish the intensities from $(00l)$ and $(00\bar{l})$. The original atomic scattering factors f_O and f_{Zn} (data are available in a literature) depend on $\lambda^{-1}\sin\theta$ where λ is the wavelength and θ is the scattering angle. In contrast, anomalous scattering terms $\Delta f_O' = f_O - f_O'$, $\Delta f_{Zn}' = f_{Zn} - f_{Zn}'$, $\Delta f_O''$, and $\Delta f_{Zn}''$ taken from Fig. 3.1 and Fig. 3.2 are independent of the scattering angle.

3.2 Quantitative Analysis of Crystal Truncation Rod

The SXRD (Surface X-Ray Diffraction) technique provides information of the atomic structure of the crystal surface. The crystallographic difference between a bulk crystal and a surface can be explained as the difference in effective structure factors. Usually a structure factor of a (hkl) reflection can be expressed by equation (3-3):

$$\left|F(hkl)\right|^2 = \left|\sum_{j_1}^{N_1}\sum_{j_2}^{N_2}\sum_{j_3}^{N_3} e^{i(ha_1 j_1 + ka_2 j_2 + la_3 j_3)}\right|^2 . \qquad (3\text{-}3)$$

The intensity distribution on reciprocal points for a bulk crystal with infinite size is localized and comparable to a δ function. In the case of a surface, half of the Fourier components in equation (3-3) is lost, because half of the bulk crystal was removed. It results in an extended intensity distribution along the surface normal that corresponds to a 3-dimensional rod-like intensity distribution in reciprocal space (see Fig. 3.3). The structure is called CTR (Crystal Truncation Rod) [Robinson, 1985], [Vlieg, 2000]. CTR includes the surface specific intensity distribution near anti-Bragg conditions as shown in Fig. 3.3. The intensity in an anti-Bragg condition is extremely low and sensitive to the surface local atomic structure. Quantitative analysis of CTR provides exact information on the local atomic structure, atomic occupancy, surface reconstruction, and atomic displacement.

Since the direct interpretation of the experimentally obtained CTR is difficult, it is therefore necessary to compare experiments with simulated results. The program package 'ROD' developed by E. Vlieg compares a series of simulations with the experimental CTR [Vlieg, 2001] and finally provides best fitting parameters of the surface structure. The basics of the simulation program are given below.

The program just calculates the structure factor F_{hkl}:

$$F_{hkl} = \sum_j f_j \exp\frac{-B_j Q^2}{16\pi^2} \exp 2\pi i(hx_j + ky_j + lz_j), \qquad (3\text{-}4)$$

where f_j is the atomic scattering factor of atoms j, B_j the Debye-Waller parameter, hkl the diffraction indices and $(xyz)_j$ the position of atoms j in fractional coordinates. For surface X-ray diffraction we have to deal with two 'unit cells': (i) all atoms defined to be in the surface and (ii) all atoms in the bulk, see Fig. 3.4. Usually, the following convention is used for surface diffraction. The lattice parameters $\boldsymbol{a}_1$ and $\boldsymbol{a}_2$ of the surface unit cell are lying in the surface plane and $\boldsymbol{a}_3$ is pointing outwards. The diffraction index l points along the out-of-plane direction.

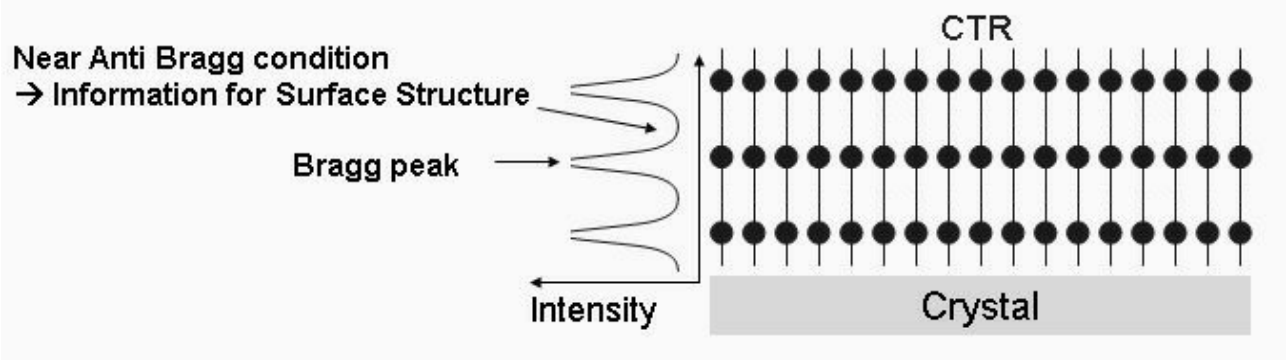

Fig. 3.3 Crystal truncation rods and the corresponding intensity profile. Reciprocal points are extended with intensity distribution along the surface normal that corresponds to a 3-dimensional rod-like intensity distribution.

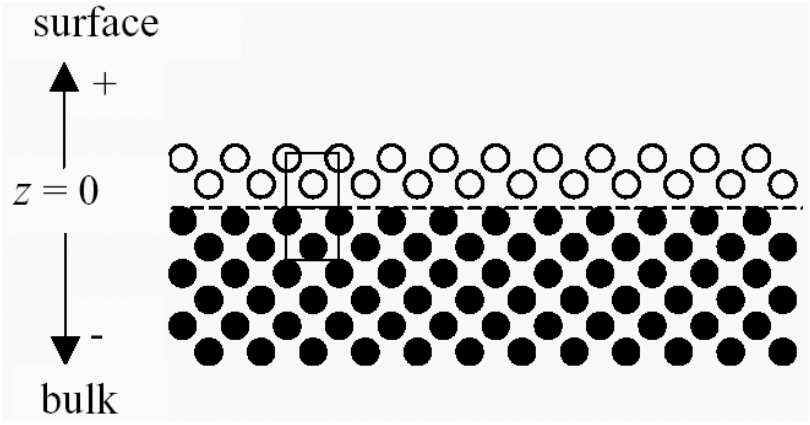

Fig. 3.4 Schematic of a surface layer on top of a bulk crystal that extends to minus infinity. Unit cells for both sides are indicated [Vlieg, 2001].

The size of $\boldsymbol{a}_3$ is chosen arbitrary for the surface unit cell (there is no true periodicity along that direction), but it is taken to be the same as that of the (well-defined) bulk cell.

The complete structure factor is given by the interference sum of both contributions:

$$F_{sum} = F_{surf} + F_{bulk} \tag{3-5}$$

with

$$F_{surf} = \sum_{j}^{\substack{surface \\ unitcell}} f_j \theta_j \exp\frac{-B_j Q^2}{16\pi^2} \exp 2\pi i(hx_j + ky_j + lz_j) \tag{3-6}$$

$$F_{bulk} = \sum_{j=-\infty}^{0} F_u \exp 2\pi i l j \exp j\alpha \tag{3-7}$$

and

$$F_u = \sum_{j}^{\substack{bulk \\ unitcell}} f_j \exp\frac{-B_j Q^2}{16\pi^2} \exp 2\pi i(hx_j + ky_j + lz_j). \tag{3-8}$$

For the definition of F_{surf} we included the occupancy parameter θ_j, because in the surface unit cell not all positions have to be fully occupied. F_{bulk} describes the bulk unit cell structure factors F_u summed from the top layer to $-\infty$. Because of the attenuation factor α, only a finite amount of unit cells contributes to F_{bulk}. The summation (3-7) leads to [Vlieg, 2001]:

$$F_{bulk} = F_u \frac{1}{1 - e^{-2\pi i l} e^{-\alpha}}. \tag{3-9}$$

F_{bulk} is the structure factor of a so-called crystal truncation rod (CTR). At integer values for l it has a very high intensity, but, owing to the termination of the crystal at a sharp interface, even for non-integer l values there is a finite intensity.

It is important to define the unit cells in such a way that the surface unit cell starts exactly above the bulk unit cell. The surface unit cell can be chosen to extend arbitrarily deep into the 'bulk'. For example, in Fig. 3.4 the line dividing surface and bulk could be lowered by half of bulk lattice spacing. This increases the amount of layers in the surface unit cell from two to three. In that case one has to choose the two layers immediately below the surface cell to form the bulk unit cell. When the atoms in this extra 'surface' layer are kept at their bulk positions, the calculated diffracted intensity will remain unchanged. Note that the intensity is proportional to the square of the structure factor.

For a reconstructed surface, so-called fractional-order reflections will appear: in the bulk lattice vectors such reflections have non-integer h and/or k indices. At the fractional positions the bulk contribution is zero and the total structure factor equals F_{surf}. The program ROD has no problem calculating structure factors also for fractional indices, but in general it is better to keep the in-plane diffraction indices integer by defining a larger unit cell. For example, for a (2 × 1) reconstruction, (n/2, m) reflections would occur in terms of the bulk unit cell with lattice parameters $\boldsymbol{a}_1$ and $\boldsymbol{a}_2$. Choosing the lattice parameters 2 × $\boldsymbol{a}_1$ and $\boldsymbol{a}_2$ leads to (2n+1, m) reflections exclusively originating from the surface, while (2n, m) reflections are the interference sum of surface and bulk contributions. Only by choosing the larger lattice parameters, one uses a genuine *unit cell*. In the larger unit cell, the bulk unit cell will have twice the number of atoms (or a different factor for a different reconstruction). It is important to give all the atoms in the bulk unit cell the proper in plane coordinates, because only then the bulk contribution will cancel for 'fractional-order' reflections.

3.3 High-Resolution Transmission Electron Microscopy

In this section, the possibilities on HRTEM are summarized. If the specimen is extremely thin and if the defocus is near Scherzer focus, inner potential structure of crystalline specimen directly reflects to image contrast. [Hirsch, 1965], [Horiuchi, 1988], [Tanaka, 2000], [Shindo, 1996]

Imaging Theory

The imaging process within a TEM is equivalent to that of an optical microscope. Specific character for image formation in an electron microscope is that fast electrons can be described as a wave. An electromagnetic field acts as a lens. The electromagnetic lens can be schematically represented by a convex lens of the optical microscope (see Fig. 3.5).

After the plane wave electron enters into the specimen, the electrons are scattered in the crystal by the positively screened Coulomb field of the atomic nucleus of the atoms. New resultant wave front can be formed after passing through the specimen. A subsequent lens system magnifies the resultant wave function onto a screen.

Wave Function on Screen

If the incident plane wave before the specimen can be represented by a wave function $1(x,y)$, the wave function at the exit surface of the specimen can be described as,

$$\Psi_s(x,y) = A(x,y)\exp i\delta(x,y), \tag{3-10}$$

where $A(x,y)$ represents the modulation of the wave amplitude while $\delta(x,y)$ represents the phase of the wave.

The wave function under the exit surface should have a periodic structure corresponding to the lattice of the specimen. Furthermore, it is well known that Ψ_s of equation (3-10) can be mathematically replaced by two dimensional Fourier transformation of the structure factor $F(h,k,l=0)$ as shown in equation (3-11), if the constant term $A(x,y)$ is being excluded.

$$\Psi_s(x,y) \propto \iint F(h,k,l=0)\exp 2\pi i(hx+ky)dhdk\,. \tag{3-11}$$

According to the projection theorem for Fourier transformation, the wave function of equation (3-11) can be described as the projected potential of the crystal potential $V(x,y,z)$ along the incident beam.

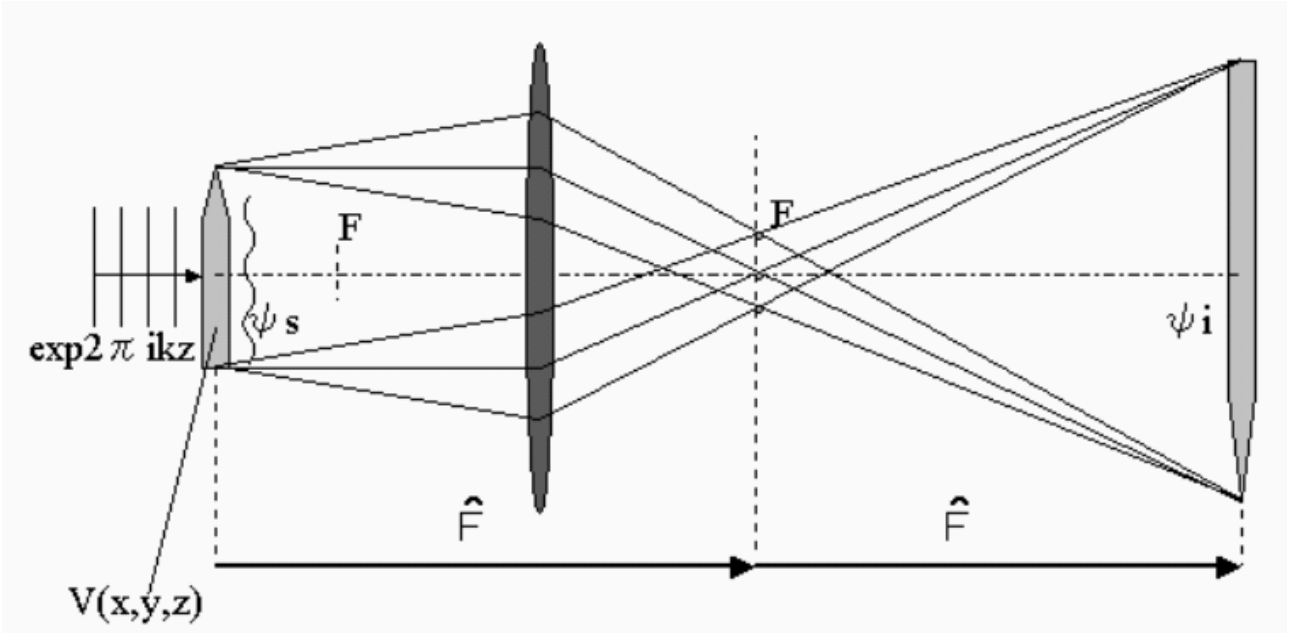

Fig.3.5 The imaging process within a TEM is equivalent to that of an optical microscope. Specific character for image formation in an electron microscope is that fast electrons can be described as a wave. An electromagnetic field acts as a lens. The electromagnetic lens can be schematically represented by a convex lens of the optical microscope.

Furthermore, the lens generates a new wave function $F(h,k,l=0)$ on the back focal plane ('*F*' in Fig, 3.5) which corresponds to the electron beam diffraction pattern. After an electron propagates across the back focal plane, a wave function Ψ_i appears on a screen. This propagation process can be described by the following equation (3-12) as well as equation (3-11).

$$\Psi_i(x,y) \propto \iint F(h,k)\exp -2\pi i(hx+ky)dhdk \propto \Psi_s(-x,-y). \tag{3-12}$$

According to two dimensional Fourier transformation $\hat{F}$, these equations (3-11) and (3-12) can be replaced into equation (3-13).

$$\begin{aligned} &F(h,k) \propto \hat{F}\{\Psi_s(x,y)\} \\ &\Psi_i(x,y) \propto \hat{F}\{F(h,k)\} = \hat{F}\cdot\hat{F}\{\Psi_s(x,y)\} = \Psi_s(-x,-y) \end{aligned}. \tag{3-13}$$

The wave function Ψ_i can be rewritten with two times Fourier transformations of Ψ_s. In addition, when a magnification was M times, Ψ_s in equation (3-13) can be replaced into

$$\Psi_s(\frac{-x}{M},\frac{-y}{M}).$$

Weak Phase Object

A lattice image on a screen is formed by interference between a transmitted beam and at least one diffracted beam. A perfect structure image on a screen is formed by interference of a transmitted beam and all diffracted beams. This structure image can reflect the real atomic structure. Therefore, the structure image is quite important for a complete analysis. However, for an easy interpretation for image contrast, specific conditions are required for a specimen and imaging parameters.

First of all, the wave function under the exit surface of the crystal which was well-aligned is considered. During propagation of the electron wave through a crystal, the phases of wave should be modulated depending on the places where electron passes, since the potential along an atomic column is different from that in vacuum within the crystal. When the acceleration voltage is E and an inner crystal potential is $V(x,y,z)$, then the refractive index n is given by equation (3-14). Since usually $V(x,y,z)$ is only a few eV ($\leq E$), then n can be approximated as written in equation (3-14).

$$n(x,y,z) = \sqrt{\frac{E+V(x,y,z)}{E}} \cong 1 + \frac{V(x,y,z)}{2E}. \tag{3-14}$$

Since the optical distance is $n\Delta Z$ when a wave travels a distance ΔZ in the crystal with reflective index n, the phase difference of the wave along atomic column is defined as the δ compared to phase in vacuum.

$$\delta = \frac{2\pi}{\lambda}(n-1)\Delta Z. \tag{3-15}$$

Therefore, the wave function under the exit surface of the specimen is given by

$$\Psi_s \cong \exp i\delta = \exp i\frac{\pi}{\lambda E}\int_0^{\Delta Z} V(x,y,z)dz \equiv \exp i\sigma V_P(x,y), \tag{3-16}$$

where the coefficient $\sigma = \frac{\pi}{\lambda E}$ is the coupling constant and the integral term V_P is the so called projected potential of the crystal. Equation (3-16) indicates that the crystal can be expressed as 'phase object' which changes only the phase of wave [Cowley, 1972].

When a specimen consists of light elements and forms a thin single crystal, the phase shift due to the crystal potential is smaller than for a heavier element and thick specimen. Then, equation (3-16) can be further approximated as following equation (3-17).

$$\Psi_s \cong 1(x,y) + i\sigma V_p(x,y). \tag{3-17}$$

This is called 'week phase object approximation'. It can be seen that the Ψ_s is proportional to the projected potential V_P. Therefore, a real crystal structure directly can reflect to a

resultant wave function when a specimen consists of light elements and forms a thin single crystal. It allows to a direct interpretation of a HRTEM image. Therefore, at lest we need a TEM specimen as thin as possible.

Contrast Transfer Function

In a real microscope, the wave function on the screen (equation (3-12)) is strongly modified by lens aberrations. The lens aberrations, in particular, the spherical aberration of the objective lens, limit the resolution. Presently, the spherical aberration cannot be avoided. Nevertheless, a spherical aberration plays also an important positive role in order to give visible contrast and it is essential for imaging in HRTEM.

The phase shift of the electron wave caused by the spherical aberration or/and the defocus was formulated by Scherzer [Scherzer, 1949]. The phase shift $\chi(\alpha)$ is given by,

$$\chi = \frac{\pi}{2\lambda}\left[C_s\alpha^4 + 2\Delta f\alpha^2\right], \tag{3-18}$$

where C_s is a spherical aberration coefficient, Δf is defocus value, and α is incident angle ($= 2\theta_{Bragg}$) for the lens. The phase shift results in the additional modulation of the wave function by $P(\alpha)$ (see equation (3-19)).

$$P(\alpha) = \exp\{-i\chi(\alpha)\}. \tag{3-19}$$

This exponential function governs an imaging property in HRTEM. It is the so called lens transfer function. The real part $\cos\chi(\alpha)$ of $P(\alpha)$ represents the amplitude contrast transfer function whereas the imaginary part $\sin\chi(\alpha)$ represents the phase contrast transfer function. This imaginary part $\sin\chi(\alpha)$ strongly affects the structure imaging and the point-to-point resolution. Although the phase shift depends on incident angle α for a lens, it is more convenient to describe by the so called spatial frequency u and v (inverse of lattice spacing d) as following equation (3-20).

$$\begin{aligned}\chi(u,v) &= \frac{\pi}{2\lambda}\left[C_s\lambda^4\left(u^2+v^2\right)^2 + 2\Delta f\lambda^2\left(u^2+v^2\right)\right] \\ &= \frac{\pi}{2}C_s\lambda^3\left(u^2+v^2\right)^2 + \pi\Delta f\lambda\left(u^2+v^2\right).\end{aligned} \tag{3-20}$$

The effect due to spherical aberration or/and defocus can be inserted by multiplying $F(u,v)$ of equation (3-12) with $\exp\{-i\chi(u,v)\}$.

Furthermore, other aberrations, e.g., fluctuations of acceleration voltage or of electric current, or energy dispersion by non-elastical scattering in a specimen inside (chromatic aberration) also can be affected to $\sin\chi(\alpha)$ (see Fig. 6.5).

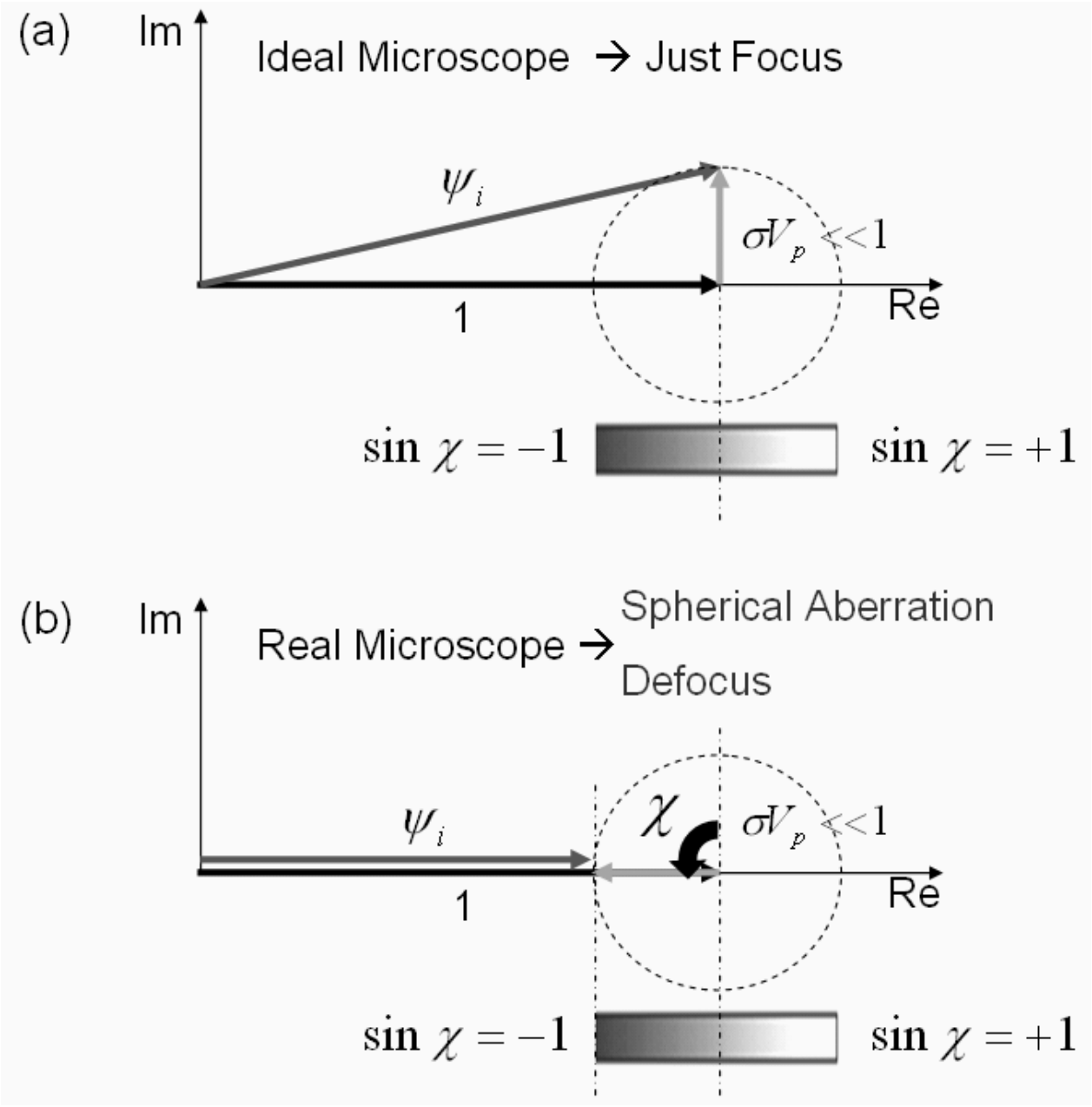

Fig. 3.6 Explanation of the additional phase shift caused by spherical aberration or/and defocus. The wave function under the exit surface of the crystal can be seen as a complex plane. A lens makes the vector of σV_p rotated on the complex plane by the additional phase shift χ. The amplitude of the wave function Ψ_i can be determined by the resultant of the two vectors, 1 and σV_p (<<1), on the complex plane. This resultant amplitude indicates the intensity.

Lattice Structure Image

The wave function under the exit surface of the specimen is given by equation (3-17) when considered as 'weak phase object approximation'. Since a multiplication of functions in reciprocal space copes with a convolution operation of functions in real space, the wave function on a screen is given with lens transfer function in reciprocal space as following.

$$\Psi_i \propto 1(x,y) + i\sigma V_p * \hat{F}\left[\exp - i\chi(u,v)\right] \tag{3-21}$$

The intensity on a screen is given by,

$$I_i = \left|\Psi_i(x,y)\right|^2 \propto 1 + 2\sigma V_p(x,y) * \hat{F}\left[\sin\chi(u,v)\right]. \tag{3-22}$$

Equation (3-22) suggests that a real crystal which includes also an atomic species is directly reflected into imaging contrast, because a projected potential V_p can be proportional to the intensity I_i under specific conditions.

The relationship between I_i and $\sin\chi$ can be understood by using the schematic diagram of Fig. 3.6. The wave function under the exit surface of the crystal can be seen as a complex plane. The $\sin\chi(u,v)$ depends on the aberration and defocus. The additional phase shift caused by χ results in a rotation on the complex plane for the vector σV_p of equation (3-17) in Fig. 3.6. In an ideal microscope and in focus, the additional phase shift does not happen. The length of the resultant vector on the complex plane is the same as the real term 1, indicating that the intensity on a screen is 1. No contrast ($I_i = \left|\Psi_i(x,y)\right|^2 = 1$) would be at the screen for $\sin\chi(u,v) = 0$ under specific conditions given by no spherical aberration and in focus in an ideal microscope (see, Fig. 3.6(a)).

Therefore, suitable aberration and suitable defocus need to be selected, to generate a contrast. In a real microscope, an additional phase shift is caused by spherical aberration or/and defocus, indicating rotation of the vector of σV_p on the complex plane. When $\chi = 90^\circ$ (see Fig. 3.6(b)), then the amplitude of the wave function Ψ_i should be $1 - \sigma V_p(x,y)$.

$$\text{Then, } I_i = \left|\Psi_i(x,y)\right|^2 \propto 1 - 2\sigma V_p(x,y). \tag{3-23}$$

This means that the potential of a crystal can most clearly reflect to contrast on screen when a microscope has a satisfaction of $\sin\chi(u,v) \approx -1$.

The specific imaging conditions which provide $\chi(\alpha) \cong 90^\circ$ within wide spatial frequency α^{-1} are important for imaging in HRTEM.

The modulation of the amplitude also has to be considered for thick specimen or heavy elements, resulting in the following equation (without approximation):

$$\Psi(u,v) = \hat{F}\left[A(x,y)\exp i\delta(x,y)\right] \times \exp - i\chi(u,v), \tag{3-24}$$

$$I_i(x,y) = \left|A(x,y)\exp i\delta(x,y) * \hat{F}\left[\exp - i\chi(u,v)\right]\right|^2. \tag{3-25}$$

The equation shows that the intensity is not proportional to the crystal projected potential V_p. This indicates that a real crystal structure is not directly reflected in the image intensity and that the interpretation is more difficult than for the case of a weak phase object.

Therefore, a quantitative analysis is essential for an interpretation of an image in the case of thick specimen or heavy elements.

3.4 Quantitative Image Analysis

Iterative Digital Image Matching

HREM images the projected specimen structure by a complicated interference pattern, because the generation of the image is a strongly nonlinear process. The main reasons for the non-trivial image interpretations are dynamical scattering, the partially coherency of the electron wave, and the nonlinear image formation by phase contrast. Therefore, in a quantitative interpretation, it is necessary to compare the experimental image with simulated image based on the multislice method [Cowley, 1957], [Horiuchi, 1978], [Ishizuka, 1987], [Stadelmann, 1987] for a correct image interpretation. Simulated images are printed out with a continuous tone contrast. In order to evaluate exact agreement between an experimental image and the simulated image, it should be compared by a numerical procedure. The residual error should be minimized. XCF (Cross Correlation Factor) value which means a level of agreement between two images is available for a numerical comparison [Möbus, 1996]. When a normalized intensity at the pixel (j, k) is defined as E_{jk}, S_{jk} on the computed and simulated image respectively, the XCF can be given by equation (3-26). The maximum XCF value (typically, > 90 %) suggests best agreement between experimental and simulated condition.

$$XCF(E,S) = \frac{\sum \left(E_{jk} - \overline{E}\right) \cdot \left(S_{jk} - \overline{S}\right)}{\sqrt{\left(\sum E_{jk} - \overline{E}\right)^2 \cdot \left(\sum S_{jk} - \overline{S}\right)^2}}, \qquad (3\text{-}26)$$

$$\text{with } \sum = \sum_{j,k=1}^{nx.ny} .$$

Parameterized imaging condition and different models of the object (specimen) are varied by numerical optimization routines (see Fig. 3.7) with IDIM (Iterative Digital Image Matching) program package developed by G. Möbus [Möbus, 1997], until the best fit of the simulated images to the experimental image is obtained. This means that, by using the IDIM program package, computer assisted image interpretations of the digitized HREM-image can recover the specimen structure with best possible accuracy.

Variable parameters are for main imaging parameters: defocus value, spherical aberration, specimen tilt angle, and beam tilt angle, and for materials parameters: specimen thickness, coordinate of atom (ion) columns, and atomic occupancy.

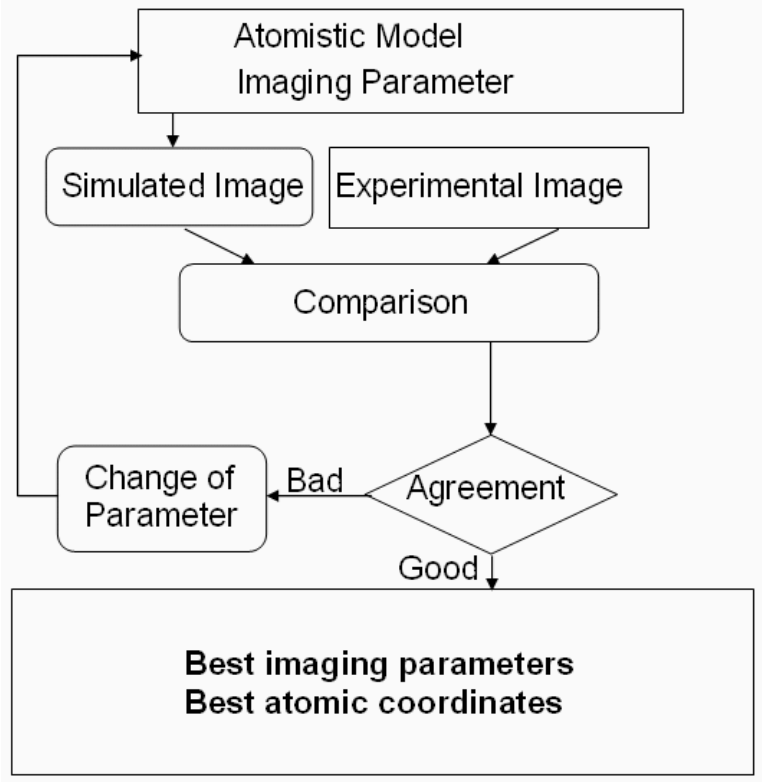

Fig. 3.7 Block diagram of IDIM (Iterative digital image matching) program package developed by G. Möbus [Möbus, 1996]. Parameterized imaging condition and different models of the object (specimen) are varied by numerical optimization routines until the best fit of the simulated images to the experimental image is obtained.

A weak and difficult point of IDIM is that there may exist many local maxima of XCF value, because many parameters are simultaneously optimized. In order to avoid these local maxima which are not realistic, a floating range of the each parameter needs to be restricted, after parameters are roughly determined by a manual mapping.

In this work, after defining an interested region from a scanned ARM image for Pd/ZnO interfaces, a dynamic range (0 to 256) of intensity on image was normalized within 0 to 1.

Following main steps were performed. (i) The best fitting imaging parameters are quantitatively determined in both bulk regions of Pd and ZnO, respectively. (ii) The translation vector between two crystals is determined with IDIM for bulk regions of Pd crystal and ZnO crystal. Then the terminating atomic species are provisionally determined. (iii) The best fitting local atomic structure is quantitatively extracted by IDIM. (iv) In addition, the best fitting atomic occupancy on the terminating layer is quantitatively determined by IDIM. The results can represent then atomic species, atomic occupancy, and the interfacial local atomic structure with the accuracy of ~10 pm.

3.5 Electron Energy Loss Spectroscopy

Fundamental of EELS

The electrons of the primary beam of the microscope lose some of their kinetic energy due to inelastic scattering processes within specimen. The inelastic interaction can lead to an excitation of an electron from the occupied states into the unoccupied states. An energy-loss dispertive plot of the recorded electrons in the detector leads to a so-called electron energy loss spectrum.

Transmission electron energy-loss spectroscopy (EELS) is a powerful technique for the analysis of chemical composition and bonding of a material. An electron microscope combined with EELS facilities allows high-spatial-resolution measurements. As the energy resolution of spectrometers improves to about ~0.2 eV (SESAM), specific information to the low-loss plasmons and the general atomic-like inner-shell-edge shapes which are always broad could be resolved. Energy loss can provide unique capabilities in the study of materials on the nanometer scale or even subnanometer scale.

The absorption edge can be found in high loss-energy region due to excitations of core electrons into the unoccupied states above Fermi level. These edges exhibit some fine structure which is so called electron energy loss near edge structure (ELNES). It would be particularly useful if information on electron charge distribution, bonding and coordination could be extracted from a simple analysis of the fine structure of an EELS spectrum. It is suitable for interface analysis, since ELNES is quite sensitive for chemical environment.

Spatial Difference Technique

Since interfacial atoms possess a different atomic environment compared to that of bulk atoms, they may also have a specific electronic structure. However, the signal from such an interfacial layer, probably only a monolayer thick, is extremely weak and with today's instrument the area probed by the electron beam is larger than the interfacial region. This means that it is difficult to distinguish between signals resulting from pure bulk region and from interfacial region which includes both bulk regions and interface. Presently, the best way to overcome these technical problems for obtaining an interfacial specific ELNES signal is given by a difference technique. The spatial difference technique was developed by Scheu [Scheu, 2002]. Measurements usually are performed, for the bulk crystal regions *A* and *B*, and an interface region with the center of a scanning area located just at the interface as shown in Fig. 3.9.

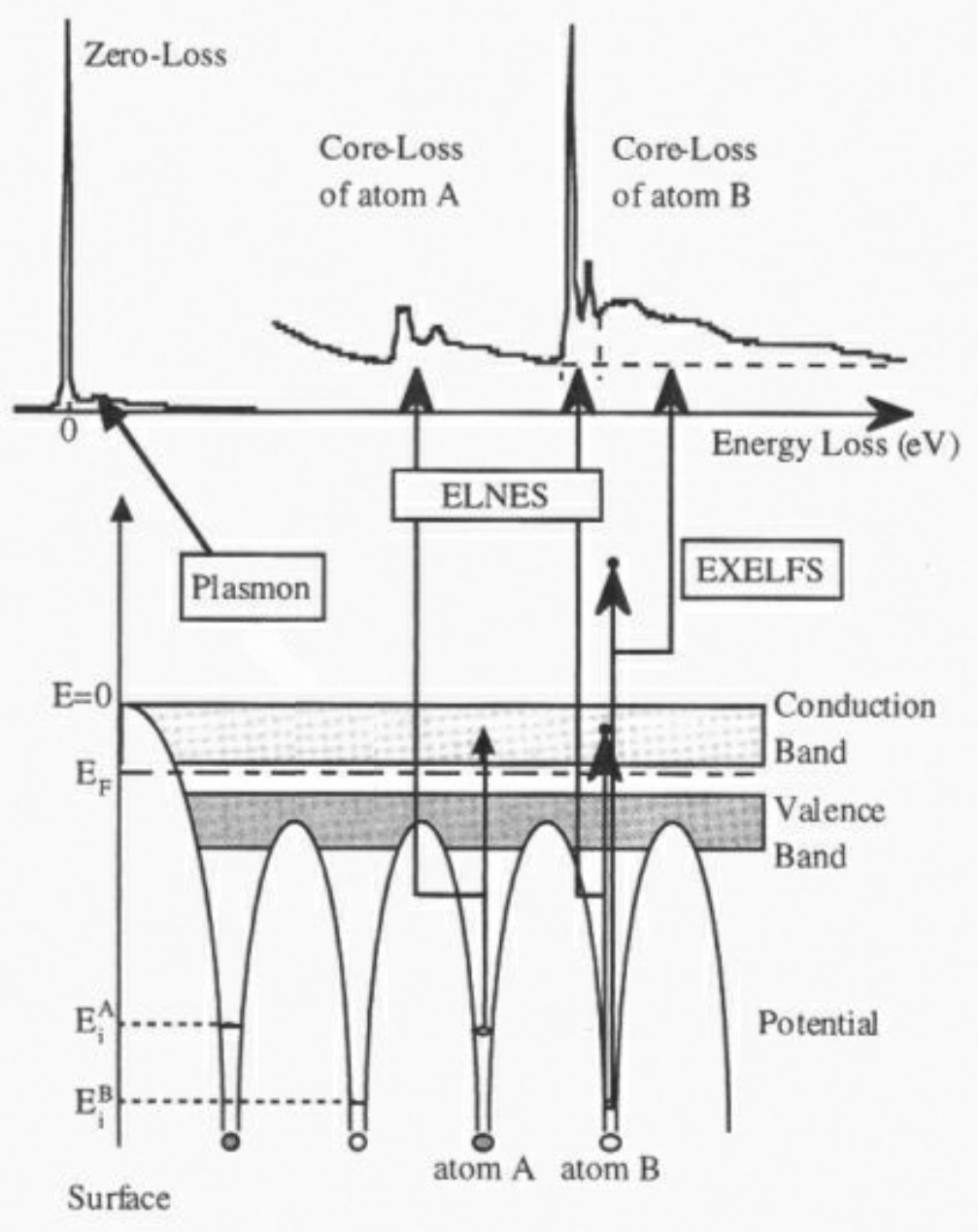

Fig. 3.8 Electron energy-loss spectrum and electron exciting process in solid. The inelastic interaction can lead to an excitation of an electron from the occupied states into the unoccupied states. An energy-loss dispertive plot of the recorded electrons in the detector leads to a so-called electron energy loss spectrum. [Kurata, 2000].

The same beam current and scanning times should be used for the 3 measurements. Subtracting background provides the pure energy loss spectra.

When the signal from the interface region is defined as I_{A+B}, the signal from the bulk crystal region A as I_A, and the signal from the bulk crystal region B as I_B, subtracting αI_A and βI_B from I_{A+B} results in an interface-specific ELNES. These coefficients α and β are scaling factors which have to be determined with high accuracy.

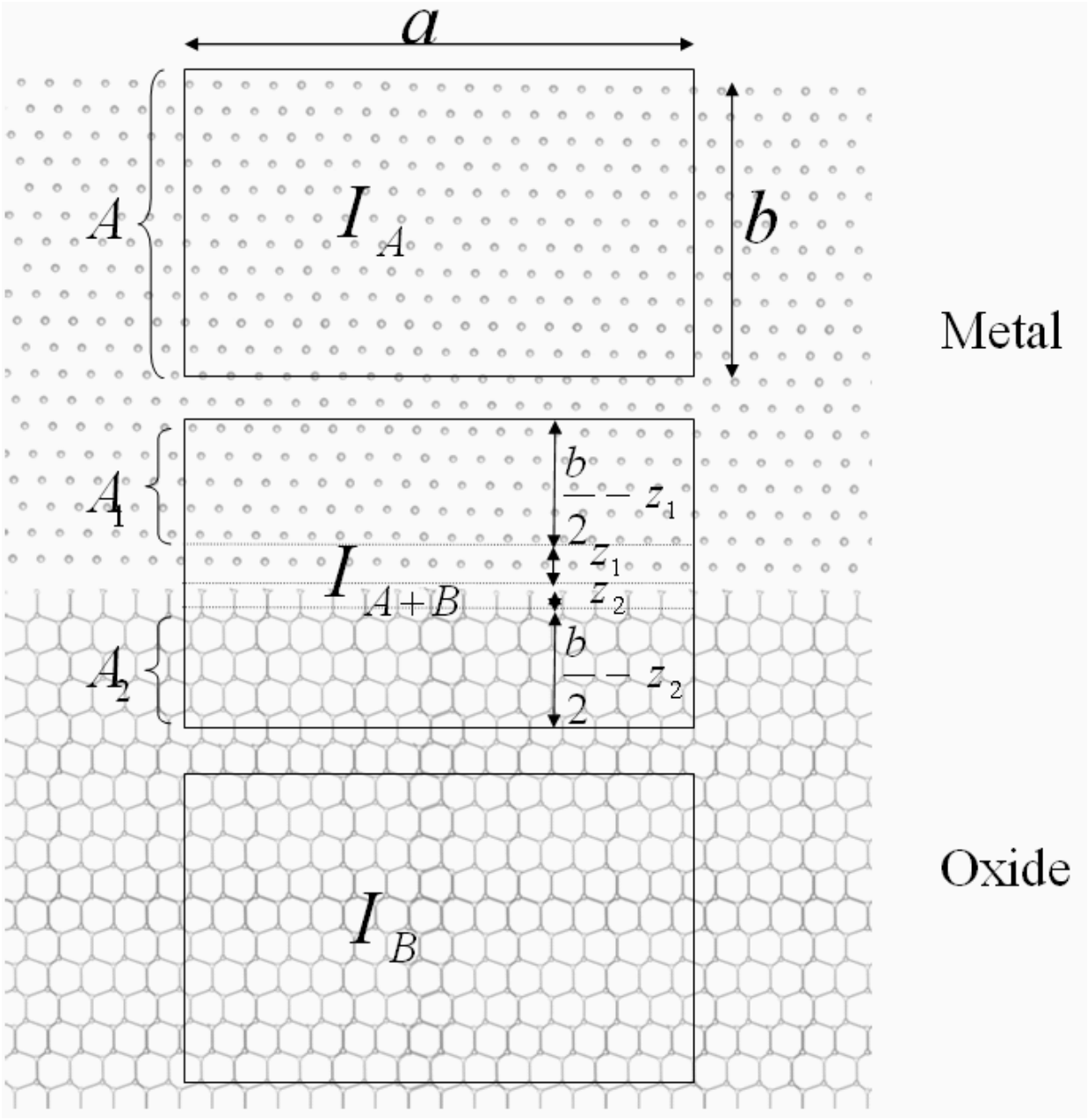

Fig. 3.9 Schematic diagram of the spatial difference technique. The scanned area is $A = a \times b$, and the length of the interfacial monolayer along the normal to the interface is defined as z_1 in crystal *A* and as z_2 in crystal *B* [Scheu, 2002].

The scaling factors can be determined by following procedure. Within the interfacial region $A + B$, the area belonging to the crystal *A* except the interfacial monolayer is defined as A_1 while the opposite area is defined as A_2. Then, these areas A_1 and A_2 should yield the same signal as in the respective bulk measurements. If it is assumed that the intensity depends on the scanned area size, then the interface-specific ELNES I_{int} should be given by equation (3-27).

$$I_{\text{int}} = I_{A+B} - \frac{A_1}{A} I_A - \frac{A_2}{A} I_B = I_{A+B} - \alpha I_A - \beta I_B . \tag{3-27}$$

During a measurement, a drift of the scanning area must be avoided. When the scanned area is $A = a \times b$, and the length of the interfacial monolayer along the normal to the interface is defined as z_1 in crystal *A* and as z_2 in crystal *B*, then the scaling factors α and β are given by equation (3-28).

$$\begin{aligned} \alpha &= \frac{A_1}{A} = \frac{1}{2}\left(1 - \frac{z_1}{b/2}\right) \\ \beta &= \frac{A_2}{A} = \frac{1}{2}\left(1 - \frac{z_2}{b/2}\right) \end{aligned} . \tag{3-28}$$

Unfortunately, in many cases, the appropriate interface-specific ELNES cannot be extracted easily by using equation (3-28). This problem can be attributed to a drift of the scanned area or a non-homogeneous thickness of the specimens. Both effects can be compensated quantitatively. Although the ELNES strongly varies near the edge of the spectrum, it has a flat intensity for higher-energy loss regions. In this higher-energy region, the intensity should depend on the position (size) of the scanned area or thickness. This means that the drift from the ideal position or the change of thickness can be estimated by these intensity differences in higher-energy region. Therefore, equation (3-28) can be rewritten to equation (3-29) [Benthem, 2002].

$$\begin{aligned} \alpha &= \frac{I_{A+B}^{High}}{I_A^{High}}\left(1 - \frac{z_1}{b/2}\right) \\ \beta &= \frac{I_{A+B}^{High}}{I_B^{High}}\left(1 - \frac{z_2}{b/2}\right) \end{aligned} . \tag{3-29}$$

In the case of the measurement of the interface-specific O-K ELNES of the Pd/ZnO interface, (*A* = Pd, *B* = ZnO), the scaling factor α should be zero as shown in equation (3-30), because the crystal *A* does not include oxygen. Therefore, only two measurements for the interface region and the crystal *B* are necessary.

$$I_{\text{int}} = I_{A+B} - \beta I_B . \tag{3-30}$$

3.6 *First Principle* DVXα Molecular Orbital Calculation

First principle DVXα [Adachi, 1998] molecular orbital calculation method applied for analysis of the electronic structures of the Pd/ZnO interface is described.

Linear Combination of Atomic Orbital Method

The wave function of a molecular can be described by the Schrödinger equation, which cannot be solved analytically. Therefore, molecular orbital method or LCAO (Linear Combination of Atomic Orbitals) method are often applied, although the accuracy and each value have to be discussed, to give a numerical solution. The wave function can be described by a linear combination of each atomic orbital function.

The method can easily be explained by describing the wave function for H_2 molecule. For this very simple case, the H atom possesses only a 1*s* orbital. When two H atoms are defined as A and B, respectively, the molecular orbital function can be written as a simple linear sum of atomic orbitals in equation (3-31).

$$\Phi(\vec{r}) = C_A \chi_A(\vec{r}) + C_B \chi_B(\vec{r}) . \tag{3-31}$$

The distance between each wave function χ_A and χ_B is the same as the atomic distance between A and B atoms. When the atomic orbital χ is known, then the molecular orbital can be described by determining the coefficients C_A and C_B. Similarly, the molecular orbital of carbon monoxide CO is given by equation (3-32) including ten coefficients.

$$\begin{aligned}\Phi(\vec{r}) = {} & C_{C,1s}\chi_{C,1s}(\vec{r}) + C_{C,2s}\chi_{C,2s}(\vec{r}) + C_{C,2p_x}\chi_{C,2p_x}(\vec{r}) + C_{C,2p_y}\chi_{C,2p_y}(\vec{r}) + C_{C,2p_z}\chi_{C,2p_z}(\vec{r}) \\ & + C_{O,1s}\chi_{O,1s}(\vec{r}) + C_{O,2s}\chi_{O,2s}(\vec{r}) + C_{O,2p_x}\chi_{O,2p_x}(\vec{r}) + C_{O,2p_y}\chi_{O,2p_y}(\vec{r}) + C_{O,2p_z}\chi_{O,2p_z}(\vec{r})\end{aligned} . \tag{3-32}$$

The molecular orbitals calculation is equivalent to determining these ten coefficients. These coefficients can be determined by solving the Schrödinger equation based on the variational principle. The ten coefficients are given as the solution of a determinant of rank 10, the molecular orbitals are given as an eigenfunction, and the molecular orbital energy is given as an eigenvalue.

Non-empirical *First Principle* Calculation Method

Such a molecular orbital calculation was performed since the early years of quantum mechanics. However, even for simple molecules, it was necessary to calculate complex equation. The calculations were simplified to avoid the direct calculation.

Solving of this integral has been in advance done based on known characters. This

simplification for the calculation is known as the empirical method.

Non-empirical method requires enormous calculations. A necessary input data is only atomic number and atomic coordinates. The method is possible to execute with an advance of computer and this is known as the *first principle* method. Therefore, non-empirical calculations are appropriate for an interface, since there is little empirical information for an interface.

Cluster Method

Electronic states of a molecule can be described by equation (3-32). Due to the limitation of the computer performance, only ~300 atoms can be treated. This means that it is not possible to perform the calculation for a real crystal. The cluster for the calculation should be reduced to an only representative structure with executable size. On the other hand, the band method is appropriate for a crystal which has a periodicity or symmetry and it provides a precise result. If the crystal includes a defect than the periodicity or symmetry, the supercell for the band calculation must be extremely huge to satisfy a periodic boundary condition. Therefore, MO (cluster) calculation is appropriate method to simulate the electronic states of the system having incomplete three-dimensional periodicity in atomic arrangement like a metal/ceramics interface without a reasonably good matching. Actually, a band method which requires a supercell is not appropriate for the Pd/ZnO interface including the large lattice mismatch. This means that local atomic geometry cannot be reproduced in an actual supercell calculation (band method) for the Pd/ZnO system.

Characters of DV-Xα Calculation

The DVXα molecular orbital method (cluster calculation) used in this work is a non-empirical method developed by Adachi [Adachi, 1978], [Adachi, 1998]. Characters of the method are summarized in the following:

1) Flexible Basis Function for Chemical Environment

A basis-function of a molecular orbital calculation is used as GTO (Gaussian Type Orbital) or STO (Slater Type Orbital) for easy and fast calculations. In the DVXα method the atomic orbital function is treated as a solution of the radial term of the Schrödinger equation based on a given chemical environment. This means that even compounds can be executed with high efficiency and reasonable accuracy.

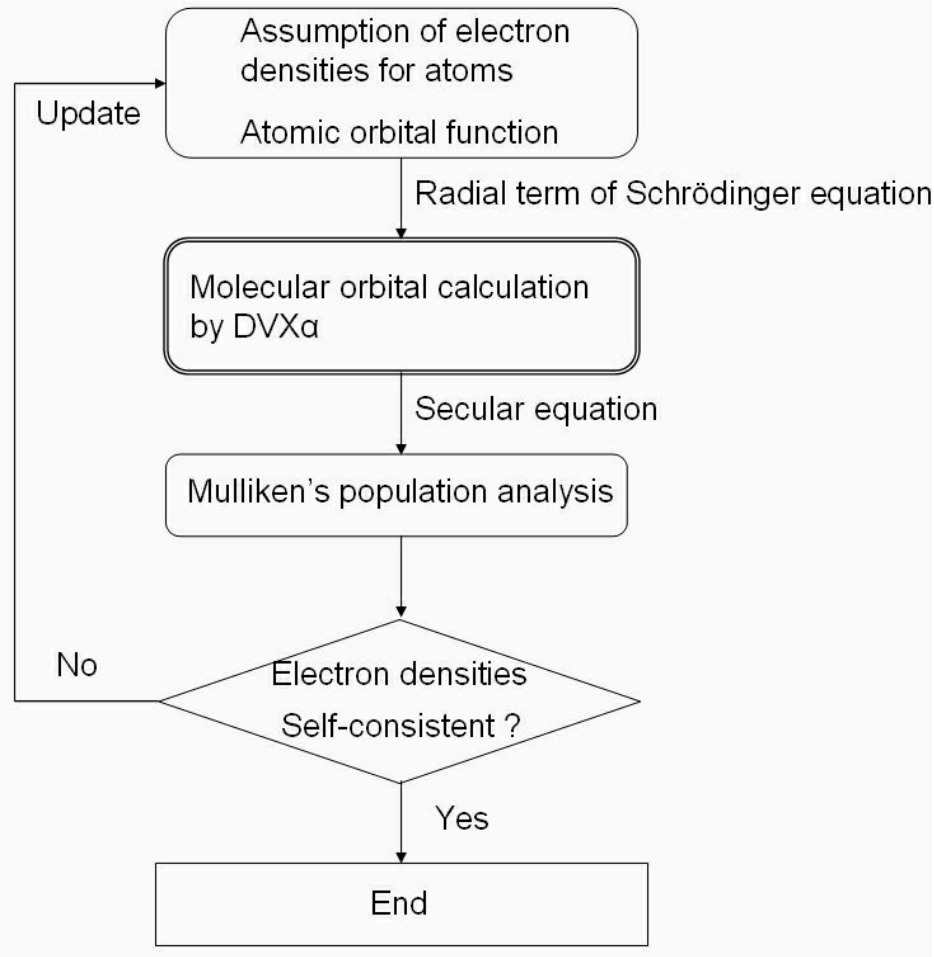

Fig. 3.10 Block diagram of DVXα method. Each numerical atomic orbital function is updated after each iteration. The iteration continues to repeat until the electron density (final value) around all atoms, solved by Mulliken's method, agrees with the initial electron density assumed before the calculation.

2) Use of All Atomic Orbitals including Inner Core Electrons

Since this method includes all atomic orbitals including inner core orbitals as parameters for the calculation, a chemical shift of the inner core orbitals can be also reproduced.

3) Calculation by Xα Method

The DV-Xα method uses Xα (exchange interaction) potentials. A character of the density functional approximation is the high efficiency of the calculation. DVXα method consists of important blocks as shown in Fig. 3.10. Each numerical atomic orbital function is updated after each iteration. The iteration continues to repeat until the electron density (final value) around all atoms, solved by Mulliken's method, agrees with the initial electron density assumed before the calculation. This means that a self-consistent calculation can be attained.

4) Bond Overlap Population

Mulliken's population analysis can be applied to evaluate ionic charges and bond overlap populations in order to discuss interfacial bonding. The BOP_{jk} between the j^{th} and k^{th} atoms is defined as the summation of overlap populations over occupied molecular orbits:

$$BOP_{jk} = \sum_{l} f_l \sum_{\nu,\mu} \left(C_j^{\mu}(l)\chi_j^{\mu}\right)\left(C_k^{\nu}(l)\chi_k^{\nu}\right). \quad (3\text{-}33)$$

In (3-30), f_l denotes the number of electrons occupying the l^{th} MO and χ_j^{μ} denotes the μ^{th} orbit of the j^{th} atom. From the definition of equation (3-33), a total BOP that is summation of BOP below Fermi level indicates the chemical bonding feature. A large positive BOP denotes to stable and strong covalent bonding while a negative BOP denotes to anti-covalent bonding.

5) Provided Physical Values

DV-Xα program package provides (i) ionic charge, (ii) net covalent charge, (iii) bond overlap population, (iv) local density of state, (v) charge density map, and (vi) cross-section of each wave function.

Disadvantage of DV-Xα Cluster Calculation

In the DV-Xα cluster calculation, the number of atoms used in cluster is less than about 300 atoms. It causes a low accuracy for calculated results compared to the band calculation. These two methods should be complementary depending on a material.

4 Specimen Preparation

4.1 Substrate Surface Treatments

Single crystalline specimens of ZnO were purchased from University Wafer. Com in USA* and from Surface Preparation Laboratory in Netherlands**, respectively. The size of the ZnO substrates for tests of the surface treatment and for Pd deposition results in the size of 10×10×0.5 mm^3*. The {0001} surfaces were mechanically polished by the vendor. The specimens for surface structure measurement have the special size and configuration (20 mmØ, 2 mm thick**) for mounting on the special sample holder for surface XRD measurement at ANKA synchrotron (Angstrom quelle, Karlsruhe, Germany). The surfaces were also mechanically polished by the vendor.

Commercial pre-polished ZnO specimens were cleaned mechanically in acetone. Afterward, ultrasonic cleaning followed (i) in acetone (10 min), (ii) in ethanol (10 min), and (iii) in distilled water (10 min). All ultrasonical cleaning steps were repeated once again. Finally, the surface was dried and possible air dust was removed with high pressure Ar gas.

ZnO Specimens for Test of Surface Treatment and for Pd deposition

All ZnO specimens were put on a flat alumina dish and were then transferred into a SiO_2 vacuum tube in an oxygen furnace. Air was removed (~1×10^{-5} Pa) by a turbo molecular pump and then pure oxygen at 1atm was charged within the tube. Finally, they were annealed for 3 hours at 950 °C. This annealing condition will be called as 'air-annealing' in the following. This condition is equivalent to the flattening treatment for the $SrTiO_3$ surface by Kawasaki [Kawasaki, 1994].

After that, specimens were annealed in UHV environment at ~1×10^{-7} Pa (MBE growth chamber) at specific temperatures (400 °C ~ 880 °C) for 1 hour in order to remove surface

---

*University Wafer. Com in USA (www.universitywafer.com) and **Surface Preparation Laboratory in Netherlands (www.surface-prep-lab.com).

impurities. The UHV-annealing at 600 °C allowed to removing air impurity (see section 5.1). Therefore, the final ZnO substrate surface treatment was fixed at 600 °C in UHV for MBE growth.

ZnO Specimens for Surface Structure Measurement by SXRD

In order to determine the dependency of ZnO surface structure on annealing environment, both, the commercial pre-polished $^{+}$**ZnO** and $^{-}$**ZnO** surfaces were annealed in different annealing environments. The following annealings were done before/after each surface structure analysis by SXRD.

1. Annealing in pure oxygen (1 atm, 950 °C) for 3 hour (‘air-annealing’).
2. Annealing in ultra high vacuum (~1×10^{-9} Pa, 600 °C) for 1 hour (‘UHV-annealing’).
3. Annealing in pure oxygen (0.1 atm, 600 °C) for 1 hour (‘reoxidation-annealing’).

4.2 Molecular Beam Epitaxy

In order to examine an epitaxial growth condition of Pd on both {0001}ZnO surfaces, 30 nm Pd films were separately grown by MBE on both $^{+}$**ZnO** or $^{-}$**ZnO** surfaces with the growth rate of 0.001 nm/sec at the growth temperature of 200 °C or 600 °C in UHV environment of $\sim 1\times10^{-7}$ Pa. The film growth was *in-situ* checked by RHEED without exposing into air. Furthermore, the morphology and crystallization of the film were checked by AFM and XRD, respectively.

4.3 TEM Specimen Preparation

For TEM observation a thin specimen (< 10 nm thickness) has to be prepared which allows penetrating of the used electrons. Specimen preparation is most critical step for successful investigation.

The specimen thinning techniques cause always a major problem for TEM observation. It is difficult to make an 'ideal' TEM specimen, in particular, of metal/ceramics (for which both the metal and the ceramic pairs have the same value of thickness also close to the interface). Furthermore, thinning to very small thickness may also cause a mechanical fracture at the interface. Therefore, the most appropriate thinning seems to be limited to ion-milling technique which usually does not give a mechanical damage and does not cause a strong selective thinning compared to other methods. Focused Ion Beam thinning generates specimens of constant thickness. It can adjust an overall shape of the specimen and thickness. However, the damage of the surface layer happens since the Ga ions of high acceleration voltage of 6 ~ 30 keV of the FIB generates the damage. For the observation on thinner region, the surface damaged layer also causes a serious problem for precise interpretation of an HRTEM image.

After all, Ar ion milling with a low voltage (several 100 eV ~ a few keV) seems to be most appropriate for metal/ceramics specimen. In order to avoid the heterogeneous thickness due to the selective thinning, the specimen should be polished as thin as possible by mechanical processes and should also be ion-milled with a small incident angle of the Ar^{+} ion. Moreover, in order to protect the interfacial bonding for the weekly bonded systems, the specimen should be mechanically thinned as thin as possible by dimpling which introduces a dimple in the specimen. The residual thickness prior to ion-milling may be ~10 μm. For a MBE specimen, a protecting layer of Si on Pd film [Strecker, 1993] prevents a selective thinning as shown in Fig. 4.1. In addition, the Si also prevents specimen from charging during TEM observation.

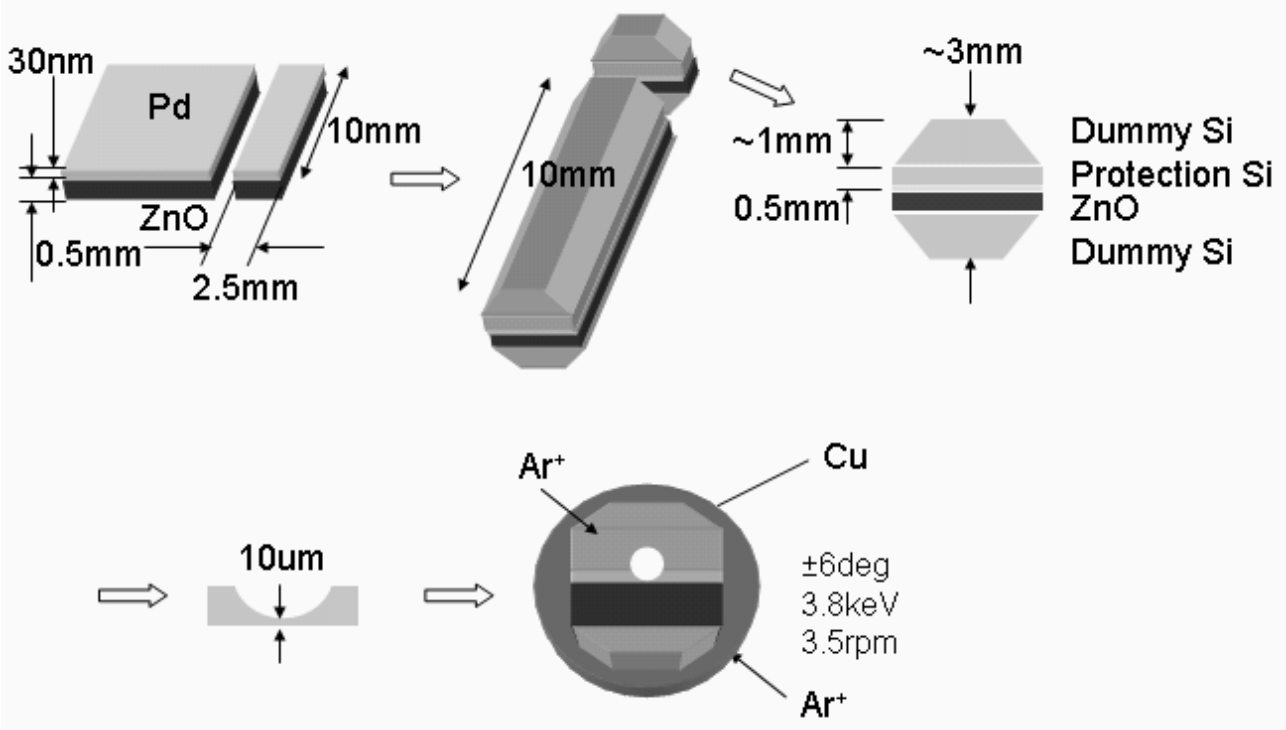

Fig. 4.1 TEM specimen preparation for Pd/ZnO interface produced by MBE. A protecting Si layer was bonded on Pd surface and the layer was fixed by a glue (Gatan M-bond 610). After the hardening of the glue by annealing at 150 °C for 30 min, the layers sandwich with two dummy Si were jointed by the same procedure.

For the TEM specimen preparation the following procedure was finally adopted (Fig. 4.1). Firstly, the Pd/ZnO specimen was cut by a diamond wire cutter (with diameter of more 200 μm), and then a protecting Si layer was bonded on Pd surface and the layer was fixed by a glue (Gatan M-bond 610). After the hardening of the glue by annealing at 150 °C for 30 min, the layers sandwich with two dummy Si were jointed by the same procedure. It was cut again (500 ~ 600 μm thickness), ground by sand paper (#1200 ~ 2400) and polished (by 0.1 μm alumina paste) to 400 μm (measured with micrometer). Then, the other side was ground to 90 μm by the sand paper and then this side was dimpled. When the protecting Si layer is transparent to light, the thickness must be less than 10 μm. Finally, after mounting on a Cu TEM holder, the specimen was ion-milled by GATAN Model 691 PIPS (Precision Ion Polishing System) under the condition (rotating velocity: 3 rpm, vacuum: 10^{-6} torr, acc. voltage: 3.8 keV, and ion beam angle: ±6 °). Finally a beam irradiation of 2.0 keV for 20 min removed a surface damaged layer.

5 Experimental Results for ZnO Surfaces

The structures of the $^{+}$**ZnO** ((0001)ZnO) surface and $^{-}$**ZnO** ($(000\bar{1})$ZnO) surfaces were determined by surface x-ray diffraction (SXRD) with synchrotron radiation prior to Pd deposition.

This experiment results in insight into stabilizing mechanisms of the ZnO and/or reveals structural changes of the ZnO caused by the deposition of Pd. Section 5.1 covers experimental studies of the two different {0001}ZnO surfaces. The surface topography was determined by AFM. Surface impurities were checked by Auger electron spectroscopy (AES). The local surface structure models were obtained by crystal truncation rod (CTR) measurements. The results will be discussed in section 5.2.

5.1 Experimental Results for ZnO Surfaces

Both $^{+}$**ZnO** and $^{-}$**ZnO** surfaces (see subsection 2.2.1), respectively, underwent the same surface treatments at various annealing temperatures and atmospheres. Subsequently, the surfaces were characterized concerning surface orientation (XRD), surface flatness (AFM), surface impurities (AES), surface reconstructions (RHEED/SXRD), step heights (AFM/SXRD), terminating layers (SXRD), and surface stoichiometry (SXRD) before and after each annealing treatment.

5.1.1 Surface Treatments

Differentiation of Surface Orientation

In a first step, the surface orientation, namely the $^{+}$**ZnO** or the $^{-}$**ZnO** were quantitatively checked by XRD of {0002}, {0004}, {0006} planes. These two {0001} planes which are structurally equivalent cannot be distinguished by conventional XRD.

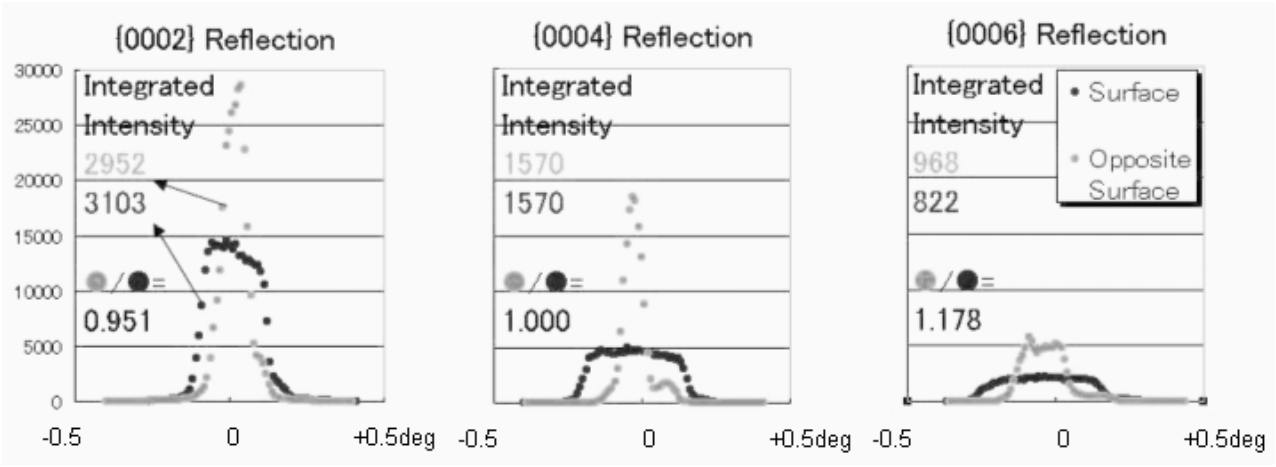

Fig. 5.1 Rocking curves of the Bragg peaks {0002}, {0004}, and {0006}: Black dots correspond to intensities from the $^{-}$**ZnO** surface and gray dots from the $^{+}$**ZnO** surface. A subtraction of the background and an integration of the intensities were done. It can be seen that the reflection integrated intensity depends on the surface orientation in the case of {0002} and {0006} Bragg reflection.

Table 5.1 Ratio of integrated intensity of Bragg peaks. The reflection intensity depends on the surface orientation, in the case of {0002} and {0006}. The experimental ratio of the intensities agrees with the theoretical ratio.

$\{000l\}$	$\{0002\}$	$\{0004\}$	$\{0006\}$
Calculated $\lvert F_{000l}\rvert^2 / \lvert F_{000\bar{l}}\rvert^2$	0.951	1.000	1.174
Experimental $\lvert F_{000l}\rvert^2 / \lvert F_{000\bar{l}}\rvert^2$	0.951	1.000	1.178

The structural difference results only on the geometries of Zn and O. Heiland [Heiland, 1963] showed that the difference can be recognized from studies of the imaginary term of the Atomic Scattering Factor (ASF) by using specific X-ray wavelengths. Both real term and imaginary term of the ASF f show anomalous behavior near the absorption edge of X-ray, see Fig. 3.1 and Fig. 3.2 [Henke, 1993]. As mentioned in section 3.1, the inclusion of the anomalous imaginary terms into reflection intensities will results in a strong dependence of the intensities on the sign of the surface orientation ($^{+}$**ZnO** vs $^{-}$**ZnO**).

Fig. 5.1 shows the rocking curves of the {0002}, {0004}, and {0006} Bragg peaks of ZnO obtained by XRD applying MoKα radiation. For an exact evaluation of the experimental intensities, a subtraction of the background and an integration of the intensities are required. It can be seen that the reflection integrated intensity depends on the surface orientation in the case of {0002} and {0006} Bragg reflection. The integrated intensities

were compared to the calculated intensities. Table 5.1 shows the ratio of the calculated intensities as well as the experimental intensities between the $^{+}$**ZnO** and $^{-}$**ZnO** surfaces. The experimental and calculated values fully agree. Therefore, both $^{+}$**ZnO** and $^{-}$**ZnO** surfaces can be quantitatively distinguished by anomalous scattering XRD (see section 3.1).

Preparations for Flat and Impurities Free Surfaces

Commercial pre-polished ZnO specimens were cleaned mechanically in acetone. Afterward, ultrasonic cleaning followed (i) in acetone (10 min), (ii) in ethanol (10 min), and (iii) in distilled water (10 min). All ultrasonical cleaning steps were repeated once again. Finally, the surface was dried and air dust was removed with high pressure Ar gas.

After this cleaning procedure, the annealing followed (i) in pure oxygen (1 atm, 3 hours, 950 °C) and (ii) in UHV environment (~1×10^{-7} Pa) at specific temperatures (400 °C ~ 880 °C) for 1 hour. Before and after each annealing step, the surface morphologies and the surface impurities were examined by AFM and AES.

AFM images [Fig. 5.2(a1), (a2)] show rough surfaces after mechanical polishing. Furthermore, Auger Electron Spectra [Fig. 5.3(a), 5.4(a)] show that the $^{-}$**ZnO** and $^{+}$**ZnO** surfaces are contaminated with S and/or C impurities, respectively. AFM images after air-annealing at 950 °C [Fig. 5.2(b1), (b2)] show that the surface morphologies were largely altered by the annealing. Steps (minimum height: ~0.26 nm) and terraces (width: 100 ~ 500 nm) structures could be identified on both surfaces by AFM line scans. The minimum step height corresponded to half the lattice constant, $c/2$ of ZnO (c: lattice constant of the ZnO along the c-axis). The air-annealing flattens a ZnO surface on the atomic level. AES spectra [Fig. 5.3(c), 5.4(c)] show that S disappeared while C is still present.

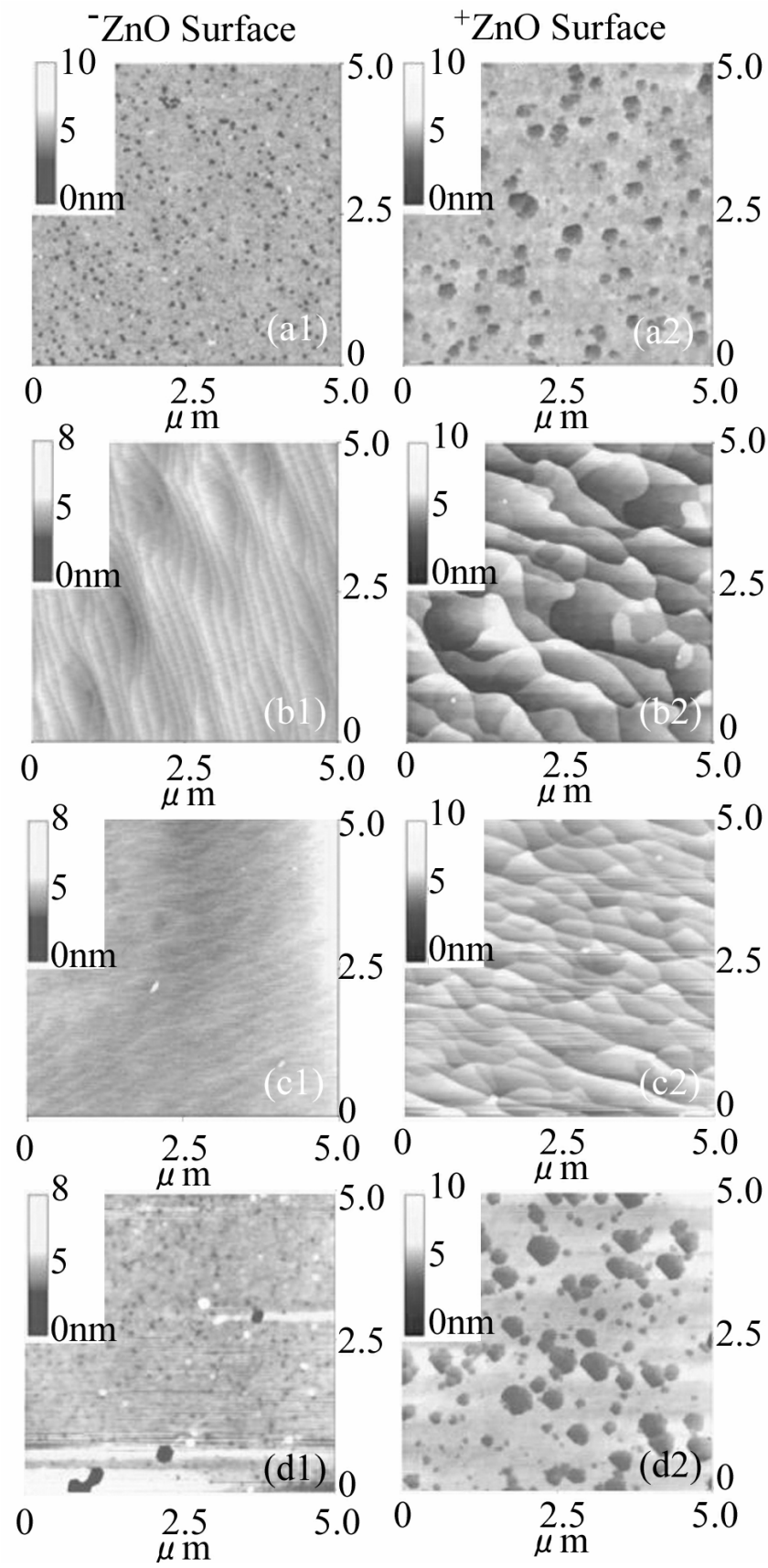

Fig. 5.2 AFM images of the ZnO surfaces (same magnification): (a) after mechanical polishing, (b) after air-annealing, (c) after UHV-annealing with air-annealing, and (d) after UHV-annealing without air-annealing.

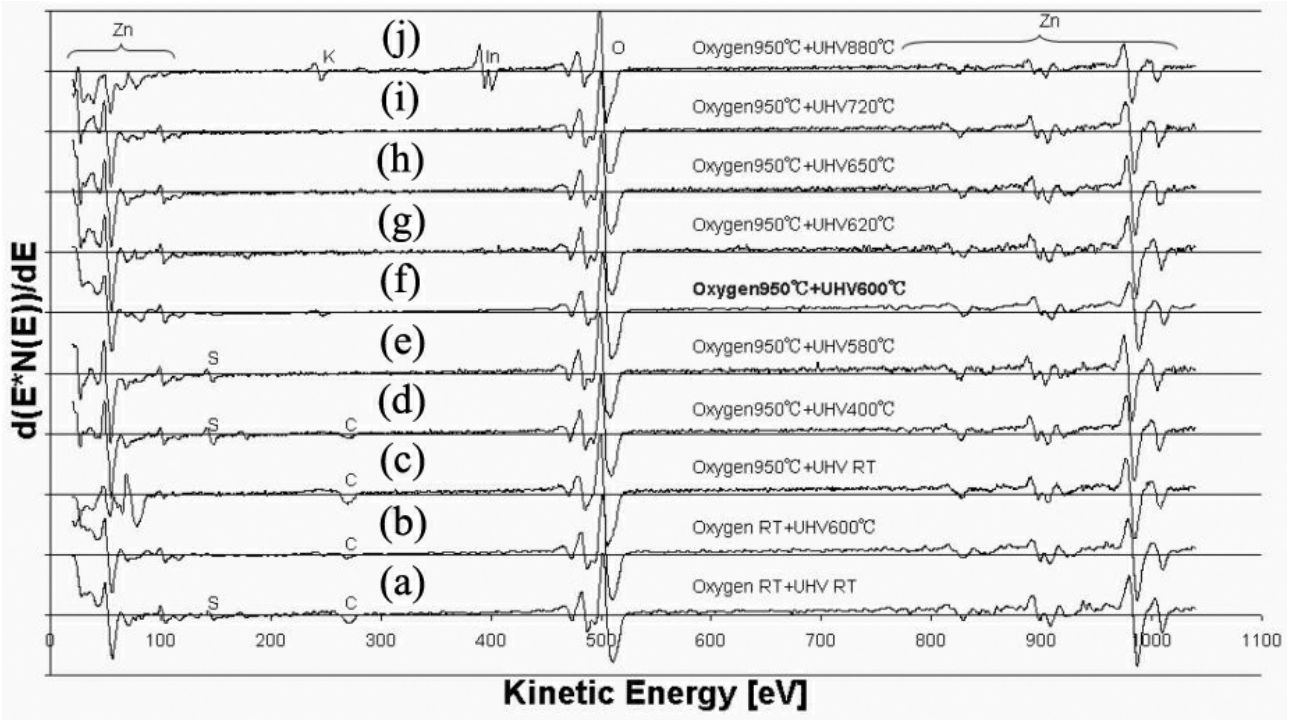

Fig. 5.3 Auger electron spectra from the $^{-}$**ZnO** surface: (a) after mechanical polishing, (b) after UHV-annealing at 600 °C without annealing in O_2, (c) after annealing in O_2 at 950 °C. RT (room temperature) denotes no annealing.

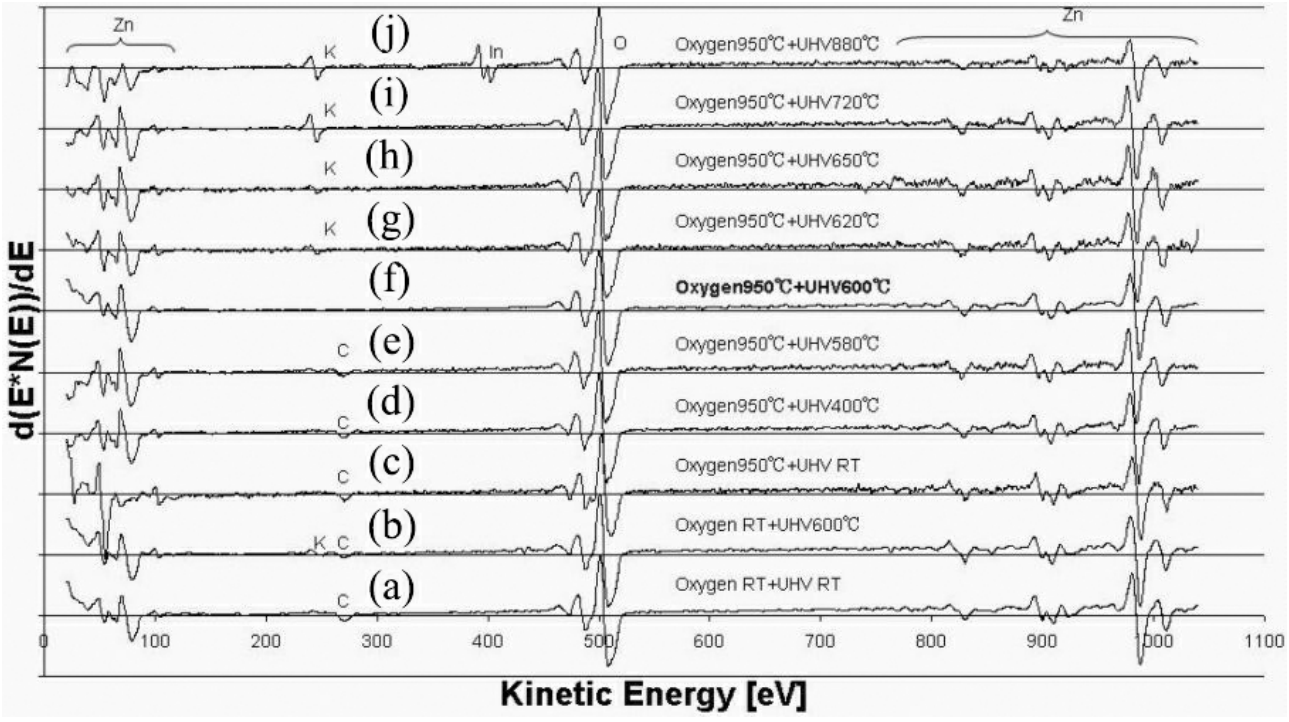

Fig. 5.4 Auger electron spectra from the $^{+}$**ZnO** surface: (a) after mechanical polishing, (b) after UHV-annealing at 600 °C without annealing in O_2, (c) after annealing in O_2 at 950 °C. RT (room temperature) denotes no annealing.

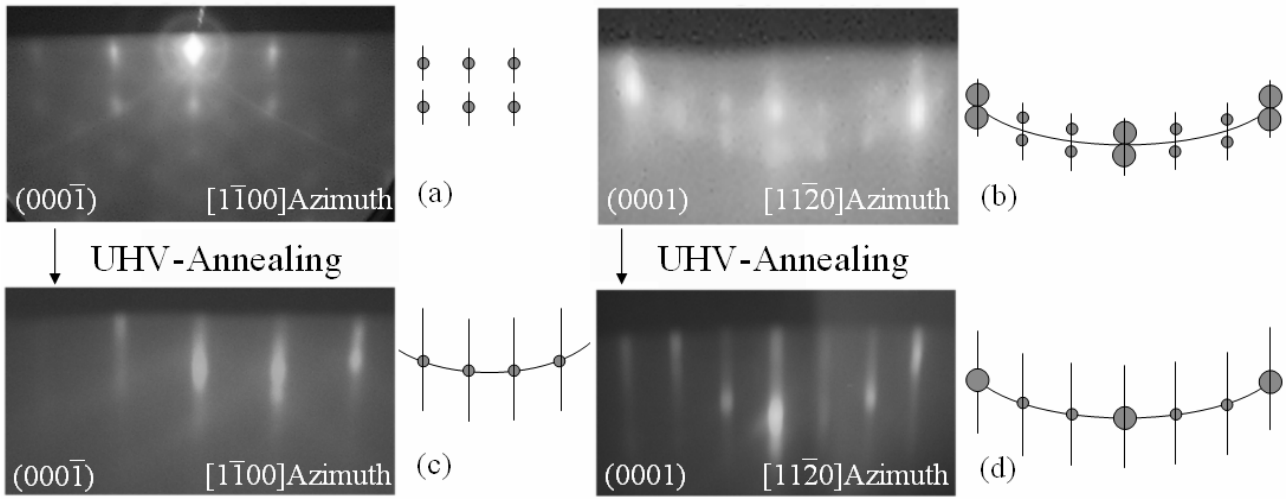

Fig. 5.5 RHEED patterns from the ZnO surfaces: (a), (b) after air-annealing, (c), (d) after UHV-annealing.

The surfaces were checked *in-situ* by RHEED. This technique can be applied for the evaluation of structural change without exposing the specimen to air. The RHEED pattern [Fig. 5.5(b)] from the air-annealed $^{+}$**ZnO** surface shows short rods which are split along the surface normal with diffused spots on Laue rings. This observation indicates that the specimen is not flat (poor flatness) and that the surface is reconstructed along the surface normal. The RHEED pattern [Fig. 5.5(a)] from the air-annealed $^{-}$**ZnO** surface consists of individual spots which is similar to a transmission electron diffraction pattern, indicating that the surface is quite rough.

Furthermore, the surfaces were UHV-annealed at various temperatures (annealing time: 1 hour). After cooling, AES spectra were recorded without breaking the vacuum. AES spectra [Fig. 5.3(d), (e) and Fig. 5.4(d), (e)] show that, below 600 °C, C and/or S still remain on the both surfaces and, at 600 °C, they could be completely removed. However, above 620 °C, K or/and In were detected. Therefore, we annealed all specimens at 600 °C to prepare for an impurity free surface.

The RHEED patterns [Fig. 5.5(c), (d)] from the surfaces after the UHV-annealing show only rods on Laue rings. This means that the UHV-annealing caused a flattening of the surfaces. Furthermore, the surface morphologies were checked in air with AFM. The AFM images [Fig. 5.2(c1), (c2)] show that the $^{-}$**ZnO** surface is similar to before UHV-annealing while the number of steps on the $^{+}$**ZnO** surface was increased indicating further flattening.

To check the influence of air-annealing, different specimens were annealed in UHV environment without air-annealing. AFM images [Fig. 5.2(d1), (d2)] show that both surfaces are quite rough.

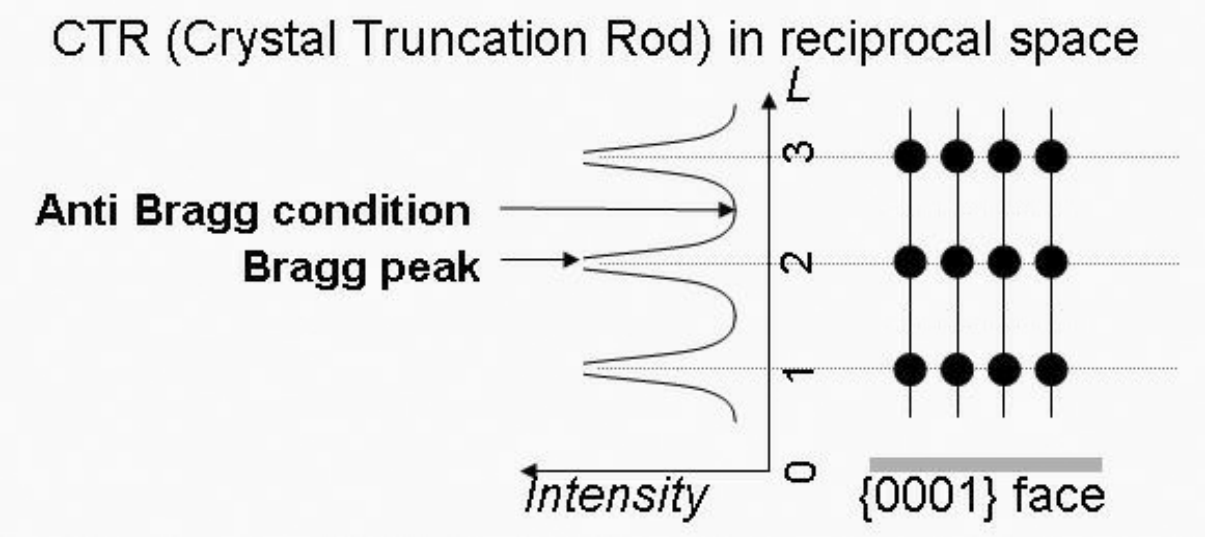

Fig. 5.6 Schematic diagram of crystal truncation rod of a surface. A CTR has an intensity distribution between Bragg reflection points in reciprocal space along the normal of a surface. The black dots correspond to Bragg reflection points in reciprocal space.

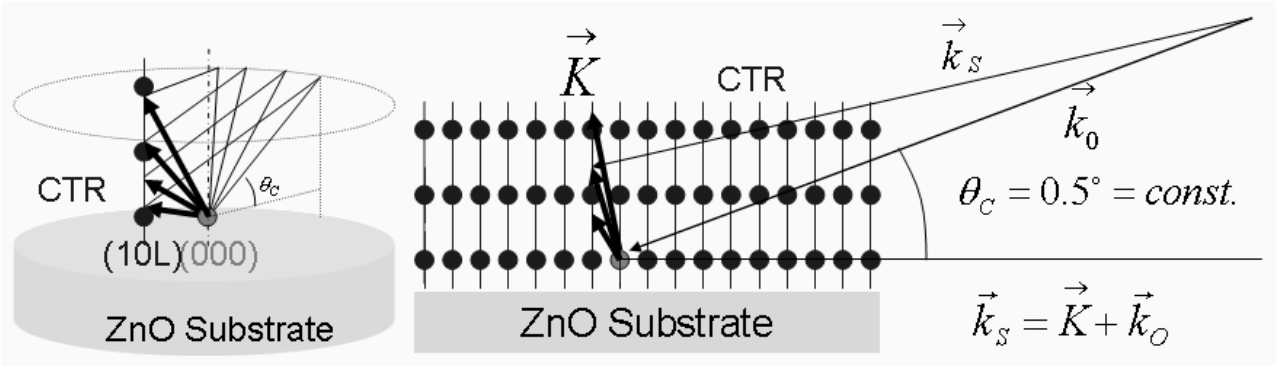

Fig. 5.7 Principle to measure CTR intensity profile for constant incident beam angle.

Furthermore, AES spectra [Fig. 5.3(b) and Fig. 5.4(b)] show that surface impurities still exist on the same concentration level as before the treatment. Therefore, air-annealing is an essential step to obtain flat and clean {0001}ZnO surfaces.

5.1.2 Surface Atomic Structures

Crystal Truncation Rod Measurement

The surface local atomic structure was preliminarily examined prior to Pd deposition. This aim is to examine the structural change of the ZnO owing to Pd deposition. Furthermore, the dependency of the surface structure on annealing condition was also examined. Therefore, analyses of the different surface structures were performed *in-situ* for ZnO specimens annealed at various temperatures and in different atmospheres, respectively.

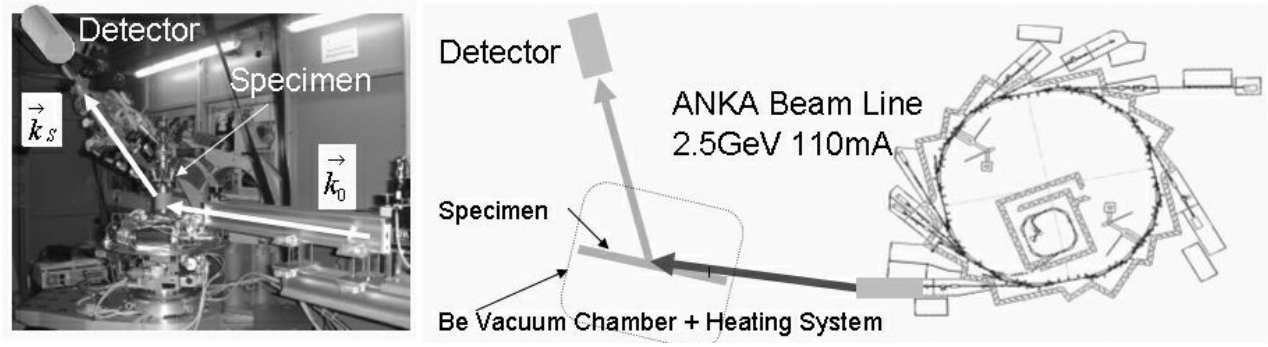

Fig. 5.8 Instruments for *in-situ* CTR measurement.

As mentioned in section 3.2, a surface structure strongly affects the intensity distribution of CTR (Crystal Truncation Rod). Since it is difficult to directly interpret experimentally obtained CTRs, the surface structure can be quantitatively determined by comparing the experimental CTR profile with a calculated CTR profile.

A CTR has an intensity distribution between Bragg reflection points in reciprocal space along the normal of a surface, see Fig. 5.6. The black dots in Fig. 5.6 correspond to Bragg reflection points in reciprocal space. When a mirror index l (of (hkl)) is integer, then the intensity would be maximized. The intensity in anti-Bragg condition ($l \neq$ integer) is extremely low compared to Bragg peak and is sensitive depending on the surface structure. Incident X-ray was entered at a grazing angle θ_C of about 0.5° close to critical angle (see Fig. 5.7). This reduces the back ground intensity. Furthermore, in order to compensate low reflection intensity, a high intensity primary beam by synchrotron radiation was used at ANKA (Angstrom Quelle Karlsruhe, Germany), see Fig. 5.8. *In-situ* measurements are possible, since the windows of the vacuum chamber consist of beryllium.

Experimental Setup

The ZnO specimens for the surface measurement which are different from the specimen used in the test for surface treatment, since the specimen holder of the beam line requires specific specimen configuration (20 mmØ, 2 mm thick). The ZnO specimens were annealed in a pure oxygen atmosphere of 1 atm at 950 °C for 3 hours after light mechanical polishing. The specimens were taken out to air and transferred to the beam line. First of all, CTR profiles of both $^{+}$**ZnO** and $^{-}$**ZnO** surfaces were measured in the beam line prior to any required treatment. Subsequently, they were annealed in UHV at 600 °C for 1 hour and cooled down to room temperature. A second measurement followed. Finally, they were annealed in pure oxygen atmosphere of 0.1 atm at 600 °C for 3 hours and cooled. A third

measurement followed. Each annealing names as air-annealing [1 atm, 950 °C, 3 hours], UHV-annealing [0 atm, 600 °C, 1 hour], and reoxidation-annealing [0.1 atm, 600 °C, 1 hour] for simplified explanation, respectively.

Surface Reconstruction

In order to check the existence of a possible periodic reconstruction of the ZnO surface, intensity profiles were measured by the scans between $i = 0$ and $i = 1$ of (i00) and (0i0) in reciprocal lattice points of ZnO before the CTR measurement. As the results, of the different annealing steps, additional peak between main Bragg peaks did not develop. From these observations it can be concluded that at least periodic in-plane reconstruction does not occur due to all annealing. Unfortunately, these data was missing. However, this agrees with the results obtained from RHEED patterns which did not show any extra spot between the main spots.

Surface Domain

All experimental CTR profiles showed perfect similarity between the experimental CTR profiles along (10L) and (01L) [L = 0 to 3]. The CTR profiles were simulated. Fig. 5.9 shows an example of the experimental CTR profile [black line with error bar] (after re-oxidation) and the calculated CTR profiles [gray line: along (10L), dotted line: along (01L)]. The calculated CTR profiles do not agree with experimental profiles at all. Furthermore, the calculated CTR profile along (01L) is completely different from that along (10L).

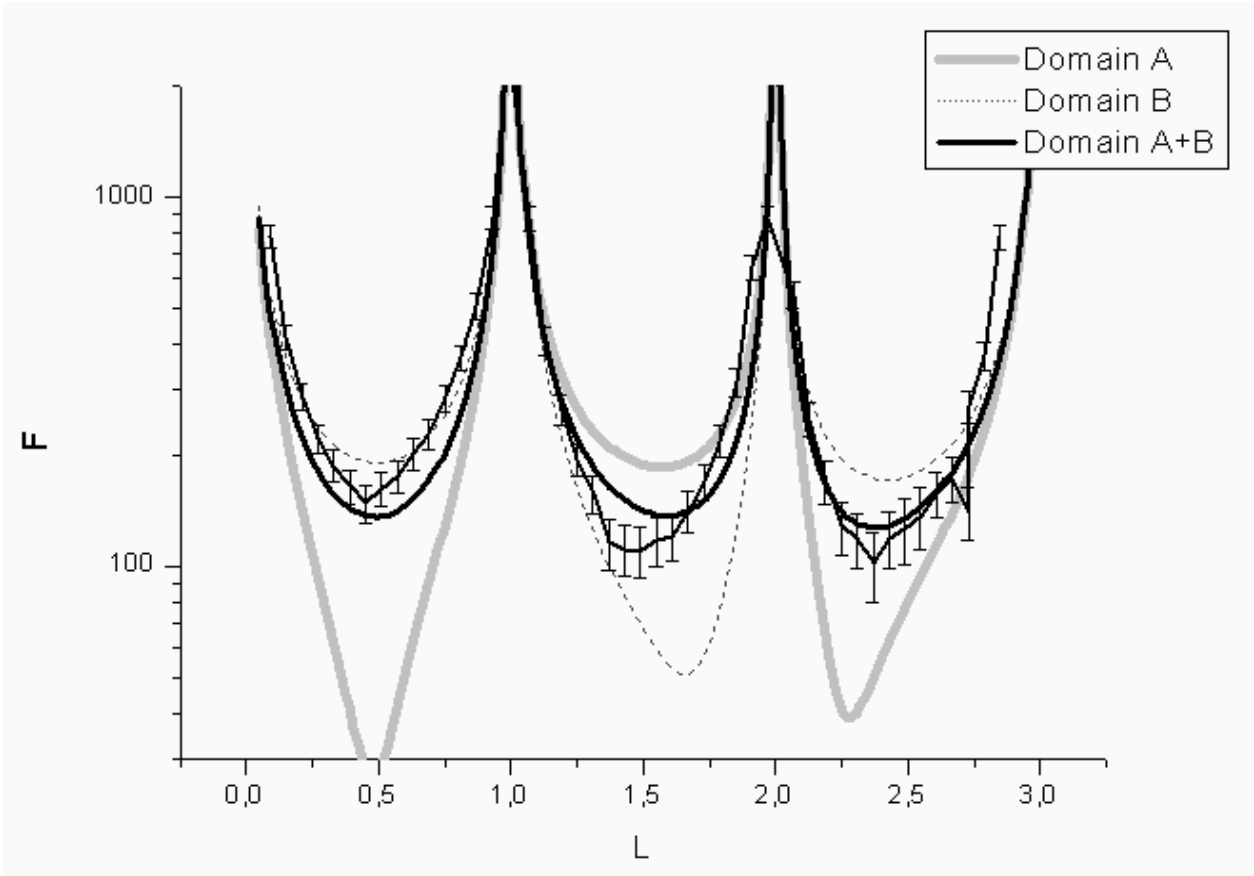

Fig. 5.9 An example of crystal truncation rods: Gray solid line from terrace A (surface domain A, see Fig. 5.10)), dot line from surface domain B, black solid line from mixed domains, black line with error bar for experimental result.

Fig. 5.10 Schematic diagram of possible terraces (surface domains) on the {0001}ZnO surface. The step height in the right figure corresponds to the half of the lattice constant: *c*/2.

If contributions by (01*L*) reflection and by (10*L*) reflection were mixed at the same rate (50 %: 50 %), the mixed CTR profile [black line] agrees with experimental one as shown in Fig. 5.9. The same results could be seen for all kind of annealed ZnO surfaces and for both surfaces. This means that each {0001}ZnO surface must exist of two kinds of terraces. If only the toplayer (Domain A) could be considered on an ideal atomically flat surface (Fig. 5.10), then the surface should have 3-folded symmetry. However, the surfaces actually showed 6-folded symmetry.

Table 5.2 The surface spatial occupancy and the translation along the interface normal of each layer near the $^{+}$**ZnO** surface. The rate in the translation is based on the lattice constant *c* of ZnO. The positive rate means an extension of the interlayer distance.

	Air-annealing	UHV-annealing	Re-oxidation
Zn Occupancy	26.54 % ± 5 %	39.12 % ± 5 %	77.30 % ± 5 %
Translation of 1st Zn atom from lattice point in bulk	-2.93 %	-3.62 %	-6.80 %
O Occupancy	100 % ± 5 %	100 % ± 5 %	100 % ± 5 %
Translation of 2nd O atom from lattice point in bulk	-0.69 %	-5.02 %	+3.03 % (outside)

When the surface has steps with a step height of *c*/2 indicating that it is terminated by the same atomic species, that the symmetry on neighboring terrace should be different by 30° + 60°*n* (*n*: integer) around the *c*-axis and then that it should belong to a different domain (Domain B). Each of the {0001}ZnO surface should have two kinds of terraces (domains) in the case that the surface has steps with a step height of *c*/2. Furthermore, Domain A and Domain B are energetically not different. This denotes that they should exist statistically with the same probability (50 %: 50 % = A: B). The (10*L*) reflection from Domain B is equivalent to the (01*L*) reflection from Domain A. That is the reason why both experimentally determined CTR profiles [(01*L*) and (10*L*)] showed perfect similarity. Therefore, both terraces (50 %: 50 % = A: B) should be considered for the simulation.

Local Atomic Structure of the $^{+}$ZnO surface

A quantitative analysis of the CTR profiles from the $^{+}$**ZnO** surface (Fig. 5.11) revealed following specific surface behaviors. The surfaces have the toplayer of Zn after each annealing process. Depending on the annealing process, however, the atomic occupancy (surface coverage) by Zn of the topmost layer was 26.5 % (950 °C, 1 atm oxygen), 39.1 % (600 °C, UHV), and 77.3 % (600 °C, 0.1 atm oxygen), while the oxygen layer next to topmost zinc layer has the atomic occupancy of 100 % after each annealing process as shown in Table 5.2 (see also Fig. 5.13). Both positions of Zn and O layer were shifted to the inner side of the crystal except O layer after reoxidation-annealing.

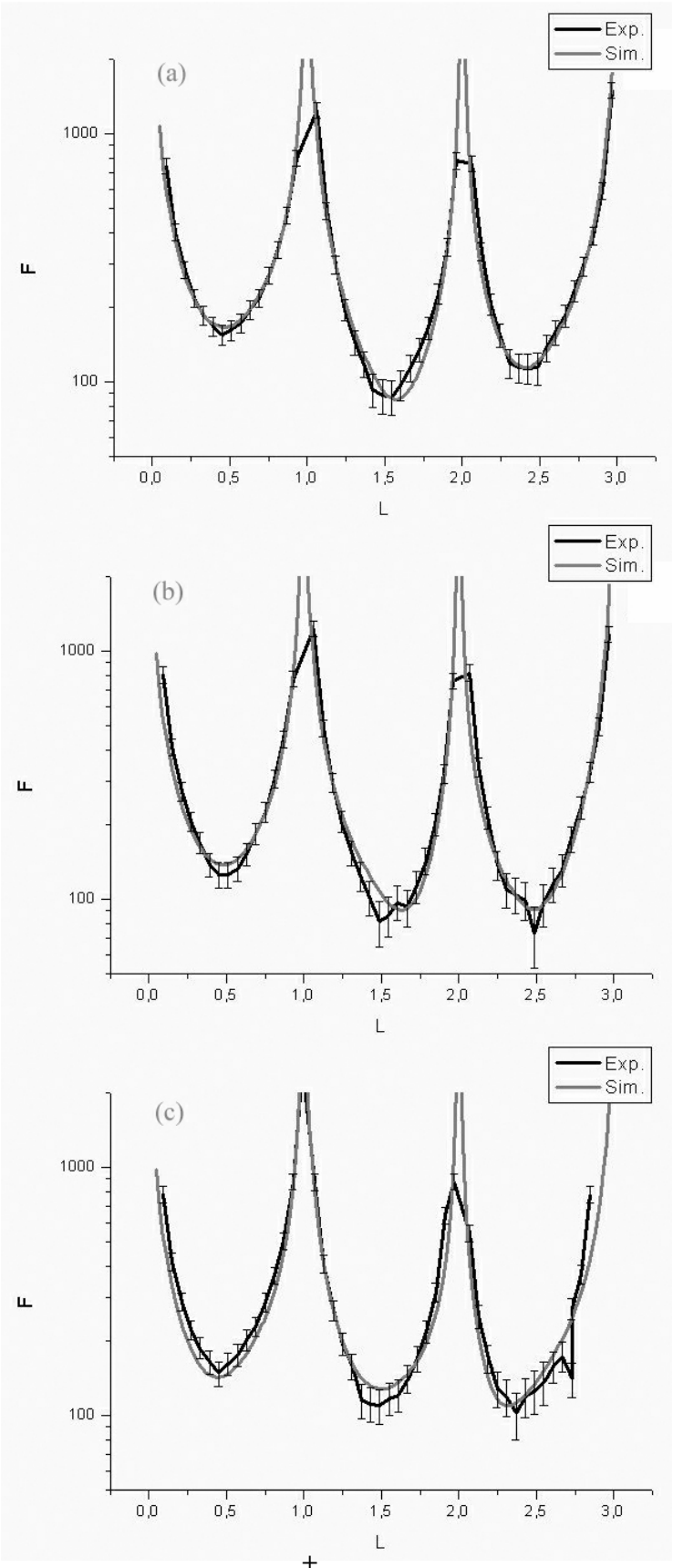

Fig. 5.11 Crystal truncation rod profiles of the $^{+}$**ZnO** surface: Gray lines are calculated profiles and black lines with error bar are experimentally measured profiles. (a) after air-annealing, (b) after UHV-annealing, and (c) after reoxidation-annealing.

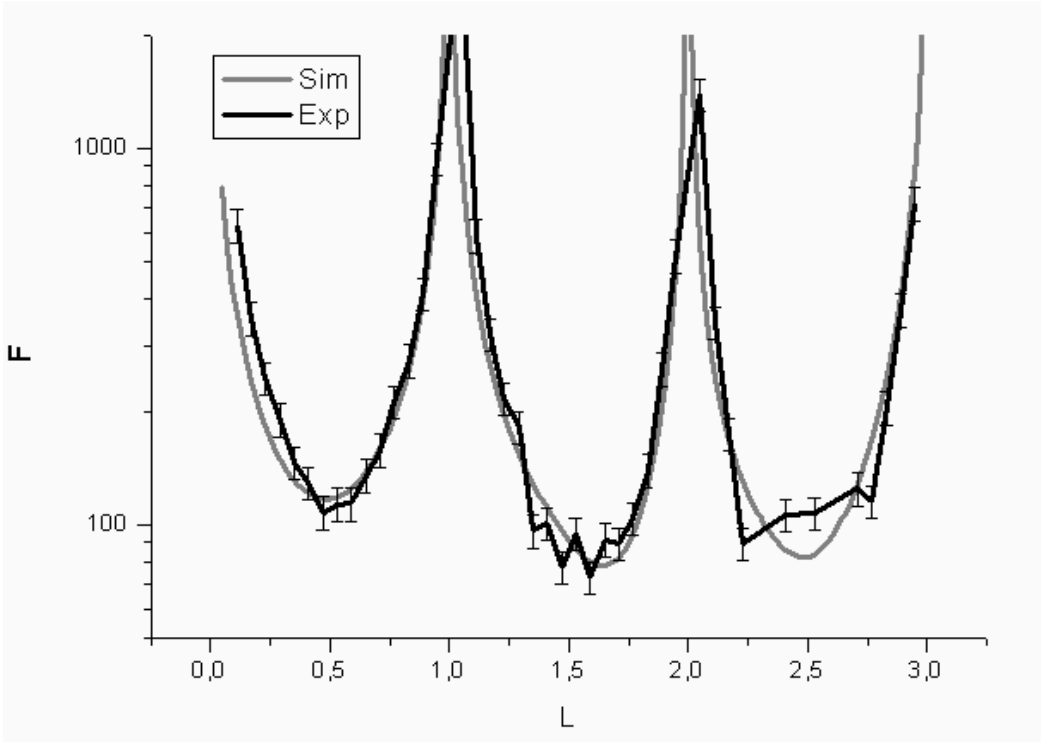

Fig. 5.12 Crystal truncation rod profile of the $\bar{}$**ZnO** surface: Grey lines are calculated profiles and black lines with error bar are experimentally measured profiles after air-annealing.

Table 5.3 The surface spatial occupancy and the translation along the interface normal of each layer near the $\bar{}$**ZnO** surface. The rate in the translation is based on the lattice constant *c* of ZnO. The positive rate means an extension of the interlayer distance.

	Air-annealing
O Occupancy	21.52 % ± 5 %
Translation of 1st O atom from lattice point in bulk	-9.70 %
Zn Occupancy	77.77 % ± 5%
Translation of 2nd Zn atom from lattice point in bulk	-2.64 %

Local Atomic Structure of the $\bar{}$ZnO surface

A quantitative analysis of the CTR profile from the $\bar{}$**ZnO** surface, shown in Fig. 5.12, revealed that the surface was O-terminated after air-annealing process. However, the atomic occupancy (surface coverage) by O of the topmost layer was 21.5 % (950 °C, 1 atm oxygen), while the Zn layer next to the topmost O layer has the occupancy of 77.8 % as shown in Table 5.3. Both positions of O and Zn layer were shifted to the inner part of the crystal.

5.2 Discussion of the Results on the ZnO Surfaces

5.2.1 The $^{+}$ZnO Surface

Topmost Atomic Occupancy of Ions for Atomic Layer on the $^{+}$ZnO Surface

In section 5.1, it was shown that the local atomic structure of the $^{+}$**ZnO** surface could be quantitatively determined within an error of ±5 %. The difference for different annealing processes is only in the occupancy (surface coverage) of the topmost Zn atom.

Depending on the annealing process, the surface spatial occupancy of the topmost Zn layer was 26.5 % (950 °C, 1 atm oxygen), 39.1 % (600 °C, UHV), and 77.3 % (600 °C, 0.1 atm oxygen) as shown in Table 5.2. The atomic occupancy of 26.5 % after the first air-annealing means an exposure of oxygen layer on 73.5 % area of the surface. It can be assumed that the surface was partially oxidized by air-annealing as shown schematically in Fig. 5.13. Furthermore, it also can be considered that the surface was partially reduced during UHV-annealing. However, a final annealing in reoxidation environment (600 °C, 0.1 atm oxygen) resulted in an increase of the occupancy to 77.3 %. Despite the oxidizing environment, the final annealing gave rise to further partial reduction of the surface. This means that the oxidation mechanism is not so simple that an oxidation state of a surface depends only on an oxygen partial pressure.

In general, the pressure and temperature can strongly affect the point defect concentration. We used the defect model of Kröger [Kröger, 1974] to calculate the point defect concentration in ZnO. Han [Han, 2002] formulated in bulk the concentration of ZnO as a function of the O_2 pressure and the temperature by using Kröger's model. Fig. 5.14 shows calculated results of all kinds of point defect concentrations for the conditions obtained by annealing processes. It seems that these calculated values are related to the defect concentration near the surface or to the surface segregation. Actual SXRD measurements were done at a RT in order to reduce a back ground noise in the measurement at high temperature. The calculations of defect concentrations were done under the process temperatures. However, it seems that the comparisons are valid, because the surfaces were comparatively rapidly cooled down and then the situation at the high temperature can be frozen in room temperature.

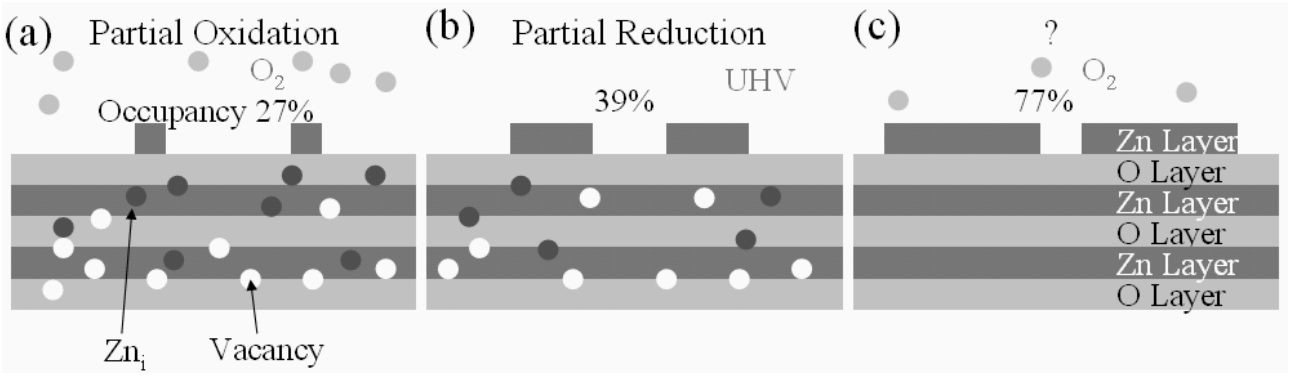

Fig. 5.13 Schematic diagram of possible atomic structure of the $^{+}$**ZnO** surface which depend on annealing environment. (a) O_2 1 atm, 950 °C, (b) UHV, 600 °C, (c) O_2 0.1 atm, 600 °C.

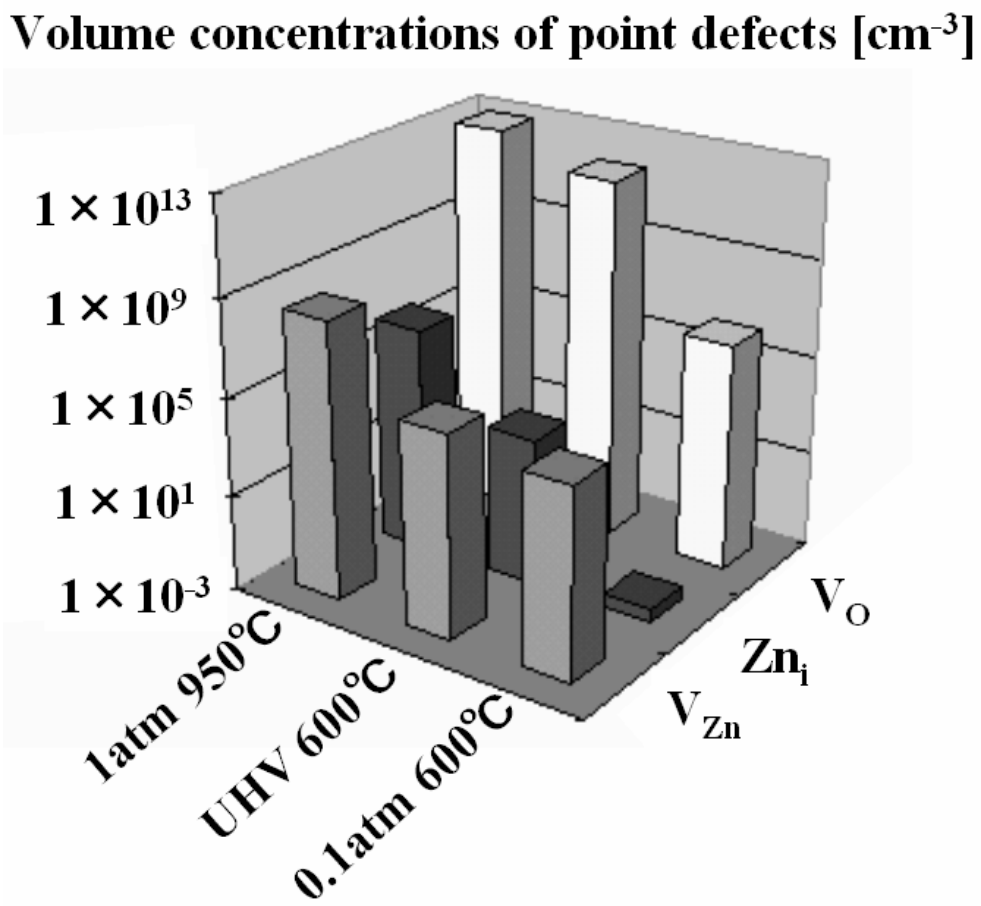

Fig. 5.14 Theoretical point defect concentrations calculated with Kröger model [Han, 2002]. The concentrations of all defects decrease with increase of annealing steps. [Zn_i]: Zn interstitial, [V_{Zn}]: Zn vacancy, and [V_O]: O vacancy.

Fig. 5.14 clearly shows that the concentrations of all defects decrease with increase of annealing steps. The defect concentration [Zn_i] of Zn interstitial Zn_i is extremely decreased at the reoxidation-annealing condition. Zn_i can only be annihilated by combining with V_{Zn}

during the final annealing step, see Fig. 5.13. However, the concentration [V_{Zn}] of Zn vacancy V_{Zn} is still much higher than [Zn_i] at the reoxidation-annealing condition. It seems that all Zn_i cannot be annihilated. This indicates that the extra Zn_i disappeared in inner part of crystal. If the extra Zn_i ions would segregate onto the surface, it would be possible to explain the experimental results. Therefore, the decreasing of Zn_i in volume seems to be related to the increasing of topmost Zn occupancy.

Expectation for the Observed Reduced Surface

The previous arguments are not sufficient to explain the Zn concentration (77 %) in the topmost Zn layer after annealing in oxygen. Experimental value of 75 % was reported by others groups. For a $^{+}$**ZnO** surface, Jedrecy [Jedrecy, 2000] performed a repeated annealing in oxygen radical and in UHV. His CTR measurement revealed that the $^{+}$**ZnO** surface has the topmost Zn atomic occupancy of 75 %. This value agrees within error bar of our CTR experiment after the reoxidation-annealing. Furthermore, Dulub [Dulub, 2003] cleaned a $^{+}$**ZnO** surface by cycles of 1 ~ 2 keV Ar^{+} sputtering and annealing at 600 ~ 750 °C for 5 ~ 30 min in UHV. His STM images showed many triangular hollows and islands on the $^{+}$**ZnO** surface which has several specific sizes and a step height of *c*/2 (*c*: lattice constant). With respect to the observed island, Dulub pointed out that all islands possess a ratio of 75: 100 = Zn: O. Although these triangular hollows or islands could not be seen in our AFM images (see Fig. 5.2), however, the concentration also agrees with our experimental result. The annealing process is different from our process. Nevertheless, our results are the same as 'universal' result. The value of 75 % was explained by considering electrostatic stability of {0001}ZnO surfaces.

A ZnO possesses dipole moments produced by the Zn-O dimmer in a crystal. These dipole moments generate an electrostatic field. This electrostatic field can be cancelled out along all in-plane directions on the {0001} plane. However, it cannot be cancelled out along the *c*-axis of ZnO, suggesting that a linear sum of electrostatic field should be diverged to infinite value along the *c*-axis. This electrostatic instability of the {0001}ZnO surface was pointed out before by Noguera [Noguera, 2000].

In the following it will be explained that this electrostatic field caused by the dipole moments can be cancelled out.

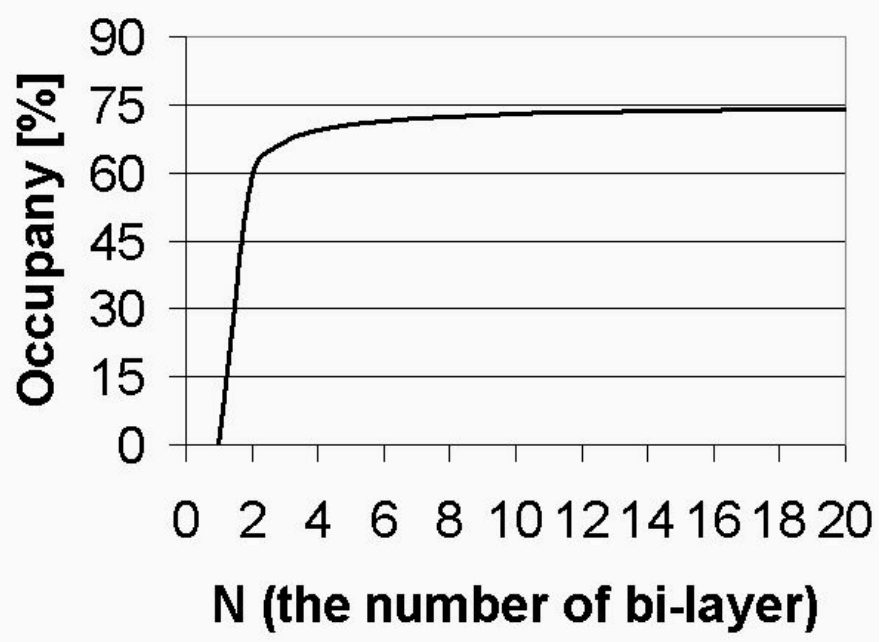

Fig. 5.15 Ideal surface atomic occupancy vs. the number of bi-layer of ZnO which is looked as a pair of Zn and O layers. The occupancy is decreasing with decreasing the number of the bi-layer.

Stabilizing Mechanisms of {0001}ZnO Surfaces

Noguera [Noguera, 2000] explained three stabilizing mechanisms of a {0001}ZnO surface by a reversed electrostatic field which is produced by (i) surface charges, (ii) surface impurities, or (iii) partial missing of topmost atoms. AES (see Fig. 5.4(f)) did not show any signal from an impurity on the $^{+}$**ZnO** surface after the UHV-annealing, indicating that the actual stabilizing is not caused by impurities. Noguera also calculated a necessary surface charge value to cancel out the electrostatic field from bulk ZnO. When the number of bi-layer of Zn-O along the *c*-axis could be assumed as infinite, the ideal surface charge should be $\Delta q = \pm q/4$ where $q = |2e|$ (the typical charge of the ions in ZnO) as shown in Fig. 2.7. Surprisingly this situation can be generated by the partial missing of 25 % of the topmost atoms on {0001}ZnO surfaces. These theoretical expectations completely agree with our experiment. Therefore, a $^{+}$**ZnO** surface can self-stabilize the electrostatic instability.

Why is there the topmost atomic occupancy depending on an annealing process? Fig. 5.14 shows that all defect concentrations largely decreased after a reoxidation-annealing condition while their concentrations were much higher at the first two annealing conditions. In addition, a balance (see Fig. 5.14) between [V_{Zn}] and [V_O] at the reoxidation condition almost gives electronic neutralization in the crystal. This means that the bulk ZnO after the final annealing can electronically be described as a perfect crystal with surface defects suggested by the Noguera.

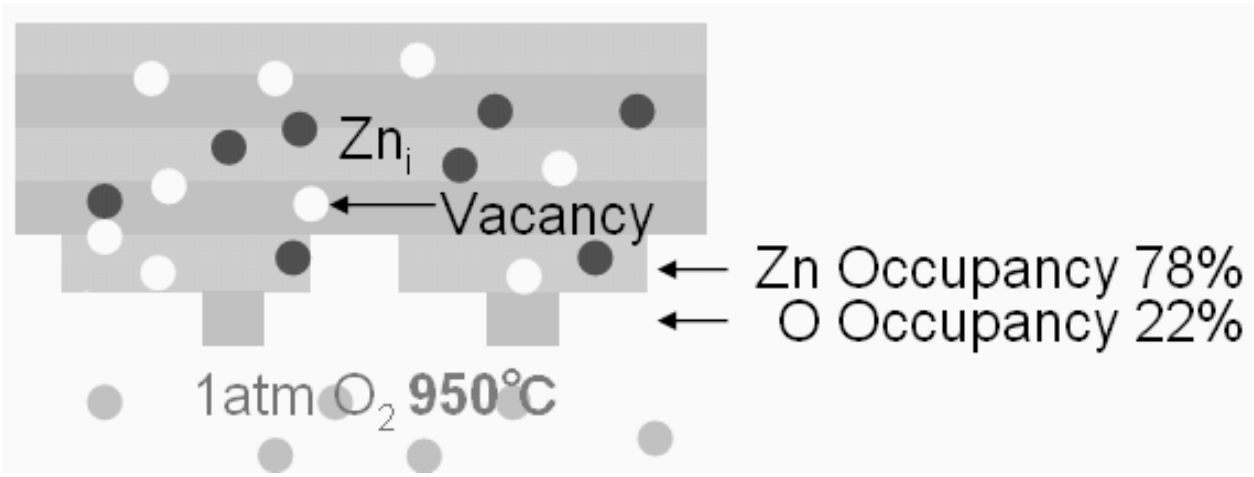

Fig. 5.16 Schematic diagram of possible atomic structure of the $^{-}$**ZnO** surface. The atomic occupancy (surface coverage) by O in the topmost layer is 21.5 % (950 °C, 1 atm oxygen) while for the second Zn layer next to the O layer it is 77.8 %.

On the other hand, it seems that it cannot be used for the first two annealing condition, because much amount of point defects might gives rise to an additional formation of the dipole moments and then they might affect the surface stability, indicating that much stronger surface virtual charges may be required. Therefore, for the first two cases, the occupancies seem to decrease from the ideal occupancy of 75 %.

Global Stabilization

Noguera's model [Noguera, 2000] resulted in an ideal atomic occupancy of 75 % when the number of the Zn-O bilayer along the *c*-axis was infinite. The ideal occupancy depends on the number of bi-layers which are pairs of Zn and O layers. Fig. 5.15 shows the calculated ideal atomic occupancy as a function of the number of bi-layers based on Noguera model. It can be seen that the ideal occupancy is rapidly decreasing with decreasing the number of the bi-layer. If the bi-layer number was higher than 3 or 4 bi-layers, the ideal occupancy could be converged to 75 %. This means that the Madelung field produced by the ionic core of ZnO might at least transmit to 3 bi-layers (0.78 nm) away. This long distance is not unusual for an ionic crystal, although depending on temperature. In addition, the topmost occupancy depended on the defect concentration in the inner part of the crystal. These mean that the surface is dominated by a global force which affects within long range.

Furthermore, the surface was terminated by both Zn and O atom, indicating that the local surface stability was neglected. Therefore, it can be considered that in a $^{+}$**ZnO** surface a global stability is more important than a local stability.

5.2.2 The $^{-}$ZnO Surface

Topmost Atomic Occupancy of Ions for Atomic Layer on the $^{-}$ZnO Surface

In section 5.1, the local atomic structure of the **$^{-}$ZnO** surface could be quantitatively determined. It could be seen that the surface has steps with the height of $c/2$ (c: lattice constant) and the topmost layer of oxygen.

The atomic occupancy (surface coverage) by O in the topmost layer is 21.5 % (950 °C, 1 atm oxygen) while for the second Zn layer next to the O layer it is 77.8 %. The atomic occupancy of 21.5% after the air-annealing means exposure of the zinc layer on 78.5 % area of the surface (see Fig. 5.16). In spite of an oxidizing and a high temperature environment, the annealing gave rise to a partial reduction of the surface. However, the surface spatial occupancy of 21.5 % on this **$^{-}$ZnO** surface is equivalent within the error bar of 5 % to that of 26.5 % on the opposite **$^{+}$ZnO** surface at same annealing condition. Furthermore, STM images by T. M. Parker [Parker, 1998] showed many triangular hollows and islands on the **$^{-}$ZnO** surface as well as the **$^{+}$ZnO** surface [Dulub, 2003]. This means that the same kind of surface stabilizing mechanism suggested by Noguera is working at this **$^{-}$ZnO** surface as well as the **$^{+}$ZnO** surface. It seems that Noguera's model could also work resulting in much higher virtual surface charge than the ideal value of 75 %. Furthermore, the **$^{-}$ZnO** surface was terminated by both Zn and O atom after the air-annealing, indicating that the local surface stability was also ignored.

Therefore, it can be concluded that both {0001}ZnO surfaces are electrostatically self-stabilized and that a global stability is more important than a local stability.

Displacement of Surface Layer

Table 5.3 specifically showed that an O surface layer at the **$^{-}$ZnO** surface was extremely shifted to the inner side of the crystal along normal to the surface by -9.7 %. Wander suggested [Wander, 2001] that the **$^{-}$ZnO** surface was metallized by transforming a sp^3 orbit to a two dimensional sp^2 orbit around O atom and by annihilating a dangling bond, which is related to that the **$^{-}$ZnO** surface can be used as a Gas-sensor. These theoretical expectations agree with our experimental result.

6 Studies of the Different Heterophase Boundaries between Pd and ZnO

In this chapter, the experimental observations by HRTEM for the Pd/ZnO interfaces will be described. All results are presented in section 6.1 and discussed in section 6.2.

In a first step, the best experimental conditions for the well-defined Pd/{0001}ZnO interfaces are elaborated via MBE experiments (subsection 6.1.1).

The cross-sectional TEM specimens are prepared for the experimental studies of the local atomic structures at the interfaces. Local atomic structure analyses in the Pd/ZnO interfaces are performed employing an ultra high resolution microscope JEOL JEM-ARM1250. Usually, HRTEM image does not allow direct image interpretation. Therefore, a best specimen thickness and a best defocus, which give straightforward image interpretation, is estimated by simple inspection via EMS image simulation in subsection 6.1.2. These optimized conditions were actually used for the observations.

Furthermore, the structure models of the Pd/ZnO interfaces are determined employing a quantitative high resolution image analysis technique [Möbus, 1996] in subsection 6.1.3 ~ 6.1.4.

The electronic state near Fermi energy which is sensible for local chemical environment can be reflected to ELNES (electron Energy Loss Near Edge Structure). The ELNES spectra from the interfaces are obtained with a dedicated scanning electron microscope (VG HB-501). The interfacial specific spectra are extracted by the spatial difference technique [Scheu, 2002] (subsection 6.1.5).

6.1 Results for Pd/ZnO Interfaces

6.1.1 Pd Film Growth on ZnO

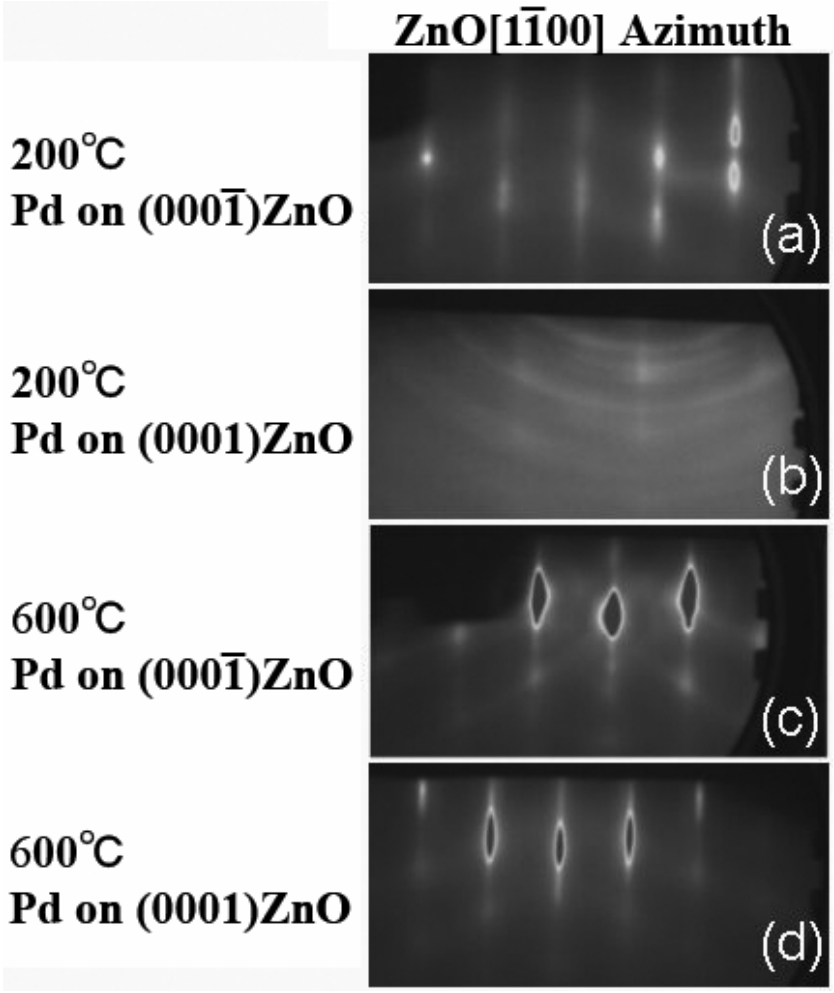

Fig. 6.1 The RHEED patterns taken along the $[1\,\bar{1}\,00]_{ZnO}$ azimuth from the Pd films grown on the: (a) $^{-}$**ZnO** substrate (at the growth temperature of 200 °C), (b) $^{+}$**ZnO** substrate (200 °C), (c) $^{-}$**ZnO** substrate (600 °C), and (d) $^{+}$**ZnO** substrate (600 °C).

Growth Condition

In order to make a well-defined interface by MBE, the Pd films with 30 nm (nominal) thickness were grown on $^{+}$**ZnO** and $^{-}$**ZnO** surfaces, respectively, at two growth temperatures of 200 °C and 600 °C, respectively, with always same deposition rate of 0.01 nm/sec in UHV. RHEED patterns for the Pd films were observed, because the quality of a film can easily be checked without exposing to air. Fig. 6.1 shows RHEED patterns generated from Pd films along the zone axis of $[1\,\bar{1}\,00]_{ZnO}$ azimuth.

All patterns have spots with long rods on Laue ring, except for the Pd film grown on $^{+}$**ZnO** at 200 °C (Fig. 6.1 (b)) which did not show any clear spots on Laue ring. The results suggest that epitaxial and atomically flat films were formed for all substrates except for the $^{+}$**ZnO** substrate at 200 °C on where a polycrystalline Pd film was formed.

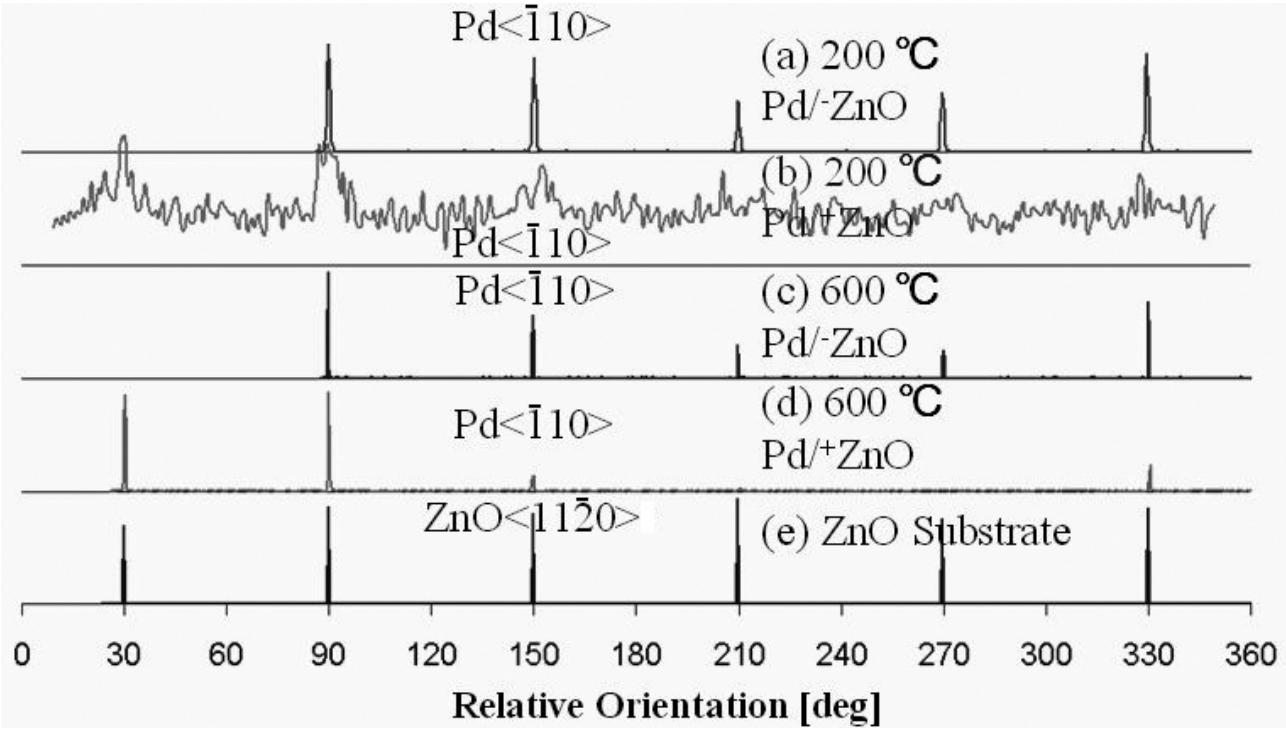

Fig. 6.2 In-plane $<\bar{1}10>_{Pd}$ and $<11\bar{2}0>_{ZnO}$ orientation distributions estimated by $\{331\}_{Pd}$ reflection and $\{11\bar{2}2\}_{ZnO}$ reflection, respectively. The nature of the films is indicated for the four types of the specimens. The reflection (Fig. 6.2 (b)) from only Pd film grown on the $^{+}$**ZnO** substrate at 200 °C indicates broad six peaks.

Table 6.1 In-plane FWHMs of the Bragg peaks from the Pd films (a) ~ (d) or the ZnO substrate (e). the FWHMs of the peaks from the Pd films grown at higher temperature of 600 °C are sharper than that at lower temperature of 200 °C. Furthermore, it can be also seen that the $^{-}$**ZnO** surface makes narrower mosaicity (degree of alignment) of Pd film than that of the $^{+}$**ZnO** surface.

Growth temp. of Pd Substrate	(a) 200°C $^{-}$**ZnO**	(b) 200°C $^{+}$**ZnO**	(c) 600°C $^{-}$**ZnO**	(d) 600°C $^{+}$**ZnO**	(e)
In-plane FWHM	0.90°	9.25°	0.32°	0.44°	0.19° (ZnO)

The in-plane orientations of the films were examined in detail by conventional XRD. They were measured by making the specimens rotated around the $<0001>_{ZnO}$. The in-plane orientations of the $<\bar{1}10>_{Pd}$ and $<11\bar{2}0>_{ZnO}$ were estimated by $\{331\}_{Pd}$ and $\{11\bar{2}2\}_{ZnO}$ Bragg reflections, respectively. The reflection (Fig. 6.2 (b)) from only Pd film grown on the $^{+}$**ZnO** substrate at 200 °C indicates broad six peaks. This means that, although there are weakly-preferred in-plane orientations, the Pd film is less aligned than the other films grown under the other conditions. The diffraction peaks in the other films possess extremely small FWHMs (full width of half maximum). The in-plane orientation of the $<\bar{1}10>_{Pd}$ is parallel to $<11\bar{2}0>_{ZnO}$, indicating that well-defined epitaxial films were formed.

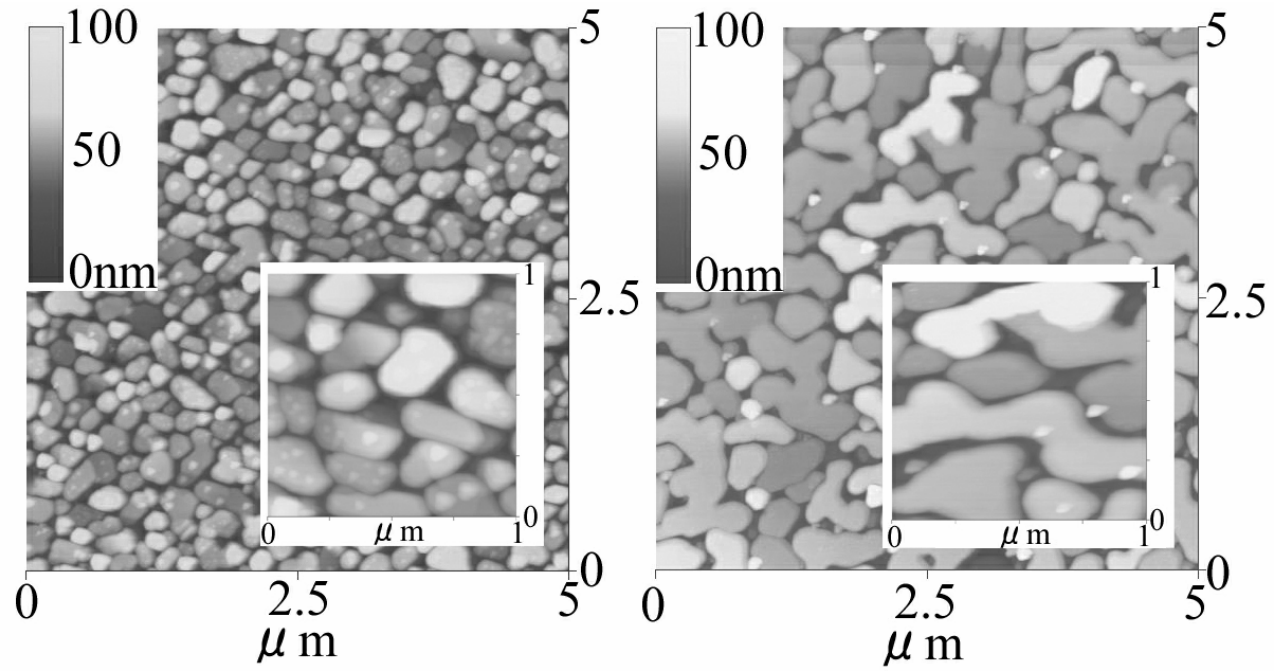

Fig. 6.3 AFM images of Pd films grown on $^{+}$**ZnO** surface at 600 °C (left image) and $^{-}$**ZnO** surface at 600 °C (right image). The large image size is 5×5 μm and the built-in image size is 1×1 μm.

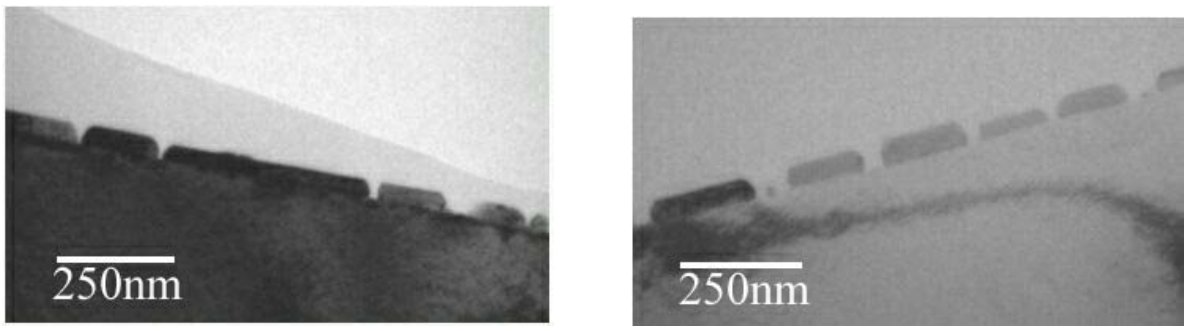

Fig. 6.4 Cross-sectional bright field images of the Pd films grown on the $^{+}$**ZnO** substrate at 600 °C (left image) and the $^{-}$**ZnO** substrate at 600 °C (right image).

As shown in Table 6.1, the FWHMs of the peaks from the Pd films grown at higher temperature of 600 °C are sharper than that at lower temperature of 200 °C. Furthermore, it can be also seen that the $^{-}$**ZnO** surface makes narrower mosaicity (degree of alignment) of Pd film than that of the $^{+}$**ZnO** surface. This means that the high temperature (~600 °C) or the $^{-}$**ZnO** surface provides better epitaxial Pd film. The high temperature condition (600 °C, UHV) which is the same as the second surface treatment of ZnO was used for TEM specimen grown by MBE.

Orientation Relationship and Step Height of the Surface

Fig. 6.2 shows six in-plane $<\bar{1}10>$ peaks from the Pd films, indicating that the Pd films possess 6 domains. When $\{0001\}$ZnO surfaces are atomically flat, it should possess only 3-fold symmetry and then the Pd films also should possess 3 domains. This disagreement can be attributed to the 6-fold symmetry of the $\{0001\}$ZnO surfaces with a step of $c/2$ (c: lattice constant), see subsection 5.1.2. However, 6 kinds of orientation relationships are crystallographically equivalent. Therefore, there exists only one orientation relationship between Pd and ZnO crystals. The experimentally determined orientation relationship is:

$$(111)_{Pd}//(0001)_{ZnO} \text{ and } [\bar{1}10]_{Pd}//[11\bar{2}0]_{ZnO}.$$

Film Topography

AFM images of the Pd film grown at 600 °C in Fig. 6.3 show that the Pd grain size on the $^{-}$**ZnO** surface is bigger than that on the $^{+}$**ZnO** surface. On the $^{+}$**ZnO** surface large islands are formed and liquid-like coalescence is observed more early. Furthermore, from the cross sectional TEM images of the Pd/ZnO interfaces (Fig. 6.3, Fig. 6.4), a film thickness of 50 ~ 60 nm (nominal thickness of 30 nm estimated by quartz thickness monitor of MBE) can be determined. The voids between the Pd grains indicate an island growth mode (nonwetting system).

6.1.2 Imaging of Pd/ZnO Interface by High-Resolution Transmission Electron Microscopy (HRTEM)

Local atomic structure analyses for the Pd/ZnO interfaces produced by MBE are performed employing an ultra high resolution microscope. Usually, HRTEM image does not allow direct image interpretation. Therefore, a best specimen thickness and a best defocus, which may give straightforward image interpretation, need to be estimated via EMS image simulation, before an observation.

Problems for the Imaging of Pd/ZnO System

The main problems for the high-resolution transmission electron microscopic observation in Pd/ZnO systems are the following, (i) extremely small lattice spacings of ZnO, (ii) low scattering factor of O compared to Zn and Pd, (iii) interpretation of contrast near the interface where a periodicity of crystal is broken, and (iv) preparation of extremely thin TEM specimen. Those factors limit the accuracy for a determination of the atomic structure on the HRTEM image by direct interpretation.

The calculated phase contrast transfer function $\sin\chi$ of the ARM (Atomic Resolution Microscope: JEOL JEM-ARM1250) at the Scherzer focus (df = -54 nm) (Fig. 6.5) shows that the $\sin\chi$ is negative within the spatial frequencies of 0.5 ~ 0.12 nm. This means that the lattices with spacings of 0.5 ~ 0.12 nm can be imaged with sufficient contrast for a recognition of the fringes. The spatial frequency of 0.12 nm [Phillipp, 1994] is the so-called Scherzer limit. The TEM provides the best point to point resolution for this condition. The specification of atomic resolution microscope JEOL JEM-ARM1250 (see Fig. 6.6) of the Max-Planck-Institut für Metallforschung Stuttgart is shown in Table 6.2. The resolution is not so sufficient for an atomic resolution of the details of the ZnO structure.

A HRTEM micrograph represents the projection of the image on the screen. Bulk ZnO crystal along the $<11\bar{2}0>$ zone axis possesses the Zn-O dumbbells with the projected interatomic distance (0.114 nm) which corresponds to 3-dimensional real interatomic distance between Zn-O of 0.198 nm, see Fig. 2.9. Furthermore, each atomic column of the Zn-O dumbbell consists of one kind of atomic species along the $<11\bar{2}0>$ zone axis. In principle, the observations along this zone axis allow to distinguishing the atomic species in ZnO. Since the spacing (0.114 nm) along the $<11\bar{2}0>_{ZnO}$ is slightly smaller than the point to point resolution of 0.12 nm, however, it may actually be difficult to distinguish separately two atoms of a dumbbell.

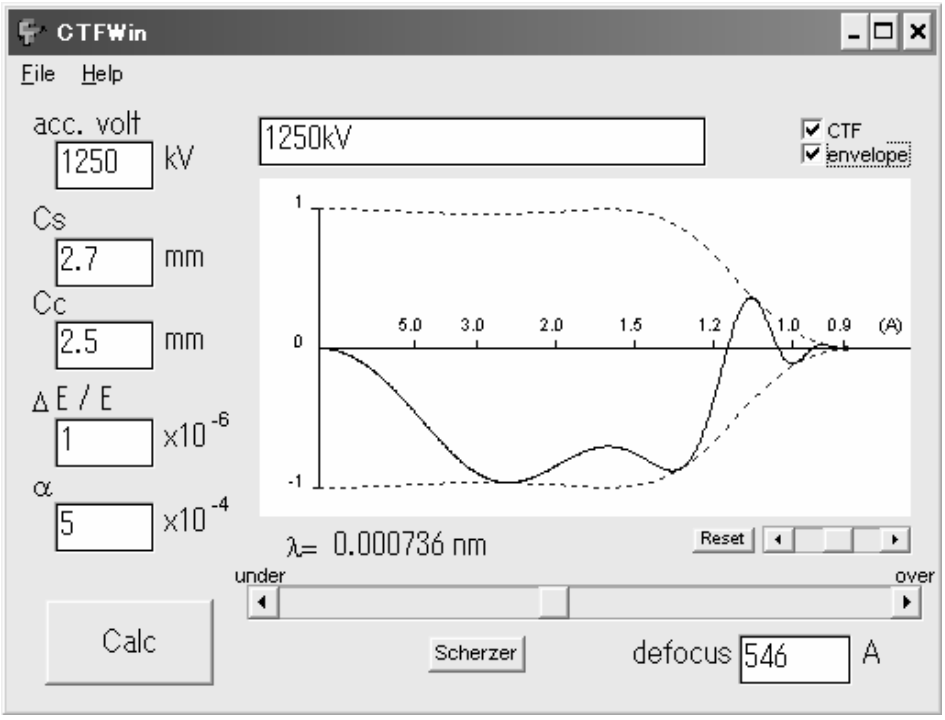

Fig. 6.5 The phase contrast transfer function $\sin\chi$ (including the envelope function due to a chromatic aberration) as a function of a lattice spacing for the Stuttgart ARM (1250 kV). It was calculated by CTFWin developed by Takeo Katoh in the Univ. of Tokyo (1996).

Table 6.2 Specification of Stuttgart Atomic Resolution Microscope JEOL JEM-ARM1250.

Column	
Acc. voltage	1250 kV
Spherical aberration [Objective lens]	*Cs* = 2.7 mm
Chromatic aberration [Objective lens]	*Cc* = 2.5 mm
Best Point to point resolution	0.12 nm
Maximum *z* control	2.5 mm
Maximum *x*, *y* tilt angles	±35°

Pumping out system	
Column/HV tank	Molecular turbo pump Ion Sputtering pump
Specimen chamber	Cryo pump

Dumper	
Air dumper	Feed back system: Q_0 = 1 Hz

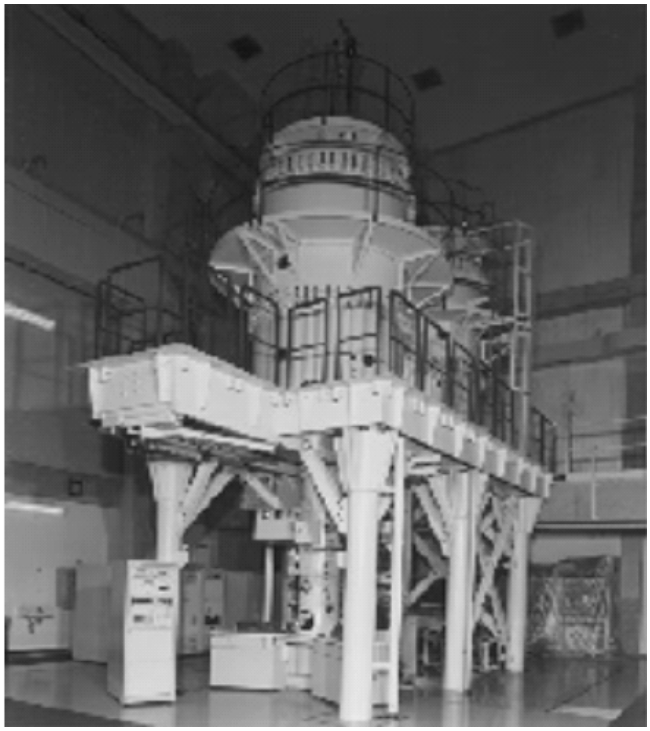

Fig. 6.6 Atomic resolution microscope JEOL JEM-ARM1250.

Theoretically, the specimen, which is thin enough, is composed by only a light element, and highly symmetric crystal, can be imaged as 'weak phase object' under Scherzer defocus. Then, the intensity of atomic columns would be proportional to the atomic number of the atoms in the specimen. The atomic structure (including atomic species) can be directly interpreted according to the observed intensity level.

However, imaging of O with heavy elements like Zn and Pd or the interface, where the periodicity of the crystal is broken, may break the applicability of a 'weak phase object approximation', even if the sufficient resolution is available. Then, the atomic core potentials often cause a complication for the contrast and the contrast center on image is often shifted from the projected center of the atoms. For that reasons, the recommended imaging conditions for Pd/ZnO system should be preliminarily examined by simulations and should be used for experimental observations.

(i) Best Possible Simulation Conditions for ZnO imaged along [$11\bar{2}0$] zone axis

The specimen thickness and the defocus are most critical for the image contrast. Since too complicated contrast causes to misjudge the atomic positions, it is necessary to prepare well-defined thin specimens and to select an appropriate defocus for an experimental observation.

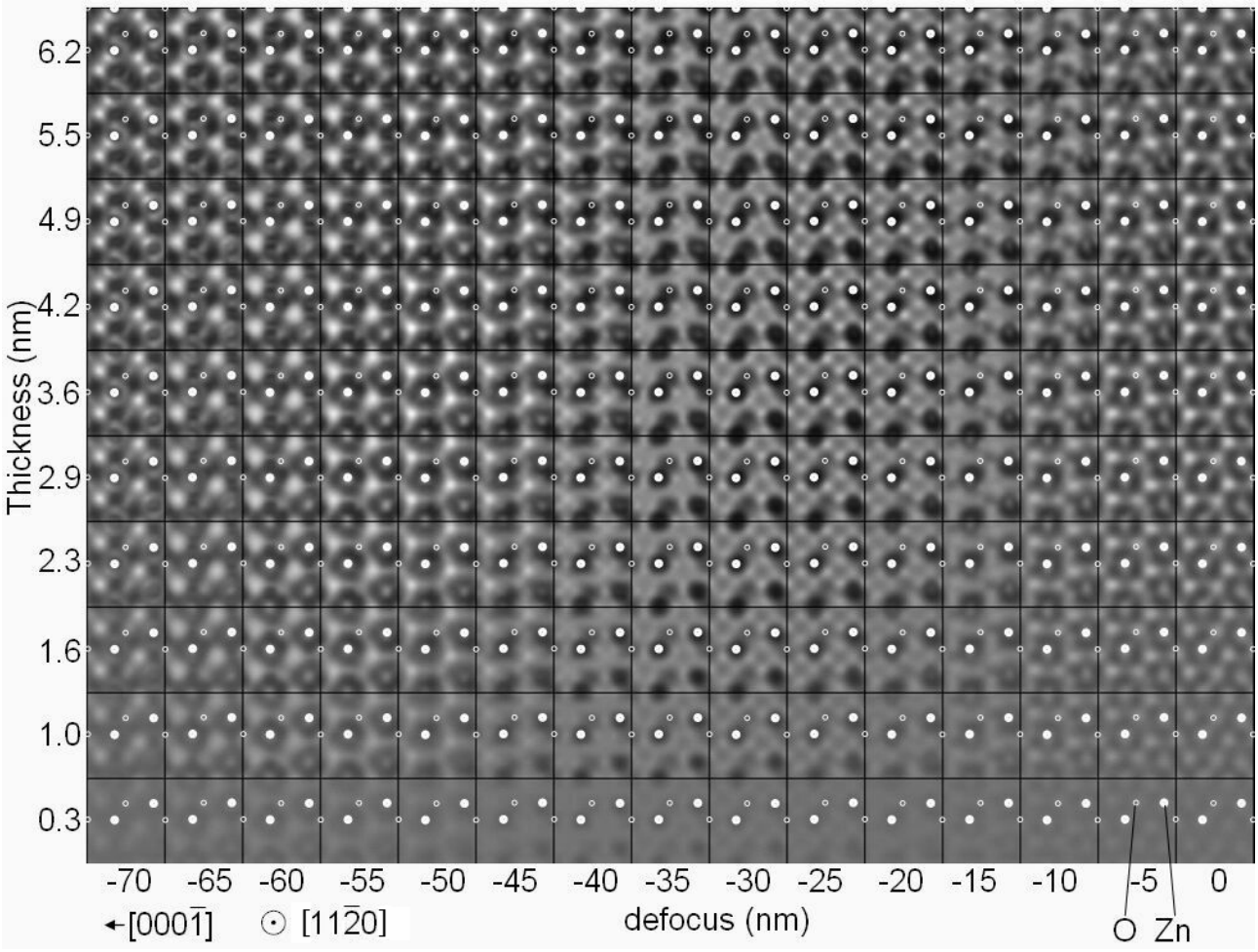

Tableaux 6.1 Calculated images of the ZnO along the [11$\bar{2}$0] zone axis as a function of thickness (0.3 ~ 6.2 nm) and defocus value (-70 ~ 0 nm). Each cell corresponds to unit cell of ZnO. Atomic positions were plotted on only half of unit cell, because it prevents confusing with the image contrast.

Best imaging conditions for experimental observation can be roughly estimated from possible simulation conditions. The calculation for bulk ZnO was carried out by using the EMS software package [Stadelmann, 1987].

Tableaux 6.1 shows calculated images along the [11$\bar{2}$0] zone axis as a function of a wide variety of thickness and defocus value. Although the Zn and O columns on each dumbbell cannot be separated as expected from the contrast transfer function in Fig. 6.5, it can be seen that the outlines of the dumbbells are visible and that the centers of the atomic columns on the images correspond to the positions of the atoms marked by dots near Scherzer focus (defocus: df = -20 ~ -45 nm) within thin thickness region (thickness: t < 4.9 nm). On the other hand, it can be seen that for all other conditions the outline of the dumbbells are not clear. Furthermore, the contrast around the atoms on the images is too complicated to

recognize the position of the center of the atoms involved.

Within the 'weak phase object approximation', theoretically, individual Zn column position may possess lower intensity (black dot) while individual O column position should possess higher intensity (light gray dot) under the ideal conditions of a thin specimen. That is why the intensity profiles (Fig. 6.7) along the dumbbells on the calculated images were examined as function of specimen thickness. The defocus was fixed at df = -30 nm, because the ideal contrast was expected by simple inspection.

It can be seen that the intensity profiles along the dumbbells are deviated, resulting from the difference in atomic numbers of the Zn and O (see Fig. 6.7). The best thickness which allows differentiation between Zn and O is determined by comparing simulated intensity profiles. Fig. 6.7 shows the calculated images and the intensity profiles for the thickness of (a) 0.3 nm, (b) 1.6 nm, (c) 2.9 nm, (d) 4.2 nm, (e) 5.5 nm, and (f) 6.8 nm at the defocus (df = -30 nm). The intensity profiles along the dumbbells were measured along the white lines on the left images of the figure in Fig. 6.7. It can be seen that Zn columns result in low intensity while O columns result in high intensity below the thickness of (c) 2.9 nm. However, above the thickness of (d) 4.2 nm, the intensity deviation is reversed. Therefore, it can be roughly expected that the recommended specimen thickness is below about t = ~3 nm, in order to clearly distinguish Zn and O.

Subsequently, the specimen thickness was fixed at t = 2.9 nm for the calculations, since the thickness is close to the actual specimen thickness. The intensity profiles along the dumbbells on the calculated images were measured for the under-defocus values of (a) -45 nm, (b) -40 nm, (c) -35 nm, (d) -30 nm, (e) -25 nm, (f) -20 nm (see Fig. 6.8). It can be seen that the thickness of (b) -40 nm ~ (d) -30nm allows differentiation between Zn and O. However, the strong under-focus (df = -45nm) or the weak under-focus (df < -25 nm) cause to an inversion of image contrast.

It can be expected by simple inspection that the defocus values between (b) -40 nm ~ (d) -30 nm and the specimen thickness of $t \leq$ 2.9 nm are recommended for experimental observation, in order to distinguish Zn and O.

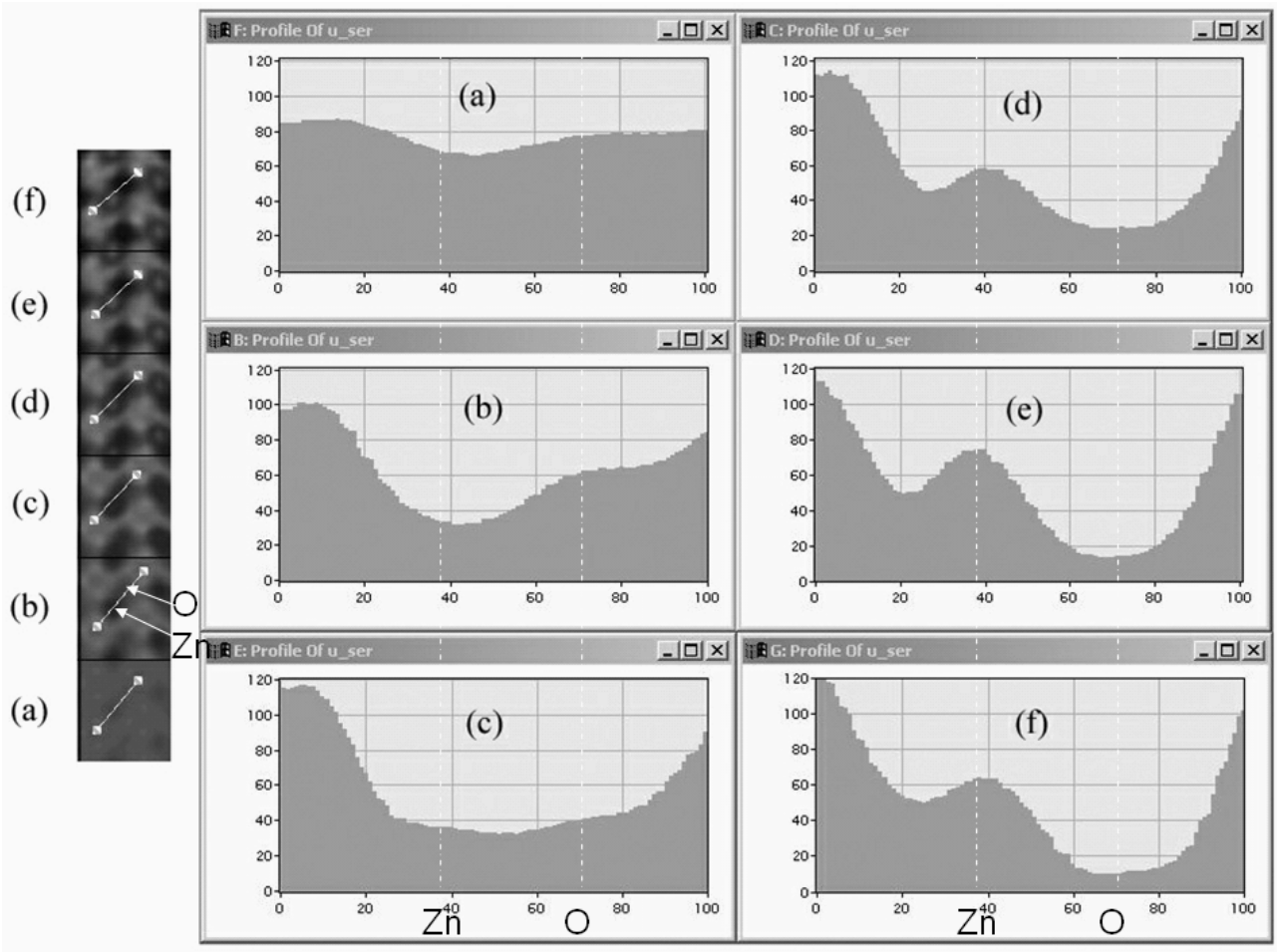

Fig. 6.7 Intensity profiles along the ZnO dumbbells on the calculated image at Scherzer focus (*df* = -30 nm) for specimen thickness of (a) 0.3 nm, (b) 1.6 nm, (c) 2.9 nm, (d) 4.2 nm, (e) 5.5 nm, and (f) 6.8 nm. X-axis corresponds to pixel on the white line while y-axis corresponds to relative intensity.

(ii) Best Possible Simulation Conditions for ZnO imaged along [$1\bar{1}00$] zone axis

Tableaux 6.2 shows the calculated images of ZnO along the [$1\bar{1}00$] zone axis as a function of a wide variety of thickness and defocus values. The small interatomic distance (0.063 nm) between Zn and O in the dumbbell on the image projected along [$1\bar{1}00$] zone axis does not allow the resolution of Zn and O. The Zn-O dimers correspond to black elliptical dots under appropriate imaging conditions (*df* = -40 ~ -20 nm, $t < 3.9$ nm). It can be seen that other image conditions result in an inversion of image contrast. The image along this zone axis provides symmetric projected ZnO structure, indicating a possibility to determine the atomic positions along the [$11\bar{2}0$] direction by the direct image interpretation, even if the contrast is reversed.

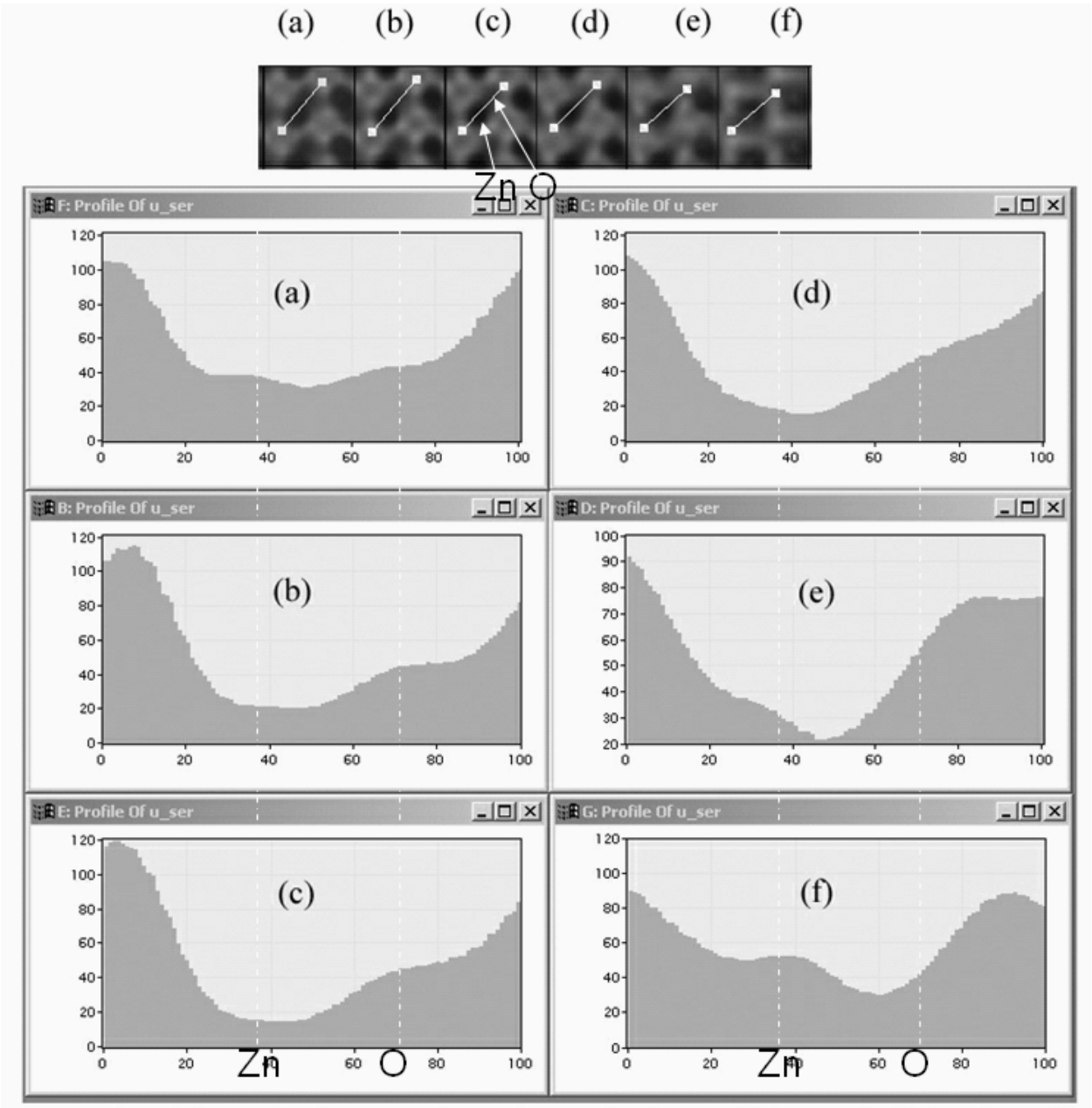

Fig. 6.8 Intensity profiles along the ZnO dumbbells on the calculated image for defocus of (a) -45 nm, (b) -40 nm, (c) -35 nm, (d) -30 nm, (e) -25 nm, and (f) -20 nm at the specimen thickness of t = 2.9 nm. X-axis corresponds to pixel on the white line while y-axis corresponds to intensity.

(iii) Best Possible Simulation Conditions for Pd

Tableaux 6.3 and 6.4 represent the calculated images of Pd along the $[\bar{1}10]$ zone axis and along the $[11\bar{2}]$ zone axis for foil thicknesses up to 7.7 nm / 4.8 nm and defocus values from 0 to -70 nm, respectively. In Tableaux 6.3, the centers of Pd atoms correspond to black dots under the specific conditions (df = -40 ~ -15 nm, t < 4.4 nm).

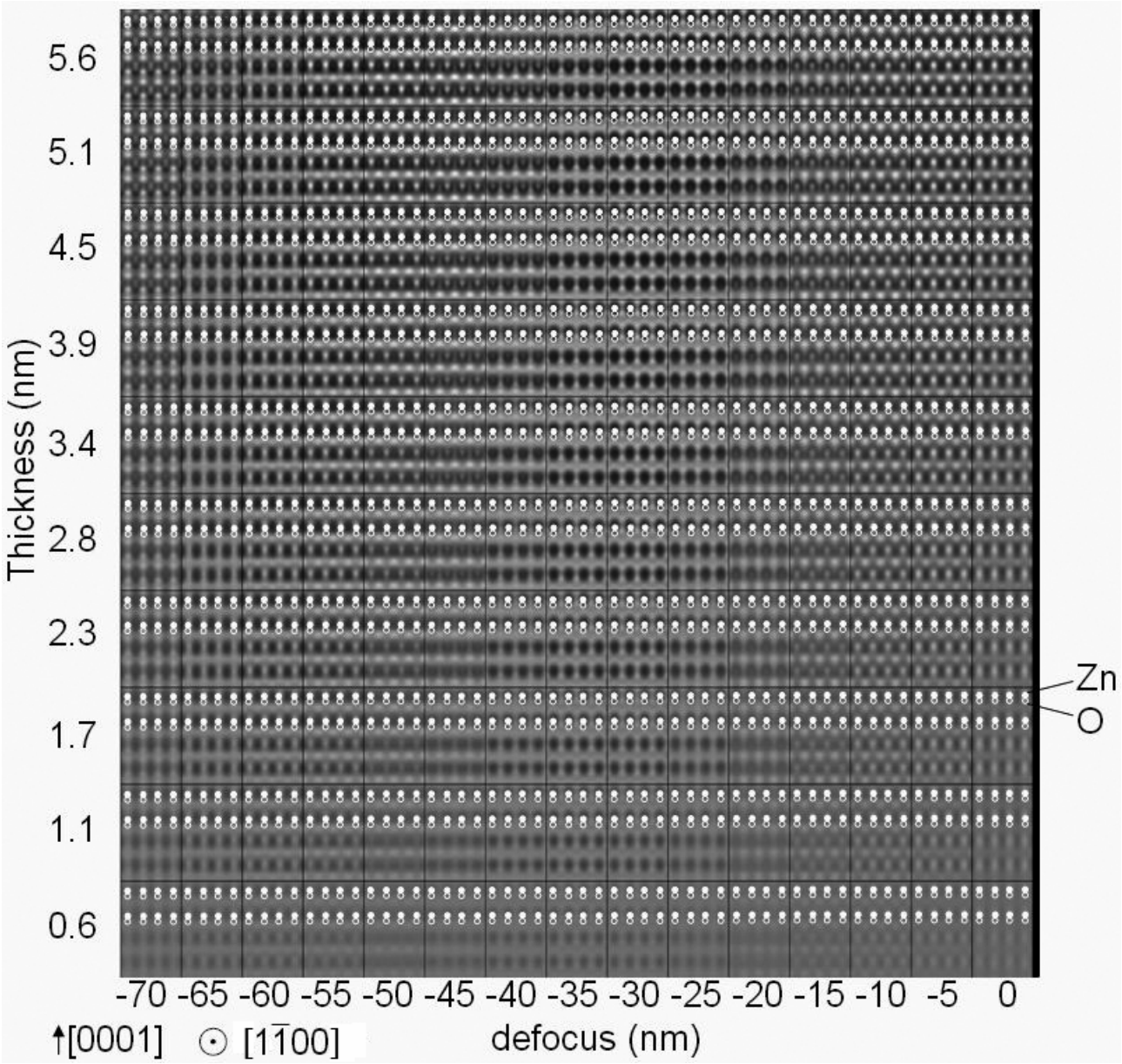

Tableaux 6.2 Calculated images of ZnO along the $[1\,\bar{1}\,00]_{ZnO}$ as a function of thickness (0.6 ~ 5.6 nm) and defocus value (-70 ~ 0 nm).

In Tableaux 6.4, the centers of Pd atoms correspond to black dots under the specific conditions (*df* = -35 ~ -25 nm, *t* < 3.3 nm). It can be seen that, for other imaging conditions, an inversion of image contrast can occur. Furthermore, the projected minimum spacing along the $[11\bar{2}]$ zone axis is 0.13nm which is close to the best point-to-point resolution of 0.12 nm. However, the $[11\bar{2}]$ zone axis provides symmetric projected Pd structure, indicating a possibility to determine the atomic positions along the $[\bar{1}10]$ direction by the direct image interpretation, even if the contrast is reversed.

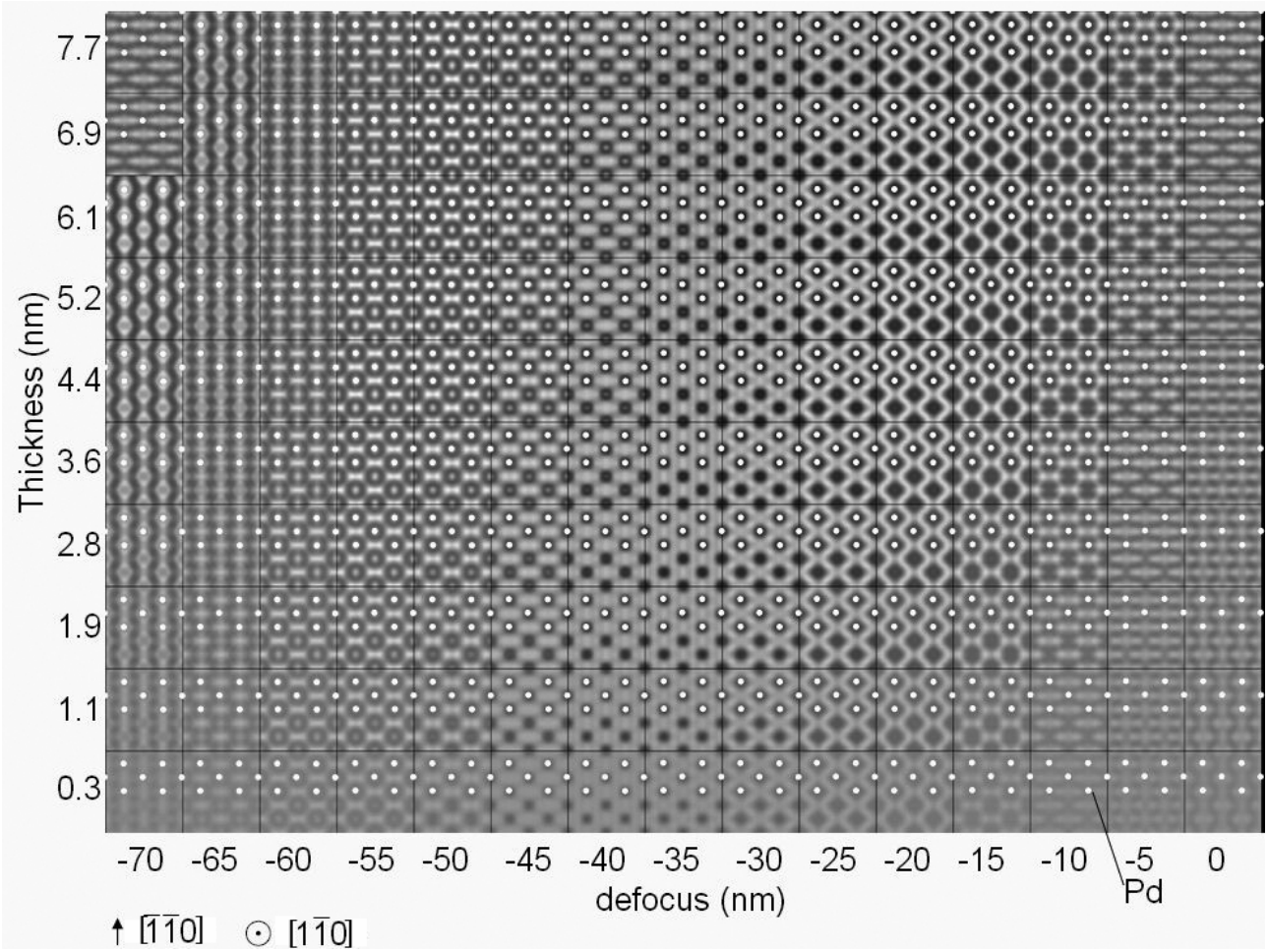

Tableaux 6.3 Calculated images of Pd along the $[\bar{1}10]_{Pd}$ zone axis as a function of thickness (0.3 ~ 7.7 nm) and defocus value (-70 ~ 0 nm).

(iv) Best Possible Simulation Conditions for Pd/ZnO Interface

The suitable imaging conditions with resolution of the system can be summarized at the defocus of *df* = -40 nm ~ -20 nm and thickness of $t < 2.9$ nm along the $[11\bar{2}0]_{ZnO}//[\bar{1}10]_{Pd}$ zone axis. We must carefully investigate the asymmetric projected structure of ZnO in the observation along the first zone axis. For the 2nd zone axis along the $[1\bar{1}00]_{ZnO}//[11\bar{2}]_{Pd}$, the suitable imaging conditions can summarized to *df* = -35 ~ -25 nm and $t < 3.3$ nm. The second zone axis provides a symmetric projected Pd and ZnO structure, indicating the possibility of direct image interpretation, even if the image contrast is reversed. A thin specimen (thickness below 2.9 nm) and a defocus near -30 nm were aimed for the experiments.

Unfortunately, the aims could not always be obtained. The observations along the first zone axis were more critical for specimen preparation and for alignment of specimen for incoming e-beam of TEM than the second zone axis.

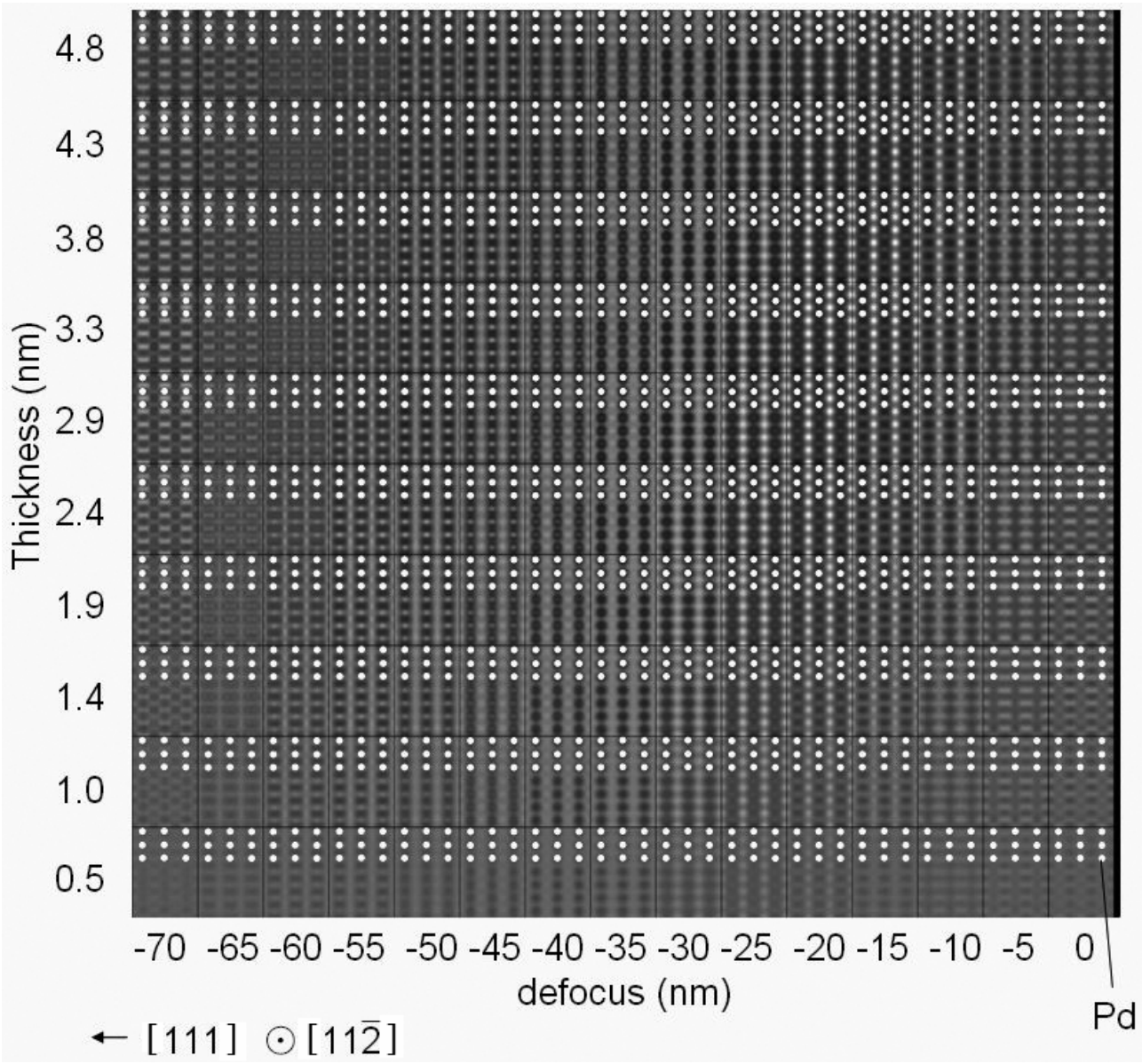

Tableaux 6.4 Calculated images of Pd along the $[11\bar{2}]_{Pd}$ zone axis as a function of thickness (0.5 ~ 4.8 nm) and defocus value (-70 ~ 0 nm).

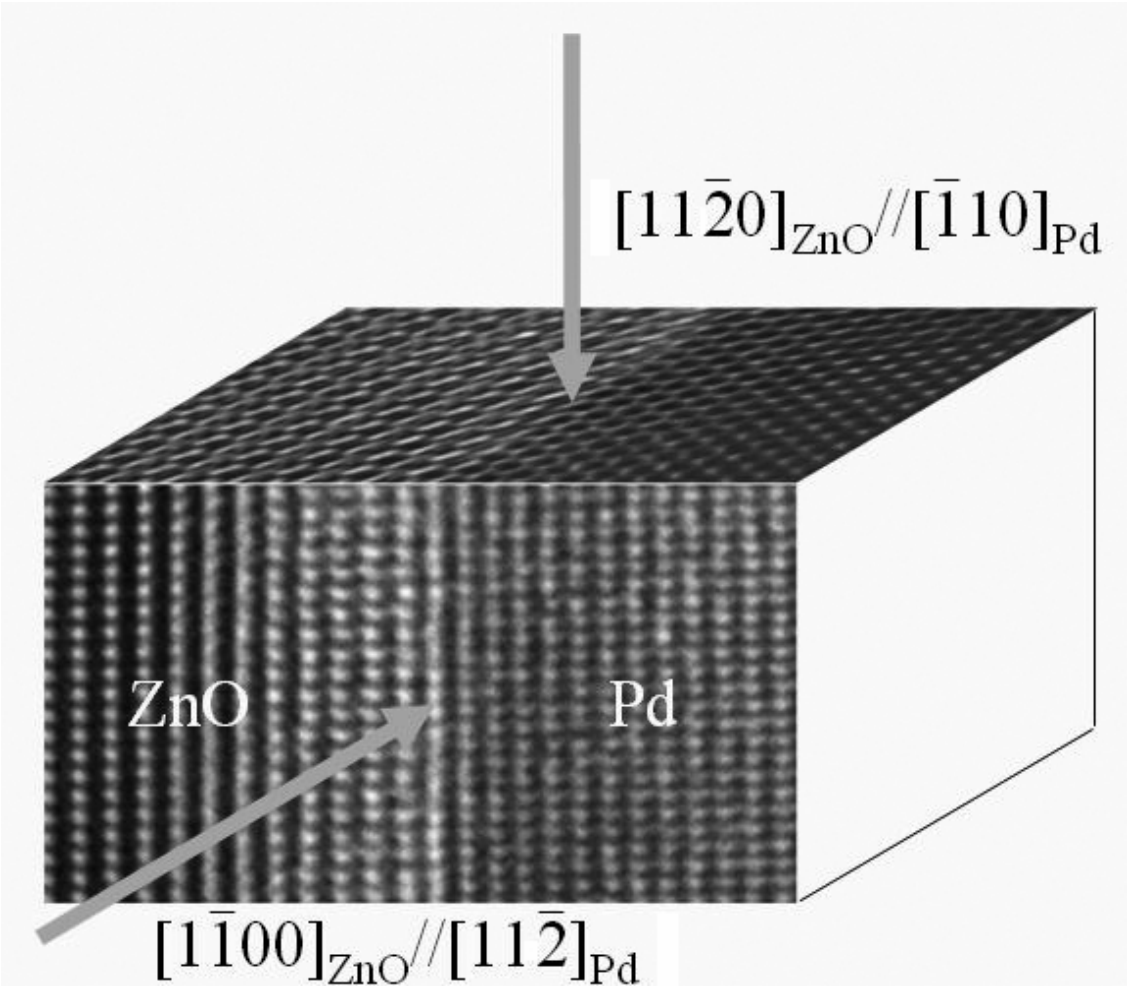

Fig. 6.9(a) 3-dimensional view of the HRTEM images of the **Pd/$^{+}$ZnO** interface taken at a defocus condition (*df* = ~ -30 nm) along the $[11\bar{2}0]_{ZnO}//[\bar{1}10]_{Pd}$ zone axes and $[1\bar{1}00]_{ZnO}//[11\bar{2}]_{Pd}$ zone axes. 3D atomic structure can be obtained by at least two projected images. For that reason, the interface was also investigated via the observations along both zone axes. The $[11\bar{2}0]_{ZnO}//[\bar{1}10]_{Pd}$ zone axis is parallel to the $[1\bar{1}00]_{ZnO}//[11\bar{2}]_{Pd}$ zone axes.

6.1.3 Pd/$^{+}$ZnO Interface

Local atomic structure analyses in the **Pd/$^{+}$ZnO** interfaces could be performed employing an ultra high resolution microscope JEOL JEM-ARM1250 and a quantitative high resolution image analysis technique [Möbus, 1996]. The interpretation of one projected image must make assumption of the 3- dimensional atomic structure. However, 3-D atomic structure can be obtained by two projected images. For that reason, a **Pd/$^{+}$ZnO** interface was investigated via the observations along both the $[11\bar{2}0]_{ZnO}//[\bar{1}10]_{Pd}$ zone axes and the $[1\bar{1}00]_{ZnO}//[11\bar{2}]_{Pd}$ zone axes as shown in Fig. 6.9(a).

(A) Pd/$^{+}$ZnO Interface ($[11\bar{2}0]_{ZnO}//[\bar{1}10]_{Pd}$)

Overview of Pd/$^{+}$ZnO Interface

Fig. 6.9(b) shows a HRTEM micrograph of the **Pd/$^{+}$ZnO** interface imaged with the JEOL JEM-ARM1250 (Stuttgart ARM). The image was taken at a defocus condition (*df* = ~ -30 nm) along the $[11\bar{2}0]_{ZnO}//[\bar{1}10]_{Pd}$ zone axes. Black dots on the image correspond to positions of Zn or Pd atoms for the selected imaging condition. In principle, the image for the ZnO along this zone axis should provide that each atom column consists of only one atomic species of Zn or O. However, it can be seen in Fig. 6.9(b) that the image of the two atomic columns within the Zn-O dumbbell (see subsection 6.1.2) are overlapping. They look like one atomic column rather than like the image of the dumbbell. The image of the atomic columns of the Pd is bigger than that of the dumbbell. Each atomic column shows clearly the difference between Pd (right) and ZnO (left) regions. An atomically flat interface between the two crystals can easily be recognized. The Pd/ZnO interfaces are atomically abrupt and, as expected due to the low reactivity of Pd, free of reaction phases.

The ZnO region near the interface possesses ‘coherent interface areas’ (CIA) which has clearly resolved columns with the same diameter and the same intensity as that in the bulk ZnO region. In addition, the ZnO near the interface possesses also ‘diffuse interface areas’ (DIA) which show diffusely imaged columns are different from that in the bulk ZnO region. These DIA periodically exist next to CIA and within the ellipses marked at the interfacial layer in Fig. 6.10(b). It can be seen that the total length of both DIA (~0.5 nm) and CIA (~1.0 nm) is ~1.5 nm along the interface. This periodicity of 1.5 nm corresponds to the periodicity dictated by the lattice mismatch of 18 % at the interface between Pd and ZnO. Therefore, the assumption may be correct that the appearance of the DIA can be attributed to the periodicity of the lattice mismatch.

It can be considered (see subsection 6.2.3) that the accommodation involves 2-dimensional movements of the atoms at or near the interface. Especially, the accommodations of the atoms in the DIA seem to involve a rearrangement of the atoms which is not parallel to the incoming beam. It suggests that it may be difficult to perform an appropriate image simulation for the DIA which requires huge supercell. Therefore, the local atomic structure was analyzed within the white frame in Fig. 6.10 which includes the CIA. As shown in the simulated image in Fig. 6.10(a), the asymmetric projected structure of ZnO does not allow a direct interpretation of the local atomic structure. Therefore, the local structure was analyzed employing a quantitative image analysis technique.

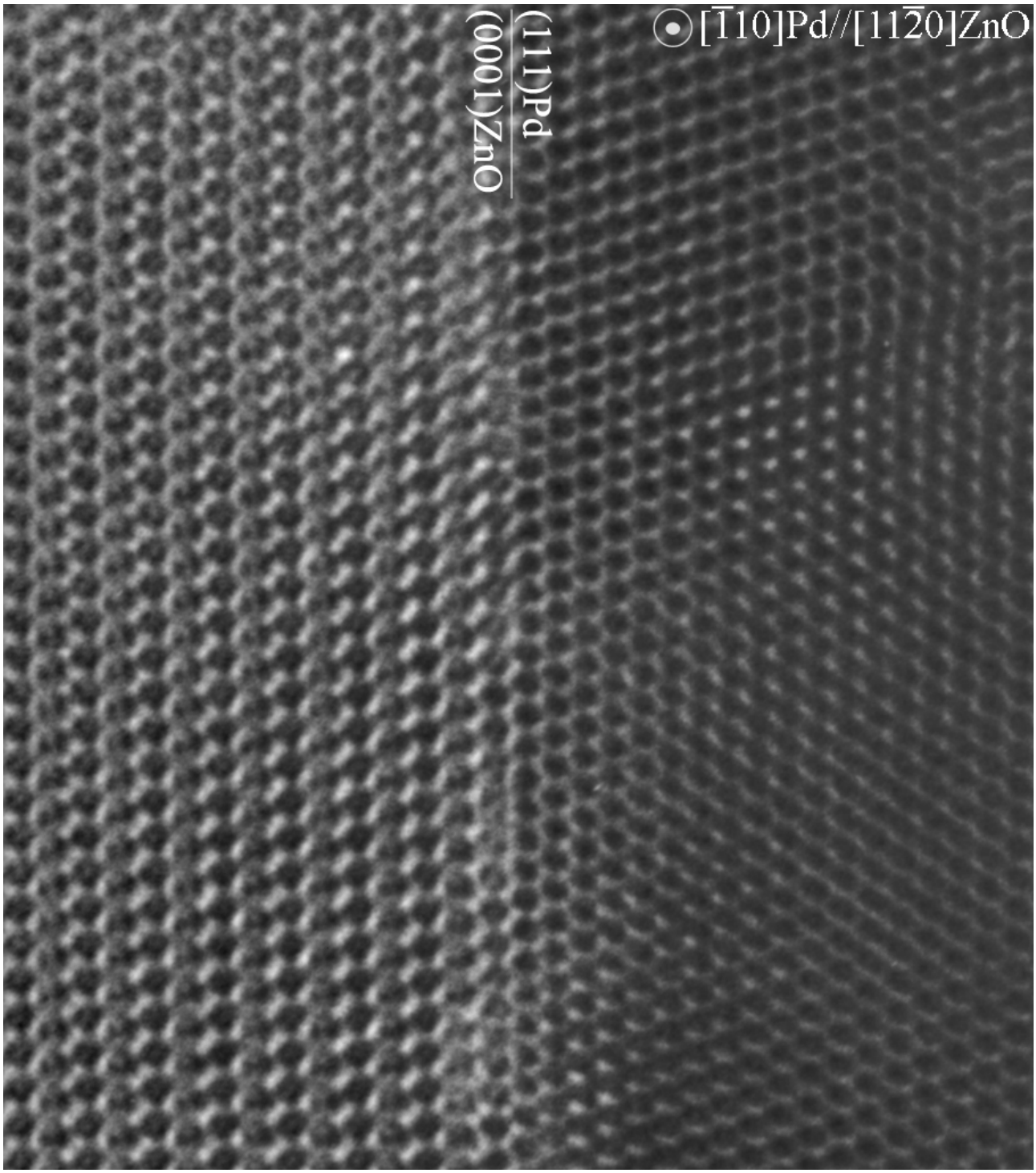

Fig. 6.9(b) HRTEM image of the **Pd/$^{+}$ZnO** interface taken at a defocus condition (*df* = ~-30 nm) along the $[11\bar{2}0]_{ZnO}//[\bar{1}10]_{Pd}$ zone axes. Black dots on the image correspond to the positions of the atoms of Zn or Pd under the condition. In principle, the zone axis provides that each atomic column should consist of a pure atomic species. Each atomic column clearly shows the difference between Pd (right) and ZnO (left) regions. An atomically flat interface between the two crystals can be easily recognized.

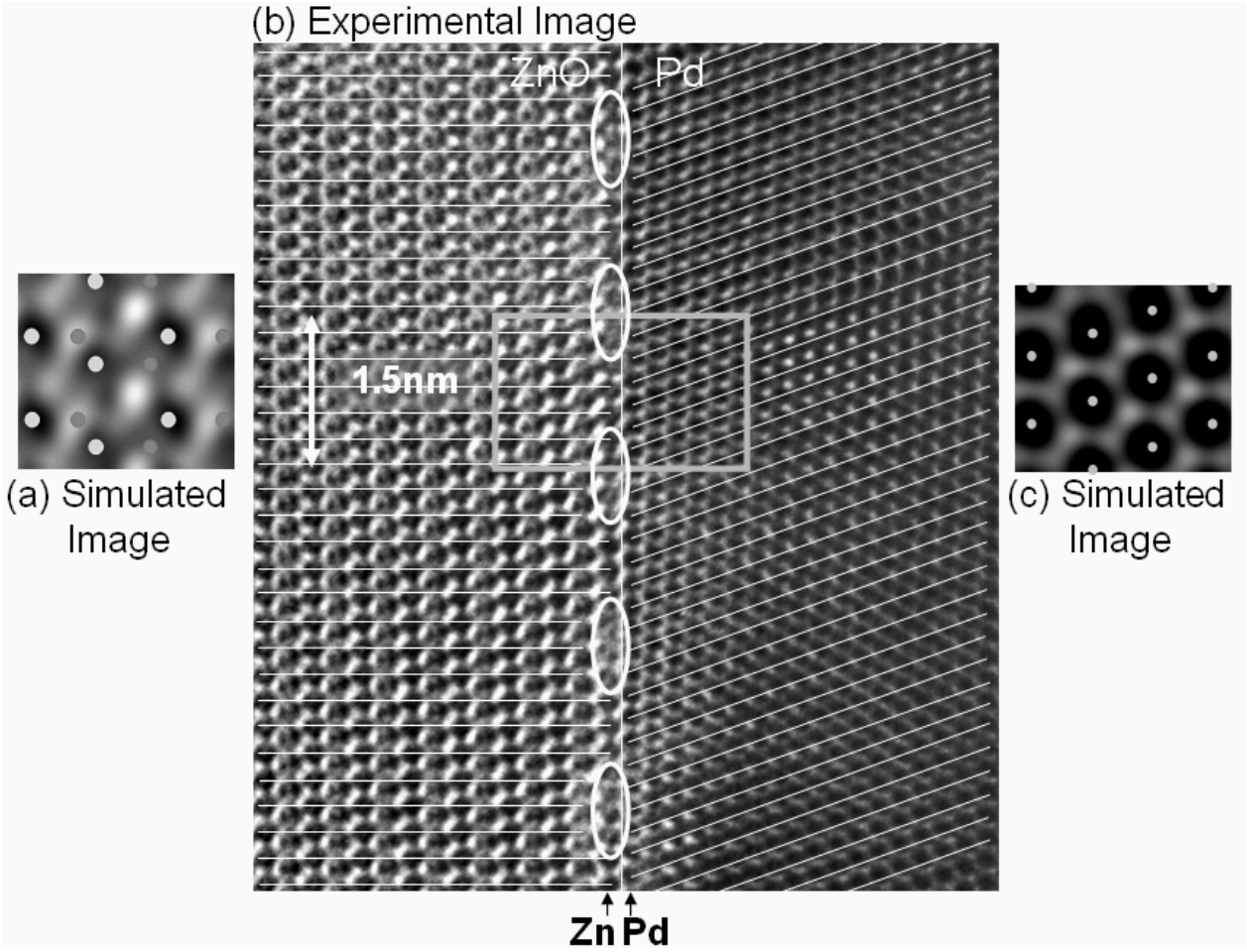

Fig. 6.10 (a) Simulated image for bulk ZnO and the positions of the atoms (white dots: Zn, grey dots: O), (b) experimental image of the **Pd/$^{+}$ZnO** interface, and (c) simulated image for bulk Pd and the positions of the atoms. Coherent interface areas (CIA) of the interfacial layer of ZnO shows clearly-resolved columns with the same diameter and the same intensity as that in the bulk ZnO region. The interface possesses also Diffuse interface areas (DIA) which show diffusely imaged columns. These DIA periodically exist next to CIA and within the ellipses marked at the interfacial layer in this figure.

HRTEM cross-sectional image reveals also the interface step, see Fig. 6.11, that the step height corresponds to the distance of *c*/2 between the bi-layers of ZnO. This observation confirms the statistical results obtained by CTR measurements (see subsection 5.1.2). Furthermore, the step height of *c*/2 has the important consequence that the terminating atomic species should be identical on all terraces of ZnO at the interface. It can be seen also that the Pd crystal is bent near the step. This seems to be attributed to that the mismatch (~13.7 %) between Pd and ZnO lattice spacings normal to the interface could not be completely compensated by the step height of *c*/2.

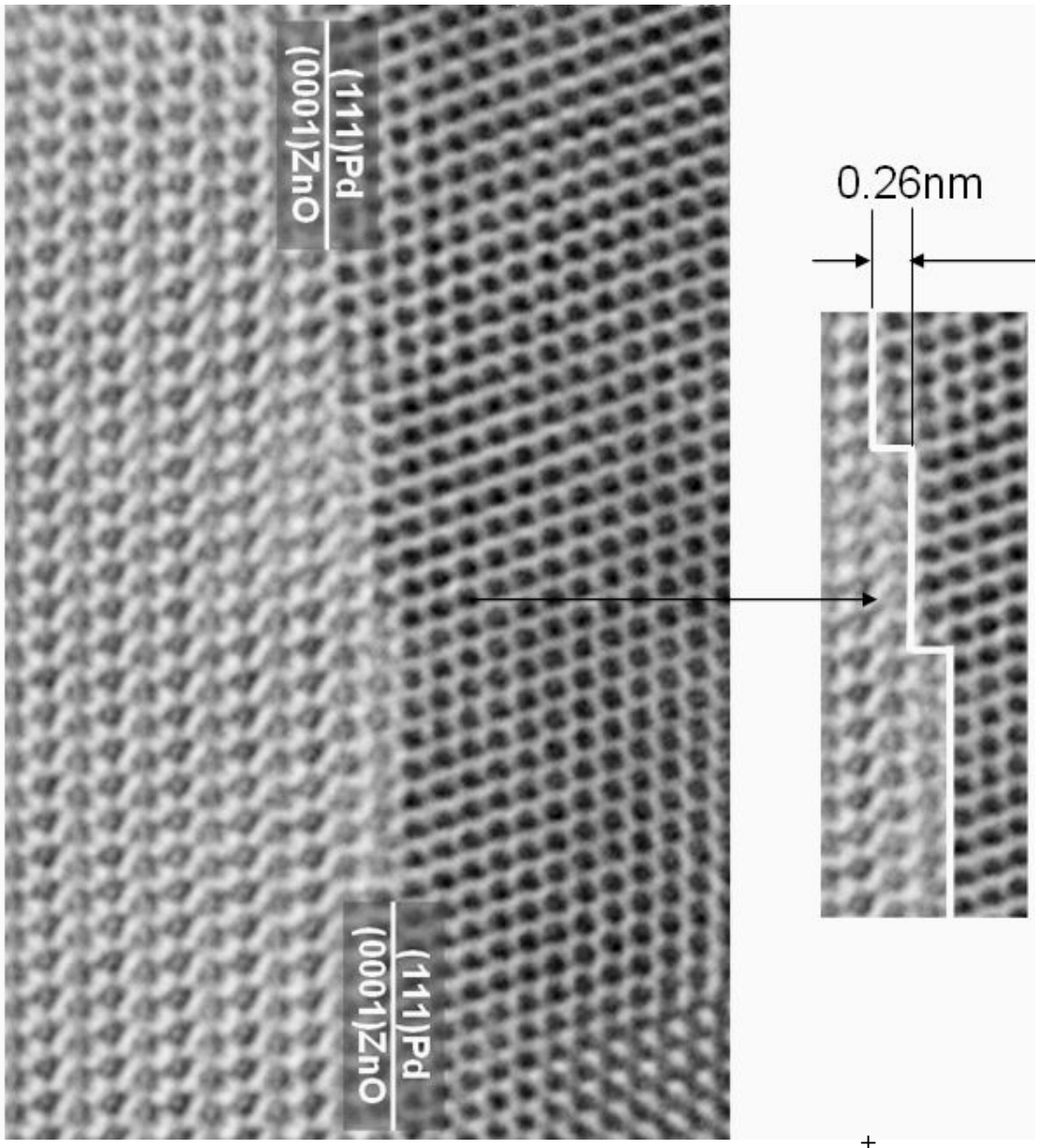

Fig. 6.11 HRTEM cross-sectional image show also the atomic steps on the **Pd/$^{+}$ZnO** interface. The step height corresponds to the distance of *c*/2 (*c*: lattice constant of ZnO) between the bi-layers of ZnO. This step height of *c*/2 has the important consequence that the terminating atomic species should be identical on all terraces of ZnO at the interface.

The interface will be fully characterized by just analyzing in all details one flat region of the interface without any step. It was hard to analyze the local atomic structure in the DIA. Furthermore, the contrast on the simulated image for the ZnO (Fig. 6.10(a)) is not so simple for direct interpretation for the image. Therefore, quantitative analyses were performed for the interface area including the CIA.

Quantitative Analysis of the Interfacial Local Atomic Structure

In order to determine the local atomic structure including the atomic species at the Pd/ZnO interface, the quantitative analysis was performed for HRTEM image using IDIM program package (Iterative Digital Image Matching) developed by G. Möbus [Möbus, 1996]. This program package provides to extract the best possible atomic structure from an experimental image by automatically comparing the experimental image with the different calculated images. The XCF (Cross Correlation Factor), which indicates similarity between experimental image and different calculated images, are repeatedly evaluated for specific data sets for the calculated image. The procedure is continued until a maximal value of the XCF is obtained. The maximal XCF value provides the best possible imaging parameters, the best possible atomic structure, and the best possible spatial occupancy of the different atoms.

Variable parameters exist for main imaging parameters (defocus value, spherical aberration, specimen tilt angle, and beam tilt angle) as well as for materials parameters (specimen thickness, coordinate of atom (ion) columns, and atomic occupancy).

A weak point of IDIM is that many local maxima of XCF value exist, since many parameters have to be adopted by IDIM. In order to avoid the unrealistic local maxima, the range for the each variable parameter should be restricted to reasonable values as well as possible. Some of the parameters, for example, defocus and specimen thickness, were roughly determined by manual mapping as shown in subsection 6.1.2.

After defining an interested interface region (Fig. 6.12) from a scanned ARM image, a dynamic range (usually, 0 to 256) of contrast on the HRTEM image was normalized within 0 to 1. Following steps were performed: (i) The best fitting imaging parameters are quantitatively determined for both bulk regions (perfect crystals) within the defined area. (ii) The positions of the atoms in the bulk regions are determined with IDIM with high accuracy of ~±10 pm. Then, the translation vector between two crystals can be estimated from the atomic positions in the bulk regions of Pd crystal and ZnO crystal. The translation vector allow constructing an atomic model (a super cell) with the lattice spacing of the bulk crystals. Furthermore, the terminating atomic species can be provisionally determined. (iii) After optimization of the super cell, the best fitting local atomic structure near the interface is quantitatively extracted by IDIM. (iv) In addition, the best fitting atomic occupancy on the terminating layer is quantitatively determined. The results represent the interfacial local atomic structure including both atomic species and atomic occupancy. For all quantities the reliability is also considered.

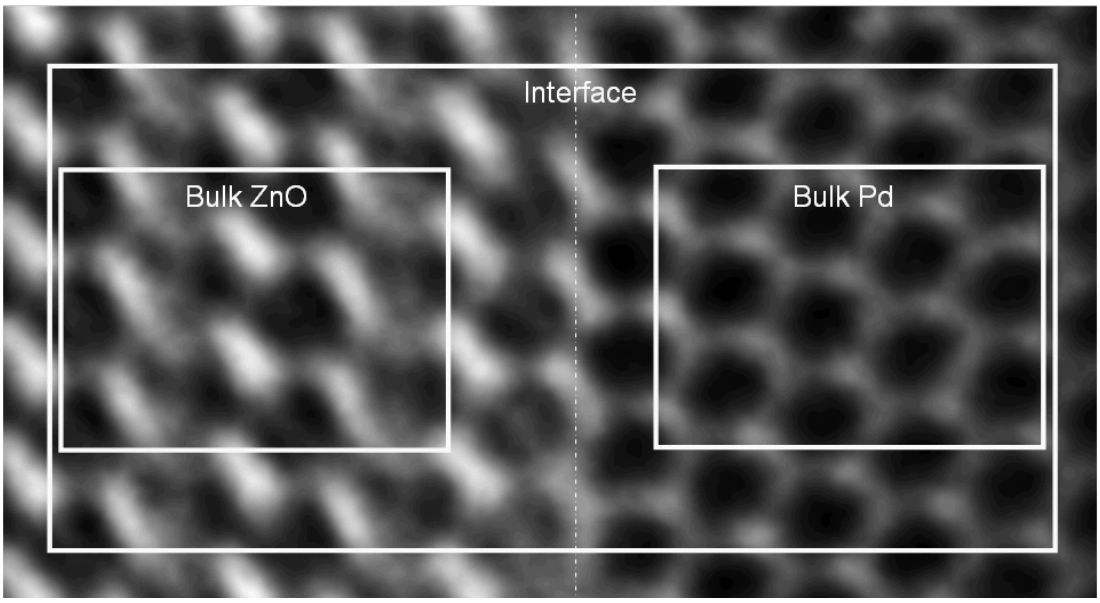

Fig. 6.12 The bulk regions and the interface region enclosed by the white frames were defined. The defined regions on these experimental images were used for iterative matching for bulk ZnO, bulk Pd, and interface regions.

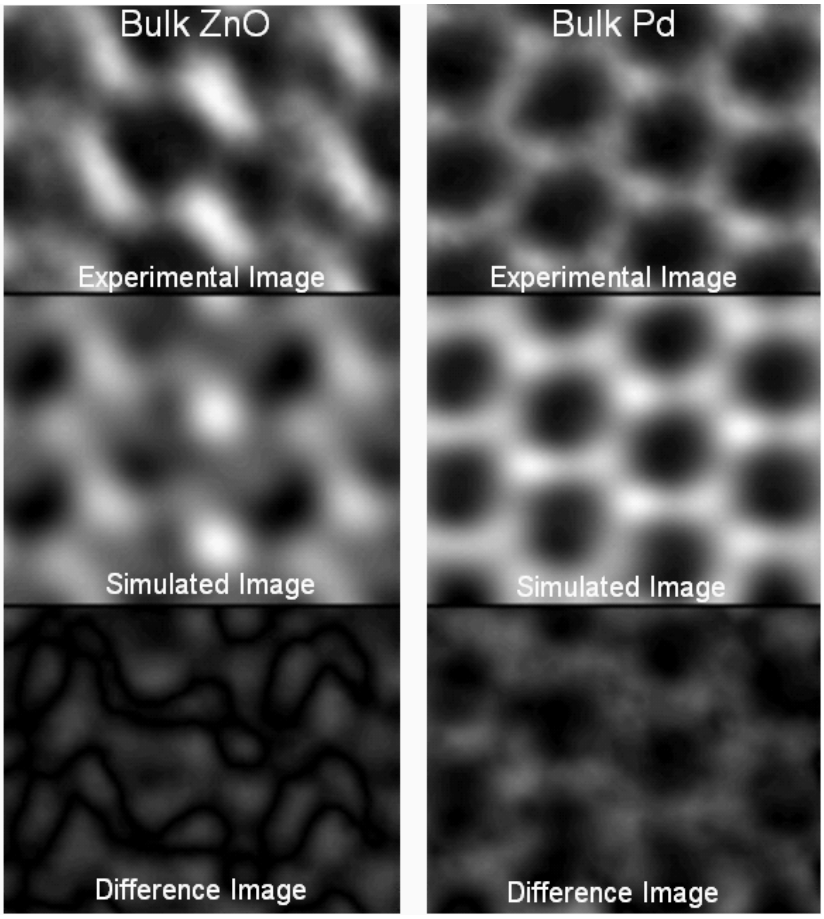

Fig. 6.13 The experimental image, the best calculated image, and the difference image for (left) bulk ZnO and for (right) bulk Pd. The difference image between the calculated images and the experimental images possesses weakly high value of the residual bright spots.

Step (i): Calculation of Imaging Parameters in Bulk (Perfect Crystals) Regions

In principle, the best imaging parameters in the bulk regions should be identical as that in the interfacial region, if the imaging parameters for the calculation were extracted from the same image (e.g., Fig. 6.12). First of all, the best possible imaging parameters in both bulk regions should be calculated. The bulk regions enclosed by the white frames in Fig. 6.12 were defined with recording the exact positions of the frames.

Best matching images for both bulk ZnO and Pd regions are shown in Fig. 6.13. The difference image between the calculated images and the experimental images possesses weakly high value of the residual bright spots. The XCF values and the resulting best fitting parameters are summarized in Table 6.3.

The XCF value for the bulk Pd region is more than 93 %, indicating that the evaluated parameters reproduce the experimental images. On the other hand, the XCF value for bulk ZnO is nearly 83 % which is a low value for a perfect lattice. Unfortunately, this value could not be improved anymore. This value is real maximal XCF. The low maximal XCF seems to indicate that the very small lattice spacings (non resolvable) of ZnO cause a decrease of the XCF values enhanced by unexpected parameters: for example, noise, silver particles on negative image, or mechanical vibration etc. Fortunately, it seems that the parameters only reduce the image quality and the absolute value of the maximal XCF. They do not affect to best fitting parameters depending on local agreement between the images.

The best fitting parameters for both bulk ZnO and Pd regions do not agree. However, the most effective parameters: defocus values, specimen tilts, and beam tilts are not so different in both regions except specimen thickness. The differences of all other imaging parameters do not matter so much, because the XCF was not critical for a large variation of the other imaging parameters. The difference of the specimen thickness is within ~20 %. This seems to be selective ion-milling. This difference will be averaged out and optimised in the simulation of the interface.

Table 6.3 Best fitting parameters for the images of the bulk (perfect crystal) regions. The XCF value for the bulk Pd region is more than 93 %, indicating that the evaluated parameters reproduce the experimental images. On the other hand, the XCF value for bulk ZnO is nearly 83 % which is a low value for a perfect lattice.

	Bulk ZnO	Bulk Pd
XCF [%]	82.564	93.255
Specimen Tilt *x* [°]	0.003	-0.080
Specimen Tilt *y* [°]	0.059	0.065
Specimen Thickness [nm]	2.5	3.0
Defocus [nm]	-21.0	-20.9
Spherical Aberration [nm]	2.80	2.50
Beam Tilt *x* [°]	-0.039	-0.012
Beam Tilt *y* [°]	0.066	0.040
Focus Spread [nm]	9.0	10.9
Beam Convergence [mrad]	0.20	0.36
Aperture Diameter [nm^{-1}]	17.4	20.7
Gaussian MTF-envelope (sigma_*x*) [nm]	0.067	0.039
Gaussian MTF-envelope (sigma_*y*) [nm]	0.060	0.020

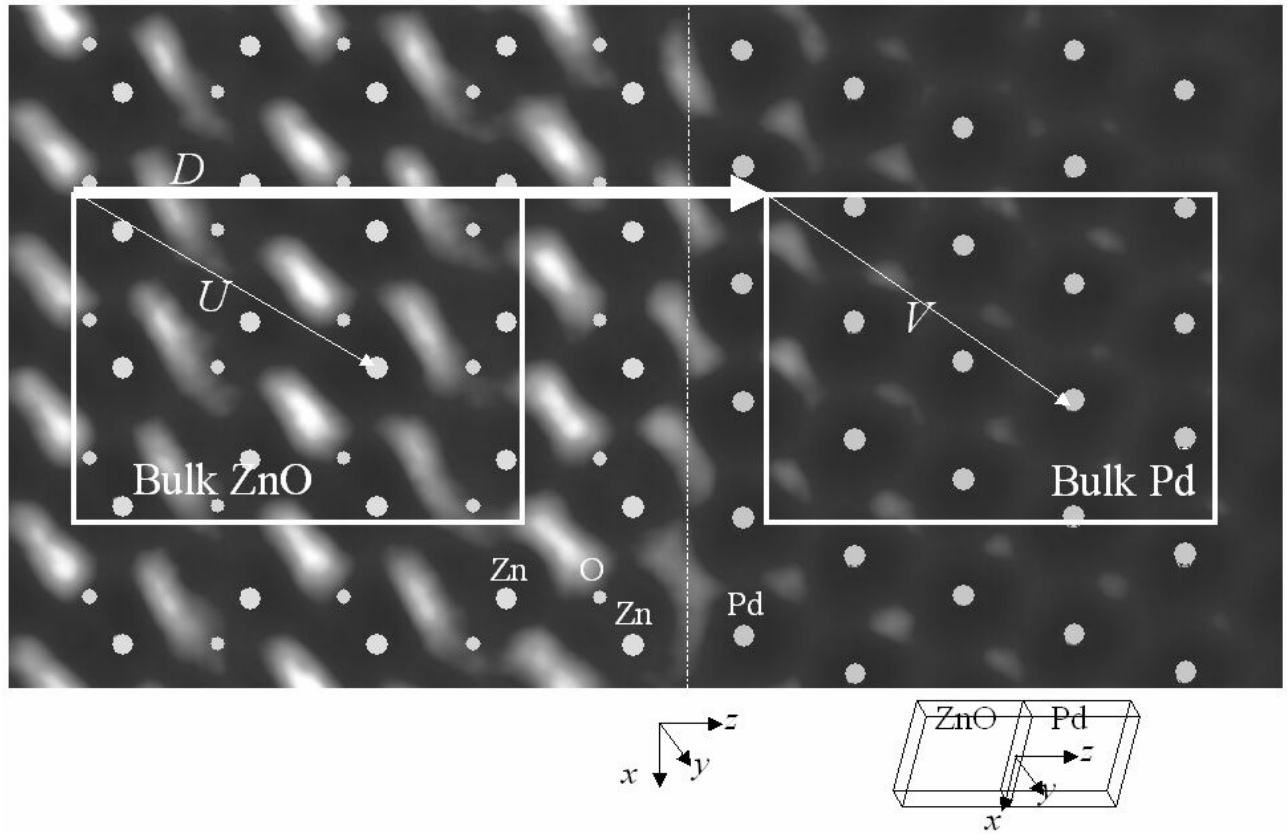

Fig. 6.14(a) Each atomic position is valid in only the defined bulk regions. IDIM allows the determination of 2 components of the translation vectors V , U between some atomic position and the origin of the defined area. Furthermore, the translation vectors V , U and the distance D between two defined areas were used for construction of the supercell for the simulation for the interface.

Step (ii): Determination of Translation Vector between Pd and ZnO

In the calculations for the bulk crystals, the position of the each supercell for the simulation can be automatically modified at every iteration for a complete fit for the experimental image. This means that IDIM allows the determination of 2 components of the translation vectors V , U (see Fig. 6.14) between some atomic position and the origin of the defined area. Furthermore, the translation vectors V , U and the distance D between two defined areas were used for construction of the supercell for the simulation for the interface as shown in Fig. 6.14. The supercell allows the determination of the exact translation vectors T across the interface between the interfacial atoms. The accuracy of the translation vectors between bulk Pd and ZnO crystals is ~±10 pm. The translation vectors (the interatomic distances) can be defined as (see Fig. 6.14)

$$\begin{aligned} T_z &= \left| D_z + (V_z + nb_z) - (U_z + ma_z) \right| \\ T_x &= \left| D_x + (V_x + nb_x) - (U_x + ma_x) \right| \end{aligned}, \qquad (6\text{-}1)$$

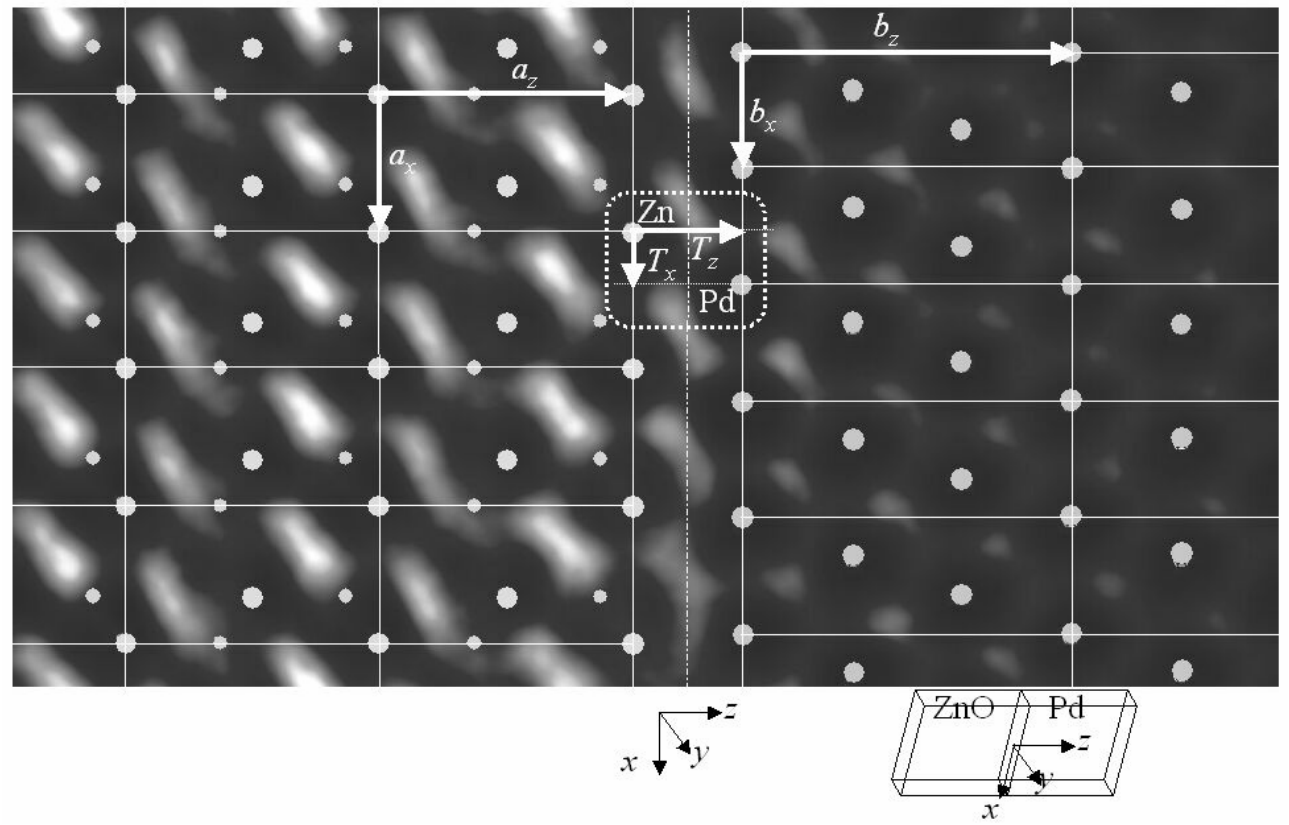

Fig. 6.14(b) The supercell allows the determination of the exact translation vectors T between atoms across the interface. Due to lattice mismatch, the translation vector T_x between the interfacial Zn and Pd atoms (nearest Pd atom for the Zn atom) should depend on the atom.

where a and b are the basis vectors of ZnO and Pd, respectively, and m and n are integer. From minimal $T_{\min,z}$ the interfacial distance between two crystals can be evaluated, because $T_{\min,z}$ does not depend on an atomic position at the interface. However, $T_{\min,x}$ which indicates a coherency at an interface between the lattices depends on an atomic position at an interface including a lattice mismatch. Therefore, a T_x should be defined for each atom at an interface, if a lattice mismatch is included.

Fig. 6.14 shows the supercell constructed by the translation vectors V, U, D and by the basis vectors a and b. Of course, the positions of all atomic columns remain unchanged as in bulk crystals. This means that the positions of atomic columns near interface and the terminating atomic species Fig. 6.14 are provisional at this point.

It can be seen that the supercell for the simulation of the interface in Fig. 6.14 fits to the image contrast in bulk regions, which the ZnO is Zn-terminated at the interface, according to simple inspection.

Step (iii) Calculation of Best Imaging Parameters for the Region of the Interface

It should be mentioned that big question exists for image calculations of the Pd/ZnO interfaces. How should a super cell include large mismatch of 18 % along the zone axis? In this system the 1 slice thickness should be thinned within a few unit cells, because of improvement of the approximation in a simulation. Therefore, the lattice constant of ZnO along the incoming beam direction has to be compressed to fit to that of Pd and then all atomic occupancies of ZnO should be changed to 0.85 in order to compensate to effective specimen thickness of ZnO. (This compensation cannot be avoided for a system including a large lattice mismatch. This approximation is valid for a thin specimen, because Fresnel propagation (see Appendix B) is actually not critical for the wave function at exit surface of the specimen which is approximately not as a function of thickness. No difference was confirmed between the simulated images with and without the compensation for ZnO.)

The final goal of the analysis is the determination of the best model for interfacial atomic structure. Firstly, the average best imaging parameters for both crystals was prepared. After that, the imaging parameters are optimized again for the interface region by IDIM without including relaxation of the atomic structure and optimization of the interfacial atomic occupancy.

The calculation was done for at least 250 iterations until XCF value could be converged as shown in Fig. 6.15. Table 6.4 shows the calculated best possible imaging parameters for the region of the interface.

It can be seen that all best fitting parameters changed from that for bulk regions. However, best specimen thickness and specimen thickness which are most effective are slightly different from that for the bulks.

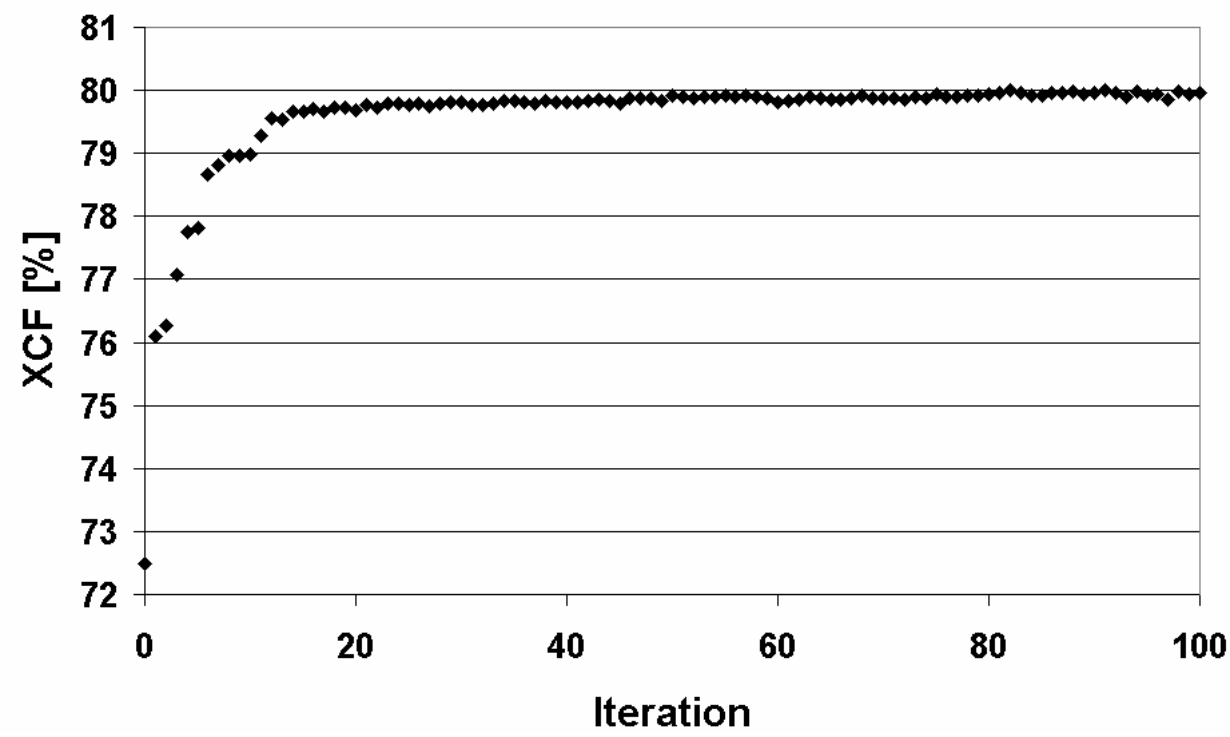

Fig. 6.15 Convergence of XCF value as function of iteration. The calculation was done for at least 250 iterations until XCF value could be converged.

Table 6.4 Best fitting imaging parameters for the interfacial region. All best fitting parameters changed from that for bulk regions. However, best specimen thickness and specimen thickness which are most effective are slightly different from that for the bulks.

	Interface
XCF [%]	80.078
Specimen Tilt *x* [°]	-0.016
Specimen Tilt *y* [°]	0.039
Specimen Thickness [nm]	3.1
Defocus [nm]	-17.8
Spherical Aberration [mm]	2.53
Beam Tilt *x* [°]	-0.014
Beam Tilt *y* [°]	0.049
Focus Spread [nm]	10.7
Beam Convergence [mrad]	0.4
Aperture Diameter [nm-1]	23.6
Gaussian MTF-envelope (sigma_*x*) [nm]	0.050
Gaussian MTF-envelope (sigma_*y*) [nm]	0.050

Step (iv): Quantitative Determination of Local Atomic Structure adjacent to Interface

The best possible local atomic structure of the interfacial region is determined by allowing only the relaxations of the positions of the interfacial Pd and Zn atoms as well as O atoms next to the interface. The super cell in Fig. 6.14 was used as an initial structure model whose ZnO is terminated by Zn. The iterations on UNIX work station required nearly one week until XCF converged sufficiently. Fig. 6.16 shows the experimental image, the simulated image, and the difference image of the region of the interface. The left images were obtained without relaxing the interfacial local atomic structure. The right images were obtained after relaxation of the interfacial local atomic structure by IDIM (only atoms near the interface were relaxed). After the optimization, white dots near the interface on the difference image were decreasing. Fig. 6.17 (bottom) shows the best fitting atomic structure on the image after the optimization of the structure. It can be seen that each atomic position was slightly shifted from the initial positions as shown in Fig. 6.17 (upper).

Fig. 6.17 (bottom) shows that the positions of the interfacial Pd atoms are the same as that of the bulk region, indicating that the Pd atomic columns adjacent to the interface are not relaxed. However, the positions of the interfacial Zn atoms and the O atoms next to the interface are largely different from that in the bulk ZnO region.

Table 6.5 indicates the translation vectors between the position of the interfacial Zn atom and the nearest neighbouring interfacial Pd atom. Before the optimization, the translation vectors $|T_x|$ of the interfacial Zn atoms for the nearest neighboring interfacial Pd atoms were distributed within 35 ~ 121 pm due to the large lattice mismatch. After the optimization, the translation vectors $|T_x|$ were converged within 71 ~ 116 pm which are closer to $|b_x|/3$ (79 pm) than $2|b_x|/3$ (158 pm) where the distance $|b_x|/3$ denotes the lattice spacings $d_{22\bar{4}}$ of Pd. This suggests that the interfacial Zn atoms fit on top of the Pd atoms on 3rd Pd layer. This means that the interfacial Zn atoms prefer to sits on fcc hollow sites of the interfacial Pd atoms. Table 6.5 also shows that the interfacial distances after the optimization is slightly increasing to 0.241 ~ 0.252 nm (average: 0.242 nm) from the initial distance of 0.229 nm. The interfacial distance is slightly wider than the spacing d_{111} (0.225 nm) of Pd. Table 6.7 shows that change of the lattice spacing near the interface from the initial lattice spacings. The interfacial Pd layer was nearly not relaxed also along the interface normal. This means that the interfacial Zn layer was slightly shifted to the inner part side of the ZnO crystal. Especially, the O layer on 2nd layer was strongly shifted to bulk ZnO side.

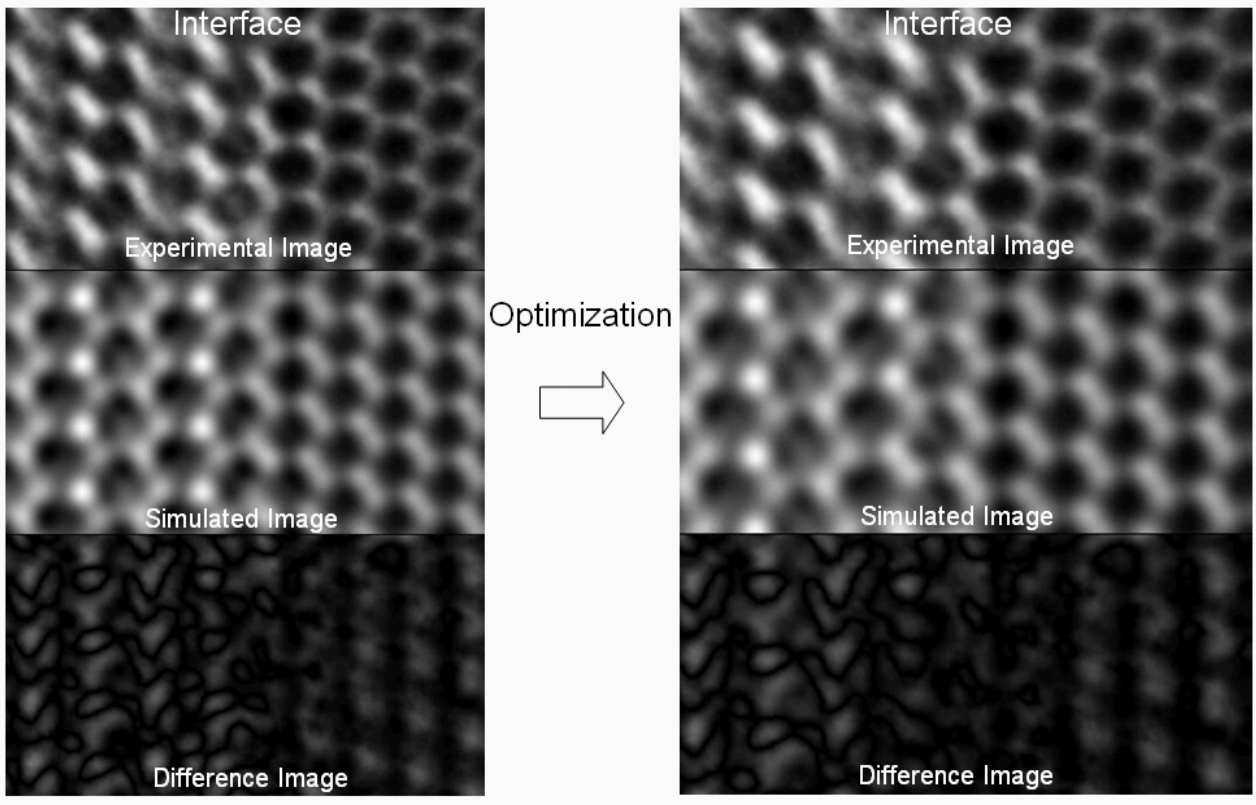

Fig. 6.16 The experimental image, the simulated image, and the difference image of the region of the interface. The left images were obtained without relaxing the interfacial local atomic structure. The right images were obtained after relaxation of the interfacial local atomic structure.

Table 6.5 Translation vectors between the interfacial Zn atoms and the interfacial Pd atoms.

Translation vector of the interfacial Zn atom for the interfacial Pd atom	$\lvert T_x \rvert$ [nm]	$\lvert T_z \rvert$ [nm]
Zn^1 before relaxation	0.121 ± 0.01	0.229 ± 0.01
Zn^1 after relaxation	0.116 ± 0.01	0.241 ± 0.01
Zn^2 before relaxation	0.078 ± 0.01	0.229 ± 0.01
Zn^2 after relaxation	0.101 ± 0.01	0.243 ± 0.01
Zn^3 before relaxation	0.035 ± 0.01	0.229 ± 0.01
Zn^3 after relaxation	0.071 ± 0.01	0.252 ± 0.01

Table 6.6 Basis vectors of ZnO and Pd. The distance $|b_x|/3$ denotes lattice spacings $d_{22\bar{4}}$ of Pd.

$\lvert a_x \rvert$ [nm]	$\lvert a_z \rvert$ [nm]	$\lvert b_x \rvert$ [nm]	$2\lvert b_x \rvert/3$ [nm]	$\lvert b_x \rvert/3$ [nm]	$\lvert b_z \rvert$ [nm]
0.281	0.513	0.238	0.158	0.079	0.674

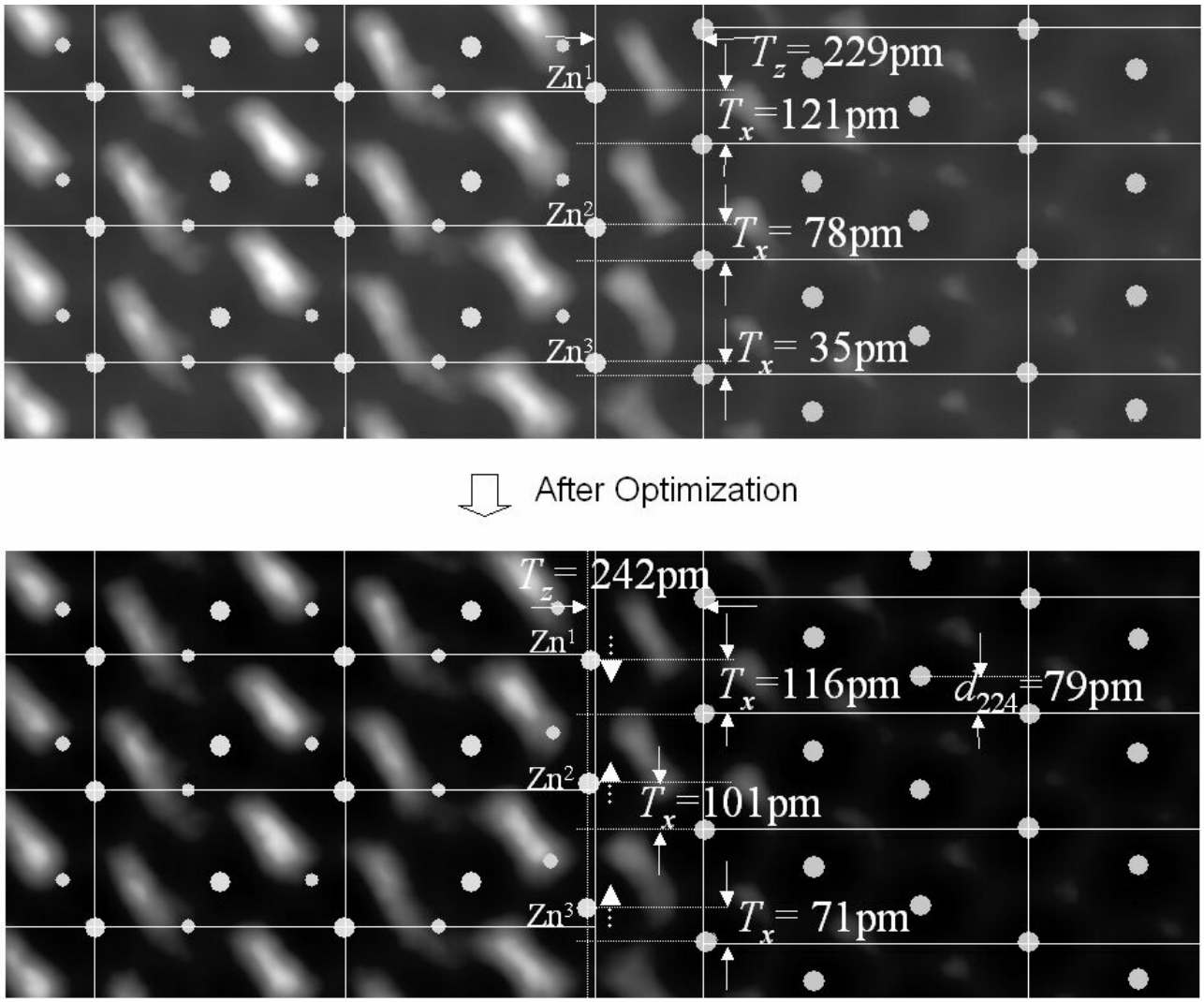

Fig. 6.17 The upper image shows atomic positions determined from the calculation for the bulks. The translation vectors *T* (the interatomic distances across the interface) between each interfacial Zn atom and the interfacial Pd atom are not the same each other. However, after optimization of the local atomic structure, the translation vectors *T* are getting close each other. The bottom image shows the best fitting atomic structure on the image after the optimization of the structure near the interface. It can be seen that each atomic position was slightly shifted from the initial positions as shown on the upper image. The model on the bottom image shows that the positions of the interfacial Pd atoms are the same as that of the bulk region, indicating that the Pd atomic columns adjacent to the interface are not relaxed. However, the positions of the interfacial Zn atoms and the O atoms next to the interface are largely different from that in the bulk ZnO region.

Table 6.7 Changes (average) of the lattice spacings along the normal to the interface compared to bulk. Rates [%] are based on the basis vectors along the interface normal.

1st Pd atom	-0.40 ± 0.04 %
1st Zn atom	-0.77 ± 0.02 %
2nd O atom	-1.33 ± 0.02 %

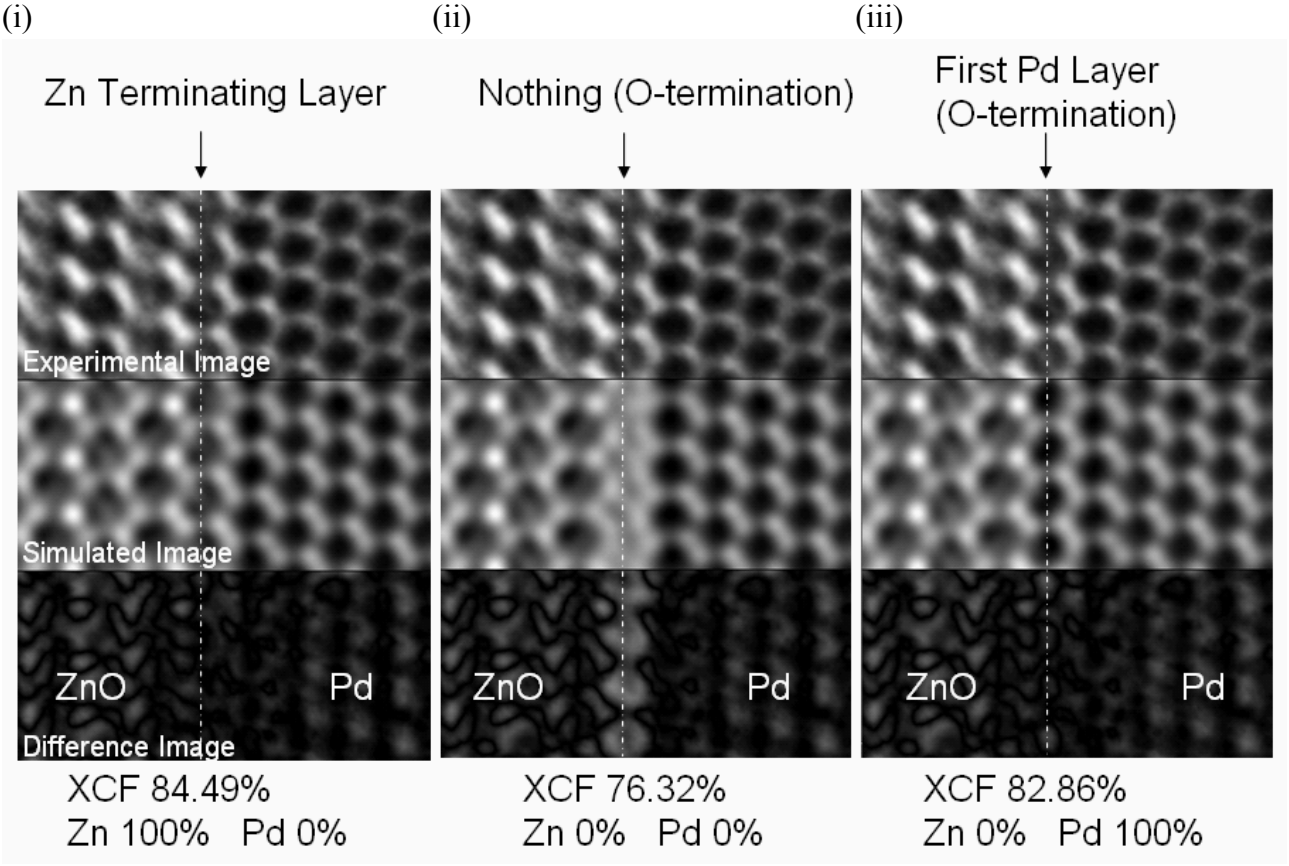

Fig. 6.18 Atomic occupancy and atomic species were exchanged in the interfacial layer shown by the dotted lines which provisionally assumed as Zn-terminating layer. XCF value and difference image between computed image and experimental image, for (i) Zn: 100% (Zn-termination), (ii) Zn: 0 % Pd: 0 % (O-termination), and (iii) Pd: 100 % (O-termination).

Step (v): Determinations of Interfacial Terminating Atomic Species and Atomic Occupancy

So far, it has been assumed that the terminating atomic species at the **Pd/$^{+}$ZnO** interface are Zn atoms with an atomic occupancy of 100 %. In order to justify the assumption, other possibilities were examined in detail by using the obtained best fitting atomic structure in the Step (iii). It seems that the used atomic structure model was valid except for the provisional terminating layer of Zn. It can be considered that other atomic species exists at this provisional layer. Although this provisional layer of the CIA possesses clearly resolved columns, it should not be forgotten that the neighboring regions in the same layer belong to the DIA, suggesting that a relaxation or a replacement of the atoms may easily occur in this layer or undetectable relaxation along the zone axis of $[11\bar{2}0]_{ZnO}$ may be included in the layer.

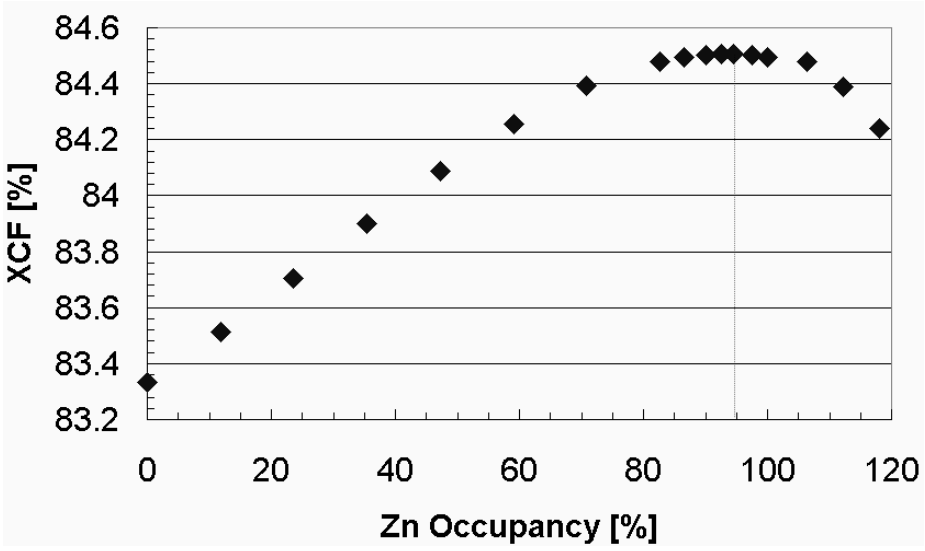

Fig. 6.19 XCF value as a function of interfacial atomic occupancy. When the occupancy of Zn is *x*, the occupancy of Pd should be (1-*x*) %. Although the atomic occupancy above 100 % is unrealistic, it was included as references because it is technically possible to calculate it. When the occupancy of Zn is above 100 %, the XCF was calculated by fixing the occupancy of Pd at 0 %.

Therefore, following three possibilities can be considered. (i) The layer (columns) may include only Zn with different atomic occupancy. (ii) It may not include both Pd and Zn that the interface would be O-termination. (iii) It may completely replace Zn atoms by Pd atoms that the interface also would be O-termination. The likely simulated images were compared to the experimental images as shown in Fig. 6.18.

Fig. 6.18 shows the experimental images, simulated images, and difference images, and XCF values for the case of [Zn: 100 % (Zn-termination)], [Zn: 0 %, Pd: 0 %] (O-termination), and [Pd: 100 % (O-termination)], respectively. Good agreement exists if the difference image possesses low intensity. It can be clearly seen that in the interfacial region high intensity on the differential image is present for O-termination [Zn: 0 %, Pd: 0 %], resulting in a comparatively low value (76.32 %) of XCF. This suggests that this situation is not likely. Both cases of Zn-termination [Zn: 100 %, Pd: 0 %] and O-termination [Zn: 0 %, Pd: 100 %] do not show the bright fringe at the difference images. The corresponding values of the XCF are relatively high (84.49 ~ 82.86 %). Since these looks and XCF values have a slight difference, however, we must be careful for determination whether the investigated layer consists of Zn or Pd. Furthermore, there is also the possibility that the investigated layer consists of mixture of Zn and Pd. If the occupancy of the Zn-terminating layer is 30 %, for example, the rest space of 70 % made by absence of Zn may be occupied by Pd.

The calculation of best atomic occupancy is possible by modifying atomic occupancies

and putting both Pd and Zn atom at the same coordinates on the input file for EMS program. [Note: In this calculation, one slice thickness for the simulation corresponds to 1 unitcell of Pd along the incoming beam direction. Therefore, the lattice constant of ZnO along the zone axis of $[11\bar{2}0]$ was compressed to fit to that of Pd and then all atomic occupancies of ZnO should be changed to 0.85 in order to compensate to effective specimen thickness of ZnO. In addition to it, the specific occupancy in the investigated layer was multiplied with the initial occupancy of 0.85. Therefore, an atomic occupancy of ZnO above 100 % is mathematically possible. Although it is not likely, an atomic occupancy above 100 % was also just tried.

Fig. 6.19 shows the XCF value as a function of atomic occupancy of the Zn. It can be seen that the XCF value increases with increasing the partial occupancy of the Zn. Best results are obtained for [Zn: 95 % and Pd: 5 %]. Therefore, it can be concluded that **Pd/$^{+}$ZnO** interface is terminated by Zn with the atomic occupancy of 95 % (and by also Pd with the atomic occupancy of 5%).

Fig. 6.19 showed the highest XCF value of 84.51 % was given under the condition for [Zn: 95 % and Pd: 5 %]. The difference image showed that the only interface region does not possess white dot (high intensity spot), suggesting that the interface region could be reproduced more precisely. This seems to be attributed to the optimization of the interfacial local atomic structure. In bulk region, an optimization was not done. Therefore, the XCF value within only interfacial layer were calculated again as shown in Fig. 6.20. It can be seen that XCF values was largely increased to 92.65 %, indicating that the interfacial model is quite valid.

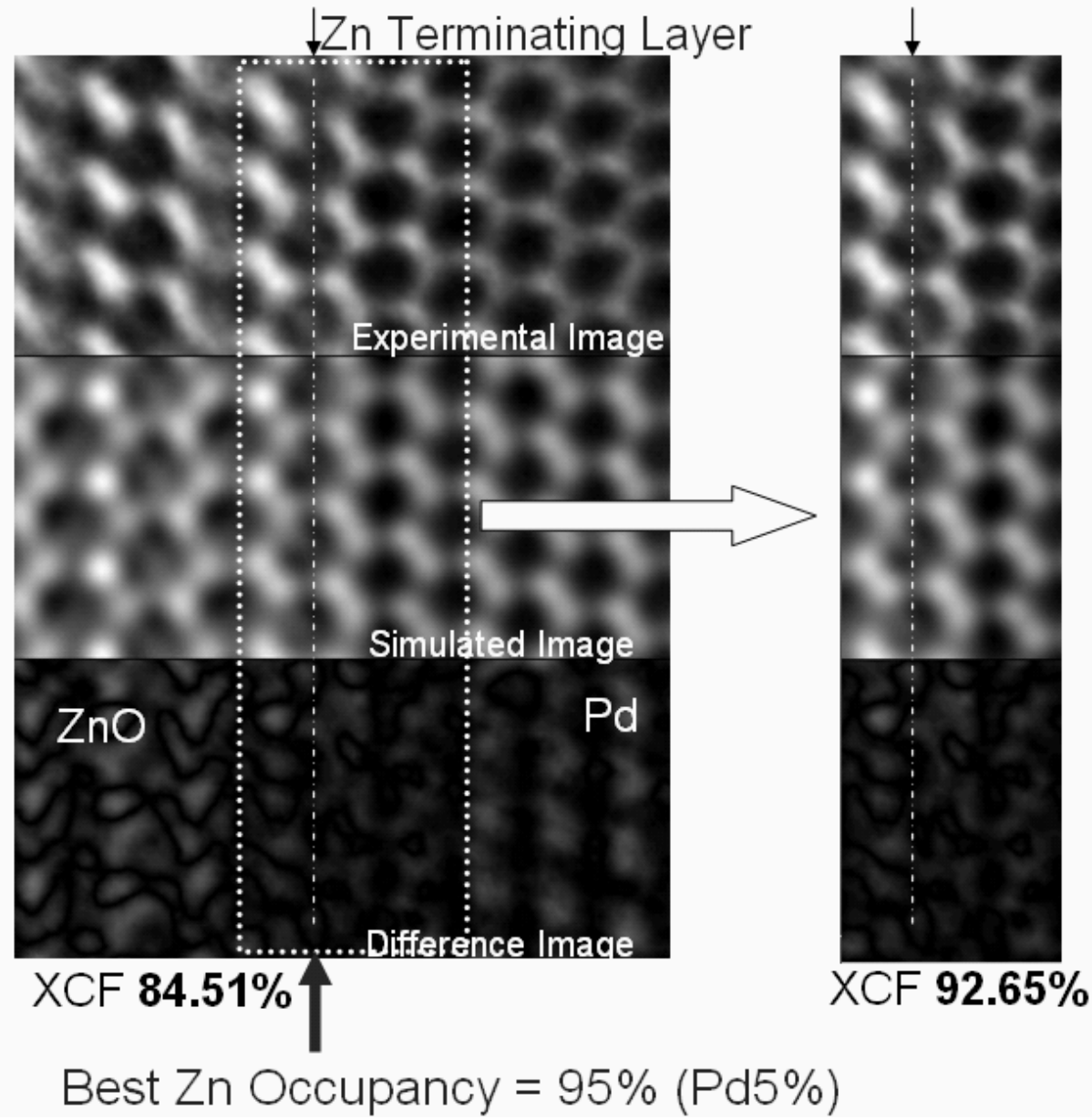

Fig. 6.20 The XCF value and the difference image calculated only within the interfacial layer. The difference image showed that the only interface region does not possess white dot (high intensity spot), suggesting that the interface region could be reproduced more precisely.

(B) Pd/$^{+Zn}$ZnO Interface ($[1\bar{1}00]_{ZnO}//[11\bar{2}]$)

Determination of Local 3-Dimensional Interfacial Atomic Structure

So far, the interfacial atomic structure has been observed along the zone axes of the $[11\bar{2}0]_{ZnO}//[\bar{1}10]_{Pd}$. The interpretation of one projected image must make assumption of the 3-dimensional atomic structure. However, 3-D atomic structure cannot be determined by only one projected image. For that reason, the interface was also investigated for the $[1\bar{1}00]_{ZnO}//[11\bar{2}]_{Pd}$ zone axes which is also parallel to the interface and which is perpendicular to the previous zone axis (subsection 6.1.3(A)). The second zone axis results in even smaller spacings (0.063 nm) for both Pd and ZnO. This means that it will be impossible to distinguish the two atoms within a ZnO dumbbell. Fortunately, the determination of the 3-D atomic structure requires only the analysis of the translation vector T_y (see Fig. 6.25), because the translation vectors T_x and T_z (see Fig. 6.17) were already determined for the CIA (coherent interface areas) (subsection 6.1.3(A)). Furthermore, the investigations described in subsection 6.1.3(A) revealed that the interface is Zn-termination and also its atomic occupancy of ~100 %. The interfacial distance $T_{\min,z}$ should be the same for the $[1\bar{1}00]_{ZnO}//[11\bar{2}]_{Pd}$ zone axes.

Fig. 6.21 shows an ARM image of the **Pd/$^{+Zn}$ZnO** taken along the $[1\bar{1}00]_{ZnO}//[11\bar{2}]_{Pd}$ zone axes for a defocus condition (*df* ~-30 nm). As mentioned in subsection 6.1.2, the position of each Pd atom corresponds to the center of black dot (low intensity), while the Zn-O dumbbell is imaged also as one column only, because the projected distance between Zn atom and O atom within the dumbbell is 0.063 nm along the zone axis of $[1\bar{1}00]_{ZnO}$.

The difference between Pd and ZnO columns can easily be distinguished, because two crystals adjacent to the interface generate different contrasts and spacings. The interface is atomically flat and no strain field can be seen in both bulk Pd and ZnO regions.

Fig. 6.22(c) shows the same ARM images as Fig. 6.21 with support lines connecting the centers of atomic columns of bulk regions. The Pd atoms next to the interface are located at perfect Pd crystal lattice positions. However, the ZnO possess both CIA and DIA as similar as the observation along the previous zone axis. The clearly resolved columns of the CIA are marked by ellipses in Fig. 6.22(c) (Fig. 6.26 showed more clearly both kinds of columns). It can be seen that the total length of both DIA and CIA is ~1 nm along the interface. The both regions are repeated. This periodicity corresponds to the distance dictated by the lattice mismatch of 18 % between Pd and ZnO.

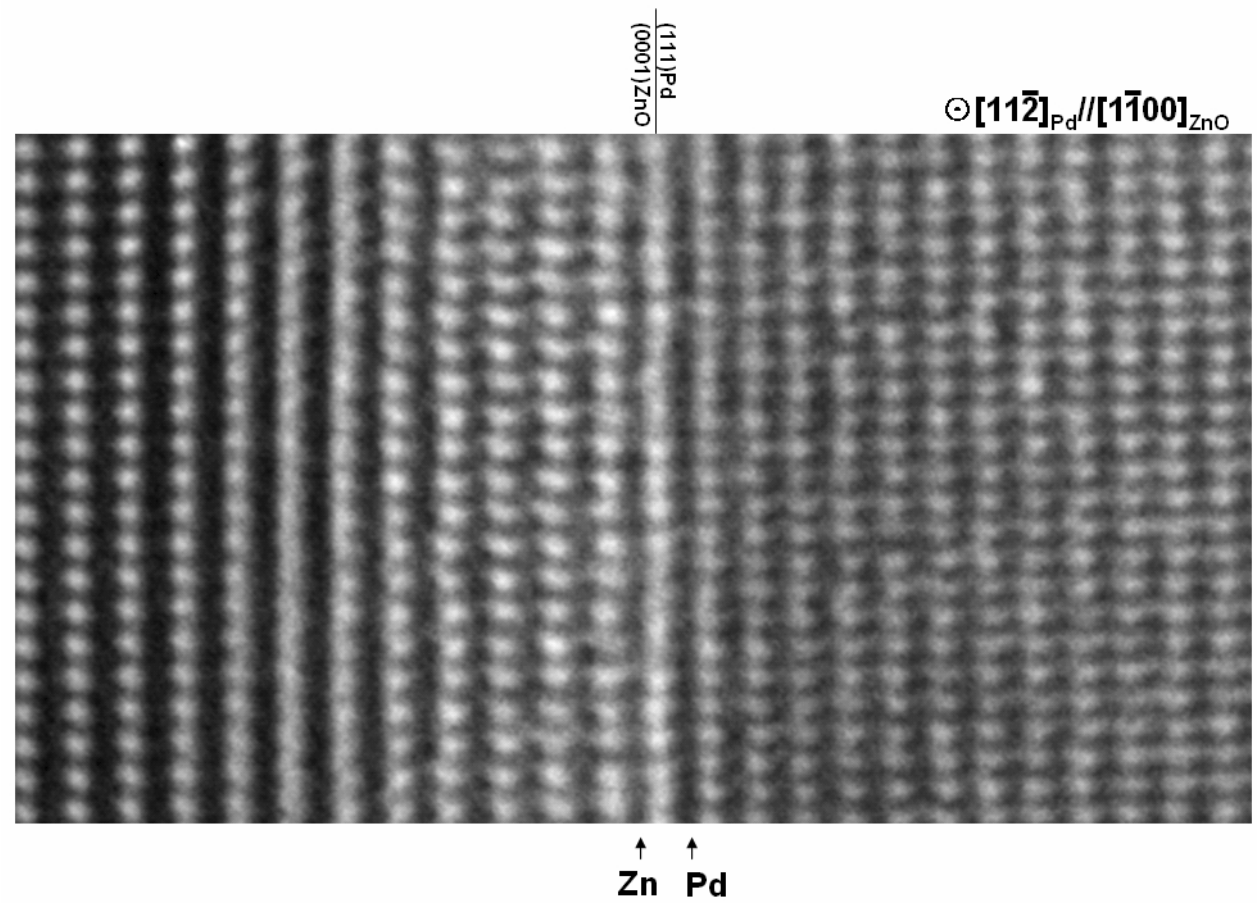

Fig. 6.21 ARM image of **Pd/$^{+Zn}$ZnO** interface observed along the $[1\bar{1}00]_{ZnO}//[11\bar{2}]_{Pd}$ zone axes.

Lattice distortion analysis was performed for the region of Pd crystal by LADIA (LAtice DIstortion Analysis) program package [Du, 2001], in order to know a strain field caused by the relaxation of the interfacial Pd atoms which was checked in the subsection 6.1.3(A). Fig. 6.22(b) shows contour map of strain detected from the image (a) of the Pd region. Compressive stress indicates low (black) intensity. Tensile stress indicates high (white) intensity. Periodic strain fields in bulk Pd region cannot be seen. This result supports that the Pd crystal does not relax at the **Pd/$^{+Zn}$ZnO** interface which is the obtained result in the subsection 6.1.3(A).

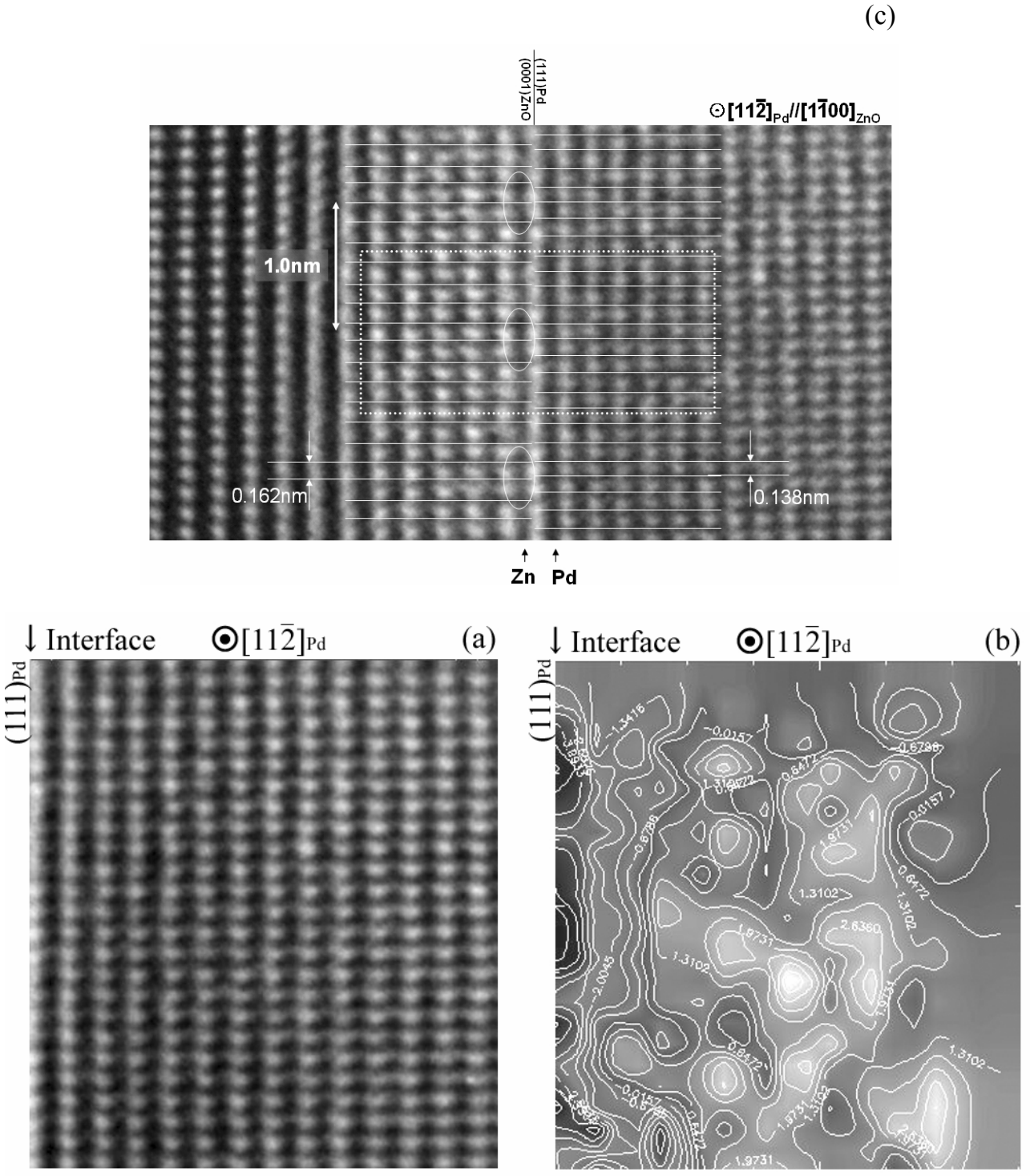

Fig. 6.22 (c) ARM image of **Pd/$^{+Zn}$ZnO** interface with supporting lines connecting the centers of atomic columns of bulk regions. The Pd atoms next to the interface are located at perfect Pd crystal lattice positions. However, the ZnO possess both CIA and DIA as similar as the observation along the first zone axis. The clearly resolved columns of the CIA are marked by ellipses. The terminating atomic species was already determined in subsection 6.1.3 (A). (a) HRTEM image of Pd region near the **Pd/$^{+Zn}$ZnO** interface. (b) Contour map of strain in the image (a) calculated by LADIA (LAttice DIstortion Analysis) [Du, 2001]. Low (black) intensity indicates compressive stress. High (white) intensity indicates tensile stress. Periodical strain cannot be seen in Pd near the interface.

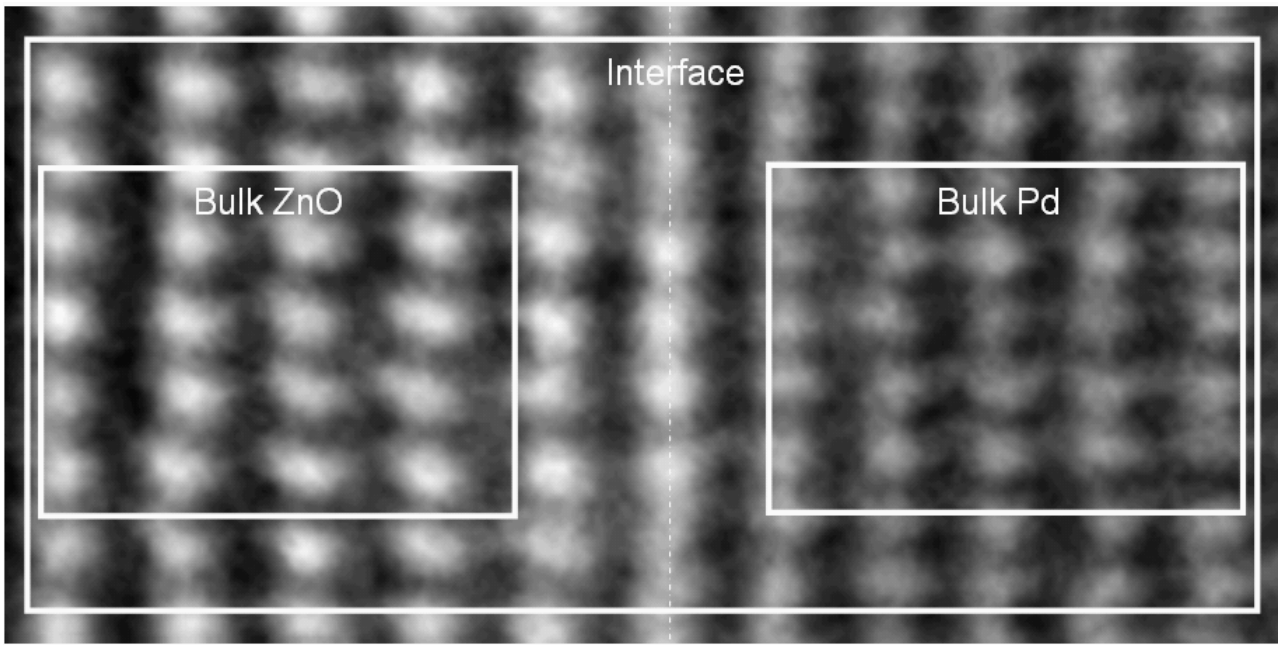

Fig. 6.23 Selected experimental images used for the image calculation. First of all, the images for both bulk regions in the white frames were simulated.

Table 6.8 Best fitting imaging parameters for both bulk regions. The most critical parameters (defocus, specimen thickness, specimen tilts, and beam tilts) are the same for both regions. The XCF values for both bulk regions are high.

	Bulk ZnO	Bulk Pd
XCF [%]	90.356	90.736
Specimen Tilt *x* [degree]	-0.041	-0.011
Specimen Tilt *y* [degree]	0.028	0.070
Specimen Thickness [nm]	5.69	5.68
Defocus [nm]	-30.0	-28.8
Spherical Aberration [nm]	2.60	2.65
Beam Tilt *x* [degree]	-0.040	0.009
Beam Tilt *y* [degree]	0.024	0.121
Focus Spread [nm]	11.0	9.2
Beam Convergence [mrad]	0.35	0.31
Aperture Diameter [nm-1]	15.3	15.3
Gaussian MTF-envelope (sigma_*x*) [nm]	0.0399	0.0385
Gaussian MTF-envelope (sigma_*y*) [nm]	0.0315	0.0239

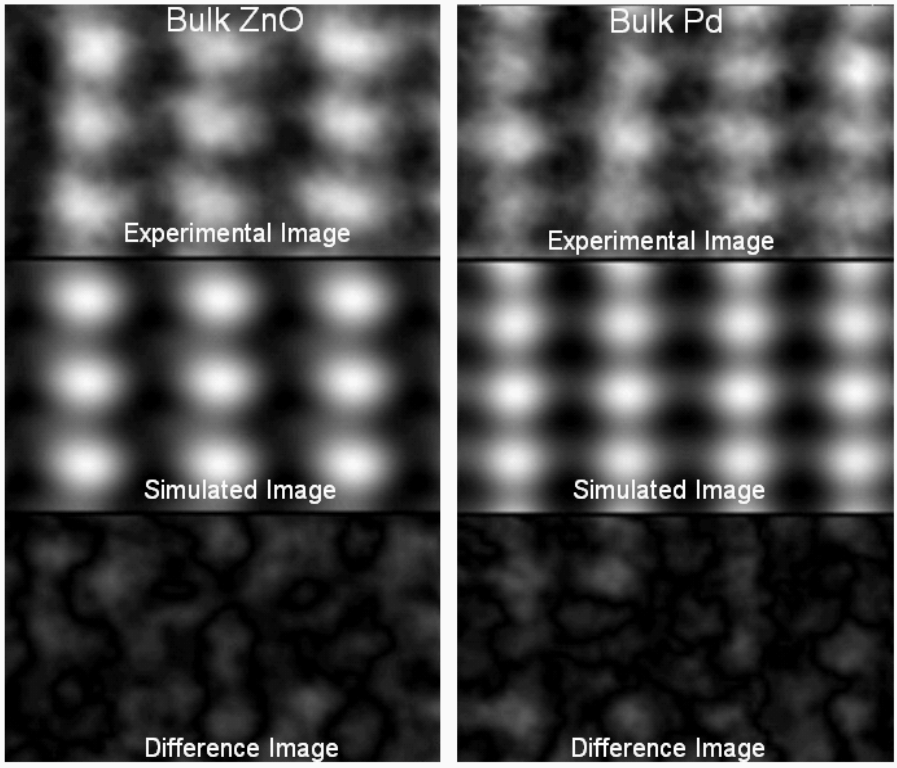

Fig. 6.24 The experimental images, the best fitting calculated images, and the difference images for (left) bulk ZnO and for (right) bulk Pd, respectively. Actually, both difference images do not show strong bright residual white dot.

Step (i): Calculation of Imaging Parameters for Both Bulk Pd and ZnO Regions

The both bulk regions close to the interface were defined for analysis as shown in Fig. 6.23. First of all, the images for both bulk regions in the white frames (Fig. 6.23) were simulated. Table 6.8 shows the best fitting imaging parameters for the bulk Pd and bulk ZnO. The most critical parameters (defocus, specimen thickness, specimen tilts, and beam tilts) are the same for both regions. The XCF values for both bulk regions are high, indicating that the experimental images can be truly reproduced with these parameters. Fig. 6.24 shows the experimental images, the best simulated images, and the difference images for the bulk Pd and the bulk ZnO, respectively. Actually, both difference images do not show strong bright residual white dot.

Step (ii): Determination of the Translation Vector between Pd and ZnO

The translation vectors between the atoms at the interface be defined as (see Fig. 6.25)

$$T_y = \left| D_y + (V_y + nb_y) - (U_y + ma_y) \right|, \tag{6-2}$$

where a and b are basis vectors of ZnO and Pd respectively, and m and n are integer. Fig. 6.25 shows a supercell constructed by the calculations for bulk regions.

Table 6.9 Translation vectors between the interfacial Zn atoms and the interfacial Pd atoms.

	$\|T_y\|$ [nm]
Zn^1	0.020
Zn^2	0.005
Zn^3	0.030

Table 6.10 Basis vectors of ZnO and Pd

$\|a_y\|$ [nm]	$\|a_z\|$ [nm]	$\|b_y\|$ [nm]	$\|b_z\|$ [nm]
0.163	0.260	0.138	0.224

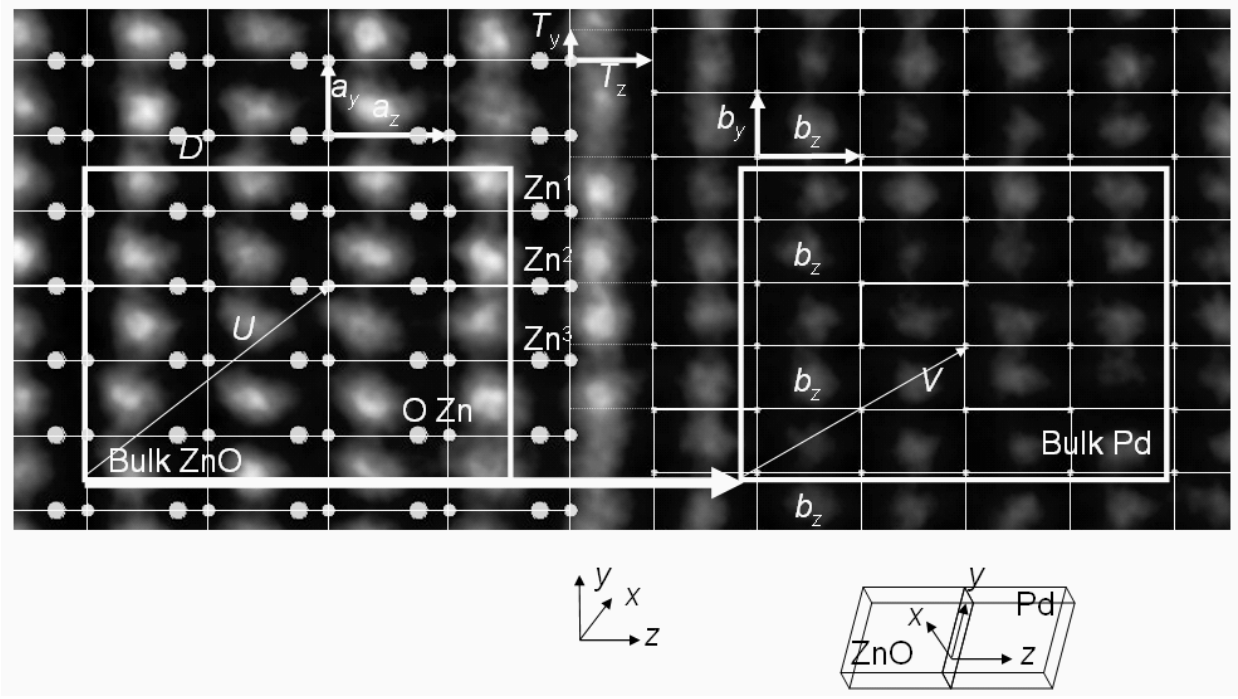

Fig. 6.25 Initial atomic model on the experimental image estimated by the calculations for bulk regions. Each atomic position is valid in only the defined bulk regions. IDIM allows the determination of 2 components of the translation vectors V , U between some atomic position and the origin of the defined area. Furthermore, the translation vectors V , U and the distance D between two defined areas were used for construction of the supercell for the simulation for the interface. The supercell allows the determination of the exact translation vectors T between atoms across the interface.

Of course, all atomic positions are fixed at the perfect crystal positions in the bulk. This means that the positions of atomic columns in Fig. 6.25 are provisional. The supercell was constructed based on the model of a Zn-termination of ZnO obtained in subsection 6.1.3(A).

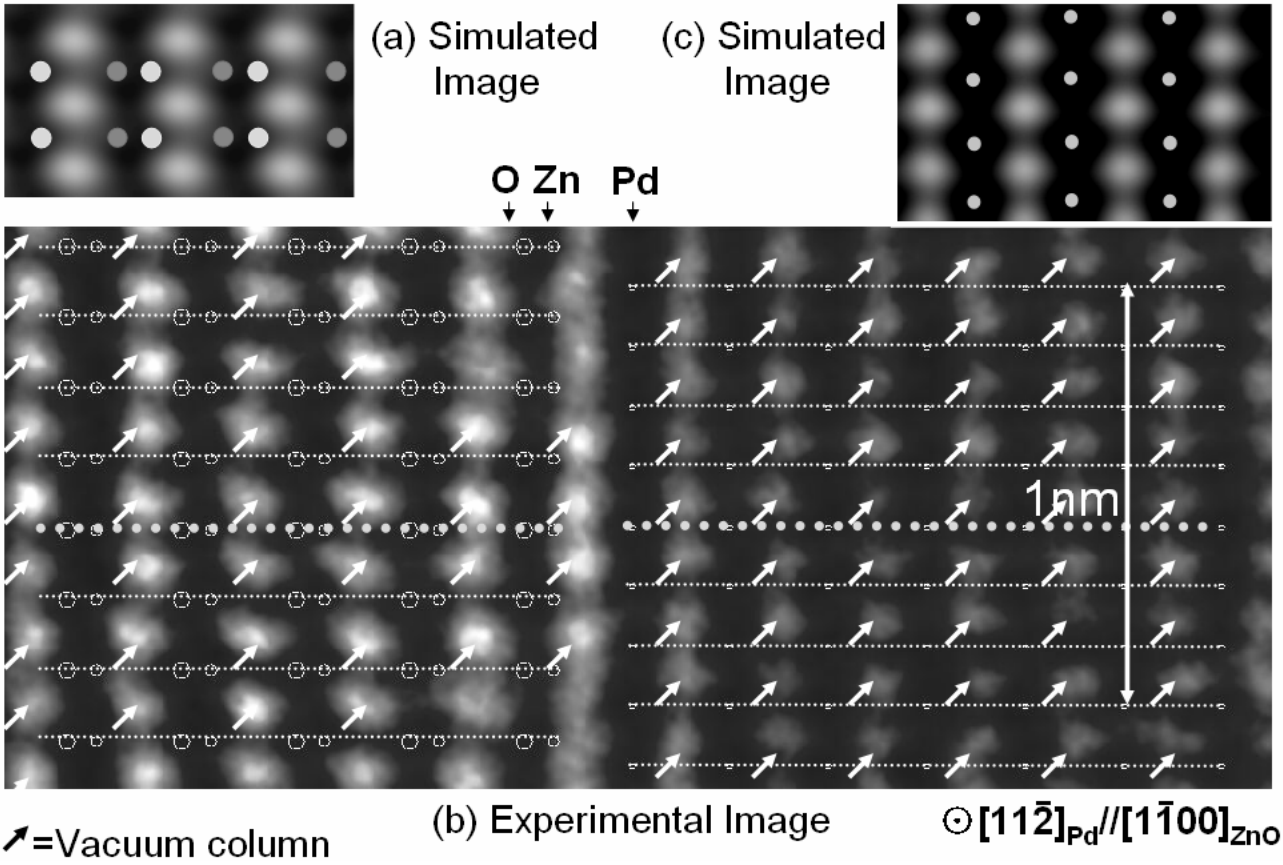

Fig. 6.26 Atomic structure model before relaxation. The white dots (of vacuum columns) neighboring the 1st Zn layer can be clearly resolved only near the solid dotted line. However, the dots were overlapped near the other dotted lines, indicating that a part of the interfacial Zn atoms is relaxed in order to fit the Pd lattice.

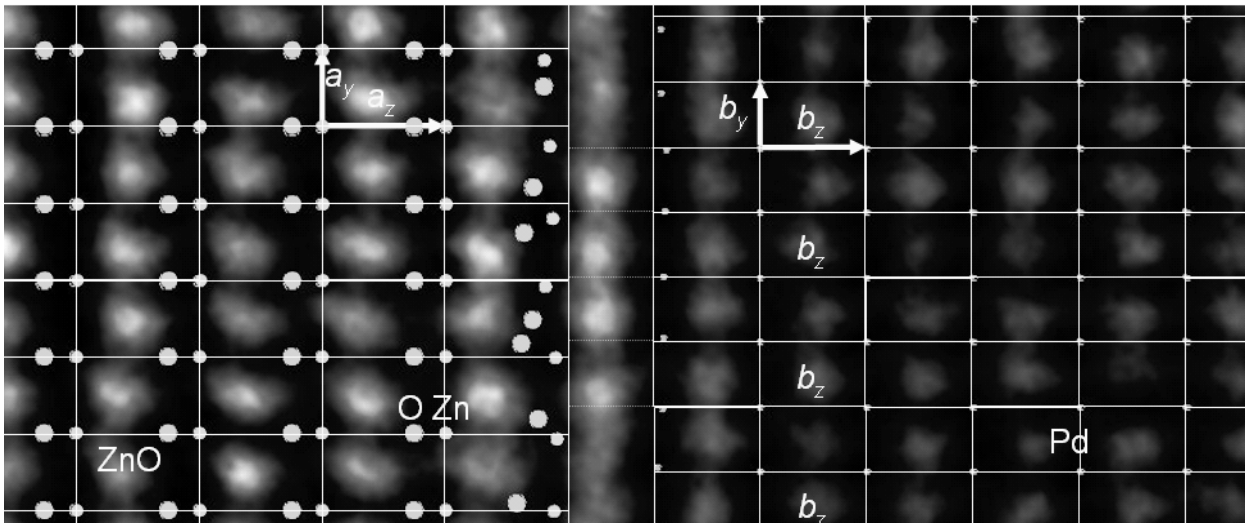

Fig. 6.27 Atomic structure model after relaxation. This is unusual structure.

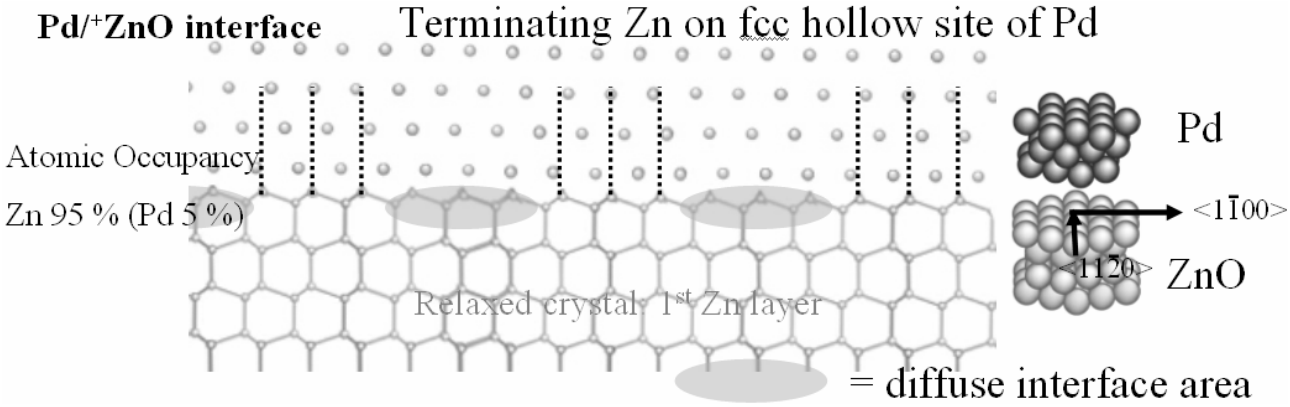

Fig. 6.28 The most stable 3-D local atomic structure is that Zn sits on the fcc hollow site of Pd lattice. At the interface, ZnO crystal is relaxed to fit Pd lattice due to the large lattice mismatch of 18 %. When the mismatch is small, the stable local structure without relaxation can be expected as shown in this figure. The cross-sectional figures are along the $[11\bar{2}0]_{ZnO}$ axis or the $[1\bar{1}00]_{ZnO}$ axis. The Pd stacks on the lattice site of the ZnO, simultaneously the interfacial Pd atoms sit on the hollow sites of the atoms in the 2nd layer of the ZnO, and the Pd atom in the 3rd layer sits on top of the interfacial atom of the ZnO.

Step (iii): Quantitative Analysis of Interfacial Local Atom Structure

The best fitting local atomic structure near the interface was determined. Fig. 6.27 shows the best possible local atomic structure on the experimental image after the optimization which results in a maximal XCF value. It can be seen that all atomic positions near the interface are shifted from the initial positions as shown in Fig 6.35. This result is unexpected, since the calculated atomic positions do not overlap to atomic columns on the image. This unusual result seems to be caused by the extremely small lattice spacing and the image with a very low S/N ratio. We could not determine quantitatively the local atomic structure via the second zone axis. Furthermore, Step (iv): determination of atomic occupancy could not be done.

Fortunately, the initial atomic model in Fig. 6.25 results in a good match with the contrast of atomic columns. Only translation vector T_y can be precisely determined by a qualitative analysis for following reasons. Fig 6.26 (a) and (c) shows simulated images with best fitting for the atomic positions of bulk ZnO and Pd, respectively. These images suggest that the positions of the Pd atoms agree well with the image contrasts while the atomic positions of the ZnO did not agree with the contrast centers. This means that it is difficult to determine the exact positions of Zn atoms by a direct observation. However, the translation vector T_y can be easily determined, because parallel to the *y* axis the atomic positions of the ZnO agree well with the contrast centers on the simulated image (Fig. 6.26(a) and (c)). We

already determined the translation vectors T_x and T_z in the analysis along the first zone axis (see Table 6.5). The translation vector T_z in the first zone axis should be identical to that in the second zone axis.

The translation vectors T_y were examined by using the initial supercell in Fig. 6.25. Table 6.9 showed that the translations along the *y*-axis are within 5 ~ 30 pm which are closer to 0 pm than $|b_y|$ (138 pm) where the distance $|b_y|$ denotes the lattice spacings $d_{\bar{2}20}$ of Pd, indicating that the positions of all $Zn^{1\sim3}$ atoms were relaxed to fit to top of the interfacial Pd. However, other Zn atoms at the interface do not fit the Pd lattice (Fig. 6.25) due to large mismatch.

Fig. 6.26 shows the atomic model supposed on the experimental image. We must notice for white dots (shown by arrows) corresponding to vacuum columns. It can be seen that some parts of the vacuum columns neighboring to 1st Zn layer are not clearly resolved, indicating that a part of Zn columns in 1st Zn layer cannot be clearly resolved. The solid dotted line across the interface in Fig. 6.26 showed that the Pd position fits to the Zn position at the interface and then the Zn column near the dotted line can be clearly resolved.

Therefore, the initial model shows that the interfacial Zn ions sit on top of the interfacial Pd atoms around the clearly resolved region. In addition, the result taken from the previous zone axis also should be considered simultaneously.

It can be concluded that the most stable 3-D local atomic structure is that Zn sits on the fcc hollow site of Pd lattice as shown in Fig. 6.28. Furthermore, only interfacial Zn layer is relaxed in the **Pd/$^{+Zn}$ZnO** interface.

6.1.4 Pd/$^{-}$ZnO Interface

Local atomic structure analyses in the **Pd/$^{-}$ZnO** interfaces could be performed employing an ultra high resolution microscope JEOL JEM-ARM1250 and a quantitative high resolution image analysis technique [Möbus, 1996]. The interface was observed along both the $[\bar{1}\,\bar{1}\,20]_{ZnO}//[1\,\bar{1}\,0]_{Pd}$ zone axes and the $[1\,\bar{1}\,00]_{ZnO}//[11\bar{2}]_{Pd}$ zone axes.

(A) Pd/$^{-}$ZnO Interface ($[\bar{1}\,\bar{1}\,20]_{ZnO}//[1\,\bar{1}\,0]_{Pd}$)

Overview of Pd/$^{-}$ZnO Interface

Fig. 6.29(b) shows a HRTEM image taken at a defocus value of *df* = -30 nm in the JEOL JEM-ARM1250 (Stuttgart). The specimen was aligned that the incoming beam is parallel to the $[\bar{1}\,\bar{1}\,20]_{ZnO}//[1\,\bar{1}\,0]_{Pd}$ zone axes. The black dots on the image correspond to the location of atomic columns under this imaging condition. Since the difference between the Pd and ZnO crystals can be clearly distinguished, the interfacial position can easily be recognized (Fig. 6.29(b)).

The interface between Pd and ZnO is atomically flat. Atoms next to the interface in the ZnO are located at the positions of the perfect crystal of ZnO. However, interfacial Pd layer share both CIA (coherent interface areas) and DIA (Diffuse interface areas) as well as the interfacial Zn layer of the **Pd/$^{+}$ZnO** interface. The locations of the DIA in Pd are periodically arranged.

The locations of the atoms in CIA fit the positions of the columns of Zn atoms, as shown in Fig. 6.30. The total length of DIA (~0.5 nm) and CIA (~1.0 nm) is about 1.5 nm along the interface as well as that of the **Pd/$^{+}$ZnO** interface. This periodicity corresponds to a lattice mismatch of 18 % between Pd and ZnO.

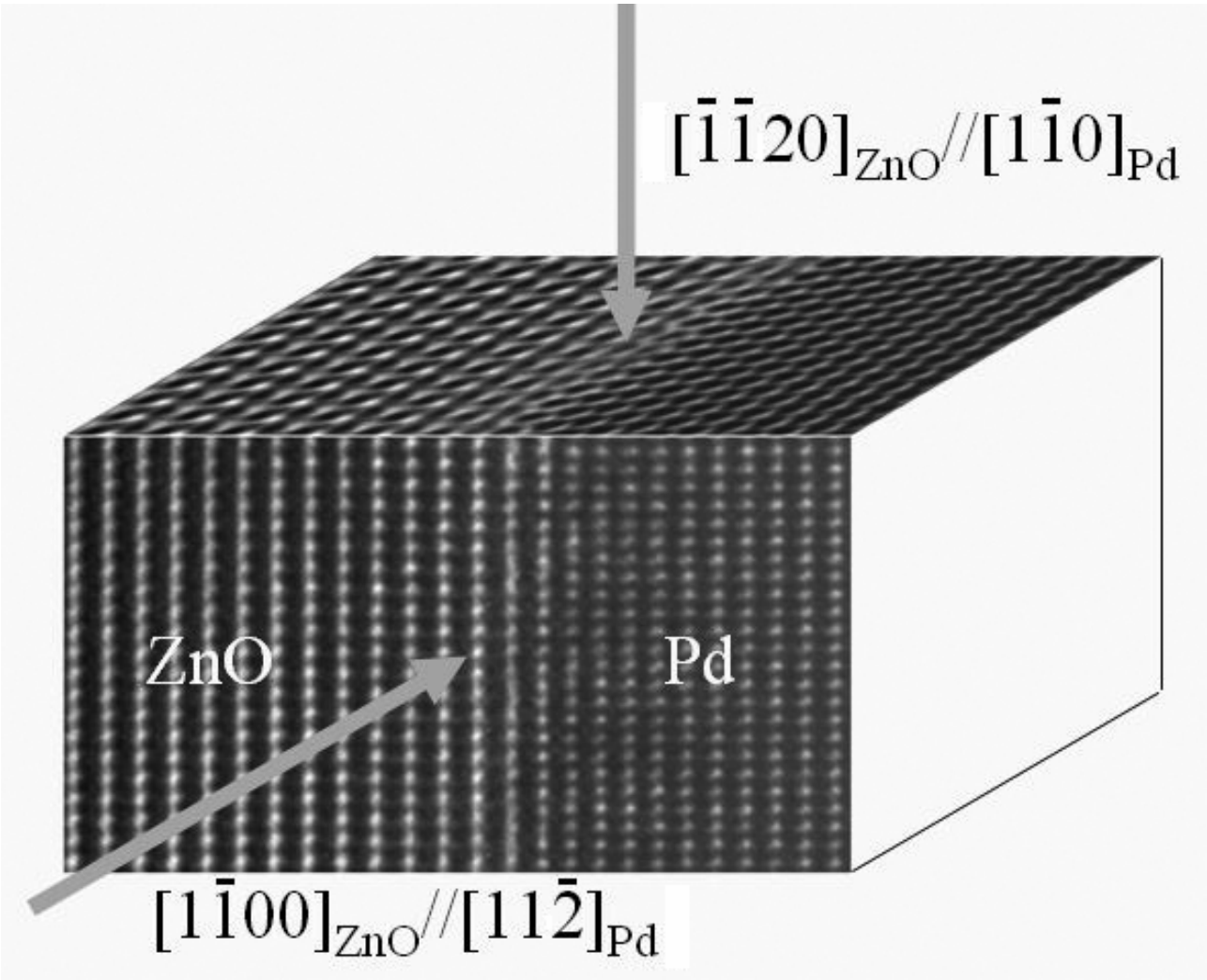

Fig. 6.29(a) 3D view of the HRTEM images of the **Pd/ZnO** interface taken at a defocus condition (*df* = ~-30 nm) along the $[\bar{1}\,\bar{1}\,20]_{ZnO}//[1\,\bar{1}\,0]_{Pd}$ zone axes and $[1\,\bar{1}\,00]_{ZnO}//[11\bar{2}]_{Pd}$ zone axes. The $[\bar{1}\,\bar{1}\,20]_{ZnO}//[1\,\bar{1}\,0]_{Pd}$ zone axes is parallel to the $[1\,\bar{1}\,00]_{ZnO}//[11\bar{2}]_{Pd}$ zone axes. 3-dimensional atomic structure can be obtained by the two projected images.

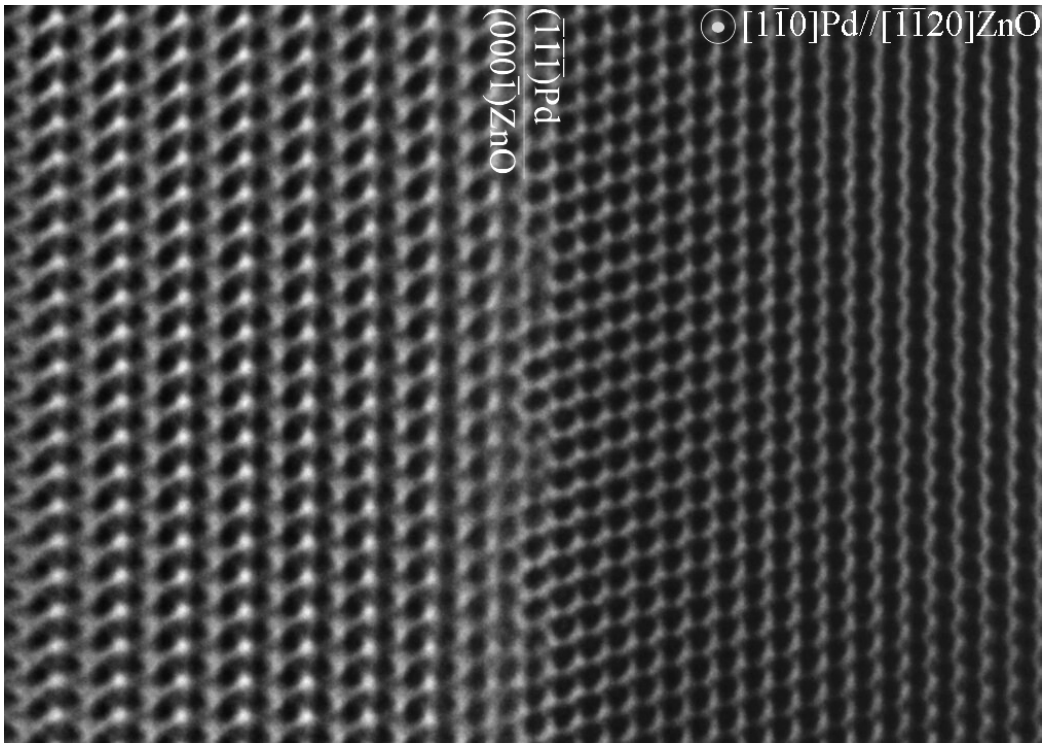

Fig. 6.29(b) ARM image of the **Pd/ZnO** interface taken at a defocus condition (*df* = ~-30 nm) along the $[\bar{1}\,\bar{1}\,20]_{ZnO}//[1\,\bar{1}\,0]_{Pd}$ zone axes.

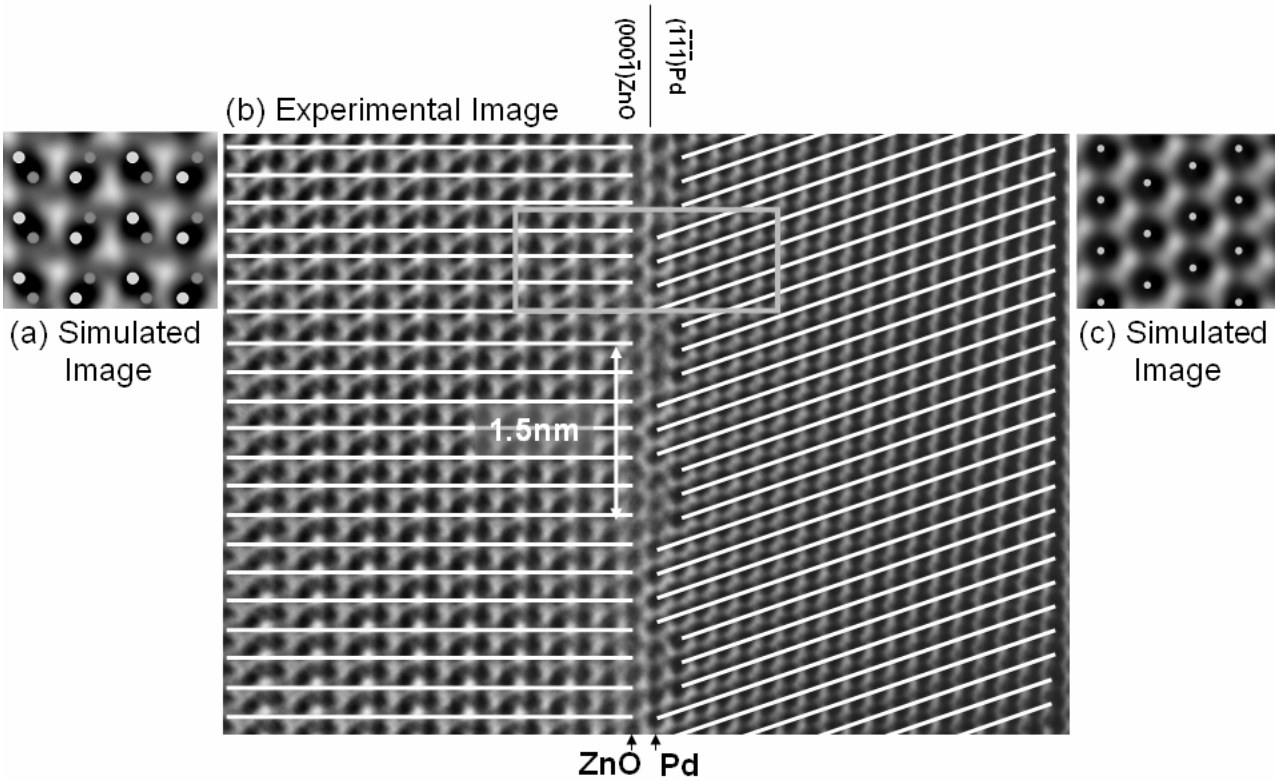

Fig. 6.30 (a),(c) Simulated images for bulk ZnO, Pd. (b) Experimental image of the **Pd/ZnO** interface. The locations of Pd atoms in CIA fit the positions of the columns of ZnO. The total length of DIA (~0.5 nm) and CIA (~1.0 nm) is about 1.5 nm along the interface. This periodicity corresponds to a lattice mismatch of 18 % between Pd and ZnO.

Table 6.11 The best possible imaging parameters for both bulk ZnO and Pd regions are different from each other. However, most critical beam tilts and specimen tilts are the same except defocus and specimen thickness.

	Bulk ZnO	Bulk Pd
XCF [%]	91.792	92.583
Specimen Tilt *x* [°]	0.014	-0.008
Specimen Tilt *y* [°]	-0.012	0.011
Specimen Thickness [nm]	4.3	3.6
Defocus [nm]	-25.6	-19.7
Spherical Aberration [nm]	2.70	2.69
Beam Tilt *x* [°]	-0.012	0.035
Beam Tilt *y* [°]	0.002	0.031
Focus Spread [nm]	11.0	11.0
Beam Convergence [mrad]	0.35	0.35
Aperture Diameter [nm^{-1}]	23.2	20.5
Gaussian MTF-envelope (sigma_*x*) [nm]	0.020	0.024
Gaussian MTF-envelope (sigma_*y*) [nm]	0.040	0.040

The interface will be fully characterized by just analyzing in all details one flat region of the interface without any step. It was hard to analyze the local atomic structure in the DIA. Furthermore, the contrast on the simulated image for the ZnO (Fig. 6.30(a)) is not so simple for direct interpretation for the image. Therefore, quantitative analyses were performed for the interface area including the CIA. Quantitative analysis of the interface is described.

Step (i): Calculation of Imaging Parameters in Bulk (Perfect Crystals) Regions

Similarly as for the **Pd/$^{+}$ZnO** interface, the detailed analysis for **Pd/$^{-}$ZnO** interface was performed. First of all, the region of the interface enclosed by the white frame in Fig. 6.30(b) was defined. Best fitting parameters for bulk ZnO and Pd regions in the white frames in Fig. 6.31 were calculated by IDIM program package [Möbus, 1996]. The difference image was determined between calculated image and experimental image. The difference image possesses bright fringe (see Fig. 6.32). However, the XCF values for both bulk regions are high (92 ~ 93 %), indicating that the simulation reproduce the experimental images with high similarity.

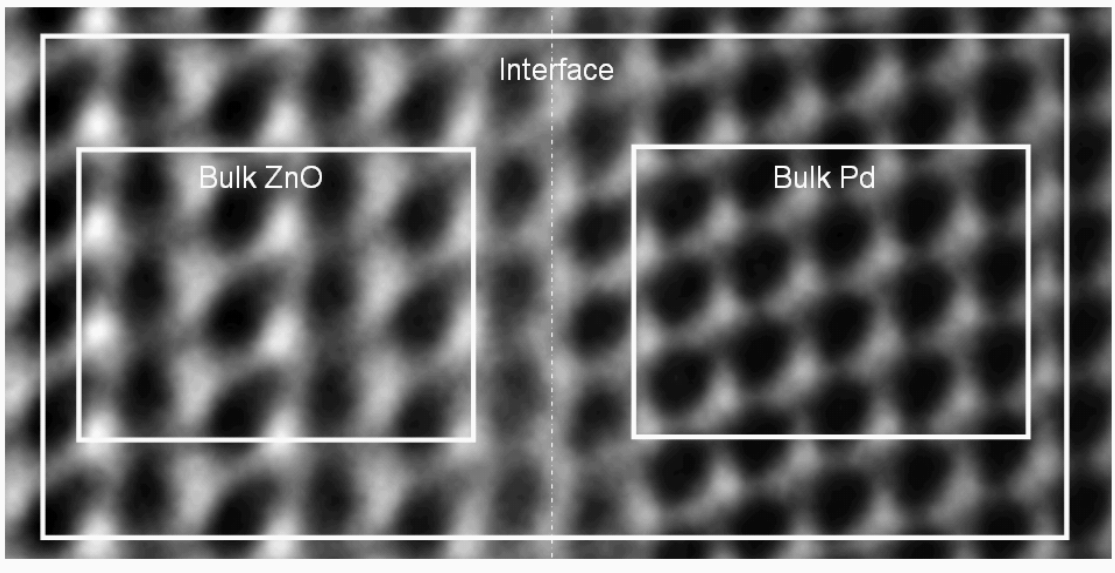

Fig. 6.31 Experimental image used for iterative image matching calculation for bulk regions and interface region (within white frames).

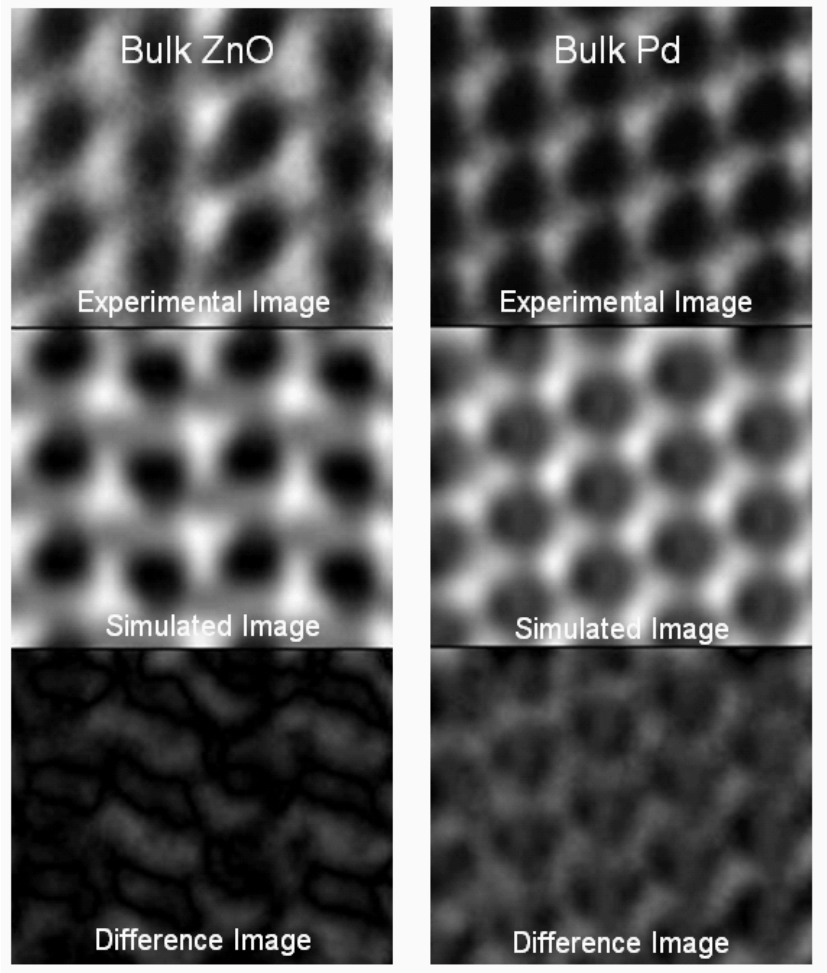

Fig. 6.32 Best calculated images for the bulk regions on the experimental image. The difference image possesses bright fringe (see Fig. 6.32). However, the XCF values for bulk regions are high.

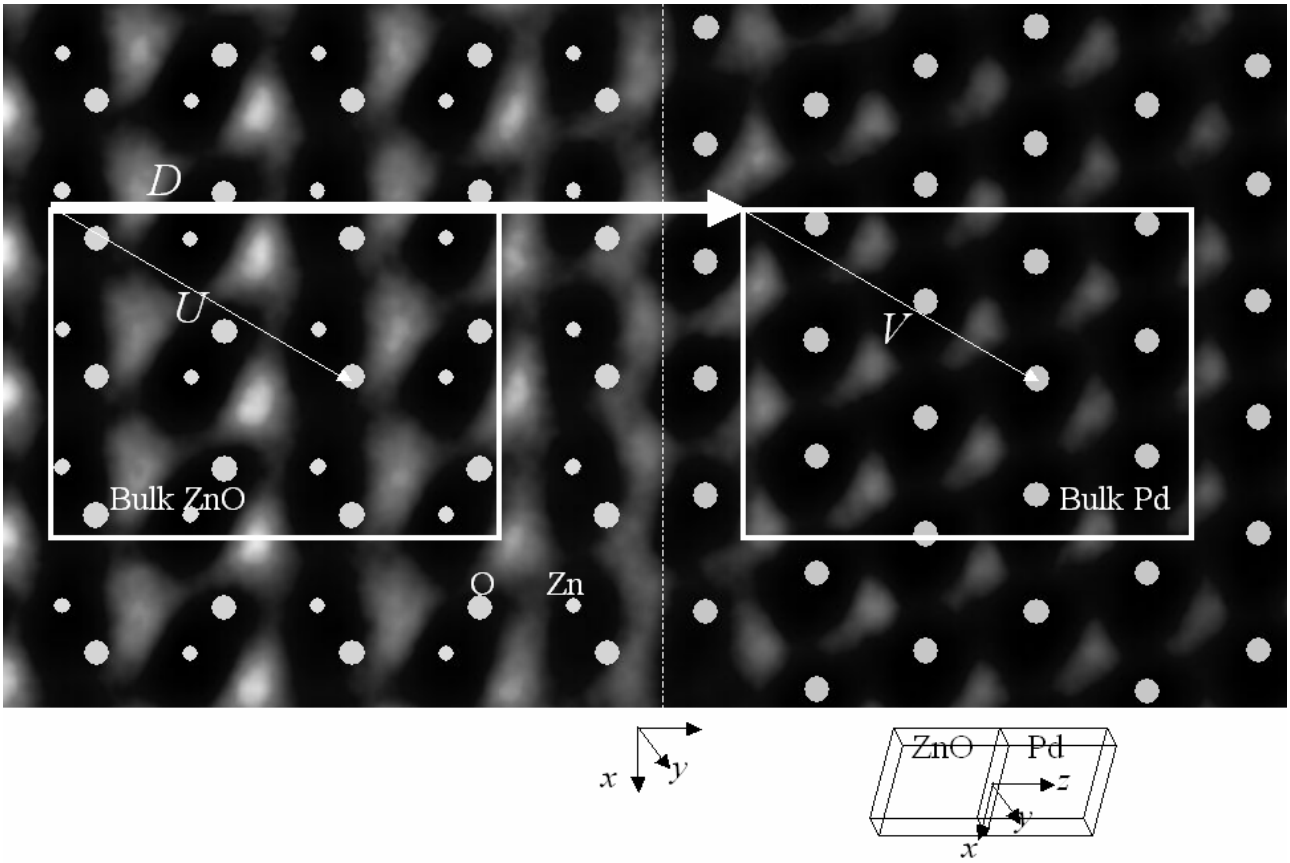

Fig. 6.33(a) The initial atomic structure model matches the experimental image in bulk regions except the interfacial layer. IDIM allows the determination of 2 components of the translation vector V , U between some atomic position and the origin of the defined area. Furthermore, the translation vectors V , U and the distance D between two defined areas were used for construction of the supercell for the simulation for the interface.

Table 6.11 shows that the best possible imaging parameters for both bulk ZnO and Pd regions are different from each other. However, most critical beam tilts and specimen tilts are the same except defocus and specimen thickness. Table 6.12 shows the best possible imaging parameters for the interface region.

Step (ii): Determination of Translation Vector between Pd and ZnO

Fig. 6.33 shows supercell constructed by the simulation for the bulk regions. Of course, the positions of all atomic columns remain unchanged (bulk crystals). This means that the positions of atomic columns near interface and the terminating atomic species in Fig. 6.33 are provisional at this point. It can be seen that the super cell in Fig. 6.33 gives almost appropriate fitting, by simple inspection, which the ZnO is O-terminated at the interface.

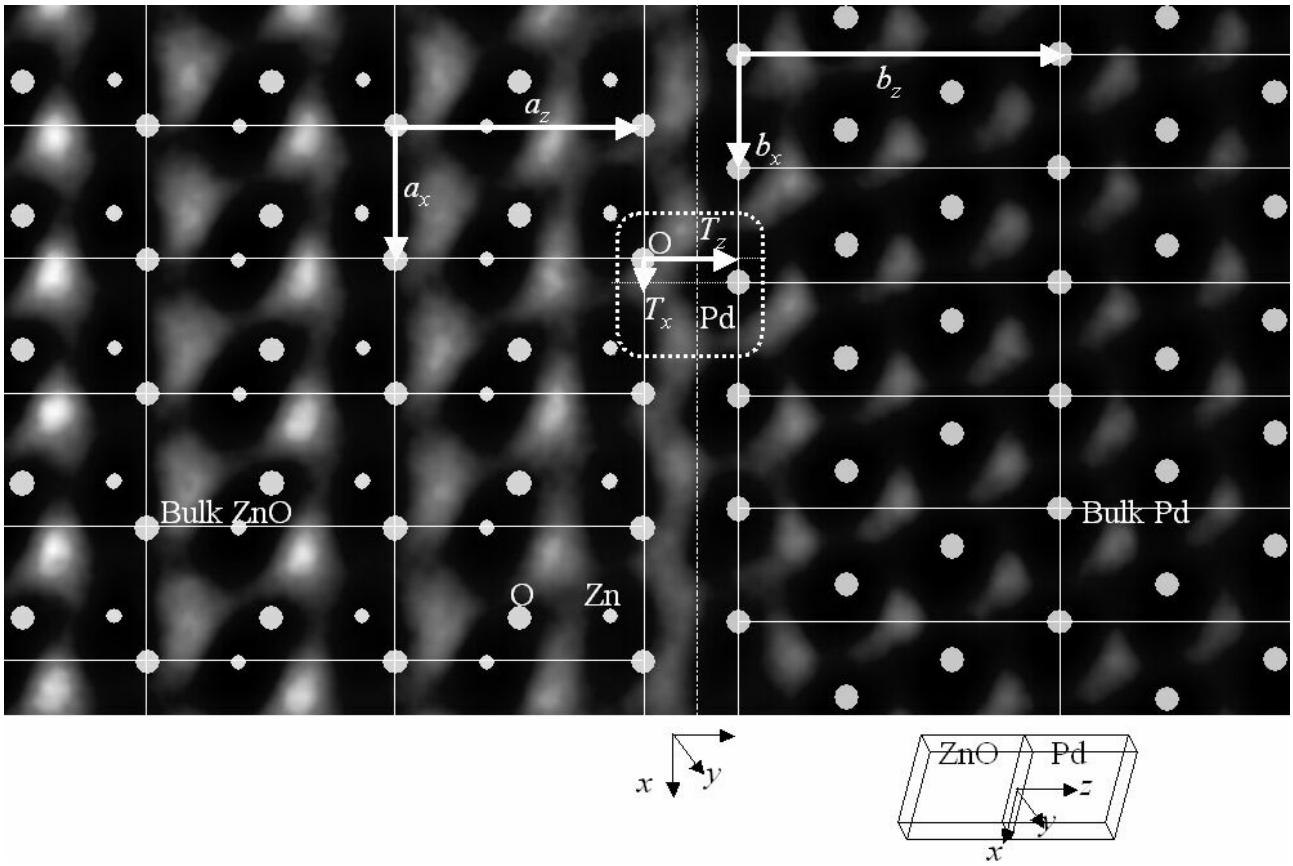

Fig. 6.14(b) The supercell allows the determination of the exact translation vectors T between atoms across the interface. Due to lattice mismatch, the translation vector T_x between the interfacial O and Pd atoms (nearest Pd atom for the O atom) should depend on the atom.

The translation vector is defined as (see Fig. 6.33)

$$\begin{aligned} T_z &= \left| D_z + (V_z + nb_z) - (U_z + ma_z) \right| \\ T_x &= \left| D_x + (V_x + nb_x) - (U_x + ma_x) \right| \end{aligned}, \tag{6-3}$$

where a and b are the basis vectors of ZnO and Pd, respectively, m and n are integer. From minimal value $T_{\min,z}$ of T_z, the interfacial distance between two crystals can be evaluated, because $T_{\min,z}$ does not depend on an atomic position at the interface. $T_{\min,x}$, which indicates the coherency between the lattices at the interface, depends on an atom at the interface. Therefore, the T_x should be defined for each atom at the interface.

Step (iii) Calculation of Best Imaging Parameters for the Region of the Interface

The final goal of the analysis is the determination of the best possible model for the interfacial atomic structure. Firstly, average best imaging parameters shared for both crystals should be determined. After that, the imaging parameters are optimized again by IDIM without relaxation of the atomic structure and optimization of atomic occupancy.

Table 6.12 Best possible imaging parameters for the interface.

	Interface
XCF [%]	85.6
Specimen Tilt *x* [°]	-0.004
Specimen Tilt *y* [°]	0.014
Specimen Thickness [nm]	5.2
Defocus [nm]	-28.2
Spherical Aberration [mm]	2.68
Beam Tilt *x* [°]	-0.012
Beam Tilt *y* [°]	0.027
Focus Spread [nm]	11.0
Beam Convergence [mrad]	0.35
Aperture Diameter [nm^{-1}]	23.3
Gaussian MTF-envelope (sigma_*x*) [nm]	0.020
Gaussian MTF-envelope (sigma_*y*) [nm]	0.040

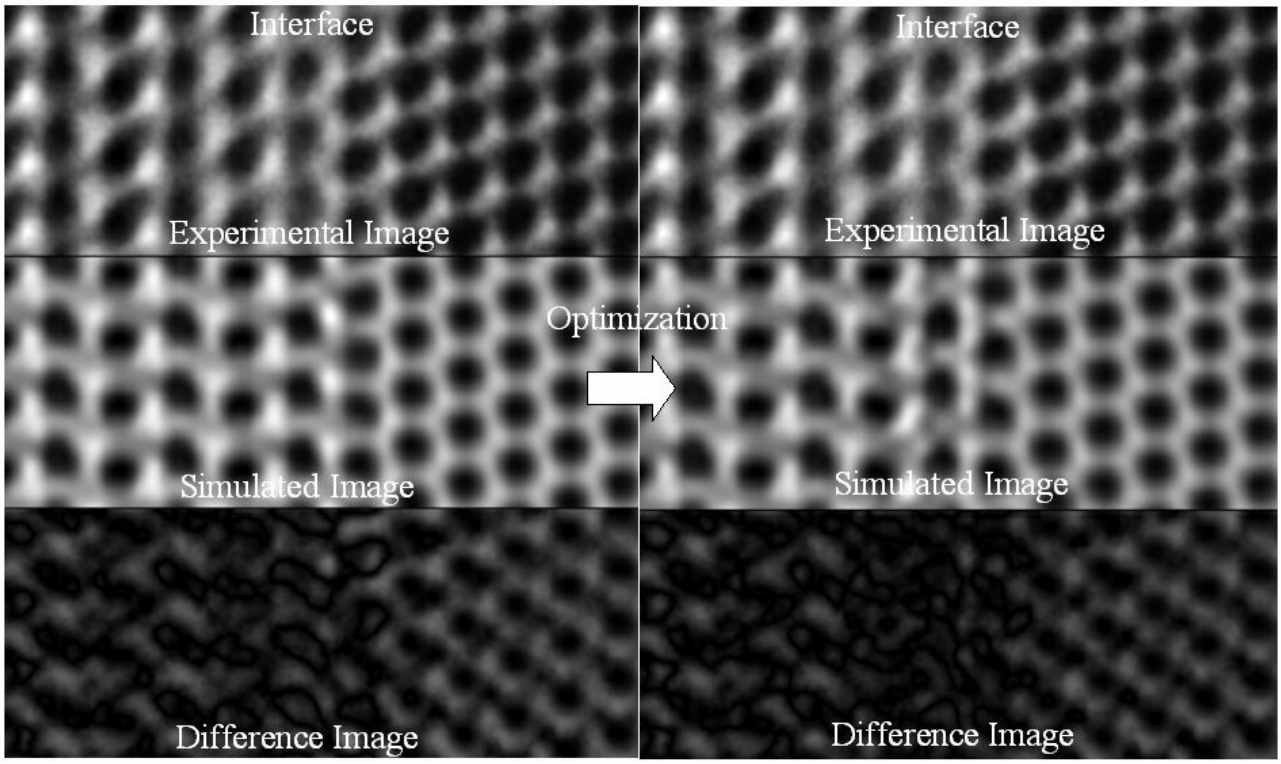

Fig. 6.34 The experimental image, the simulated image, and the difference image of the region close to the interface. The left simulated image was obtained without relaxing the interfacial local atomic structure. The right simulated image was obtained after the relaxation.

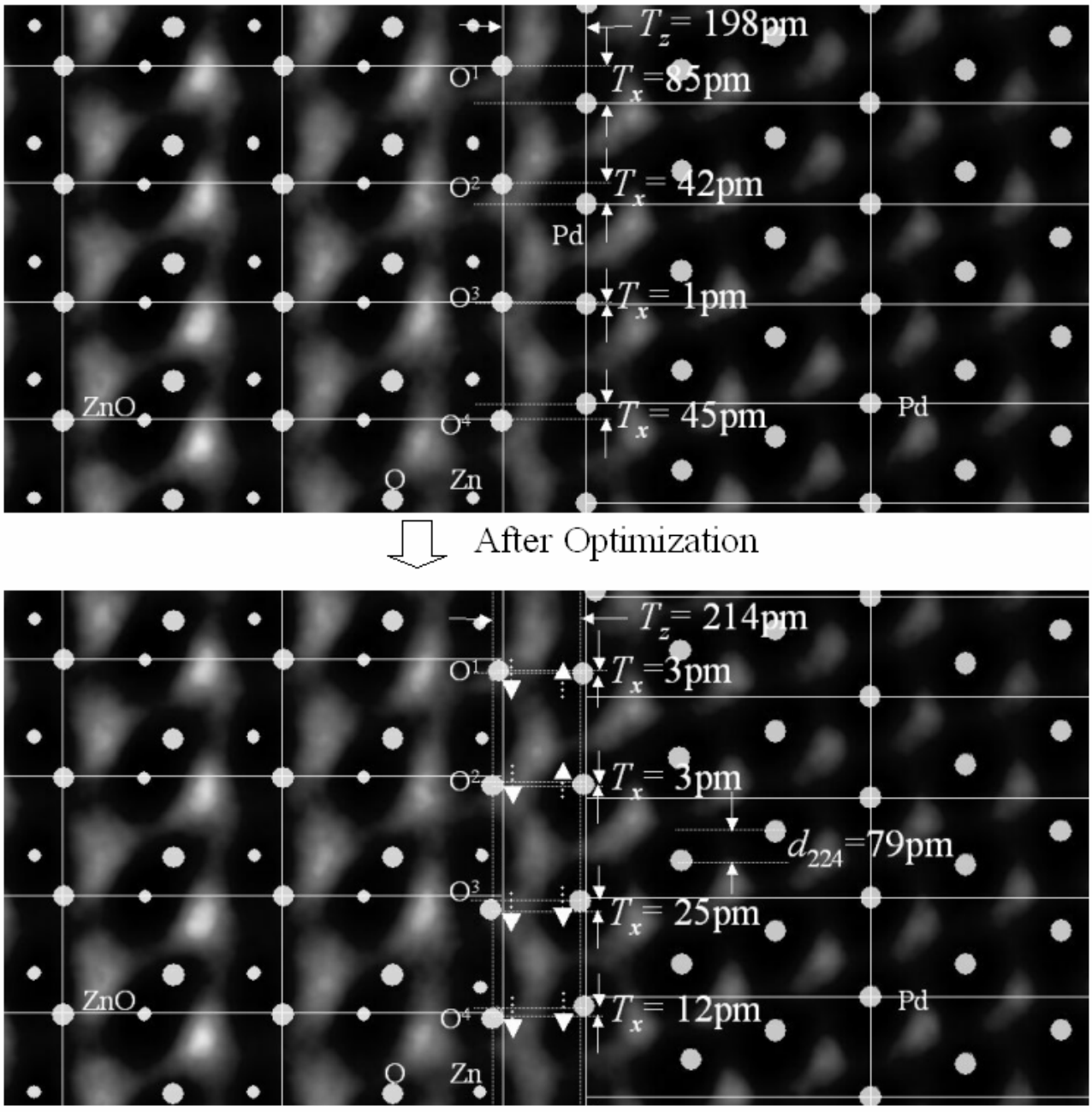

Fig. 6.35 Best fitting atomic model before / after relaxation by IDIM. Bottom image indicates the best possible atomic structure on the image after the optimization of the structure. It can be seen that each atomic center was slightly shifted from the initial positions near the interface as shown in the upper image. The bottom image also shows that the backbonds of the interfacial O atoms are strongly bent and the interfacial Pd atoms also are strongly shifted along the $[11\bar{2}]_{Pd}$ from bulk lattice sites The spacing between the interfacial O atoms is the same as that in bulk ZnO while the spacing between the interfacial Pd atoms is expanded to fit ZnO.

Step (iv): Quantitative Determination of Local Atomic Structure adjacent to Interface

The best local atomic structure of the interface were determined by allowing to relax only interfacial Pd and O atoms, and also the Zn atoms next to interfacial layer. The super cell (Fig. 6.33) was used as the initial structure model where the ZnO is terminated by O. Fig. 6.34 shows that the residual intensity near the interface on the difference image was reduced after the structural optimization. Fig. 6.35 (bottom) shows the best possible atomic structure on the image. It can be seen that individual atomic center adjacent to the interface was slightly shifted from the bulk lattice sites as shown in Fig. 6.35 (upper).

Fig. 6.35 (bottom) shows that the backbonds of the interfacial O atoms are strongly bent and that the interfacial Pd atoms also are strongly shifted along the interface. The spacings between the interfacial O atoms are the same as in bulk ZnO while the spacings between the interfacial Pd atoms are expanded in order to fit to the lattice of the ZnO.

Table 6.13 indicates the translation vectors of the positions of the interfacial O atoms for the nearest neighbouring interfacial Pd atoms. Before the optimization, the translation vectors $|T_x|$ of the interfacial O atoms were distributed within 1 ~ 85 pm due to the large lattice mismatch. After the optimization, the translation vectors $|T_x|$ of the interfacial O atoms were converged within 3 ~ 25 pm which are closer to 0 pm than $|b_x|/3$ (79 pm) (see Table 6.14) where the distance $|b_x|/3$ denotes the lattice spacings $d_{22\bar{4}}$ of Pd. This suggests that the interfacial O atoms fit on top of the Pd atoms on the interfacial layer.

Table 6.13 also shows that the interfacial distances between two crystals after the optimization is slightly increasing to 0.204 ~ 0.223 nm (average: 0.214 nm) from the initial values of 0.198 nm. The interfacial distance after the optimisation is narrower than the spacing $d_{\bar{1}\bar{1}\bar{1}}$ (0.225 nm) of Pd.

Table 6.15 shows that the interfacial layer of Pd moved to slightly outer side perpendicular to the interface from bulk position while the interfacial layer (O) of the ZnO moved to the inner part of the crystal and the second layer (Zn) of the ZnO moved away from bulk side.

Table 6.13 Translations of individual atom columns. The interfacial distances between two crystals after the optimization is slightly increasing to 0.204 ~ 0.223 nm (average: 0.214 nm) from the initial values of 0.198 nm. The interfacial distance after the optimisation is narrower than the spacing $d_{\bar{1}\bar{1}\bar{1}}$ (0.225 nm) of Pd.

Translation vector of the interfacial O atom for the interfacial Pd atom	$\|T_x\|$ [nm]	$\|T_z\|$ [nm]
O^1 before relaxation	0.085 ± 0.01	0.198 ± 0.01
O^1 after relaxation	0.003 ± 0.01	0.207 ± 0.01
O^2 before relaxation	0.042 ± 0.01	0.198 ± 0.01
O^2 after relaxation	0.003 ± 0.01	0.220 ± 0.01
O^3 before relaxation	0.001 ± 0.01	0.198 ± 0.01
O^3 after relaxation	0.025 ± 0.01	0.223 ± 0.01
O^4 before relaxation	0.045 ± 0.01	0.198 ± 0.01
O^4 after relaxation	0.012 ± 0.01	0.204 ± 0.01

Table 6.14 Basis vectors of ZnO and Pd. The distance $|b_x|/3$ denotes the lattice spacings $d_{22\bar{4}}$ of Pd.

$\|a_x\|$ [nm]	$\|a_z\|$ [nm]	$\|b_x\|$ [nm]	$\|b_z\|$ [nm]	$\|b_x\|/3$ [nm]
0.281	0.513	0.238	0.674	0.079

Table 6.15 Changes of the (average) lattice spacings compared to bulk. Rates [%] are based on the basis vectors along the interface normal. The interfacial layer of Pd moved to slightly outer side perpendicular to the interface from bulk position while the interfacial layer (O) of the ZnO moved to the inner part of the crystal and the second layer (Zn) of the ZnO moved away from bulk side.

1st Pd atom	+1.6 ± 0.04 % (average)
1st O atom	-5.1 ± 0.02 % (average)
2nd Zn atom	+1.9 ± 0.02 % (average)

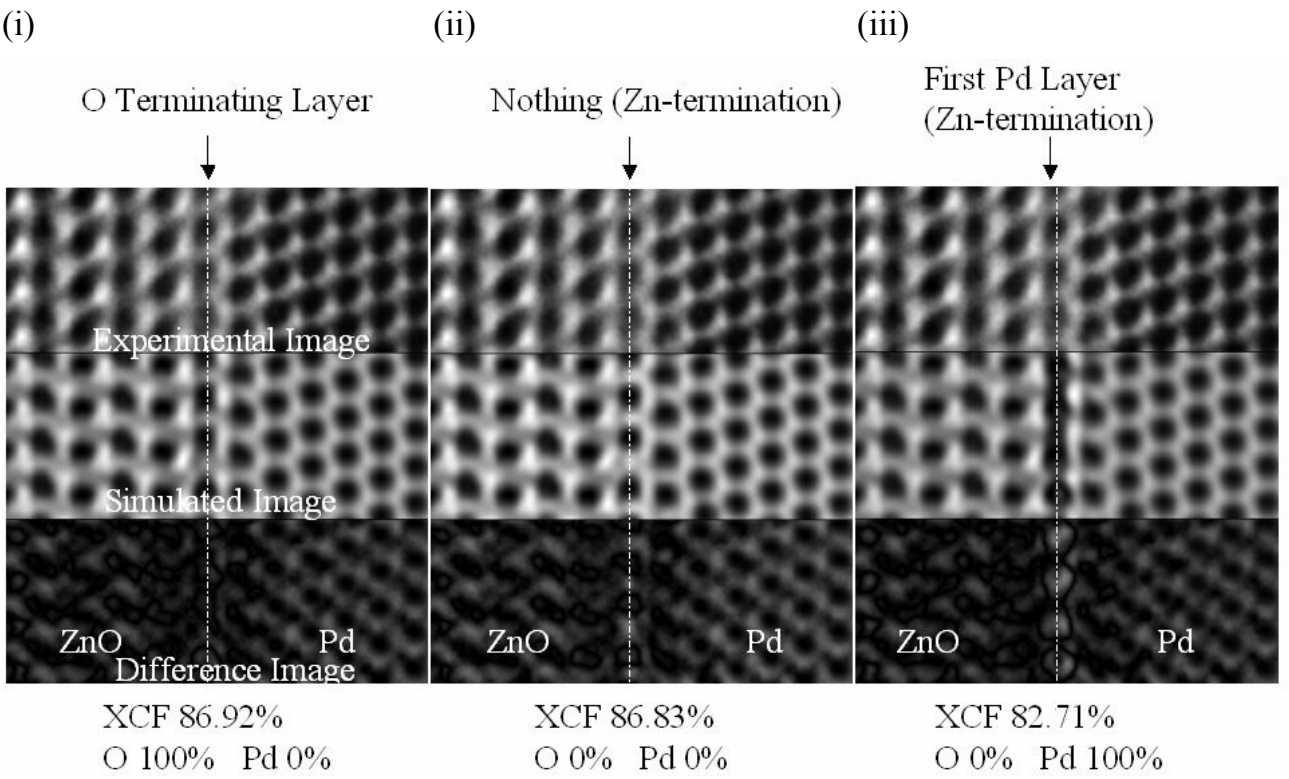

Fig. 6.36 Atomic occupancy and atomic species were exchanged in the interfacial layer on the dotted lines which was provisionally assumed as O-terminating layer. XCF value and difference image between computed image and experimental image are shown for (i) O: 100 % (O-termination), (ii) O: 0 % Pd: 0 % (Zn-termination), and (iii) Pd: 100 % (Zn-termination).

Step (v): Determinations of Interfacial Terminating Atomic Species and their Occupancies

A quantitative evaluation showed that the used atomic structure model represents a good approximation. So far it has been assumed that the terminating atomic species at the **Pd/ZnO** interface were O ions with an atomic occupancy of 100 % (i.e. each ion site along each atomic column is occupied with an O ion.). With respect to perfect simulation, this assumption has to be justified by simulations for partial occupancy and comparing these calculated results with experimental observations. For the provisional final O layer on the dotted line (Fig. 6.36), the following three possibilities can be considered. (i) The O layer includes only O, (ii) no Pd or O atom is included in this layer, indicating Zn-termination, and (iii) all the O atoms are completely replaced by Pd atoms, indicating Zn-termination. For those three cases, images were simulated and then compared to the experimental image as shown in Fig. 6.36.

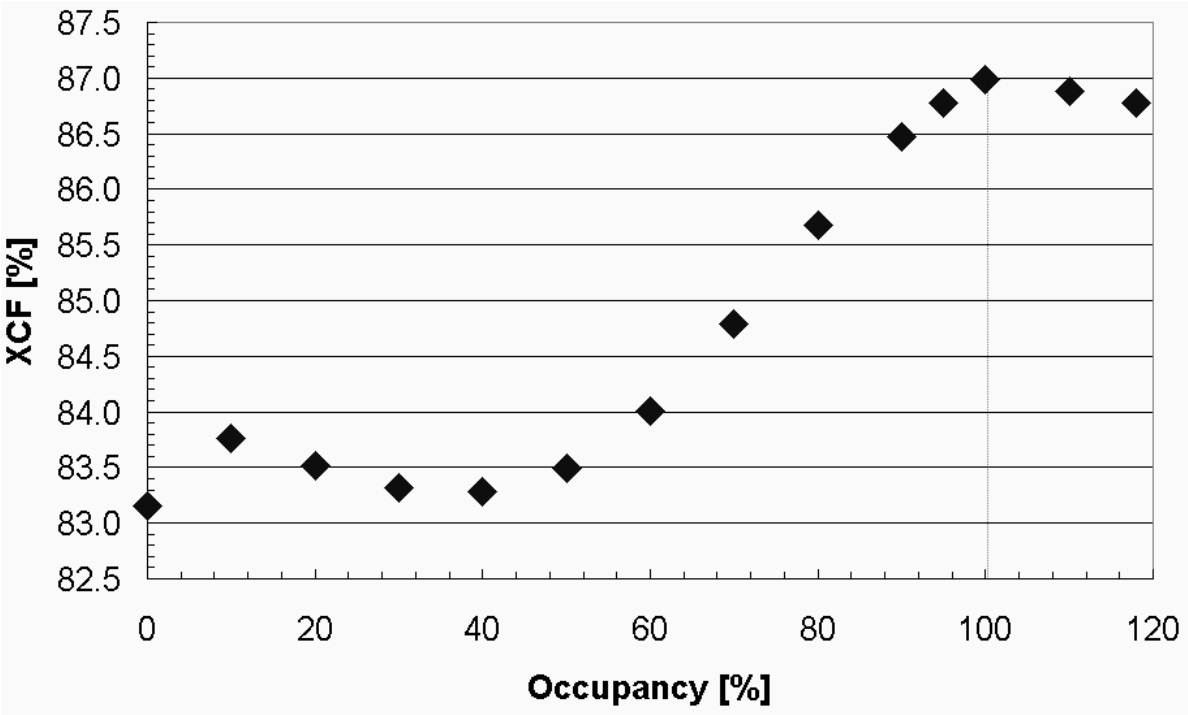

Fig. 6.37 XCF value as a function of interfacial atomic occupancy. When the occupancy of O is *x* %, the occupancy of Pd should be (1-*x*) %. Although the atomic occupancy above 100 % is unrealistic, it was included as references because it is technically possible to calculate it. When the occupancy of O is above 100 %, the XCF was calculated by fixing the occupancy of Pd at 0 %.

Fig. 6.36 shows experimental image, simulated image, and difference image. It also includes XCF values for each case. It can clearly be seen that the investigated columns have white spots on the difference image in the case (iii) [O: 0 %, Pd: 100 %] which corresponds to a rather comparatively low XCF, indicating that this model is unlikely. For the case (i) and (ii) the bright white dots appear on the difference images. However, it results in rather high XCF values. Since the XCF are quite similar, it is difficult to distinguish between the two cases. It can be also considered that the observation is caused by a mixture of O atoms and small amount of Pd atoms.

The calculation of the occupancies is possible by modifying atomic occupancies and putting both Pd and Zn atom at the same coordinates on the input file for EMS program.

Fig. 6.37 shows the XCF value as a function of atomic occupancy. It can be seen that the XCF value increases with increasing the occupancy of O. Best results can be obtained for O: 100 % and Pd: 0 %. Therefore, it can be concluded that the **Pd/¯ZnO** interface is terminated by O with occupancy of 100 %.

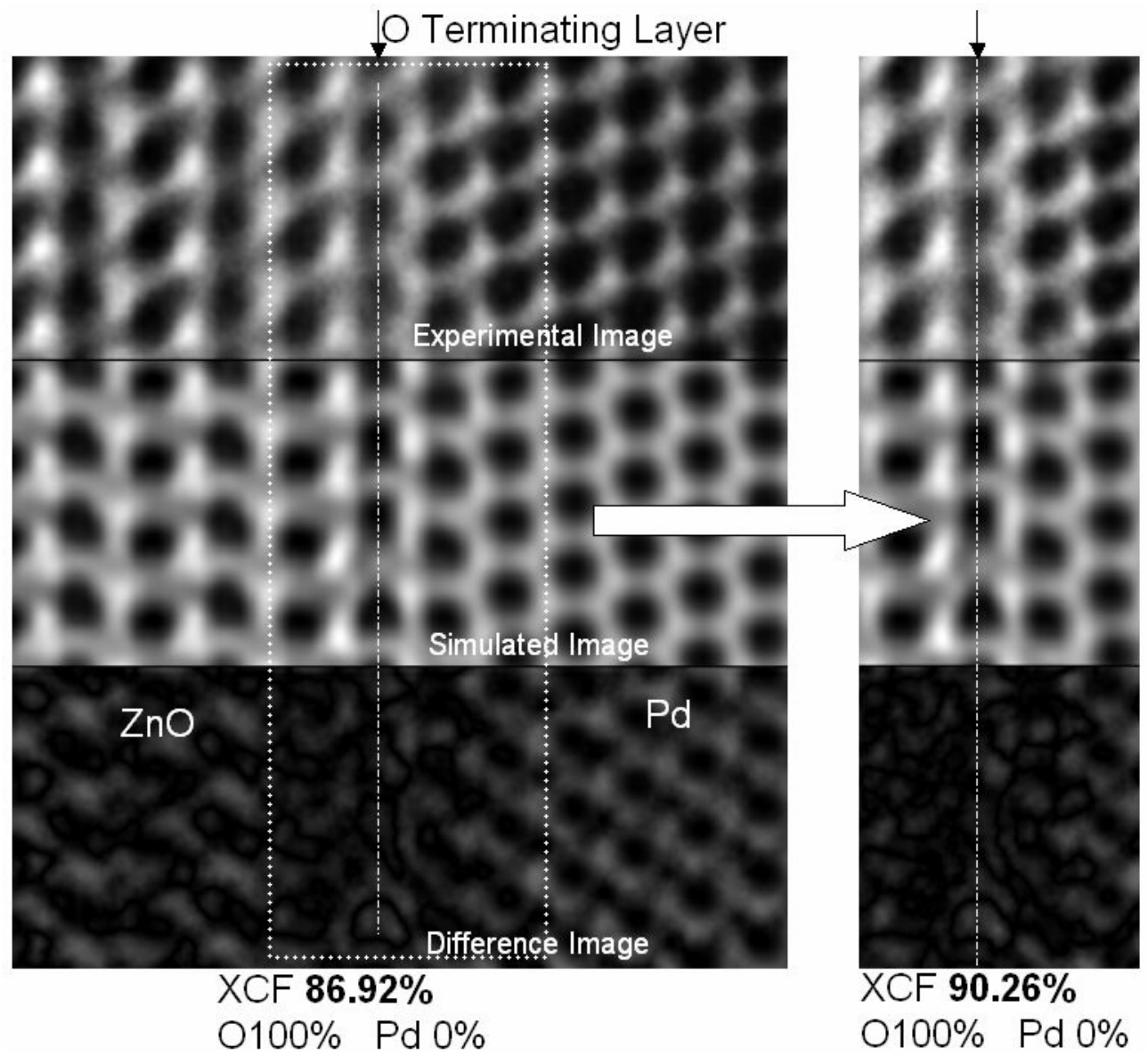

Fig. 6.38 The XCF value and the difference image calculated only within the interfacial layer. The difference image (i) in Fig. 6.36 showed that the only interface region does not possess white dot (higher intensity spot), suggesting that the interface region could be reproduced more precisely.

Fig. 6.37 showed the highest XCF value of 86.92 % obtained for the case (i) [O: 100 % and Pd: 0 %]. The difference image (i) in Fig. 6.36 showed that the only interface region does not possess white dot (higher intensity spot), suggesting that the interface region could be reproduced more precisely. The XCF value within only interfacial layer were calculated again as shown in Fig. 6.38. It can be seen that XCF values was largely increased to 90.26 %, indicating that the obtained interfacial model is quite valid.

(B) Pd/$^{-O}$ZnO Interface ($[1\bar{1}00]_{ZnO}//[11\bar{2}]_{Pd}$)

Determination of Local 3-Dimensional Interfacial Atomic Structure

The interface was investigated also for a second zone axes which are parallel to the $[1\bar{1}00]_{ZnO}//[11\bar{2}]_{Pd}$ zone axes and which are perpendicular to the first zone axes. For the second zone axes, the projected lattice spacings for Pd and ZnO are even smaller than that for the first zone axes.

Fig. 6.39 and 6.40 represent a HRTEM image of the region close to the **Pd/$^{-O}$ZnO** interface taken along $[1\bar{1}00]_{ZnO}//[11\bar{2}]_{Pd}$ zone axes at the defocus condition (*df* = -30 nm). Pd and ZnO can be easily distinguished. An atomically flat interface and no strain field in ZnO bulk region near the can be seen. Lattice distortion analysis was performed for the region of Pd crystal by LADIA (LAtice DIstortion Analysis) program package [Du, 2001], in order to know a strain field caused by the relaxation of the interfacial Pd atoms which was checked in the subsection 6.1.4(A). Fig. 6.40(b) shows contour map of strain detected from the image (a) of the Pd region. Compressive stress indicates low (black) intensity. Tensile stress indicates high (white) intensity. Periodic strain fields in bulk Pd region can be seen. Pd layer relaxes within the 1st to about nearly 6th Pd layer (see Fig. 6.40(b)). This result supports that the Pd crystal relaxes at the **Pd/$^{-O}$ZnO** interface which is the obtained result in the subsection 6.1.3(A).

The determination of the 3-dimensional atomic structure requires only the analysis of the translation vector T_y (see Fig. 6.44), because, in the CIA at the interface, the translation vectors T_x and T_z (see Fig. 6.35) were already determined in subsection 6.1.4(A). Furthermore, the investigations described in subsection 6.1.4(A) revealed that the interface is O-termination and also its atomic occupancy of 100 %. The interfacial distance $T_{\min,z}$ should be identical to the $[1\bar{1}00]_{ZnO}//[11\bar{2}]_{Pd}$ zone axes.

Fig. 6.41 shows the same HRTEM images with supporting lines which connect between contrast centers of the adjacent bulk regions. Interfacial O atoms are located at the O^- sites of the perfect ZnO crystal, indicating no relaxation of the ZnO.

Pd columns with the clearly resolved white dots (vacuum columns) within the regions encircled in Fig. 6.41 indicate that the Pd atoms can be clearly resolved within the ellipses.

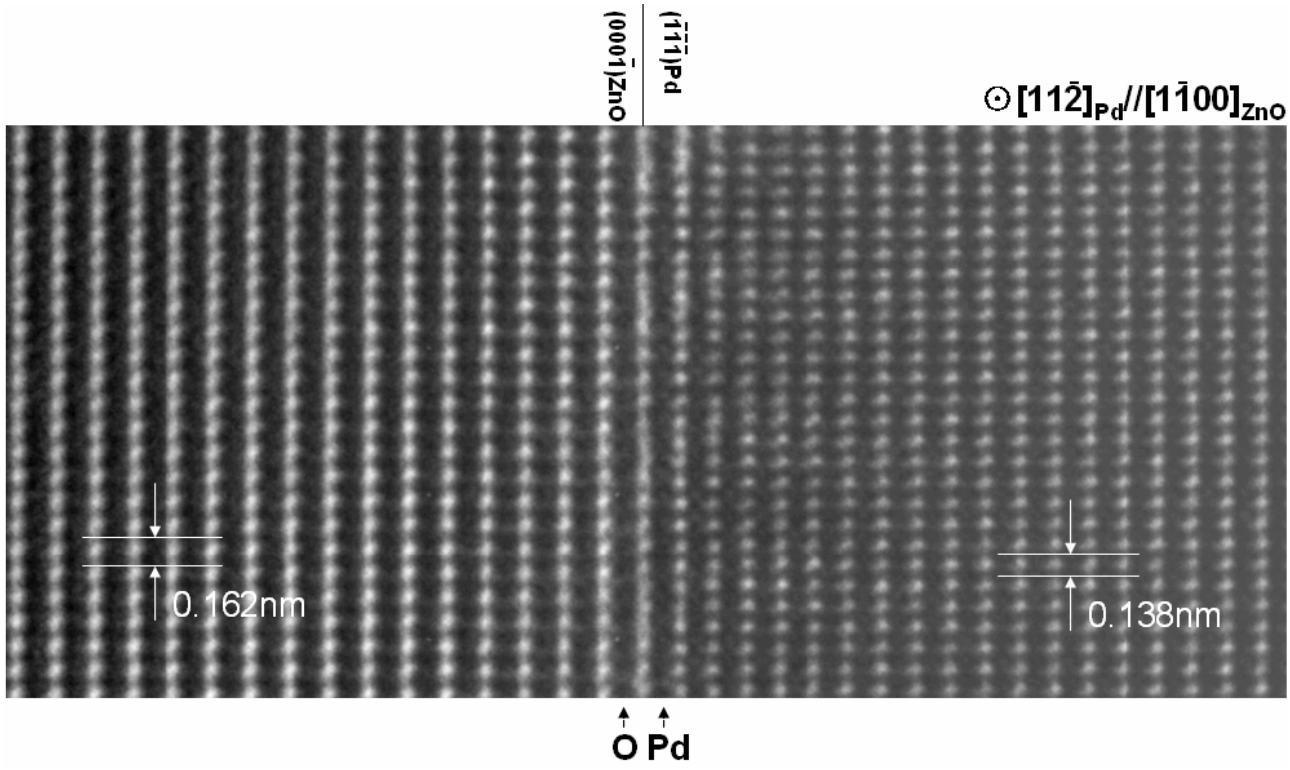

Fig. 6.39 HRTEM image of the region close to the **Pd/$^{-O}$ZnO** interface taken along $[1\bar{1}00]_{ZnO}//[11\bar{2}]_{Pd}$ zone axes at a defocus condition (*df* = -30 nm). The terminating atomic species was determined in subsection 6.1.4 (A). An atomically flat interface and no strain field in ZnO bulk region can be seen. However, weak periodic strain fields in bulk Pd region can be seen.

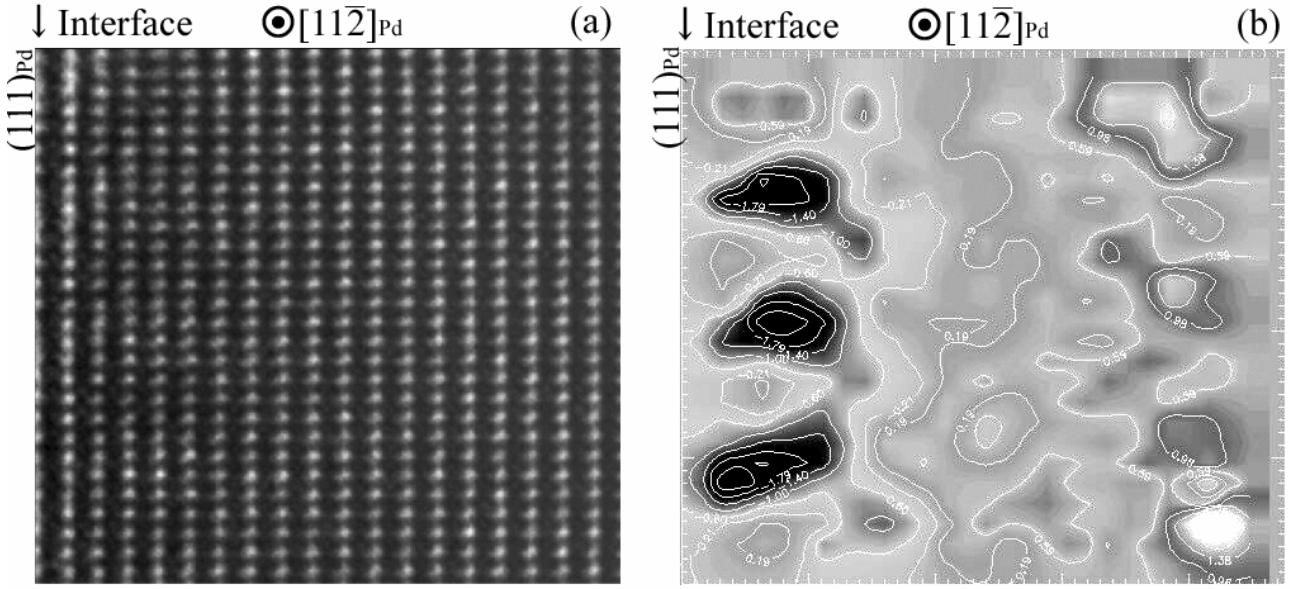

Fig. 6.40 (a) HRTEM image of Pd region (Pd region in Fig. 6.39) near the **Pd/$^{-O}$ZnO** interface. (b) Contour map of strain detected from the image (a) by LADIA (LAttice DIstortion Analysis) [Du, 2001]. Low (black) intensity indicates compressive stress. High (white) intensity indicates tensile stress. Periodical strain field can be seen. Compressive stress periodically exists on the DIA. In the periodic arrangement parallel to the interface, the periodicity is nearly 1 nm along the interface.

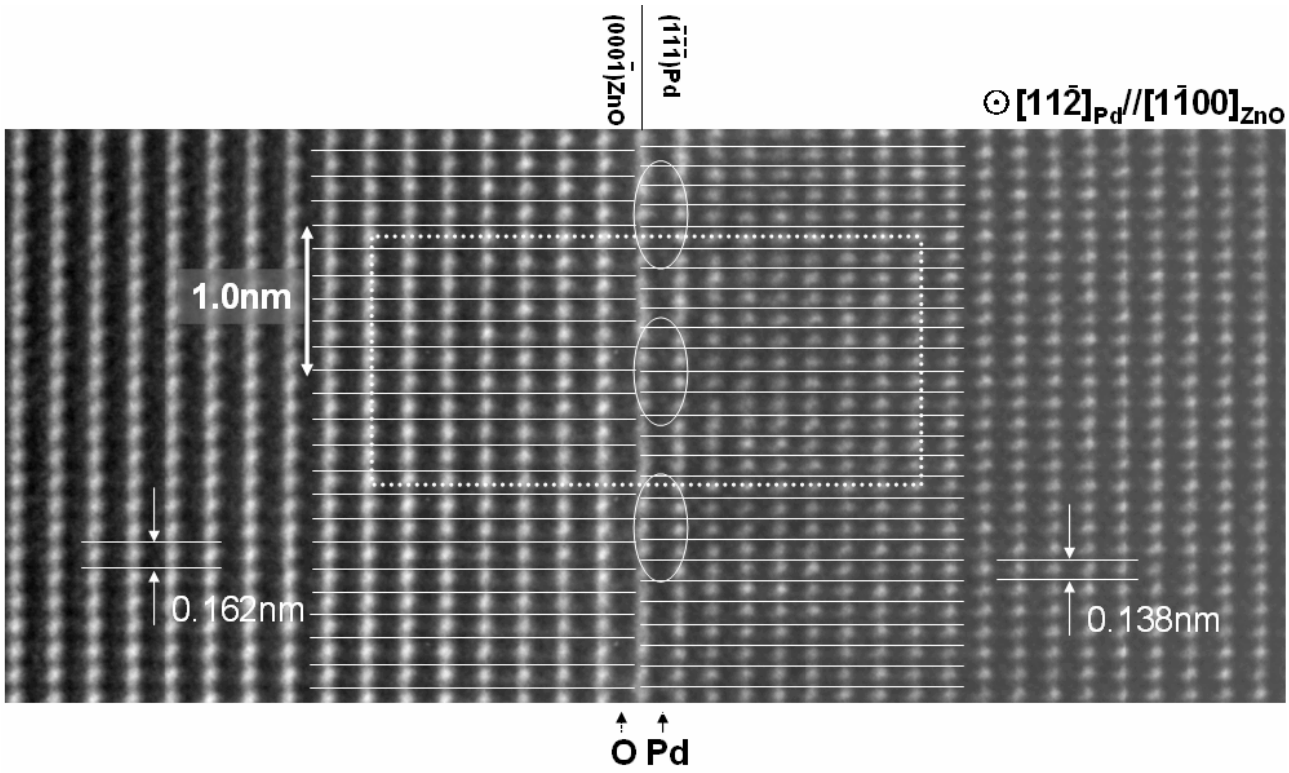

Fig. 6.41 HRTEM image of the **Pd/$^{-O}$ZnO** interface shows a relaxation of the interfacial Pd columns. In the periodic arrangement parallel to the interface, the periodicity is nearly 1 nm along the interface.

Other columns of Pd at the interface outside the ellipses do not have the clearly separated white dots (vacuum columns) around the Pd columns. This indicates that the Pd atoms at the interface outside the ellipses cannot be clearly resolved Therefore, the interfacial Pd layer has both CIA and DIC. Fig. 6.40(a) and (b) show also that compressive stress periodically exists on the DIA. In the periodic arrangement parallel to the interface, the periodicity is nearly 1 nm along the interface. This periodicity corresponds to a lattice mismatch of 18 % between Pd and ZnO. The interface was analyzed in detail in the following four steps.

Step (i): Calculation of Imaging Parameters in Bulk (Perfect Crystals) Regions

Table 6.16 summarized the best fitting imaging parameters for bulk ZnO and Pd within the white frames in Fig. 6.42. Individual fitting parameters of Pd are quite different from that of ZnO. However, the XCF values for both bulk regions are high, indicating that the parameters must reproduce the experimental image. Best fitting calculated images and the difference images are shown in Fig. 6.43.

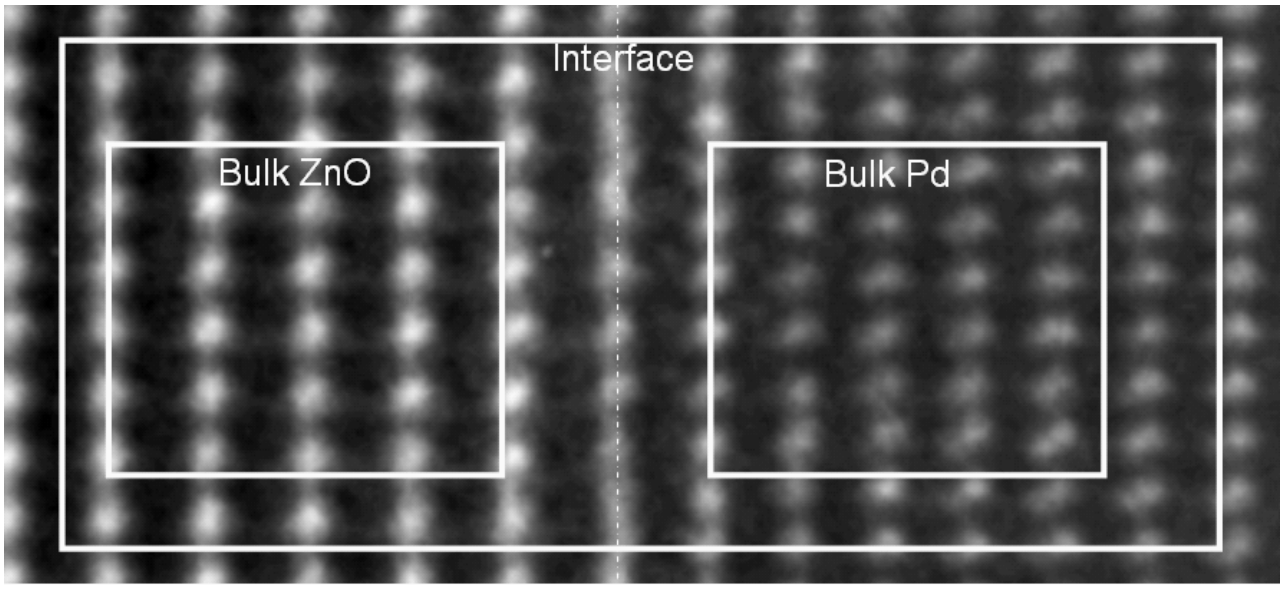

Fig. 6.42 Selected experimental images used for calculation of the best fitting imaging parameters for bulk ZnO and Pd within the white frames.

Table 6.16 Best imaging parameters for experimental images. Individual fitting parameters of Pd are quite different from that of ZnO. However, the XCF values for both bulk regions are high.

	Bulk ZnO	Bulk Pd
XCF [%]	91.104	90.964
Specimen Tilt *x* [°]	0.003	-0.001
Specimen Tilt *y* [°]	0.012	0.016
Specimen Thickness [nm]	3.7	2.9
Defocus [nm]	-24.8	-17.2
Spherical Aberration [nm]	2.65	2.68
Beam Tilt *x* [°]	0.003	-0.007
Beam Tilt *y* [°]	0.011	0.002
Focus Spread [nm]	9.5	9.4
Beam Convergence [mrad]	0.31	0.28
Aperture Diameter [nm^{-1}]	22.4	17.6
Gaussian MTF-envelope (sigma_*x*) [nm]	0.0296	0.0238
Gaussian MTF-envelope (sigma_*y*) [nm]	0.0292	0.0288

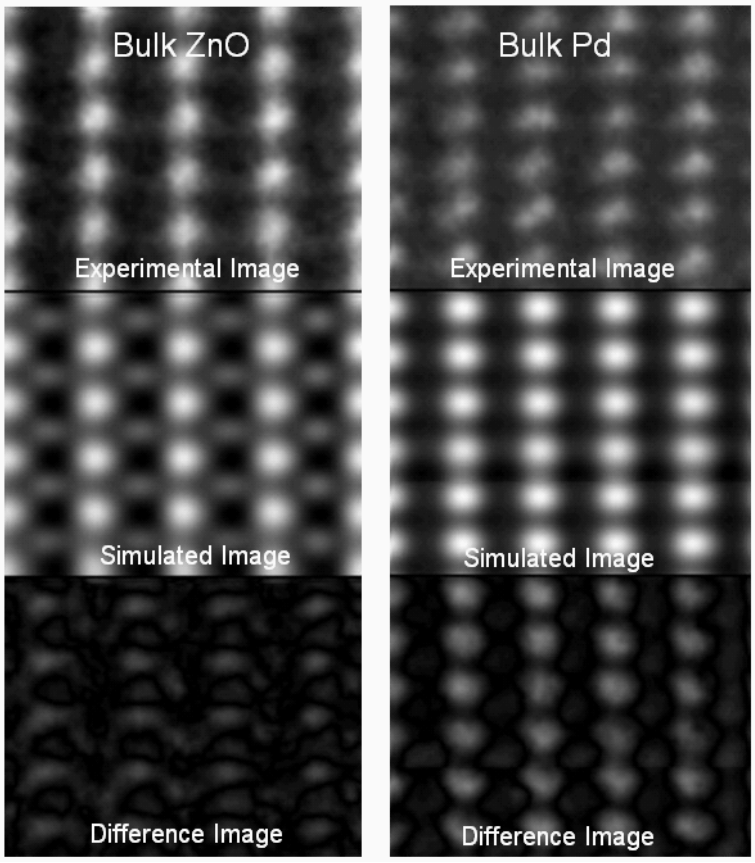

Fig. 6.43 Best calculated images of both bulk regions on experimental image.

Table 6.17 Translation vectors of the interfacial O atoms for the interfacial Pd atoms.

Translation vector of the interfacial O atom for the interfacial Pd atom	$\lvert T_y \rvert$ [nm]
O^1	0.025 ± 0.01
O^2	0.000 ± 0.01
O^3	0.025 ± 0.01

Table 6.18 Basis vectors of ZnO and Pd

$\lvert a_y \rvert$ [nm]	$\lvert a_z \rvert$ [nm]	$\lvert b_y \rvert$ [nm]	$\lvert b_z \rvert$ [nm]
0.163	0.260	0.138	0.224

Step (ii): Determination of Translation Vector between Pd and ZnO

The translation vector can be defined as (see Fig. 6.44)

$$T_y = \left| D_y + (V_y + nb_y) - (U_y + ma_y) \right|, \tag{6-4}$$

where a and b are basis vectors of ZnO and Pd respectively, and m and n are integer. Fig. 6.44 shows a supercell constructed by the calculations for bulk regions. All atomic positions are fixed at the lattice sites in the bulk. This means that the center positions of atomic columns near the interface in Fig. 6.44 are provisional and do not match on the contrast. The supercell was constructed based on the model of an O-termination of ZnO (see subsection 6.1.4(A)).

Step (iii): Analysis of Interfacial Local Atomic Structure

The local atomic structure of the interface was examined allowing relaxing atomic structure of Pd and ZnO near the **Pd/$^{-O}$ZnO** interface. However, we could not determine quantitatively the local atomic structure in the second zone axes due to technical reason of calculation. Extremely small lattice spacings did not allow determining the local atomic structure. Furthermore, Step (iv), determination of atomic occupancy, could not be done similarly for the **Pd/$^{+Zn}$ZnO** interface.

Fortunately, the initial atomic model before the optimization in Fig. 6.44 results in a good match with the contrast of atomic columns by simple inspection. The translation vectors T_y can only be precisely determined by qualitative analysis similarly for the **Pd/$^{+Zn}$ZnO** interface.

Fig 6.45 (a) and (c) shows that the best possible simulated images and the atomic structure models used for the simulations of bulk ZnO and Pd, respectively. The translation vector T_y can be easily determined by simple inspection, because, along the y axis, the atomic positions agree well in simulation with the contrast centers in Fig. 6.45(a) and (c). The translation vectors T_y were determined by starting with the initial supercell (Fig. 6.44).

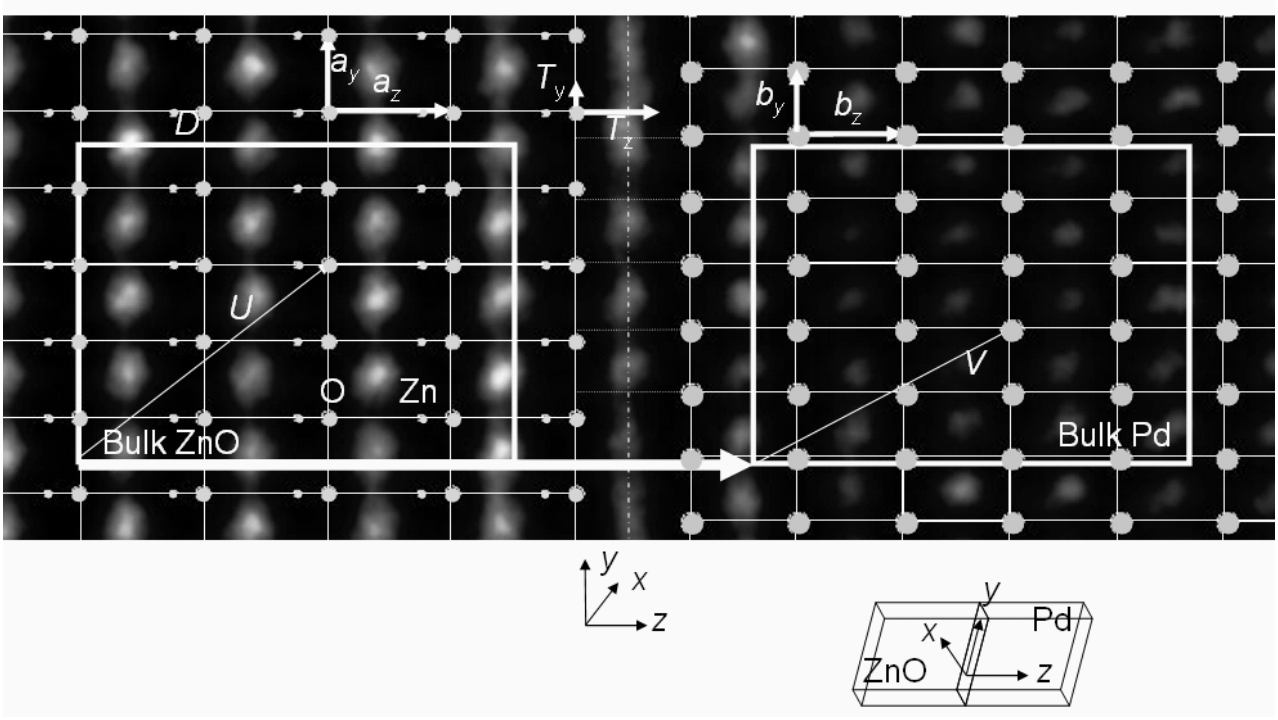

Fig. 6.44 Atomic structure model without relaxation. Each atomic position is valid in only the defined bulk regions. IDIM allows the determination of 2 components of the translation vectors V, U between some atomic position and the origin of the defined area. Furthermore, the translation vectors V, U and the distance D between two defined areas were used for construction of the supercell for the simulation for the interface. The supercell allows the determination of the exact translation vectors T between atoms across the interface.

We must notice that white dots (shown by arrows in Fig. 6.45(b)) correspond to vacuum columns. It can be seen that a part of the vacuum columns neighboring to the 1st Pd layer is not clearly resolved, indicating that a part of Pd columns in the 1st Pd layer cannot be clearly resolved. Near the solid dotted line across the interface in Fig. 6.45, both lattices have coherency. Table 6.17 showed that the translation vectors T_y of O atoms near the solid dotted line in Fig. 6.45(b) are extremely small (0 ~ 25 pm), indicating that the positions of the Pd atoms fit top on the interfacial O. However, other Pd atoms at the interface do not fit the ZnO lattice due to the mismatch as shown in Fig. 6.45(b).

Therefore, it can be concluded that the most stable 3-D local atomic structure is that Pd sits on top of O of ZnO as shown in Fig. 6.46. Furthermore, only Pd layer is relaxed in the **Pd/$^{-O}$ZnO** interface.

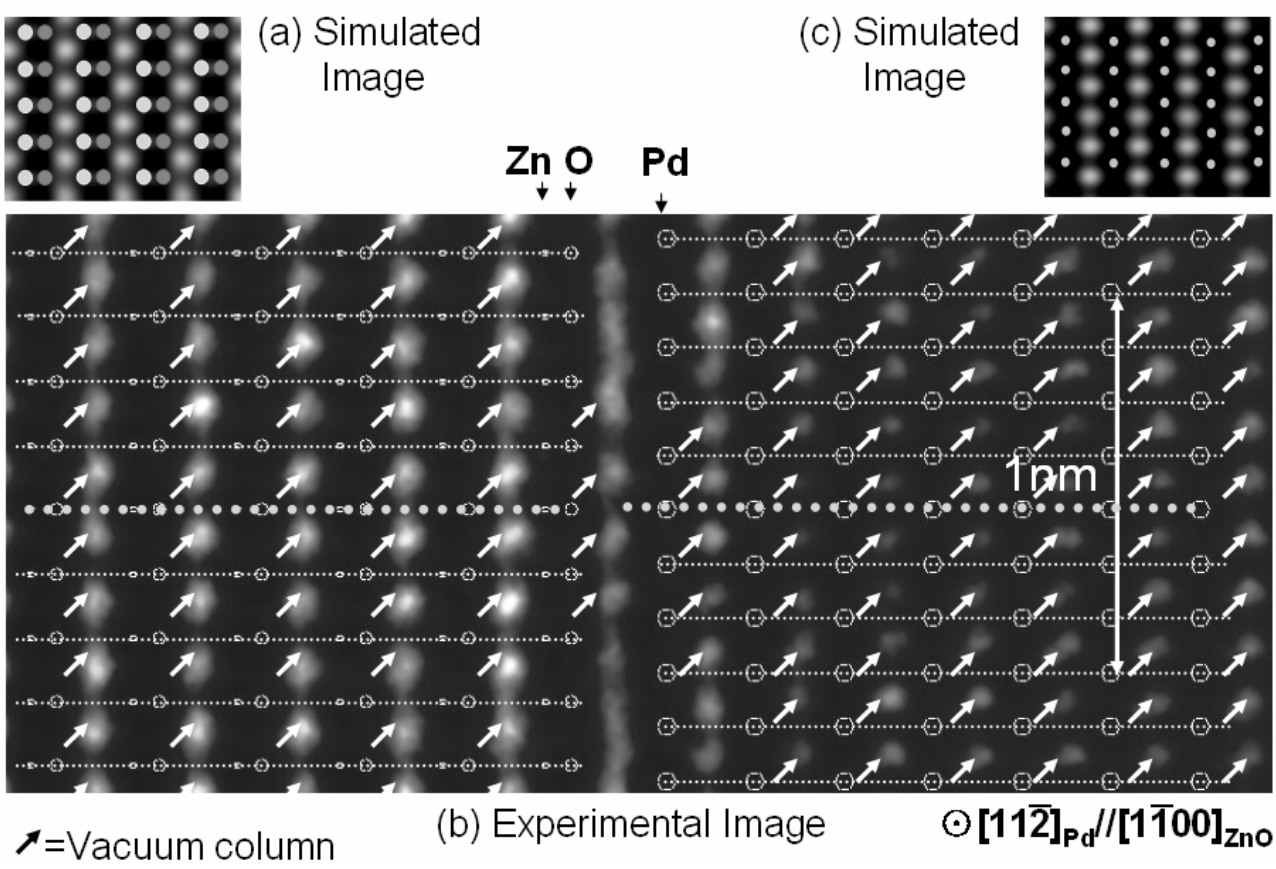

Fig. 6.45 Atomic structure model before relaxation. The white dots (of vacuum columns) neighboring the 1st Pd layer can be clearly resolved only near the solid dotted line, indicating that a part of the interfacial Pd atoms is relaxed in order to fit the ZnO lattice as shown near the dotted line.

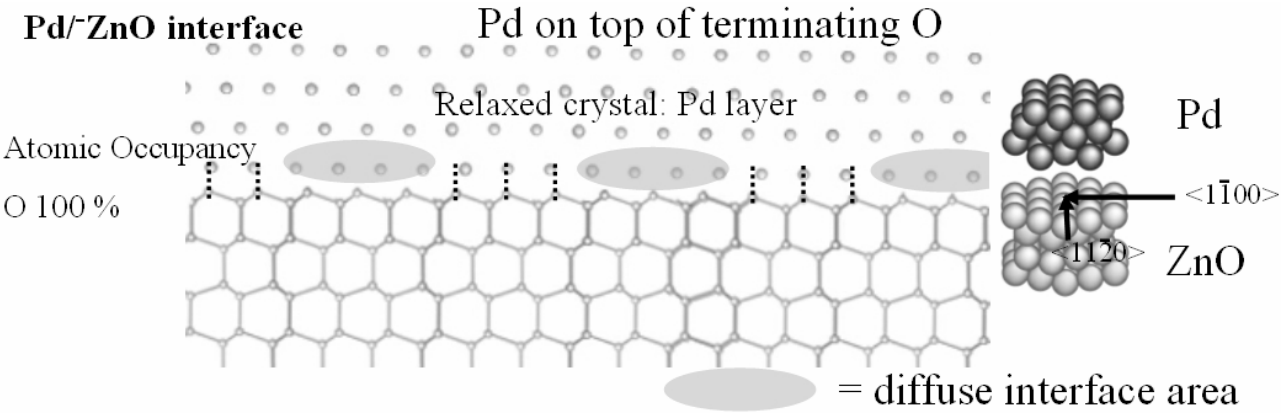

Fig. 6.46 The most stable 3-D local atomic structure is that Pd sits on top of O of ZnO. At the interface, Pd crystal is relaxed to fit ZnO lattice due to the large lattice mismatch of 18 %. When the mismatch is small, the stable local structure without relaxation can be expected as shown in this figure. The cross-sectional figures are along the $[\bar{1}\,\bar{1}\,20]_{ZnO}$ axis or the $[1\,\bar{1}\,00]_{ZnO}$ axis.

6.1.5 Interfacial ELNES

Electron Energy Loss Spectra (EELS) and electron Energy Loss Near Edge Structures (ELNES) were investigated for the different interfacial regions. It is expected that the investigations allow an examination of the interfacial specific electronic structure. Furthermore, the EELS/ELNES studies will be critical checks of results obtained by QHRTEM.

The O-K edge, the Zn-L edge, and the Pd-M edge ELNES at both the **Pd/$^{+Zn}$ZnO** interface and the **Pd/$^{-O}$ZnO** interface were analyzed. The interfaces were aligned edge on with respect to the incoming e-beam. Then, the zone axis was slightly inclined from the incident direction around the normal of the interface in order to avoid channeling effects. The scanning area was fixed to 4×3 nm^2 for all measurements. Each measurement was performed 3 times for 10 seconds for Pd bulk region, ZnO bulk region, and the interface-containing region. The data were automatically averaged. For the measurement including the interface region, the center of the scanning area has to be adjusted at the interface (see Fig. 3.9). Since only effective loss spectra should be evaluated, back grounds caused by other absorption edges or by the zero loss peak were extracted by special software processed by Gatan. Furthermore, interfacial specific ELNES (see section 3.5) could be extracted by the spatial difference technique [Scheu, 2002]. The scaling factors in the spatial difference technique were elaborated by using the intensity difference in the higher energy side from the edge onset in where the intensity does not vary [van Benthem, 2002].

As a result, the Zn-L edge and the Pd-M edge showed a broad, low intensity profile with no remarkable peak. They were not suitable for an evaluation. The research was concentrated on measurements at the O-K edge. Spectra from Pd region are not necessary. Since all measured spectra were very noisy and the sensitivity of each channeltron was disperse, all spectra were smoothened by using a normalized ‘Window function’ with a Gaussian distribution which has so width that can cancel out the deviation owing to noise with homemade software.

Fig. 6.47 shows the O-K ELNES for the **Pd/$^{+Zn}$ZnO** interface generated from interface containing region and from the bulk ZnO region. The interfacial specific spectra were calculated by the spatial difference technique. It can be seen that there exist (i) one sharp peak and (ii) two broad peaks for the interfacial specific spectrum near (i) 530 eV and (ii) 540 ~ 550 eV and 558 ~ 570 eV, respectively. This interface is Zn-terminated, which means that the signal results from the O under the terminating Zn layer.

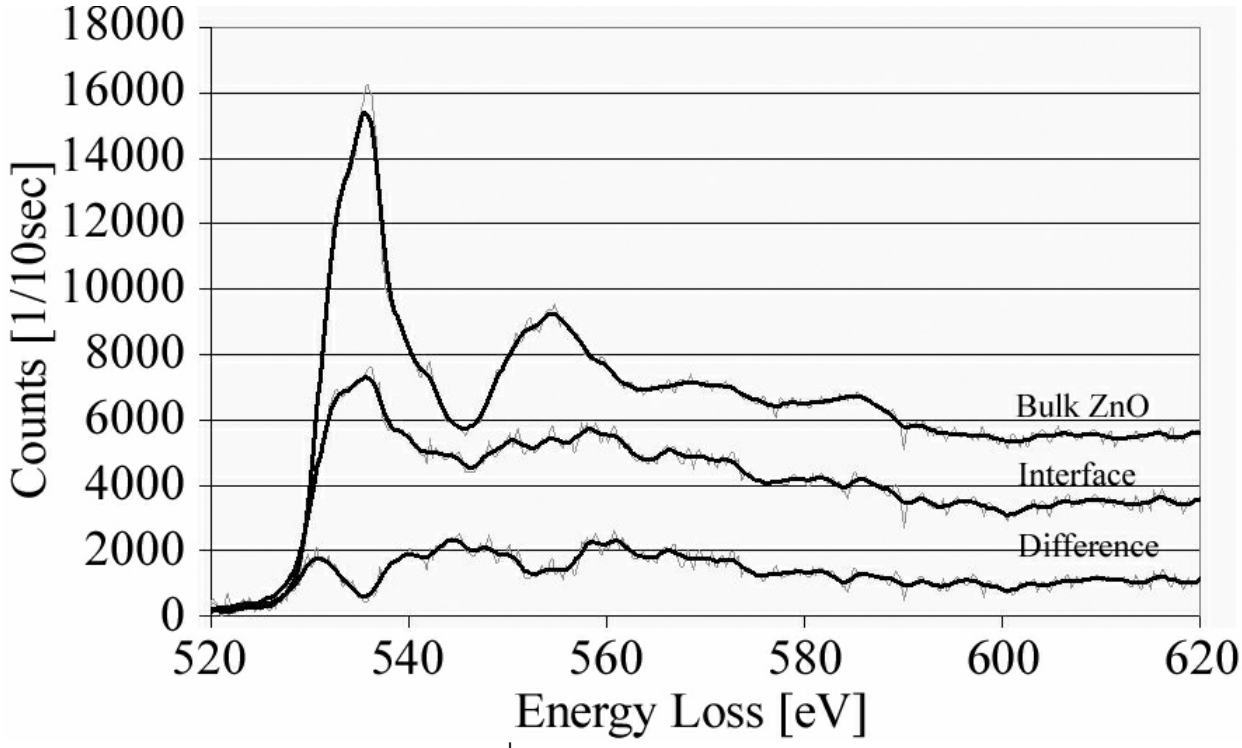

Fig. 6.47 The O-K ELNES from the **Pd/$^{+Zn}$ZnO** interface: Solid black lines mean smoothed spectra and light grey lines are original spectra. Most upper line is from bulk region, middle line from interfacial region, and lowest line is differential spectra.

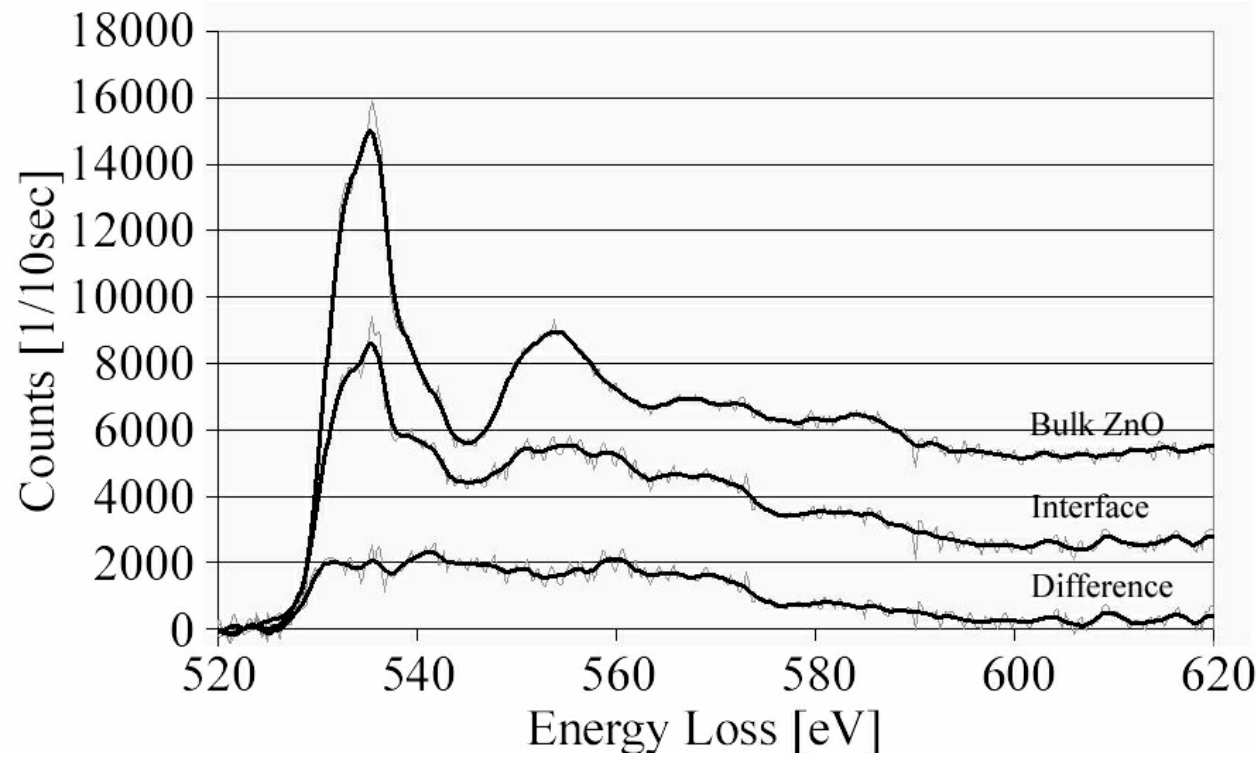

Fig. 6.48 The O-K ELNES from the **Pd/$^{-O}$ZnO** interface: Solid black lines mean smoothed spectra and light grey lines are original spectra. Most upper line is from bulk region, middle line from interfacial region, and lowest line is differential spectra.

Nevertheless, interfacial specific peaks exist. This means that the environment around the O atoms closer to the interface is different from the environment in bulk. In the bulk O atoms are located at tetrahedral sites. These specific peaks seem to be attributed to (i) the specific charge of the neighboring Zn at the interface or to (ii) the change of a crystal field due to the relaxation.

Fig. 6.48 shows the O-K ELNES of the **Pd/$^{-O}$ZnO** interface generated from interfacial region, from the bulk ZnO, and the calculated interfacial specific spectra. There exists only one continuous broad peak between 530 ~ 570 eV for the interfacial specific spectrum. This interface is O-terminated, indicating this terminating O layer should be in contact with the Pd atom. The environment around those O atoms should be different from bulk environment. This specific peak seems to be attributed to (i) the interaction with Pd (specific charge transfer) or to (ii) a change of the crystal field from the bulk environment

The detailed configurations of these interfacial specific peaks still remain unclear. It is essential for an understanding to simulate an excite state by *ab-initio* calculation. However, we can recognize at least the difference depending on a polarity of the ZnO substrates.

6.2 Discussions

6.2.1 Pd Film Growth on ZnO

Diffusion of Pd on the ZnO

It is easy to explain the dependency of crystallizing or the growth mode on the growth temperature. Fig. 6.49 [Wagner, 2001], [Wagner, 2001b] shows an observed crystallizing and growth mode of a metal film with a low oxygen affinity on an oxide substrate, like Pd on ZnO. It can be seen that at low growth temperature polycrystalline film and quasi 2-D film easily form. Surface diffusivity of an adsorbed atom is lower at lower growth temperature and then the atom can be easily frozen on the surface due to a high driving force for nucleation.

In spite of the same growth temperature and the same kind of substrate, however, it was seen that, especially at low temperatures (200 °C), the crystallizings largely depend also on the surface orientations in the case of Pd/ZnO system. In subsection 6.1.1, it was described that RHEED patterns and XRDs revealed that the Pd film grown on the $^{+}$**ZnO** substrate at 200°C was polycrystalline which is randomly orientated along the in-plane with slightly preferred orientation. On the other hand, the other conditions which are on the $^{-}$ZnO substrate or at the high growth temperature (~600 °C) allow an epitaxial growth. Furthermore, the mosaicity (degree of FWHM of in-plane orientation distribution) of the Pd film grown on the $^{-}$**ZnO** substrate or grown at the higher growth temperature was well-aligned than that grown on $^{+}$**ZnO** substrate or at the lower temperature.

Therefore, it seems that the activation energy of diffusion of Pd atom on the $^{+}$**ZnO** substrate should be higher than that on the $^{-}$**ZnO** substrate and that the lower temperature cannot give enough energy to pass the energy barrier for the diffusion on the $^{+}$**ZnO** substrate. These results indicate lower atomic mobility of Pd atom on the $^{+}$**ZnO** substrate than that on the $^{-}$**ZnO** substrate.

The difference in the substrate surface orientations is the atomic species which form the terminating layer. ARM observations (see subsection 6.1.3 and 6.1.4) showed that the ZnO at the **Pd/**$^{+}$**ZnO** interface was Zn-terminated while the ZnO at the **Pd/**$^{-}$**ZnO** interface was O-terminated. This means that the lower atomic mobility of Pd atom on the $^{+}$**ZnO** substrate can be attributed to the stronger bonding of Pd-Zn, compared to Pd-O. The weak Pd-O bonding results in a decrease of the activation energy of diffusion and even the lower temperature gives a higher possibility of a ledge growth on the surface, suggesting that a large grain or an epitaxial film can be easily grown.

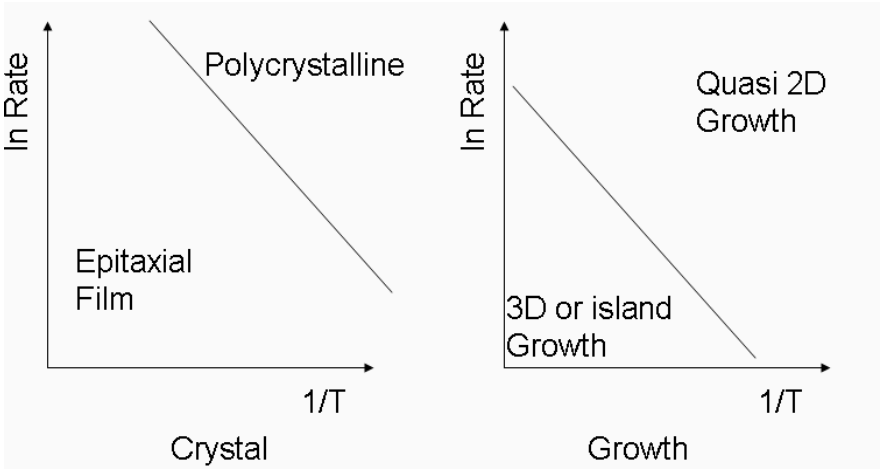

Fig. 6.49 Crystallizing and growth mode of a metal with a low oxygen affinity on an oxide substrate depend on a growth temperature and rate. [Wagner, 2001], [Wagner, 2001b].

Table 6.19 Possible orientation relationships and lattice mismatches between Pd and {0001}ZnO. The x-direction is defined along $[1\bar{1}00]_{ZnO}$ while the y direction (perpendicular to the x) is defined along $[11\bar{2}0]_{ZnO}$.

Orientation relationships	*x*	*y*
$(0001)_{ZnO}//(001)_{Pd}$ & $[11\bar{2}0]_{ZnO}//[100]_{Pd}$	44.7 %	16.5 %
$(0001)_{ZnO}//(011)_{Pd}$ & $[11\bar{2}0]_{ZnO}//[100]_{Pd}$	2.3 %	58.2 %
$(0001)_{ZnO}//(110)_{Pd}$ & $[11\bar{2}0]_{ZnO}//[\bar{1}10]_{Pd}$	27.7 %	40.9 %
$(0001)_{ZnO}//(111)_{Pd}$ & $[11\bar{2}0]_{ZnO}//[\bar{1}10]_{Pd}$	**18.1 %**	**18.1 %**
$(0001)_{ZnO}//(111)_{Pd}$ & $[11\bar{2}0]_{ZnO}//[11\bar{2}]_{Pd}$	104.6 %	31.8 %

The AFM images showed that, at the growth temperature of 600 °C, the size of the Pd grain on the $^{-}$**ZnO** substrate was larger than on the $^{+}$**ZnO** substrate. It was confirmed again that the surface atomic diffusivity on the $^{-}$**ZnO** substrate is higher than the $^{+}$**ZnO** substrate. It can be concluded that the Pd-Zn bonding is stronger than the Pd-O bonding.

Optimum Growth Temperature

Voids between Pd grains on the substrate surface could be seen by the AFM images or the cross-sectional TEM images, respectively, suggesting an island growth mode. This is attributed to a high diffusivity on a surface due to a high temperature and a weak interfacial bonding. Fig. 6.49 also show that a high temperature cause 3-D or island growth mode [Wagner, 2001], [Wagner, 2001b]. The high growth temperature during growth resulted in a defined orientation relationship:

$(111)_{Pd}$ //$(0001)_{ZnO}$ and $[\bar{1}10]_{Pd}$ //$[11\bar{2}0]_{ZnO}$ for both substrates.

Table 6.19 shows likely orientation relationships and the mismatches. The x-direction is defined along the $[1\bar{1}00]_{ZnO}$ while the y direction is defined along the $[11\bar{2}0]_{ZnO}$. This epitaxial orientation relationship is favored by a lower lattice mismatch of 18 % between Pd and ZnO and the relatively low energy of the $\{111\}_{Pd}$ surface. This means that the geometrical coherency dominates the orientation relationship in Pd/ZnO system.

The optimum growth temperature for this epitaxial orientation relationship is 600 °C. This temperature was sufficiently high to promote a well alignment of the islands (high enough Pd atom mobility) and low enough to suppress the segregation of S, K, and In (see subsection 5.1.1) to the ZnO surfaces.

6.2.2 Weak Phase Object Approximation in HRTEM

In this subsection, the applicability of the appropriate specimen thickness estimated from the simulated images for bulk ZnO in subsection 6.1.2 is theoretically checked. Fig. 6.50 shows the calculated intensities of the transmitted beam and the $\{0002\}$ diffracted beams as a function of the thickness of ZnO along the $[11\bar{2}0]_{ZnO}$ zone axis. The incoming beam was normalized as 1.

It can be seen that the intensities of the diffracted beams increase linearly with thickness while the intensity of the transmitted beam decreases. However, with a larger thickness of 5 nm (Fig. 6.50(c)), the intensity of $(000\bar{2})$ beam starts to deviate from the linear dependency, indicating the breakdown of the kinematical approximation which is also the limit for the weak phase object. Those results suggest that it is possible to treat ZnO as a weak phase object up to a thickness of ~5 nm. It should be also mentioned that the influence on the critical thickness depends on the sign of the diffracted beam. The critical thickness of (0002) diffracted beam is different from that of $(000\bar{2})$ diffracted beam, suggesting a possibility to distinguish Zn and O atomic species.

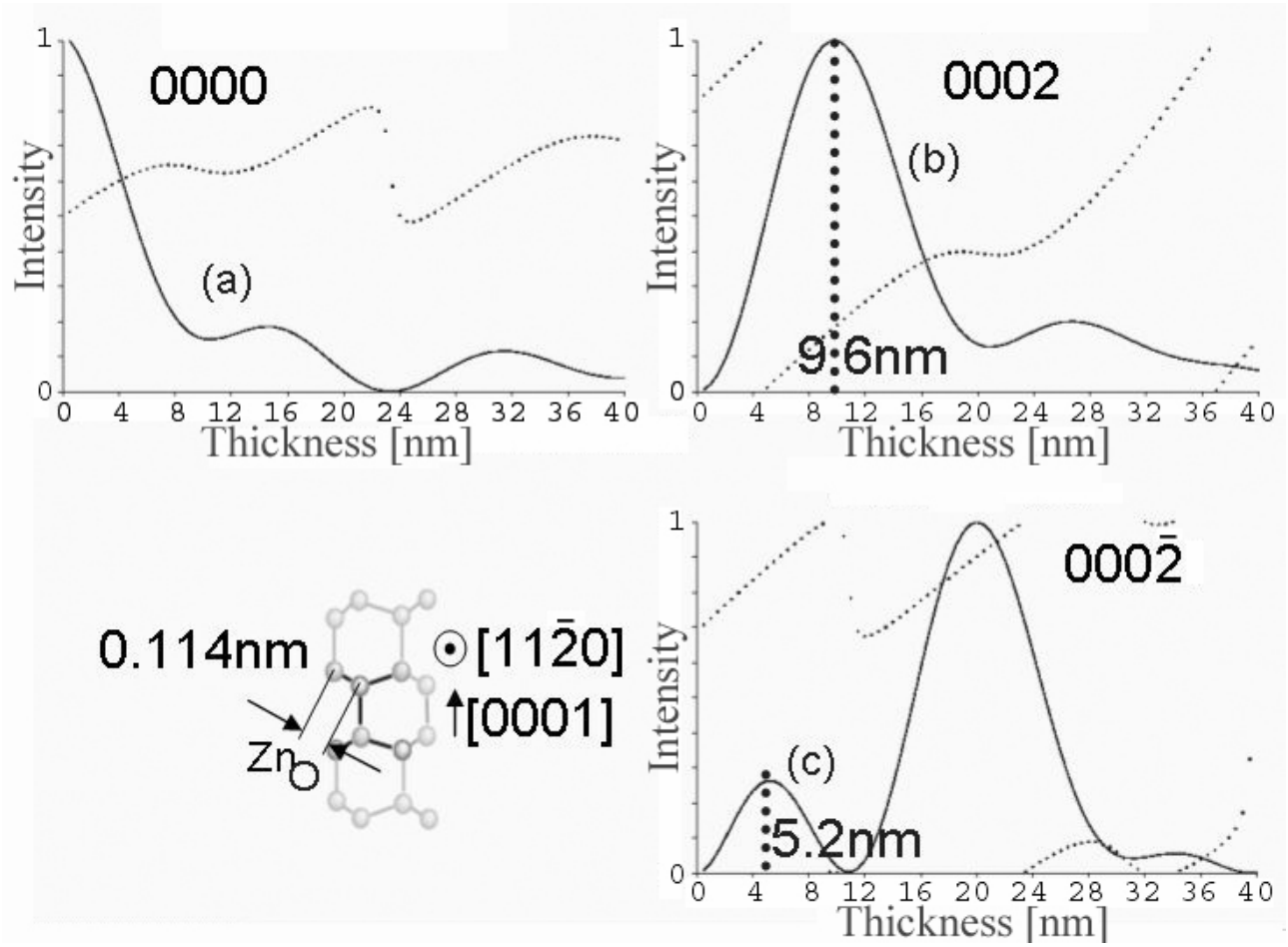

Fig. 6.50 Calculated (by EMS) intensities of (a) transmitted beam, (b) (0002) diffracted beam, and (c) $(000\bar{2})$ diffracted beam, as a function of thickness along the $[11\bar{2}0]$ zone axis. The solid (dotted) line represents to the amplitude (phase) of the beam.

From a theoretical point of view, it can be concluded that thin specimen below 5 nm thick may allow to distinguish Zn and O. This expectation embodies the result (t < 2.9 nm) of image simulation (Tableaux 6.1) by EMS.

6.2.3 Pd/$^{+}$ZnO Interface

It could be shown that the **Pd/$^{+}$ZnO** interface is Zn-terminated and the Zn atoms are positioned on Pd lattice sites. The distance between the interfacial Pd layer and the terminating Zn layer increased by 0.02 nm compared to the distance between the $\{111\}_{Pd}$ lattice planes. Pd coverage resulted in a segregation of Zn atoms to the interface until 100 % coverage was reached. The periodic relaxations at the **Pd/$^{+}$ZnO** interface were located only in the terminating Zn layer.

Accommodation of Mismatch

The **Pd/$^{+}$ZnO** interface is atomically flat, Zn-termination, and only the interfacial Zn layer next to the interface is relaxed. The interfacial Zn layer has both, CIA (coherent interface areas) as well as DIA (diffuse interface areas). The two kinds of regions are repeated at the interface, periodically. This periodicity can be explained by the following model.

Fig. 6.51 shows in the $<0001>_{ZnO}$ projection a schematic diagram of the atoms (ions) at the interface assuming the same spacings as in the bulk. The spatial repeat of the moiré pattern should be noticed. The region enclosed by a circle in Fig 6.51 shows a good coincidence between the interfacial Pd and Zn atoms. Such regions exist periodically. The outer regions around the regions enclosed by a circle in Fig 6.51 possess a poor coincidence. In order to accommodate the lattice mismatch, the atoms in the region with poor coincidence at the interface have to be moved. Then, a hexagonal network can be drawn by connecting the poor coincident positions as shown in Fig. 6.51.

It can be assumed that the hexagonal network corresponds to a dislocation network. The lattice mismatch can be localized onto the line of the network. Since the shifts of the atoms are expected along the normal to the dislocation network, the relaxing directions of the atoms on the region A in Fig. 6.51 should include only parallel component to the incident e-beam along the $[11\bar{2}0]_{ZnO}//[\bar{1}10]_{Pd}$ zone axes. Since a HRTEM image provides a projected structure, the relaxation of the atoms in the region A in Fig. 6.51 does not reflect to an image on a screen. On the other hand, the moving direction in the region B possesses a component along the normal to the e-beam direction, indicating that the relaxation can reflect DIA.

If this model for generation of misfit dislocation is correct, the repeat unit of both the region A (~1.0 nm) and B (~0.5 nm) should be ~1.5 nm. This agrees with the experimental value of 1.5 nm. Therefore, this relaxation model of the hexagonal network is valid.

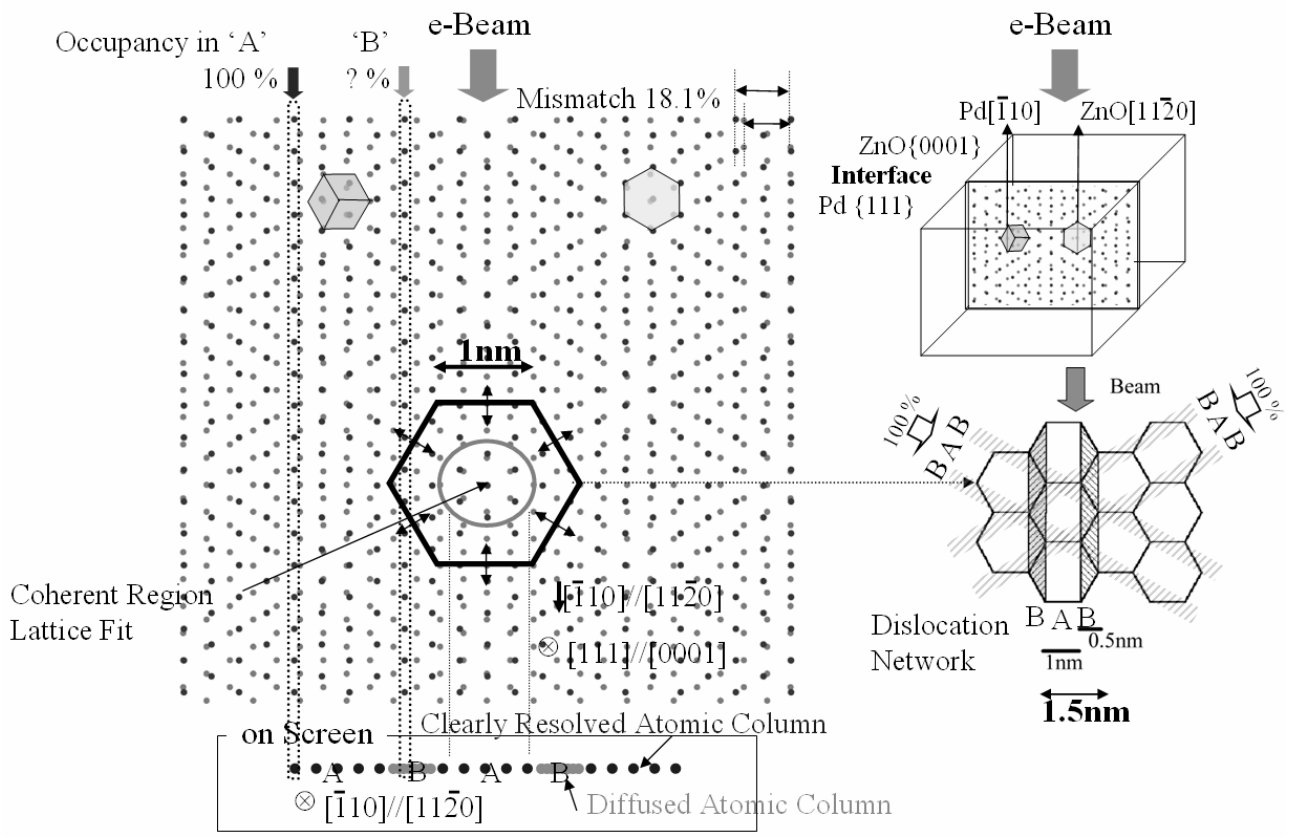

Fig. 6.51 Schematic diagram of interfacial atoms. This dichromatic pattern means that black dots are ZnO and grey dots are Pd. If the interfacial atoms without relaxation are projected along the incoming beam direction, all projected atoms should be clearly separated. This means that the **Pd/ZnO** interface was relaxed, because DIA were observed periodically.

The observation along only one zone axis does not allow the determination of a 3-dimensional interfacial structure. For this reason, the atomic structure was observed for the same specimen as before also along the second zone axes of $[1\bar{1}00]_{ZnO}//[11\bar{2}]$. Atomically flat interface and no strain field except the interfacial Zn could be seen in the second zone axis. The only interfacial Zn layer has both CIA and DIA similarly as for the previous zone axis.

Fig. 6.52 shows a schematic diagram of both interfacial atoms of Pd and ZnO. Since the movements of the atoms on the interface are expected along the normal to the dislocation network, all movements cannot be parallel to the incident e-beam direction in the case of the observation along the $[1\bar{1}00]_{ZnO}//[11\bar{2}]$ zone axes. Therefore, the clearly resolved columns (CIA) at the interface cannot be theoretically shown.

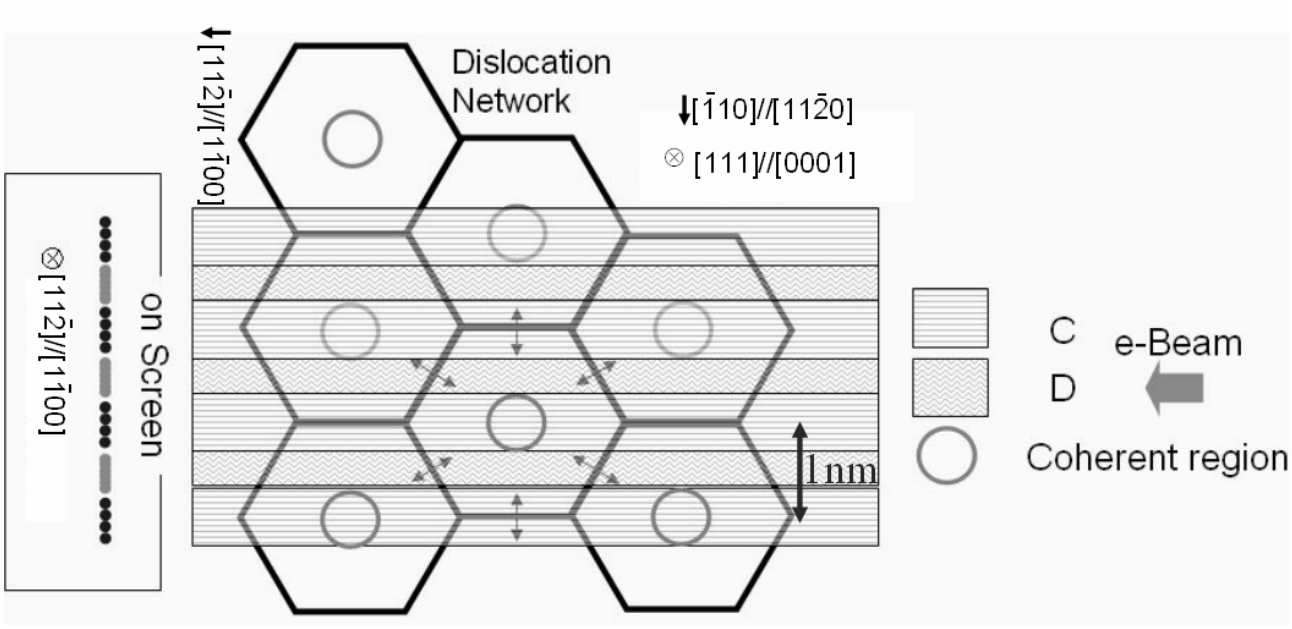

Fig. 6.52 Schematic diagram of interfacial atoms at the interface. It should be noticed that the region C includes several coherent regions while the region D does not completely include the coherent region. Since the atomic row along each column in the coherent region in the region C cannot be disturbed, they seem to contribute to the contrast of the clearly resolved atomic columns (CIA) in left screen.

However, CIA could also be seen. This can be explained by considering Fig. 6.52. It should be noticed that the region C includes several coherent regions while the region D does not completely include the coherent region. Since the atomic row along each column in the coherent region in the region C cannot be disturbed, they seem to contribute to the contrast of the clearly resolved atomic columns (CIA) in left screen.

However, the atoms near the dislocation line in the region C seem to slightly affect a diffusion of the column on the image. On the other hand, the region D completely generates DIA. The periodicity of repeat of the region C and D should be ~1.0 nm under the relaxation model. This expectation agrees well with experiment value of ~1.0 nm. It can be reconfirmed that the relaxation model constructed for the previous zone axis is valid.

Most Stable Local Atomic Geometry at the Pd/$^{+}$ZnO Interface

A quantitative HRTEM image analysis revealed an accommodation of the interfacial Zn atoms to fit to Pd lattice which does not completely relax.

The relaxation in the region A in Fig. 6.51 should not reflect an image according to the relaxation model as mention before. However, the atomic relaxations (T_x) along the interface and along the normal to the zone axis were detected even in the CIA corresponding

to region A. This means that the model cannot be completely correct. Actually, the atoms seem to relax not only near the dislocation network but also near the coherent regions (encircled by a circle in Fig. 6.51), because the slight mismatch exists even in the coherent regions. Therefore, the interface possesses most stable coherent geometry by completely accommodating such slight mismatch.

The relaxation in the coherent regions also should involve the atomic relaxations which are not parallel to the e-beam. However, the atomic columns corresponding to the region A seems to be not diffused on a screen. Fortunately, the relaxation in the coherent regions does not allow to disturbing the atomic row along the each column, because the atoms in the coherent regions seem to move with keeping center symmetry.

This slight relaxation in the coherent region provides a most stable local atomic geometry between the interfacial Pd and Zn atoms. Quantitative analysis revealed that the Pd atoms on the third layer were located on top of the interfacial Zn atom. It can be concluded that the interfacial Zn atoms sit on the fcc hollow sites of Pd lattice. Simultaneously the oxygen atoms next to the interfacial Zn layer are located at the hollow sites of the interfacial Pd atoms.

Furthermore, quantitative analysis of HRTEM taken along the second zone axes revealed that the Pd atoms at the interface are located on top of the interfacial Zn atom.

Finally, it can be concluded that, the interfacial Zn atoms 3-dimensiionally sit on the fcc hollow sites of the Pd and simultaneously the oxygen atom next to the interfacial Zn layer is located at the hollow sites of the interfacial Pd atom. This observed local atomic geometry agrees with the calculated most stable atomic geometry by Zaoui [Zaoui, 2004] (see subsection 2.2.4).

Distance between Pd and ZnO Crystals

Quantitative HRTEM image analysis revealed the average interfacial distance of 0.24 ± 0.01 nm between the interfacial Zn and Pd layers. This value is wider than a bulk spacing (d_{111} = 0.225 nm) of Pd, indicating that the ionic radius of the interfacial Zn atom is larger than that of bulk Pd atom. It is different from the calculated result of 0.185 nm by Zaoui [Zaoui, 2004].

Nominal Atomic Occupancy and Real Atomic Occupancy

After preparation of the ZnO surface, the surface coverage of topmost Zn atom was 40 %. After Pd deposition, the spatial occupancy of the interfacial Zn layer increased to about

100 %. The former value is a real one while the latter value is a nominal one. Unfortunately, in DIA, a quantitative analysis was technically not possible. Nevertheless, the real spatial occupancy of Zn atom in the 1st layer of the ZnO at the interface can be determined to be 100 %. They can be explained by the following.

For example, it can be assumed that an increase of the occupancy to 100 % from the initial 40 % is attributed to local segregation of Zn atoms to the coherent regions, indicating that the outer regions around the coherent regions might have the occupancy below 40 % and then the total occupancy might be still 40 % in all regions.

However, this assumption is wrong. Because {0001}ZnO plane has three equivalent zone axes along the plane as shown in Fig. 6.51. Even if the interface was observed along the other equivalent zone axis, the same occupancy of 100 % should be observed in the CIA. The region A (resulting in the CIA) observed along the other zone axis includes a part of the region B (resulting in the DIA) observed along the initial zone axis as shown in Fig. 6.51. In spite of including the region B in the observation along the initial zone axis, the occupancy should be 100 %. This means that the interfacial Zn layer in all regions should have the real occupancy of 100 % (in even the region B). We must be careful that the region B should NOT have nominal occupancy of 100 % due to a diffusion of atomic row along the each column. However, it should have real occupancy of 100 %.

Although the CIA only could be observed, fortunately, it was enough for a determination of the real atomic occupancy. Therefore, the 1st Zn layer of the ZnO at the **Pd/$^{+}$ZnO** interface possesses the real spatial occupancy of 100 %.

Relaxed Crystal

It could be seen that the relaxation does not occur in not Pd but ZnO near the **Pd/$^{+Zn}$ZnO** interface. A lattice relaxation of a ceramic like a ZnO rather than a metal like a Pd would be unusual, if the bulk crystals of ZnO and Pd were compared. Actually, the relaxation in the bulk region of the ZnO could not be seen. It happened in only 1st Zn layer at the interface.

A chemical environment around an atom at an interface is different from that in a bulk. At the interface, the interfacial Zn atom neighbors to Pd atoms, suggesting that the different environment may affect an ionic and covalent bonding of the backbonds with the O atoms next the interfacial Zn layer. Actually, the DVXα calculation showed a specific ionic charge of the interfacial Zn. It can be seen (see section 7.2) that the chemical environment near the interface is clearly different from that in the bulk ZnO. Therefore, we should distinguish a bulk environment and an interfacial environment. Then, a relaxation of the 1st layer of a

ceramic like a ZnO can be explained. Details for the explanation for the relaxed crystal, the terminating atomic species, most stable atomic geometry, and the spatial occupancy will be done with all results in section 7.3.

6.2.4 Pd/$^{-}$ZnO Interface

Quantitative image analysis of the HRTEM micrographs from the **Pd/$^{-}$ZnO** interface shows O termination of this interface. The interfacial Pd and O atoms are located top-on-top and the distance between them is about 0.01 nm smaller than the distances in the Pd lattice. The coverage of the interfacial O layer is 100 %. In contrast to the **Pd/$^{+}$ZnO** interface, the lattice relaxations at the **Pd/$^{-}$ZnO** interface were located in the Pd.

Relaxation of Mismatch

The **Pd/$^{-}$ZnO** interface showed atomically flatness, O-termination, and relaxation structure in Pd region.

The interfacial Pd layer has both CIA (coherent interface areas) and DIA (diffuse interface areas). These two kinds of regions in this interfacial Pd layer were periodically repeated. This periodicity can be explained by the relation model as mentioned in subsection 6.2.3. The expectation agreed well with experiment results. This indicates that the interfacial Pd lattice accommodates to the ZnO lattice. Actually, the relaxation of the 1st Pd layer caused to periodic weak strain fields in bulk Pd region as shown in Fig. 6.40.

Most Stable Local Atomic Structure at the Pd/$^{-}$ZnO Interface

Quantitative HRTEM image analyses for the CIA along the two different zone axes revealed that the interfacial Pd atoms are 3-dimensionally located on top of the interfacial O atoms of the ZnO. This observed atomic geometry agreed with the calculated most stable atomic geometry by Zaoui [Zaoui, 2004] (see subsection 2.2.4).

Distance between Pd and ZnO Crystals

Quantitative HRTEM image analysis revealed the average interfacial distance of 0.21 ± 0.01 nm between the interfacial O and Pd layers at the **Pd/$^{-}$ZnO** interface. This value is less than a bulk spacing ($d_{\bar{1}\bar{1}\bar{1}}$ = 0.225 nm) of Pd. This means that the ionic radius of bulk Pd atom is less than that of interfacial O atom. It is different from the experimental result for the **Pd/$^{+}$ZnO** interface, indicating that the terminating atomic species is clearly different kind of species. It is quite different from the calculated result of 0.185 nm by A. Zaoui

[Zaoui, 2004].

Inherently, in bulk ZnO, an ionic radius of O is much bigger than that of Zn. However, the interfacial bonding distance between Pd-Zn layers was bigger than between Pd-O layers. This can be explained by considering interfacial specific charge transfers which Zn was negatively charged while O was positively charged (see subsection 7.2).

Atomic Occupancy of 100 %

Unfortunately, in the DIA, a quantitative analysis was technically not possible. However, the total occupancy can be predicted as 100 % by the previous explanation as mentioned in subsection 6.2.3. Therefore, the 1st O layer of the ZnO at the **Pd/$^{-}$ZnO** interface possesses the real spatial occupancy of 100 %. Details for the explanation for the relaxed crystal, the terminating atomic species, most stable atomic geometry, and the spatial occupancy will be done with all results in section 7.3.

6.2.5 Interfacial ELNES

The obtained interfacial spectra are evaluated and analyzed. The interfacial specific spectra should not be taken by an artifact in this work. If a wrong scaling factor was used or an inappropriate background subtraction was done, the difference spectra should have the some peaks with the same configuration as that from the bulk ZnO. Furthermore, the peak position of the difference spectra also should be the same as that for the bulk ZnO. In this work, the configuration of the interfacial specific spectra and the peak positions were clearly different from that in bulk ZnO. If an energy scale of an instrument was shifted during a measurement, it would give rise to artifact which the differential spectra should have the peaks at different energy region from bulk ZnO. However, our measurements were done within a few minutes without adjusting a spectrum analyzer and the O-K edge onsets were completely coincident for all scanned areas, indicating an energetic drift is not likely. This means that the obtained specific ELNES is not attributed to an artifact.

As a result, the interfacial specific O-K ELNES could be detected from two interfaces. They showed that the environments around the O are completely different each other depending on polarity. Furthermore, the environment is clearly different from bulk.

Fig. 6.47 for the **Pd/$^{+Zn}$ZnO** interface shows that there are one sharp peak and two broad

peaks in the interfacial specific spectrum near 530 eV, 540 ~ 550 eV, and 558 ~ 570 eV, respectively. This interface was Zn-terminated, indicating O layer should be located in not interfacial layer but second layer. Nevertheless, these additional three peaks existed. This means that the environment around the O atom should be different from bulk one. For this, two mechanisms can be considered. It can be attributed to (i) a change of the number of coordinates due to a relaxation of the interfacial Zn or to (ii) a change of Madelung field around O atom due to a change of ionic charge of the terminating atom. Actually, the interfacial Zn was relaxed to fit to Pd lattice and an ionic charge transfer around interfacial Zn was theoretically expected (see section 7.2).

Fig. 6.48 for the **Pd/$^{-O}$ZnO** interface shows that there is continuous one broad peak between 530 ~ 570 eV in the interfacial specific spectrum. This interface is O-terminated, indicating this terminating O layer should be contacted with Pd atom. This means that the environment around the O atom should be different from bulk one. It seems that it can be attributed to (i) an interaction with Pd, to (ii) an appearance of dangling bond due to mismatch, or to (iii) a change of the ionic charge of the O itself. Actually, the interfacial Pd was relaxed to fit ZnO lattice and an ionic charge transfer around the interfacial O was theoretically expected (see section 7.2).

The configurations and the difference of these spectra still remain unclear. However, at least, we can say from these ELNES studies that the environment around the O atoms near the interface clearly depends on polarity of the ZnO and are different from that in bulk ZnO, suggesting a possibility of (i) the different terminating atomic species depending on the polarity, (ii) unusual ionic charge of the atoms near the interfaces, or (iii) the relaxation of the interfacial atoms. It is essential for an understanding to simulate the ELNES by *ab-initio* calculation. Unfortunately, the theoretical calculation for the excited states was not done in this work.

7 Theoretical Calculations

In this chapter, theoretical results for Pd/ZnO interfaces calculated by the DVXα method are shown and discussed. These calculations were performed in order to interpret the experimental results for Pd/ZnO interfaces. The DVXα cluster calculation [Adachi, 1978] is appropriate for simulating and guessing the electronic states of the system which has incomplete three-dimensional periodicity like a crystal surface or a metal/ceramic interface.

7.1 Bulk ZnO

First of all, theoretical calculations of the electronic structures of bulk ZnO was performed for $Zn_{43}O_{43}$ cluster. This calculation can be useful as reference for the calculation results in the Pd/ZnO interfaces.

Net Covalent Charge and Net Ionic Charge of ZnO Surfaces

Table 7.1 summarizes the net ionic charge of the Zn or O atom and the net covalent charge between Zn and O atoms. The net covalent charge is +0.24e, the net ionic charges are +1.07e (Zn) and -1.10e (O), indicating mixed covalent and ionic characters. The values for the bulk were compared with the values in the interfaces as a reference.

Table 7.1 Calculated net ionic charges and covalent charges in the bulk ZnO. The net covalent charge is +0.24e, the net ionic charges are +1.07e (Zn) and -1.10e (O).

Net Ionic Charge [e]	+1.07 (Zn)
Net Covalent Charge [e]	+0.24
Net Ionic Charge [e]	-1.10 (O)

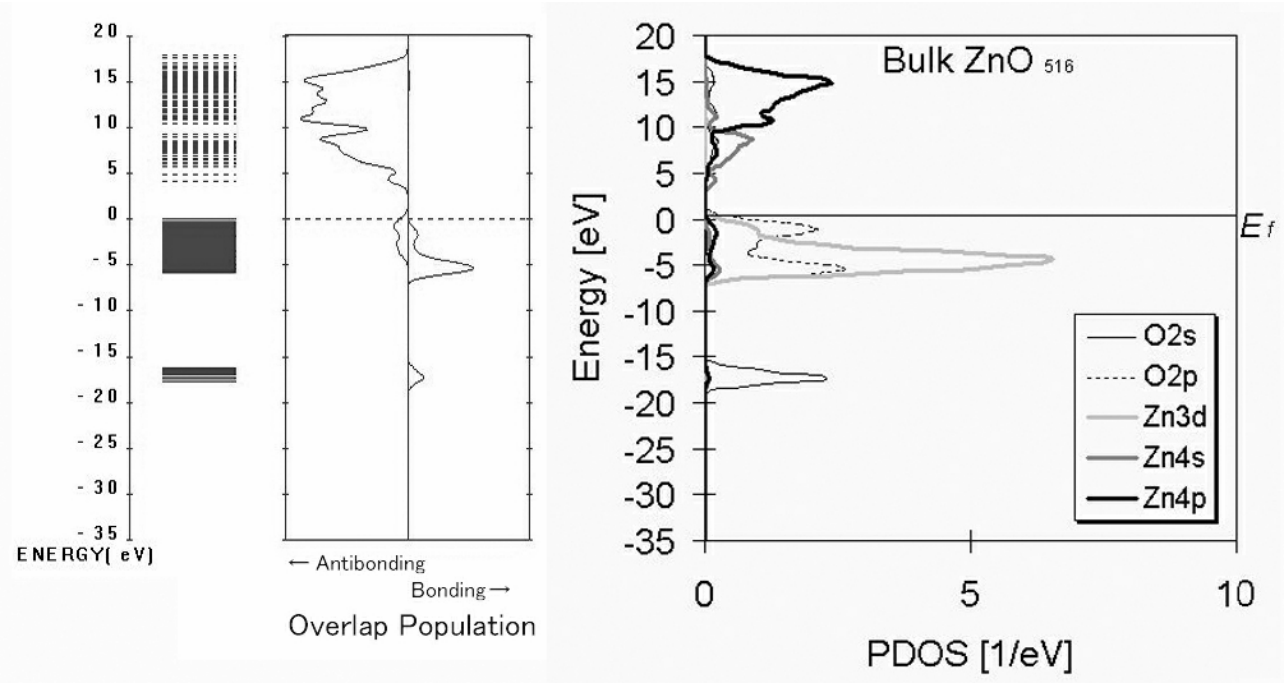

Fig. 7.2 The energy states (left), bond overlap population between Zn and O, and local density of state (right) for the Zn and O atoms which are located near the center of bulk ZnO cluster. The main component of Zn3*d* orbit is located within -7 ~ 0 eV and shares almost the same energy region as the O2*p* orbit. Furthermore, BOP shows strong bonding feature within -7 ~ 0 eV.

Local Density of States and Bond Overlap Population

The local density of states (LDOS) of the Zn and O atoms and the bond overlap population (BOP) between the Zn and O atoms which are located near the center of the bulk ZnO cluster were calculated. The LDOS was normalized per unit cell of ZnO.

Mulliken's population analysis can be applied to evaluate bond overlap. As shown from the definition of equation (3-33), a total BOP (a net covalent charge), that is the sum of the BOP below Fermi level, indicates the chemical bonding feature. A large positive total BOP corresponds to stable and strong covalent bonding while a negative total BOP corresponds to unstable chemical (anti-covalent) bonds.

Fig. 7.2 shows the energy states, BOP between the Zn and O atoms, and LDOS near the Fermi level for bulk ZnO. There exists a band gap 3 ~ 4 eV above the Fermi level resulting in a character of ZnO as insulator. This indicates a sufficiently high accuracy of our calculations. The main component of Zn3*d* orbit is located within -7 ~ 0 eV and shares almost the same energy region as the O2*p* orbit. These orbits are hybridizing each other and then are emphasized. Furthermore, BOP shows strong bonding feature within -7 ~ 0 eV which are responsible for covalent bonding. The net covalent charge which is the sum of the BOP below the Fermi level is +0.24e in this calculation.

7.2 Pd/ZnO Interfaces

The theoretical results by semi-quantitative *first principle* calculation for the Pd/ZnO interfaces will be described here. These calculations were performed in order to interpret the experimental results for the ZnO surfaces and for the Pd/ZnO interfaces. Usually, a band calculation method requires a supercell which satisfies a periodic boundary condition. In a system with incomplete three-dimensional periodicity, however, it is impossible at present to treat huge supercells including periodic mismatches. For this reason, the DVXα cluster method was used in this work because it takes into account for the realistic and representative local atomic geometry including the mismatch of the Pd/ZnO system.

The Pd/ZnO interface can be classified by 5 kinds of local atomic geometries (a) ~ (e) of Pd on ZnO as shown in Fig. 7.3 and Fig. 7.4. Accuracy of calculation can be best for the atoms near the interfaces enclosed by squares in Fig. 7.4, because the atoms are located near center axis of the cluster. Therefore, the classification should be done by considering the atomic geometry of the atoms near the center of the cluster.

The case (Cluster model (a)) corresponds to a local atomic geometry that the interfacial Pd atoms sit **on top** of the interfacial atoms of the ZnO. The cases (b) and (e) correspond to the orientation relationship (**OR-A**) of $(0001)_{ZnO}//(111)_{Pd}$ and $[11\bar{2}0]_{ZnO}//[1\bar{1}0]_{Pd}$. The cases (c) and (d) correspond to the orientation relationship (**OR-B**) of $(0001)_{ZnO}//(111)_{Pd}$ and $[11\bar{2}0]_{ZnO}//[\bar{1}10]_{Pd}$. The case (d) and (e) give a local atomic geometry that the interfacial Pd atoms sit on top of the atoms in the 2nd layer of the ZnO. The case (b) and (c) give different local atomic geometry that the interfacial Pd atoms sit on the hollow sites of the atoms in the 2nd layer of the ZnO (see top view of Fig. 7.4). The different interatomic distances between the interfacial Pd atom and the atom in the 2nd layer of the ZnO lead to different interactions. Furthermore, the stackings in the cases (b) and (c) are **fcc** because the Pd atom in the 3rd layer sits on top of the atom of the ZnO. The stackings in the cases (d) and (e) are **hcp** because the Pd atoms in the 2nd layer sit on top of the atom of the ZnO (see Fig.7.4).

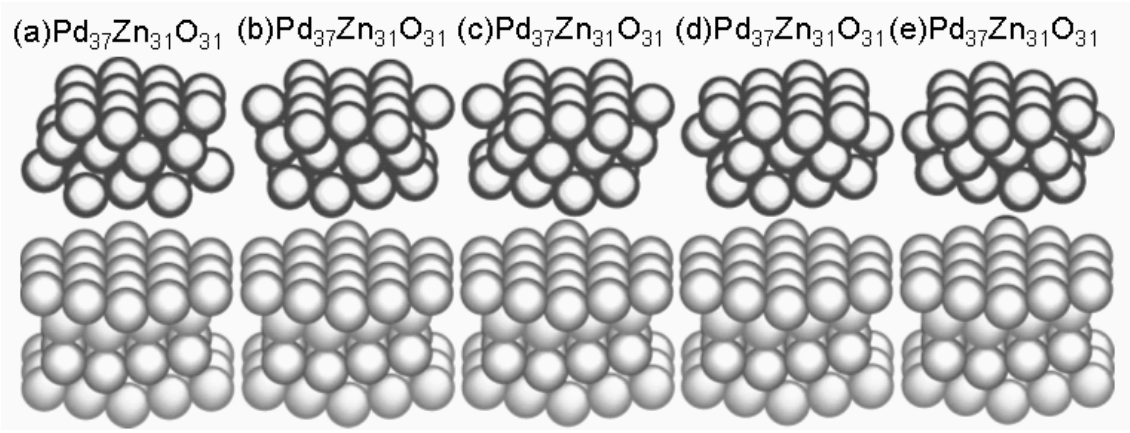

Fig. 7.3 Calculated $Pd_{37}Zn_{31}O_{31}$ cluster models: The case (a) corresponds to a local atomic geometry that the interfacial Pd atoms sit **on top** of the interfacial atoms of the ZnO. The case (b) and (e) corresponds to the orientation relationship (**OR-A**) of $(\ 0001\ )_{ZnO}//(\ 111\ )_{Pd}$ and $[\ 11\bar{2}0\ ]_{ZnO}//[\ 1\bar{1}0\ ]_{Pd}$. The case (c) and (d) correspond to the orientation relationship (OR-B) $(0001)_{ZnO}//(111)_{Pd}$ and $[11\bar{2}0]_{ZnO}//[\bar{1}10]_{Pd}$.

Table 7.2 Net ionic charge and net covalent charge of atoms at the **Pd/$^{+Zn}$ZnO** interface. The Pd-Zn bonding at the **Pd/$^{+Zn}$ZnO** interface consists of the mixture of an ionic bonding ($Pd^{+0.05e\sim+0.29e}$, $Zn^{-0.86e\sim-0.94e}$) and a covalent bonding (+0.14e ~ +0.17e). The main bonding type consists of a covalent bonding.

Pd/$^{+Zn}$ZnO	(a)	(b)	(c)	(d)	(e)
Net Charge [e]: 1st Pd	+0.29	+0.28	**+0.05**	+0.10	+0.10
Covalency [e]: 1st Pd-1st Zn	+0.17	+0.14	**+0.15**	+0.14	+0.15
Net Charge [e]: 1st Zn	-0.94	-0.86	**-0.89**	-0.89	-0.88
Covalency [e]: 1st Zn-2nd O	*-0.13*	-0.12	**-0.13**	-0.12	-0.13
Net Charge [e]: 2nd O	-0.75	-0.81	**-0.71**	-0.81	-0.77
Covalency [e]: 1st Pd-2nd O	-0.02	-0.04	**-0.03**	-0.03	-0.03

Since both terminating atoms can be considered, the calculations were done for the 10 kinds of atomic geometries without considering a relaxation. The interfacial distance in the clusters was fixed at the experimentally obtained distance. These calculations revealed the LDOS, the net ionic charge, the net covalent charge, and the BOP (bond overlap population) for the atoms (enclosed by squares in Fig. 7.4) near the interface.

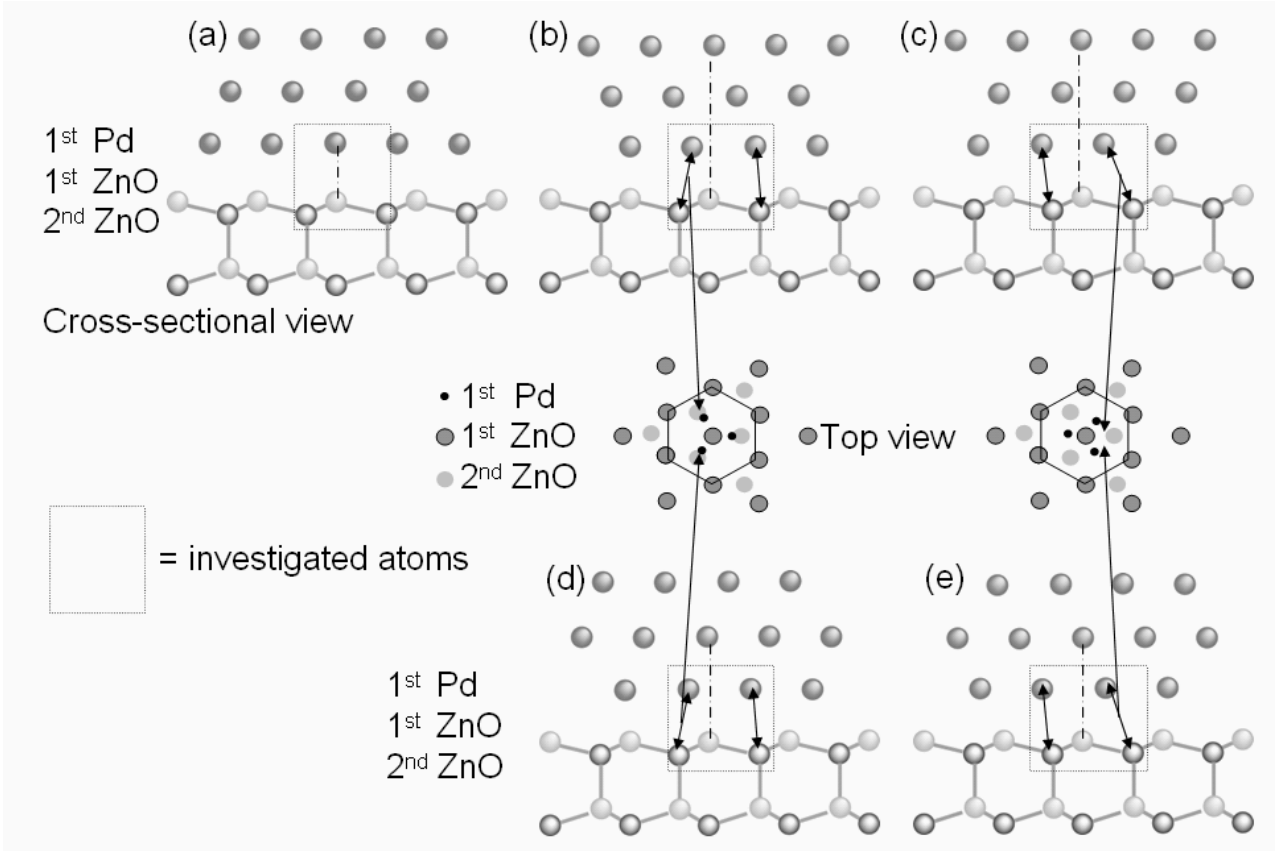

Fig. 7.4 Calculated cluster models: The cross-sectional figures are along the $[11\bar{2}0]_{ZnO}$ axis. The figures of the top view are along the $<0001>_{ZnO}$ axis. The case (b) and (e) corresponds to the orientation relationship (**OR-A**) of $(0001)_{ZnO}//(111)_{Pd}$ and $[11\bar{2}0]_{ZnO}//[1\bar{1}0]_{Pd}$. The case (c) and (d) correspond to the orientation relationship (**OR-B**) of $(0001)_{ZnO}//(111)_{Pd}$ and $[11\bar{2}0]_{ZnO}//[\bar{1}10]_{Pd}$. [(a): '**on top**' geometry] The interfacial Pd atom sits on top of the interfacial atom of the ZnO. [(b): '**fcc hollow with OR-A**'] The Pd stacks on the lattice site of the ZnO, simultaneously the interfacial Pd atoms sit on top of the atoms in the 2nd layer of the ZnO, and the Pd atom in the 3rd layer sits on top of the interfacial atom of the ZnO. [(c): '**fcc hollow with OR-B**'] The Pd stacks on the lattice site of the ZnO, simultaneously the interfacial Pd atoms sit on the hollow sites of the atoms in the 2nd layer of the ZnO, and the Pd atom in the 3rd layer sits on top of the interfacial atom of the ZnO. [(d): '**hcp hollow with OR-B**'] The Pd stacks on the lattice site of the ZnO, simultaneously the interfacial Pd atoms sit on top of the atoms in the 2nd layer of the ZnO, and the Pd atom in the 2nd layer sits on top of the interfacial atom of the ZnO. [(e): '**hcp hollow with OR-A**'] The Pd stacks on the lattice site of the ZnO, simultaneously the interfacial Pd atoms sit on the hollow sites of the atoms in the 2nd layer of the ZnO, and the Pd atom in the 2nd layer sits on top of the interfacial atom of the ZnO.

Table 7.3 Net charge and covalent charge of atoms at the **Pd/$^{-O}$ZnO** interface. The Pd-O bonding at the **Pd/$^{-O}$ZnO** interface consists of weak ionic bonding ($Pd^{-0.08e \sim -0.56e}$, $O^{+1.59e \sim +1.63e}$) without a covalent character (+0.00e ~ +0.06e).

Pd/$^{-O}$ZnO	(a)	(b)	(c)	(d)	(e)
Net Charge [e]: 1st Pd	**-0.56**	-0.13	-0.08	-0.19	-0.21
Covalency [e]: 1st Pd-1st O	**+0.06**	+0.00	+0.01	+0.00	+0.00
Net Charge [e]: 1st O	**+1.61**	+1.60	+1.59	+1.63	+1.63
Covalency [e]: 1st O-2nd Zn	**+0.31**	+0.28	+0.28	+0.27	+0.28
Net Charge [e] : 2nd Zn	**+0.31**	+0.34	+0.33	+0.33	+0.34
Covalency [e]: 1st Pd-2nd Zn	**-0.01**	+0.16	+0.08	+0.17	+0.09

Net Ionic Charge and Net Covalent Charge

Table 7.2 and Table 7.3 show that the atoms with the each atomic geometry (a) ~ (e) change their ionic and covalent characters compared to that in the bulk ZnO (see subsection 7.1). These tables clearly indicate that a definitive difference between the **Pd/$^{+Zn}$ZnO** interface and the **Pd/$^{-O}$ZnO** interface is an interfacial bonding type.

Although it can be seen in Table 7.2 that the Pd-Zn bonding at the **Pd/$^{+Zn}$ZnO** interface consists of the mixture of an ionic bonding ($Pd^{+0.05e \sim +0.29e}$, $Zn^{-0.86e \sim -0.94e}$) and a covalent bonding (+0.14e ~ +0.17e), the main bonding type consists of a covalent bonding, if compared to that of bulk ZnO (see subsection 7.1). The Pd atoms at **Pd/$^{+Zn}$ZnO** interface are positively charged while the Zn atoms at **Pd/$^{+Zn}$ZnO** interface are negatively charged. There exists a charge transfer (e^-) from the Pd to the Zn (see Fig. 7.5).

On the other hand, it can be seen in Table 7.3 that the Pd-O bonding at the **Pd/$^{-O}$ZnO** interface consists of weak ionic bonding ($Pd^{-0.08e \sim -0.56e}$, $O^{+1.59e \sim +1.63e}$) without a covalent character (+0.00e ~ +0.06e), if compared to that of bulk ZnO. Surprisingly, the Pd atoms at **Pd/$^{-O}$ZnO** interface are negatively charged while the O atoms at **Pd/$^{-O}$ZnO** interface are positively charged. There exists charge transfer (e^-) from the O to the Pd (see Fig. 7.5).

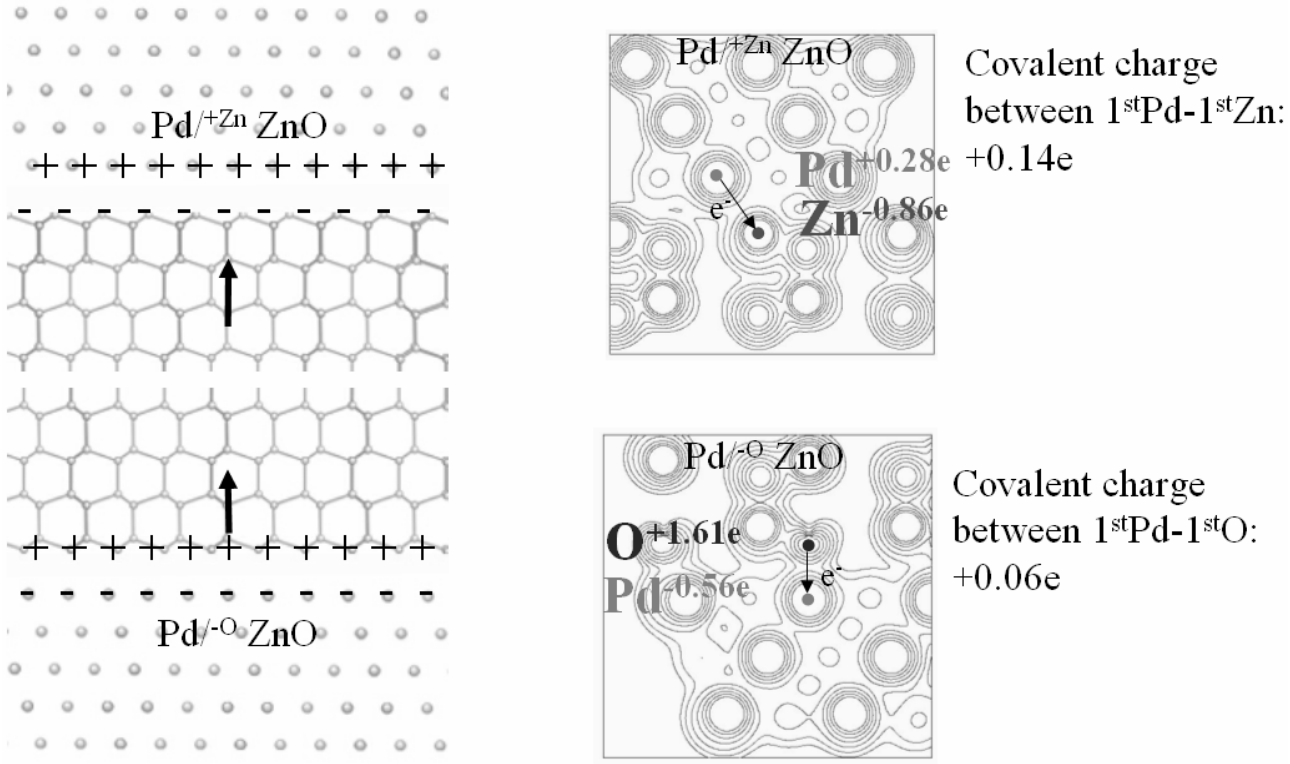

Fig. 7.5 Calculated charge transfers in the observed Pd/ZnO interfaces. Charge density distributions near the interfaces. There exist unusual charge transfers (e^-) from the O to the Pd and from the Pd to the Zn.

Dependency of Interfacial Bonding on Atomic Geometries of Pd on ZnO

For the **Pd/$^{+Zn}$ZnO** interface (see table 7.2), it can be seen that there is no strong difference between all cases (a) ~ (e) in the net covalent charges across the interface. The main interfacial bonding for the **Pd/$^{+Zn}$ZnO** interface does not strongly depend on an atomic geometry between the interfacial atoms. On the other hand, the net ionic charge of the interfacial Pd atom at the **Pd/$^{-O}$ZnO** interface (see table 7.3) depends sensively on the location of the Pd on the ZnO. The '(a) on top' location provides strongest ionic bonding ($Pd^{-0.56e}$, $O^{+1.61e}$) which is quite different from that in other locations, suggesting that the main interfacial bonding depends on an atomic geometry of the interfacial Pd atoms at the **Pd/$^{-O}$ZnO** interface. These dependencies are related to an anisotropic charge density distribution in an oxide bonding and an isotropic charge density distribution in a metallic bonding. In the **Pd/$^{-O}$ZnO** interface, the '(a) on top' location of the Pd on the ZnO allows to terminating a dangling bond of O. On the other hand, the isotropic metallic bonding of the Pd-Zn at the **Pd/$^{+Zn}$ZnO** interface does not strongly restrict the atomic location of Pd on ZnO. These results have a good agreement with the theoretical results (see Table 2.5) by Zaoui [Zaoui, 2004]

Local Density of State

The detailed analyses were performed for the experimentally observed 'case (c)' location at the **Pd/$^{+Zn}$ZnO** interface and for the experimentally observed 'case (a)' location at the **Pd/$^{-O}$ZnO** interface. Their atomic geometries were confirmed to exist with HRTEM observations (see Fig. 6.17 and Fig. 6.35).

Fig. 7.6 and Fig. 7.7 show the local density of states (LDOS) of the atoms near the **Pd/$^{+Zn}$ZnO** interface and the **Pd/$^{-O}$ZnO** interface, respectively. The LDOS of the atoms in the 2nd layer have almost same structures and same peak positions near the Fermi level as that of the bulk ZnO (see. Fig.7.2). However, the LDOS of the interfacial atoms strongly depend on polarity.

In the LDOS at the **Pd/$^{+Zn}$ZnO** interface (see Fig. 7.6), the band structure is continuous across Fermi level, indicating a locally conductive. Furthermore, the Zn 3*d* orbit is located at deeper level compared to the bulk ZnO, suggesting a charge transfer near the interface.

On the other hand, in the LDOS at the **Pd/$^{-O}$ZnO** interface (see Fig. 7.7), the band structure is continuous. This indicates a locally conductive interface. Furthermore, the O 2*sp* orbits were shifted to higher energy region, suggesting a charge transfer near the interface. The LDOS of Pd near the -20 eV at the **Pd/$^{-O}$ZnO** interface seems to be slightly enhanced by O 2*sp* orbit, because the peak positions are same each other.

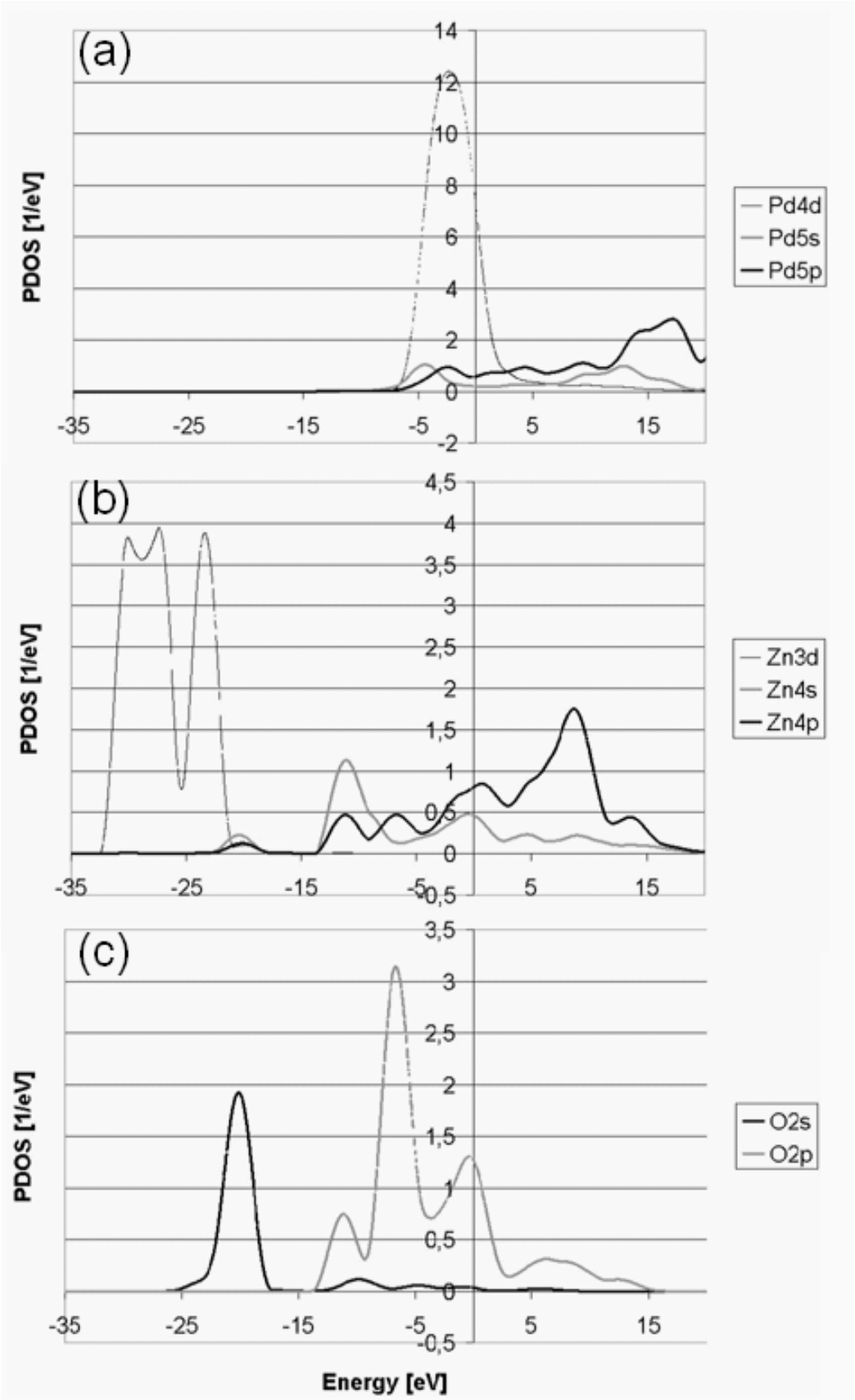

Fig. 7.10 LDOS of (a) interfacial Pd, (b) interfacial Zn, and (c) Oxygen in 2nd layer next to the Zn layer for the **Pd/$^{+Zn}$ZnO** interface. LDOS is per unit cell.

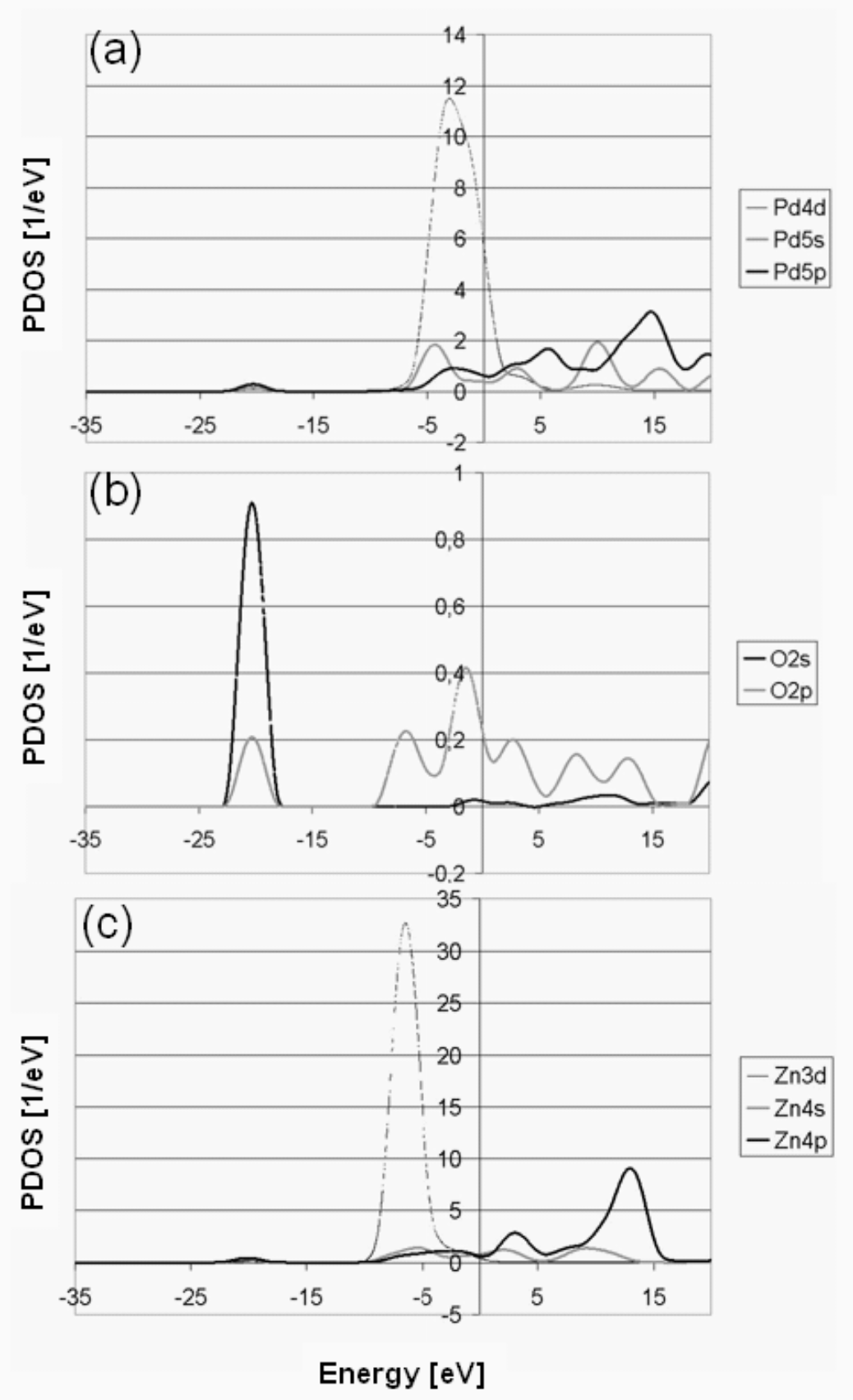

Fig. 7.11 LDOS of (a) interfacial Pd, (b) interfacial O, and (c) Zn in 2nd layer next to the O layer for the **Pd/$^{-O}$ZnO** interface. LDOS is per unit cell.

Bond Overlap Population (BOP)

A large positive BOP (the number of shared electron) means to stable and strong covalent bonding while a negative BOP means to unstable chemical bonds.

Fig. 7.8 for the **Pd/$^{+Zn}$ZnO** interface and Fig. 7.9 for the **Pd/$^{-O}$ZnO** interface show BOP between interfacial atoms in left figure and BOP between the back bond of the ZnO at the interface in right figure. Positive value corresponds to a covalent (bonding) feature and negative value corresponds to an anti-covalent (anit-bonding) feature as a function of energy level.

For the **Pd/$^{+Zn}$ZnO** interface, BOP between interfacial atoms in Fig. 7.8(a) shows no anti-bonding feature below Fermi level and a remarkable bonding feature near -2.5 eV. This hybridisation near -2.5eV consists of the Pd 4*d* and Zn 4*sp* orbits as shown in Fig. 7.6(a), (b). The hybridization plays an important role as main bonding feature. Net covalent charge is positive value, which contributes to a strong covalent bonding at the **Pd/$^{+Zn}$ZnO** interface. The BOP within the interface back bond of the ZnO in Fig. 7.8(b) has strong anti-bonding feature near Fermi level. This anti-bonding feature causes negative net covalent charge, indicating a weak covalent bonding between the interfacial Zn and O atoms near the **Pd/$^{+Zn}$ZnO** interface compared to that of bulk ZnO.

For the **Pd/$^{-O}$ZnO** interface, BOP between interfacial atoms in Fig. 7.9(a) has a quite strong anti-bonding feature within narrow energy region below Fermi level and also a weak and broad bonding feature below Fermi level. Furthermore, a strong hybridisation between Pd 5*p* and O 2*sp* orbits was detected near -20 eV. Nevertheless, the net covalent charge is nearly zero, resulting in no covalent bonding. BOP within the interfacial back bond of the ZnO in Fig. 7.9(b) has strong bonding feature within wide energy region below Fermi level. The net covalent charge is +0.31e, indicating quite stronger covalent bonding between the interfacial O and Zn atoms near the **Pd/$^{-O}$ZnO** interface than that of bulk ZnO.

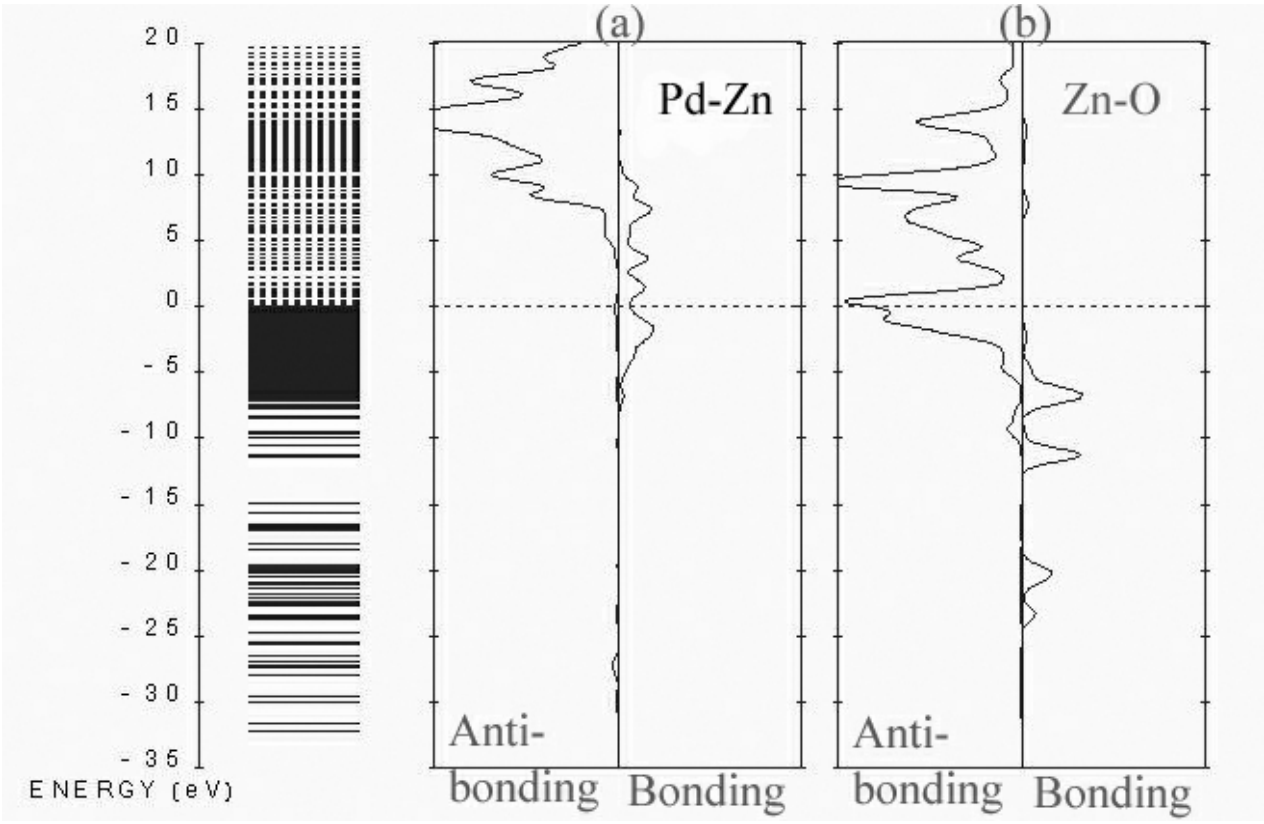

Fig. 7.8 Bond overlaps population near the **Pd/$^{+Zn}$ZnO** interface: (a) between Pd-Zn, (b) between Zn-O.

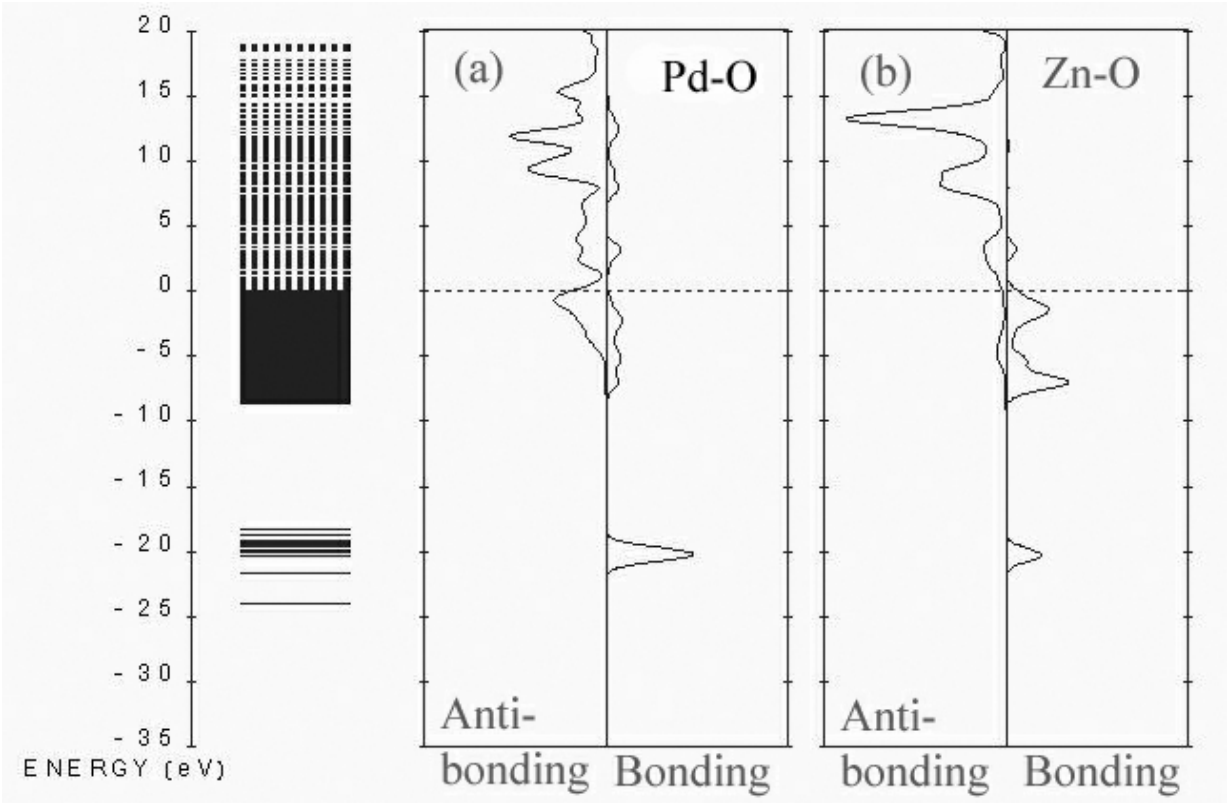

Fig. 7.9 Bond overlaps population near the **Pd/$^{-O}$ZnO** interface: (a) between Pd-O, (b) between O-Zn.

7.3 Discussion

In this section, all experimental results obtained by surface XRD, by MBE experiments, and by HRTEM image analyses will be related to the theoretically calculated results.

Charge Transfer near the Interfaces and Interfacial Bonding Type

The difference between the **Pd/$^{+Zn}$ZnO** interface and the **Pd/$^{-O}$ZnO** interface is the interfacial bonding type, the charge of the interfacial atom, and the most stable local atomic geometry.

The Pd-Zn bonding at the **Pd/$^{+Zn}$ZnO** interface consists of the mixture of the ionic bonding ($Pd^{+0.05e \sim +0.29e}$, $Zn^{-0.86e \sim -0.94e}$) and the covalent bonding (+0.14e ~ 0.17e). There is no strong difference of the local electronic states between all possible atomic geometries. This insensitivity for the atomic geometry seems to be attributed to a metallic-like character of interfacial bonding. Furthermore, the band structure is continuous across the Fermi level, indicating conductive character. In addition to such a metallic-like character, slight ionic character was seen. Surprisingly, the interfacial Pd atoms are positively charged while the interfacial Zn atoms are negatively charged. The charges of the Zn ions are unusual for that in a bulk ZnO.

On the other hand, the Pd-O bonding at the **Pd/$^{-O}$ZnO** interface consists of the ionic bonding ($Pd^{-0.08e \sim -0.56e}$, $O^{+1.59e \sim +1.63e}$) without a covalent character (+0.00e ~ +0.06e). The interfacial bonding of the **Pd/$^{-O}$ZnO** interface was sensitive for the location of Pd on ZnO. The 'on top' location of the Pd which sits on top of O provides most strong ionic bonding ($Pd^{-0.56e}$, $O^{+1.61e}$), which is quite different from that in others location. This sharp sensitivity for local atomic geometry seems to be attributed to an asymmetric orbital around O^{2-} ion of the ZnO. The dangling bond of the O at the interface can be terminated by the interfacial Pd. The interfacial Pd is negatively charged while the interfacial O is positively charged. The charges of the O ions are unlikely for that in a bulk ZnO.

It is quite unusual for a ZnO that an O is positively charged while a Zn is negatively charged. This can be explained by considering the following stabilizing mechanism of a {0001}ZnO surfaces

A ZnO has dipole moments produced by the Zn-O dimer, indicating that these dipole moments generate an electrostatic field. The electrostatic field due to dipole moments can be cancelled along all in-plane directions on the {0001} plane.

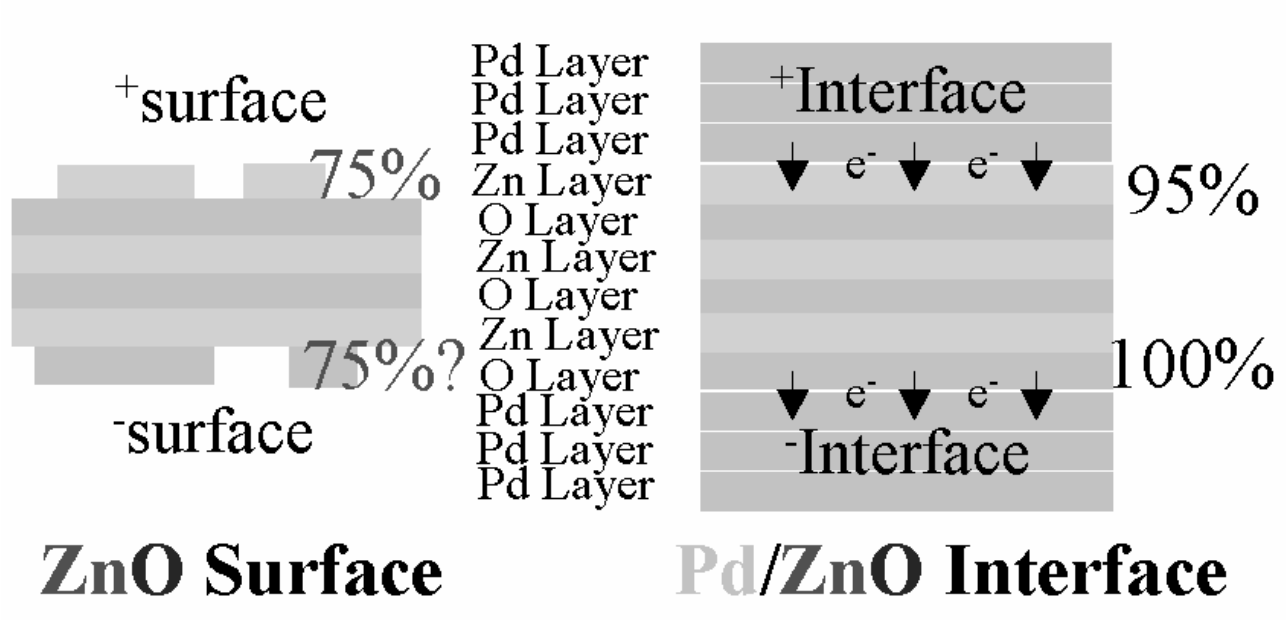

Fig. 7.10 The change of the stabilizing mechanism of ZnO. (Virtual charges by partial missing of the toplayers at the ZnO surfaces → Real charges by charge transfers across the Pd/ZnO interfaces). For example, at the ZnO surface, the partial missing of Zn^{2+} ion leads to negative charge on the surface.

However, it cannot be cancelled along the *c*-axis of ZnO, suggesting that a linear sum of electrostatic field must be diverged to infinite value along the c-axis. Then, the surface energy also must be diverged to infinity. This instability of the {0001}ZnO surfaces was pointed out by a classical model. How can this electrostatic field cause by the dipole moments be cancelled?

Noguera [Noguera, 2000] predicted that a partial coverage of the surface leads to an electrostatic charging of the surface which compensates the electrostatic field caused by the Zn-O dipoles, stabilizing the surface structure. Then, the ideal surface spatial atomic occupancy should be 75 %. The surface charge can be supplied by (i) a real surface charge, (ii) a surface impurity, or (iii) absence of topmost atoms.

HRTEM image showed atomically flat and stoichiometric interfaces. Furthermore, EELS spectra did not show any signal from impurities, indicating that the actual stabilizing mechanism of the ZnO in the Pd/ZnO interface should happen by a real surface charge (i) of ZnO at the interface as shown in Fig. 7.10.

The DVXα calculation showed the interfacial specific charge transfers. Their charges are locally unusual but globally possible. The real-charging of the terminaters of the ZnO, which is supplied by the charge transfers across the interfaces, allow to stabilizing the ZnO.

Interatomic Bonding Strengths near the Interface

The HRTEM observation, the MBE experiment, this DVXα cluster calculation, or the *first principle* calculation results by Zaoui [Zaoui, 2004] revealed that the relaxed crystal and the bonding strength between the atoms near the **Pd/$^{+Zn}$ZnO** interface and between the atoms near the **Pd/$^{-O}$ZnO** interface.

In order to check a contradiction between the results, all obtained bonding strengths are compared each other. The discrimination between ^{1st}Zn-O bonding, ^{1st}O-Zn bonding and ^{bulk}Zn-^{bulk}O bonding (1st Zn means the Zn atom in the surface or at the interface) is appropriate, because the interfacial atom of the ZnO has a specific electronic state which is quite different from that in bulk ZnO.

The relaxation of the interfacial Zn at the **Pd/$^{+Zn}$ZnO** interface observed with HRTEM allows to working the following inequality (7-1) or (7-2) with respect to a bonding strength.

^{1st}**Pd-**^{1st}**Zn**>^{1st}Pd-Pd>^{1st}Zn-O (7-1) or ^{1st}Pd-Pd>^{1st}**Pd-**^{1st}**Zn**>^{1st}Zn-O (7-2)

The relaxation of the interfacial Pd at the **Pd/$^{-O}$ZnO** interface observed with HRTEM allows to working the following inequality (7-3) or (7-4) with respect to a bonding strength.

^{1st}**Pd-**^{1st}**O**>^{1st}-O-Zn>^{1st}Pd-Pd (7-3) or ^{1st}O-Zn>^{1st}**Pd-**^{1st}**O**>^{1st}Pd-Pd (7-4)

Furthermore, the MBE experimental results (or the *first principle* calculation results by Zaoui [Zaoui, 2004]) showed the inequality of ^{1st}**Pd-**^{1st}**Zn**>^{1st}**Pd-**^{1st}**O**. Since then inequality (7-2) gives rise to a contradiction with (7-3) and (7-4), inequality (7-2) should be ignored. When inequality (7-4) was considered with inequality (7-1), then inequality (7-5) can be obtained.

[^{1st}O-Zn ? ^{1st}Pd-^{1st}Zn]>^{1st}Pd-^{1st}O>^{1st}Pd-Pd>^{1st}Zn-O (7-5)

Similarly, when inequality (7-3) was considered with inequality (7-1), inequality (7-6) can be obtained.

^{1st}Pd-^{1st}Zn> ^{1st}Pd-^{1st}O >^{1st}O-Zn>^{1st}Pd-Pd>^{1st}Zn-O (7-6)

From inequality (7-5) and (7-6) it can be seen that ^{1st}O-Zn>^{1st}Zn-O are possible. The ^{1st}Zn-O bond is most weak bonding in all cases in the interface. This relationship of ^{1st}O-Zn>^{1st}Zn-O could be confirmed in a mechanical polishing. The O-face was hard to polish while the Zn-face can be easily polished and scratched. This DVXα cluster calculation revealed that the covalency within the back (Zn-O) bonds on the **Pd/$^{-O}$ZnO** interface was much higher than that on the **Pd/$^{+Zn}$ZnO** interface and even in bulk ZnO.

Usually, ZnO should be rigid and Pd should be relatively soft. The inner parts of the ZnO, which should be at least rigid, were actually not relaxed according to the HRTEM observation for the **Pd/$^{+Zn}$ZnO** interface. However, only 1st layer of the ZnO at the

Pd/$^{+Zn}$ZnO interface was relaxed (while Pd crystal has stress until the inner parts (1^{st} ~ 6^{th} layer near the **Pd/$^{-O}$ZnO** interface). Discrimination between interfacial region and an inner part of a crystal leads to the reason why (the 1^{st} layer of) the ZnO was relaxed.

These inequalities (7-5) and (7-6) have no contradiction with all experimental and computational results.

8 Summary and Conclusion

In this chapter, the experimental results and the theoretical calculation results, for the ZnO surfaces and the Pd/ZnO interfaces, are summarized and concluded.

Terminating Atomic Species at the Interfaces

Atomically flat surfaces of ZnO substrates with impurity free could be prepared by the annealing in an oxygen environment and UHV at specific temperature. After that, single crystalline Pd films could be grown on both ZnO polar surfaces via molecular-beam-epitaxy. Pd forms three-dimensional clusters (islands) on the ZnO surfaces. With XRD, RHEED, and TEM investigations the following well-defined epitaxial orientation relationship between Pd islands and ZnO crystal was observed (deposition temperature 600 °C):

$$(111)_{Pd} \,//(0001)_{ZnO} \text{ and } [\bar{1}10]_{Pd} \,//[11\bar{2}0]_{ZnO}$$

This epitaxial orientation relationship is favored by lower lattice mismatch of 18 % between Pd and ZnO and the relatively low energy of the $\{111\}_{Pd}$ surface. The optimum growth temperature for this epitaxial orientation relationship is 600 °C. This temperature was sufficiently high to promote a well alignment of the islands (high enough Pd atom mobility) and low enough to suppress the segregation of S, K, and In to the ZnO surfaces.

Local atomic structure analyses in the Pd/ZnO interfaces could be performed employing an ultra high resolution microscope JEOL JEM-ARM1250 and a quantitative high resolution image analysis technique [Möbus, 1996]. HRTEM investigations revealed that the Pd/ZnO interfaces are atomically abrupt and, as expected due to the low reactivity of Pd, free of reaction phases. The $^{+}$**ZnO** and $^{-}$**ZnO** substrate surfaces are structurally equivalent. Nevertheless, the interface between the substrate and the palladium film showed completely different behaviors depending on a sign of polarity of a ZnO.

Structural defects were detected in the **Pd/**$^{+}$**ZnO** and the **Pd/**$^{-}$**ZnO** interfaces. These defects are misfit dislocations which are formed by the relaxation of the lattice misfit

between Pd and ZnO. The structurally matching regions between the dislocations were used to perform a quantitative analysis.

It could be shown that the **Pd/$^{+}$ZnO** interface is Zn-terminated. Pd coverage resulted in a segregation of Zn atoms to the interface until 100 % coverage was reached.

Quantitative image analysis of the HRTEM micrographs from the **Pd/$^{-}$ZnO** interface shows O termination of this interface. The coverage of the interfacial O layer is 100 %.

However, the theoretical calculation [Zaoui, 2004] suggested that, in both interfaces, a Zn-termination provides lowest interface energy (highest work of separation energy between Pd and Zn layers) at both interfaces. It is not possible to explain the experimental results that the O was selected as a terminating atomic species at the **Pd/$^{-}$ZnO** interface.

Source of Stabilization of the Pd/ZnO Interface

The disagreement between the experimental result and the theoretically expected result can be explained by considering a stabilizing mechanism of {0001}ZnO polar surfaces. Since, in the case of atomically flat {0001}ZnO surfaces, an electrostatic field generated by Zn-O dipoles diverges to infinity along the *c*-axis of ZnO, the {0001}ZnO surfaces which cannot grow in free space are inherently unstable. Noguera [Noguera, 2000] predicted that a partial coverage of the surface leads to an electrostatic charging of the surface which compensates the electrostatic field caused by the Zn-O dipoles, stabilizing the surface structure. Then, the ideal surface spatial atomic occupancy should be 75 %.

Both polar ZnO surfaces, the (0001)ZnO ($^{+}$**ZnO**) and the $(000\bar{1})$ZnO ($^{-}$**ZnO**) surface, were analyzed in detail with surface XRD via CTR measurement. These investigations showed that the coverage of the surface depends very sensitively on the surface preparation process. The oxygen prepared $^{+}$**ZnO** surface was Zn-terminated with a mean reduced coverage of 77 % (±5 %) at the specific condition. This coverage is in good agreement with that calculated by Noguera [Noguera 2000] as 75 %.

This means that {0001}ZnO surfaces actually become so stable by a virtual charge caused by the partial missing of the atoms in the toplayer. From point of view of local stability, however, one kind of atomic species should be preferred as the terminater. Nevertheless, the surface actually showed both kinds of terminations. Therefore, in {0001}ZnO surfaces, the global stability seems to be more important than the local stability.

After Pd deposition, both interfaces showed an atomically flatness, no impurity, and one kind of terminater with a spatial occupancy of ~100 %. This means that there exists no virtual charge, indicating that it is unable to cancel such an unwished electro static field.

This suggests that real charge transfer should exist across the interfaces for compensation of ZnO.

The charge distribution and bonding at both Pd/ZnO interfaces were investigated by semi-quantitative *first principle* DVXα calculations. The calculations revealed that the terminating Zn layer at the **Pd/$^{+}$ZnO** interface was charged negative and the terminating O layer at the **Pd/$^{-}$ZnO** positive. This is a change in interfacial charge distribution compared to the clean ZnO surfaces. In the case of the Zn-terminated **Pd/$^{+}$ZnO** interface, the structural defects (e.g. Zn vacancies at the interface) which are compensating the electrostatic field of the Zn-O dipoles are now not necessary because electrons are supplied from Pd to Zn. The electrostatic field of the Zn-O dipoles is now compensated via the charged interfacial Zn layer. Thus, segregation of Zn to the **Pd/$^{+}$ZnO** interface seems to take places. In the case of the O-terminated **Pd/$^{-}$ZnO** interface, electrons are supplied from O to Pd leading to a segregation of O to the interface.

After all, the {0001}ZnO polar planes in the interface as well as on the surface can be stabilized by 'charging mechanisms'.

The ionic charges of the terminating atomic species are quite unusual. This suggests that a local stability is completely neglected. These unusual ionic charges need to be quantitatively examined. Unfortunately, it was not yet done. Inherently, in bulk ZnO, an ionic radius of O is much bigger than that of Zn. However, the interfacial bonding distance (0.242 nm) between Pd-Zn layers was actually bigger than the interfacial bonding distance (0.214 nm) between Pd-O layers. This can be explained by considering the interfacial specific charging that Zn was negatively charged while O was positively charged. The difference of interfacial bonding distances seem to be related to such unusual interfacial ionic charges.

Furthermore, the bonding strength between a Pd and a ZnO generally seems to be weak, because a Pd is non-reactive metal and it is hard to oxidize. This means that such a weak interfacial bonding does not affect the total energy of a system. On the other hand, the {0001}ZnO surface is so unstable that surface energy can be diverged to infinity at special condition due to dipole moments. The electrostatic stabilization of the ZnO allows to decreasing largely the total energy of the system. Therefore, the local stability does not matter for the total energy of the system. That is why the **Pd/$^{-}$ZnO** interface cannot avoid selecting O-termination which provides appropriate surface charge.

The behavior of the Pd/ZnO interfaces seems to be dominated mainly by the global stabilizing mechanism which can contributes to stabilization of ZnO. At the same time, the terminating atomic species are chosen in order to make the appropriate interfacial charges

depending on surface polarity. This global mechanism seems to be related to 'the image charge theory [Ernst, 1994] (see subsection 2.1)' that an image charge in a metal allows to canceling an electrostatic field (in the metal) generated by oxide. This is also a global stabilization mechanism for decreasing a total energy of a system by an imaging potential.

Local Atomic Structure at the Pd/ZnO Interface

The local atomic structures can be summarized as followings. The lattice mismatch at both interfaces was accommodated by forming a misfit dislocation network on the interfaces in spite of the large lattice mismatch of 18 %. The experimentally determined distance between the cores of the dislocations is 1.5 nm and corresponds to the theoretical misfit dislocation distance.

It could be shown that at the **Pd/$^{+}$ZnO** interface the Zn atoms are positioned on Pd lattice sites. This geometry can be understood with considering the general stacking geometry between metals. Furthermore, *first principle* DVXα calculation revealed that the Pd-Zn bonding consists of mixture of ionic and covalent bonding and is formed with widely delocalized electron density distribution at the interface. The distance between the interfacial Pd layer and the terminating Zn layer increased by 0.02 nm compared to the distance between the $\{111\}_{Pd}$ lattice planes. The periodic relaxations at the **Pd/$^{+}$ZnO** interface were located only in the terminating Zn layer. That is why the Pd film holds an ideal single crystal without strain. In spite of the relaxation of interfacial Zn layer, however, the bulk region of ZnO does not have strain field. This seems to be attributed to high rigidity of ZnO crystal. The relaxed crystal can be explained by distinguishing the Zn-O bonding strength of bulk ZnO with that of the backbond of the interfacial atom of the ZnO.

Quantitative image analysis of the HRTEM micrographs from the **Pd/$^{-}$ZnO** interface revealed that the interfacial Pd and O atoms are located top-on-top and the distance between them is about 0.01 nm smaller than the distances in the Pd lattice. This geometry also can be understood with considering the general geometry of an oxide, because the terminating O atom has a dangling bond along the *c*-axis which should be terminated. This geometry can terminate the dangling bond by the interfacial Pd. Furthermore, theoretical calculation revealed that the Pd-O bonding consists of ionic bonding. In contrast to the **Pd/$^{+}$ZnO** interface, the lattice relaxations at the **Pd/$^{-}$ZnO** interface were located in the Pd. This is attributed to high elasticity of a Pd crystal.

Bonding Strength, Relaxation, and Film Growth

The following inequalities could be deduced from the theoretical calculations [Zaoui, 2004] of the bonding at the different interfaces:

$$^{1.}\text{Pd-}^{1.}\text{Zn (Zn-terminated surface)} > {}^{1.}\text{Pd-}^{1.}\text{O (O-terminated surface)}$$

(„1.“ means 1. layer at the interface or interfacial layer).

These differences in interfacial bonding result also in a different growth behavior of the Pd islands. In the case of the O-terminated interface large islands are formed, liquid-like coalescence is observed more early which indicates that the Pd atoms on this surface are more mobile (less strongly bonded).

Furthermore, a qualitative comparison of the *first principle* calculations with HRTEM results (relaxation behavior, termination) allows deducing the following inequalities for the interatomic bonding near the differently terminated interfaces:

$$[^{1.}\text{O-Zn} ; {}^{1.}\text{Pd-}^{1.}\text{Zn}] > {}^{1.}\text{Pd-}^{1.}\text{O} > {}^{1.}\text{Pd-Pd} > {}^{1.}\text{Zn-O}$$

or

$$^{1.}\text{Pd-}^{1.}\text{Zn} > {}^{1.}\text{Pd-}^{1.}\text{O} > {}^{1.}\text{O-Zn} > {}^{1.}\text{Pd-Pd} > {}^{1.}\text{Zn-O}$$

From these inequalities one obtains that the $^{1.}$Zn-O bond is the weakest bond in the region near the interface. The inequality $^{1.}$O-Zn > $^{1.}$Zn-O indicates why the Zn terminated surface is mechanically softer than the O terminated surface.

This result is an impressive example demonstrating how different terminated oxide surfaces strongly influence the formation of interfacial defects. These differences will also be reflected in different physical properties of the interfaces. In the case of the more strongly bonded **Pd/$^{+}$ZnO** interface, epitaxial strain is transferred into the ZnO crystal. This is due to the relatively weak $^{1.}$Zn-O bond in ZnO. The more weekly bonded **Pd/$^{-}$ZnO** interface behaves different. The relatively weak $^{1.}$Pd-Pd bond favors relaxations in the Pd.

This shows how the growth behavior can be tuned by selecting the termination of the ZnO surface.

Final Conclusion For the Pd/{0001}ZnO Interfaces

Depending on surface polarity the terminating atomic species are adjusted in such a manner that the total energy of the Pd/ZnO system (especially, the surface energy of ZnO) is

minimized. This also results in the establishment of an interfacial local structure that preserves high geometrical coherency and a chemically interactive geometry as a function of interfacial termination, in the Pd/ZnO system.

Appendices

A: CTR Simulation

The simple situation described in the preceding section 3.2 may not always represent reality. Things that may occur are [Vileg, 2001]:

1. the surface layer covers the bulk only partly
2. more than one type of surface layer is present (rarely occurs)
3. several symmetry-related surface unit cells are present
4. the crystal (bulk + surface) is rough.

All these situations can be dealt with, but a more complicated expression is necessary for F_{sum}. Fig. a.1 schematically shows how different parts of the crystal may be covered by different surface layers.

Define the following parameters:

S scale factor,

R roughness factor,

f_s fraction of crystal that is covered by surface layer,

f_{s2} fraction of f_s that is covered by second type of surface layer (normally 0),

N_d total number of symmetry-related domains,

α_j occupancy of domain j.

When calculating F_{sum}, the following structure factors play a role:

$F_{b,j} = F_{b,j} + iF_{b,j}$ structure factor of j-th domain of the bulk

$F_{s,j} = F_{s,j} + iF_{s,j}$ structure factor of j-th domain of first surface unit cell

$F_{s2,j} = F_{s2,j} + iF_{s2,j}$ structure factor of j-th domain of second surface unit cell.

The important structure factors are now:

$$F_{bulk} = SR\left[\sum_j \alpha_j F_{b,j}^2\right]^{1/2}, \qquad \text{(a-1)}$$

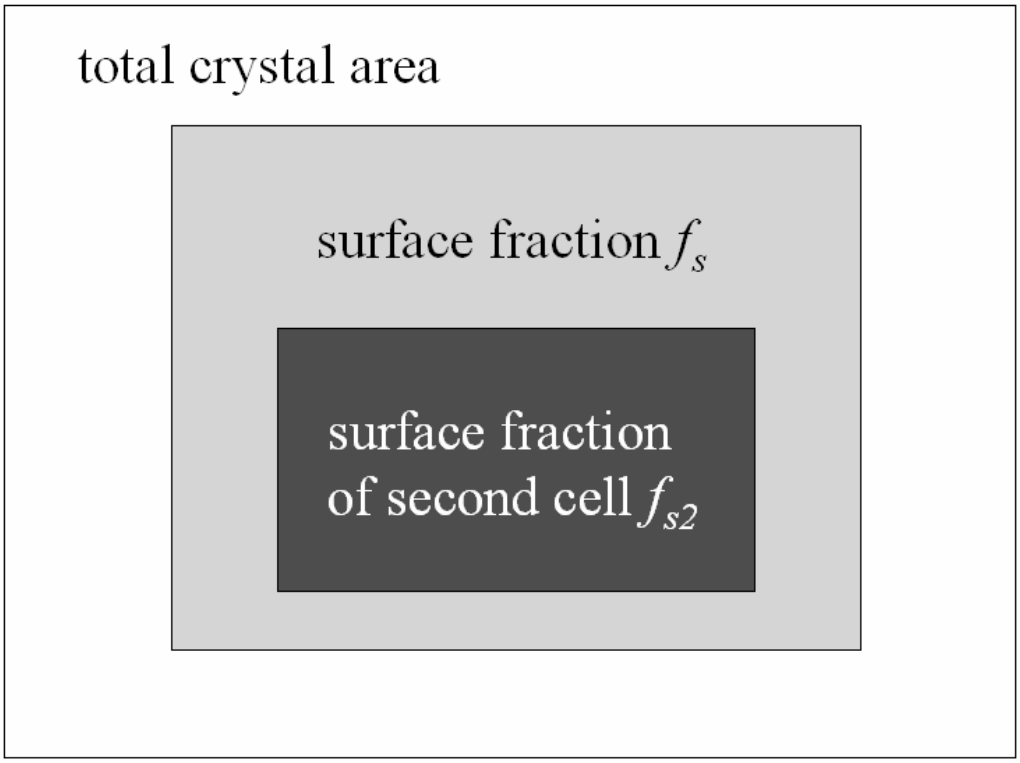

Fig. a.1 A schematic top view of a crystal that is partially covered by two different surface unit cells.

$$F_{surf} = SR\left[f_s(1-f_{s2})\sum_j \alpha_j F_{s,j}^2 + f_s f_{s2}\sum_j \alpha_j F_{s2,j}^2 \right]^{1/2}, \quad \text{(a-2)}$$

$$F_{sum} = SR\left[(1-f_s)\sum_j \alpha_j F_{b,j}^2 + f_s(1-f_{s2})\sum_j \alpha_j (F_{s,j}+F_{b,j})^2 + f_s f_{s2}\sum_j \alpha_j (F_{s2,j}+F_{b,j})^2 \right]^{1/2}. \quad \text{(a-3)}$$

ROD always computes all three structure factors simultaneously. In these expressions, it is assumed that the symmetry-related domains are completely structurally uncorrelated and that therefore their contributions add incoherently. Depending on the distribution of the domains, it may also happen that the various contributions need to be added coherently. In that case first the summation is performed and after that the result is squared:

$$F_{sum,coh} = SR\left[(1-f_s)[\sum_j \alpha_j F_{b,j}]^2 + f_s(1-f_{s2})[\sum_j \alpha_j (F_{s,j}+F_{b,j})]^2 + f_s f_{s2}[\sum_j \alpha_j (F_{s2,j}+F_{b,j})]^2 \right]^{1/2}. \quad \text{(a-4)}$$

ROD allows choosing either of these situations.

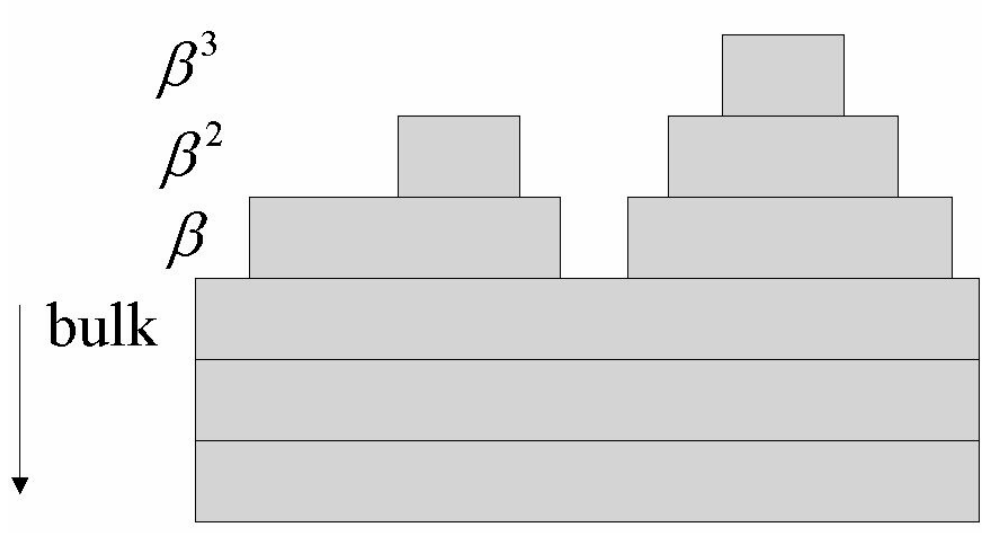

Fig. a.2 Surface roughness according to the so-called β model [Vileg, 2001].

A) Surface Roughness

Approximate β-model

Various methods are available to include the effect of roughness. In general, surface roughness always leads to a decrease in scattered intensity. A very simple roughness model is the so-called β-model, in which surface level n has occupancy β^n, see Fig. a.2.

For the simple cubic case illustrated in Fig. a.2 and assuming that each layer consists of a complete unit cell it is straightforward to derive the roughness factor R by which the structure factor is reduced. For non-cubic crystals, or if, within a unit cell, the occupancy varies from layer to layer, the calculation becomes more complicated. A formula that nevertheless is valid for many cases is:

$$R = \frac{1-\beta}{\left[(1-\beta)^2 + 4\beta \sin^2 \frac{\pi(l - l_{Bragg})}{N_{Layers}}\right]^{1/2}}, \qquad \text{(a-5)}$$

where l_{Bragg} is the l-value of the nearest Bragg peak and N_{layers} is the number of layers in the unit cell. Equation (a-5) works fine if N_{layers} denotes the number of equidistant layers within the unit cell. This situation is described within ROD as 'approximated beta'. Different roughness distributions, or an exact calculation within the β-model, consume more computer time. It is therefore convenient to use equation (a-5) until proven otherwise.

B) Symmetry-Related Domains

It may happen that on a surface many domains occur that are symmetry-related. E.g. a (100)Si surface that is (2 × 1) reconstructed will in general also have (1 × 2) domains (with normally the same occupancy). At 'fractional-order' positions, only one of the two domains contributes, but at CTR positions one has to add the contributions of both. Rather than adding a second unit cell to the computation, it is more convenient to add the structure factor for the original unit cell, but computed for the corresponding, symmetry-related diffraction indices. This is explained below.

Suppose the surface has N_d domains. The structure factor of domain n is given by (ignoring the atomic scattering factor and the Debye-Waller factor):

$$F_{n,\vec{H}} = \sum_j \exp 2\pi i \vec{r}_{n,j} \cdot \vec{H} \,, \tag{a-6}$$

Let matrix $\vec{A}_n$ transform the coordinates of the first unit cell into that of number n:

$$\vec{r}_{n,j} = \vec{A}_n \vec{r}_{1,j} \,. \tag{a-7}$$

Then,

$$F_{n,\vec{H}} = \sum_j \exp 2\pi i \vec{A}_n \vec{r}_{1,j} \cdot \vec{H} \,. \tag{a-8}$$

Instead of transforming the real space coordinates, we can arrive at the same structure factor by transforming the diffraction indices, since:

$$\vec{A}_n \vec{r}_{1,j} \cdot \vec{H} = \vec{r}_{1,j} \cdot \vec{A}_n^{-1} \vec{H} \equiv \vec{r}_{1,j} \cdot \vec{H}_n^{'} \text{, with } \vec{H}_n^{'} = \vec{A}_n^{-1} \vec{H} \,. \tag{a-9}$$

In the summation over all domains we can thus use one unit cell, but calculate the corresponding $\vec{H}_n^{'}$ for each domain.

More detailed information can be found at the web site:

www.esrf.fr/computing/scientific/joint_projects/ANA-ROD/index.html

B: HREM Image Simulation by the Multi Slice Algorithm

HREM images the projected specimen structure into a complicated interference pattern, because the image procedure is strongly non linear. The main causes for the non-trivial image interpretations are dynamical scattering, the partial coherency, and the nonlinear image formation by phase contrast. Therefore, it is necessary to compare the experimental image with the simulated image based on the multi slice method [Cowley, 1957], [Horiuchi, 1978], [Ishizuka, 1987], [Stadelmann, 1987] for a correct image interpretation.

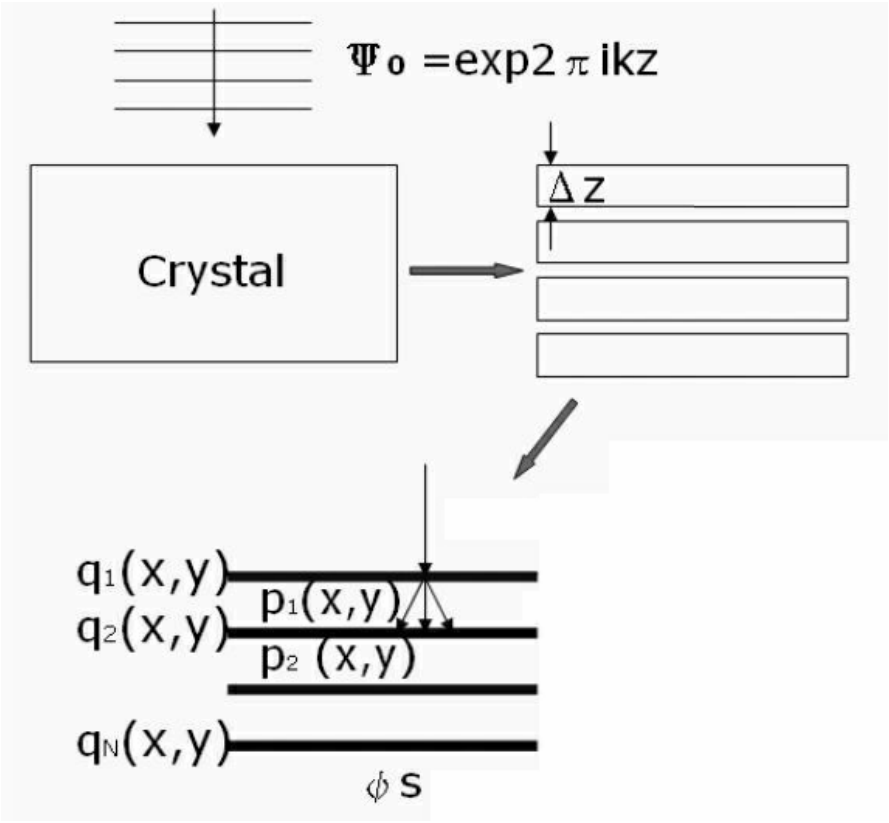

Fig. a.3 Schematic diagram of the scattering process in each slice which can be divided into two processes that is the first phase shift $q(x, y)$ due to different optical distances given by different atomic potential and the second phase shift $p(x, y)$ due to wave propagation. [Tanaka, 2000]

Change of scattering amplitude due to interactions between the transmitted wave and the scattered wave or between the scattered waves is known as the dynamical diffraction effect. Although this dynamical diffraction effect can be mathematically treated [Darwin, 1914], [Howie, 1961] [Bethe, 1928], here it is being described by the so-called multi slice method [Horiuchi, 1978], [Ishizuka, 1987] which is a physical optical method suggested by Cowley and Moodie [Cowley, 1957] and it is widely used for HRTEM image simulation.

In the multi slice method a specimen is sliced to thin slices along the direction of the e-beam and then for each thin slice kinematical scattering can be assumed. Usually, the thickness of each slice should be 0.2 nm ~ 0.5 nm which corresponds to an actual unit cell size along the direction of the e-beam. The scattering process in each slice can be divided into two processes: (i) the first phase shift $q(x, y)$ due to different optical distances given by different atomic potential and, (ii) the second phase shift $p(x, y)$ due to wave propagation as shown in Fig. a.3.

Fig. a.3 shows N slices with thickness of Δz. For the algorithm it is assumed that the 3-dimensional atomic inner potential can be projected to a 2-dimensional potential V_p either

onto upper or lower surface of each slice, suggesting that it forms a phase grating which results in the phase shift $q(x, y)$. This approximation is appropriate, because the thickness of each slice is extremely thin. Incident beam is assumed as a plane wave with amplitude of 1. The wave function of electron after penetrating into the first phase grating is given by equation (a-10).

$$\psi(x, y) = \exp i\frac{\pi}{\lambda E}\int V(x, y, z)dz = \exp i\sigma V_p(x, y) = q_1(x). \tag{a-10}$$

It assumes that subsequently this electron wave propagates during the distance Δz in the medium which has average inner potential V_0. This Fresnel propagation can be expressed as the convolution operation shown in equation (a-11).

$$\begin{aligned}\psi(x, y) &= 1/i\lambda d\iint \psi_s(x_0, y_0)\exp[2\pi i\{(x-x_0)^2 + (y-y_0)^2\}/2\lambda d]dx_0 dy_0 \\ &= \psi_s(x_0, y_0)\otimes 1/d\lambda \exp[2\pi i(x^2 + y^2)/2\lambda d]\end{aligned}, \tag{a-11}$$

$$f(x)\otimes g(x) = \int f(x-x')g(x')dx'. \tag{a-12}$$

The Gaussian function behind the convolution operation in equation (a-11) can be defined as

$$p(x) = (i/\lambda\Delta z)\exp[ik(x^2 + y^2)/2\Delta z]. \tag{a-13}$$

Therefore, the wave function before reaching at the next phase grating is given by equation (a-14).

$$q_1(x)\otimes p_1(x). \tag{a-14}$$

Finally, after penetrating the N^{th} phase grating, the wave function is given by equation (a-15).

$$\psi_s(x) = [\ldots[[q_1(x)\otimes p_1(x)]\times q_2(x)]\otimes p_2(x)]\ldots\times q_N(x). \tag{a-15}$$

In a multi slice method, the calculation of the wave function at an exit surface of the specimen is based on these approximations.

References

[Adachi, 1978] H. Adachi, M. Tsukada and C. Satoko, J. Phys. Soc. Japan., 45, 875 (1978).

[Adachi, 1998] H. Adachi, Y. Owada, I. Tanaka, H. Nakamatsu, and M. Mizuno, '*Basics of DVXα Molecular Orbital Calculation*', Sankyoshuppan, Tokyo, Japan (1998).

[Ashby, 1963] M. F. Ashby and G. C. Smith, J. Inst. Met. 91 (1963) 182.

[Backhaus-Ricoult, 2003] M. Backhaus-Ricoult, L. Samet, M. F. Trichet, M. J. Hÿtch, and D. Imhoff, J. of Solid State Chemistry, 173, 1 , June, 172-188 (2003).

[Backhaus-Ricoult, 1992] M. Backhaus-Ricoult and S. Hagège, Acta metall. mater. 40 (1992) S139.

[Banhart, 1996] F. Banhart and P. M. Ajayan, Nature 382 (1996) 433.

[Bauer, 1958] E. Bauer, Z. f. Krist. 110, 372 (1958), 110, 385 (1958).

[Benedek, 1996] R. Benedek, M. Minkoff, and L. H. Yang, Phys. Rev., B54, 7697 (1996).

[Bethe, 1928] H. Bethe, ann. Phys., 87, 55 (1928).

[Bishop, 1968] G. H. Bishop and B. Chalmers, Scripta Met. 2 (1968) 133.

[Bollmann, 1980] W. Bollmann, '*Crystal Defects and Crystalline Interfaces*', Springer-Verlag (1980).

[Bonnet, 1975a] R. Bonnet and F. Durand, J.Phys., 36 (1975) c4-441.

[Bonnet, 1975b] R. Bonnet and F. Durand, Phil. Mag., 32 (1975) 997.

[Bragg, 1940] W. L. Bragg, Proc. R. Soc. 52 (1940) 54.

[Brandon, 1964] D. G. Brandon, B. Ralph, S. Ranganathan and M. S. Wald, Acta Metall. 12 (1964) 813.

[Brandon, 1966] D. G. Brandon, Acta Met., 14 (1966) 1479.

[Burgers, 1940] J. M. Burgers, Proc. R. Soc. 52 (1940) 23.

[Chalmers, 1971] B. Chalmers and H. Gleiter, Phil. Mag. 24 (1971) 1541.

[Chang, 1974] S. C. Chang and P. Mark, Surf. Sci., 46, 293 (1974).

[Chen, 1994] F. R. Chen, S. K. Chiou, L. Chang, and C. S. Hong, Ultramicroscopy 54 (1994) 179.

[Cowley, 1957] J. M. Cowley and A. F. Moodie, Acta Crystallog., 10, 609 (1957).

[Cowley, 1972] J. M. Cowley and S. Iijima, Z. Naturforsch., 27, 445 (1972).

[Darwin, 1914] C. G. Darwin, Philos. Mag., 27, 315 (1914).

[Dehm, 1996] G. Dehm, F. Ernst, J. Mayer, G. Möbus, H. Mullejans, F. Phillipp, C. Scheu, and M. Rühle, Z. Metallkd., 87 (1996) 11.

[Disko, 1991] M. M. Disko, C. C. Ahn, and B. Fultz, '*Transmission Electron Energy Loss Spectrometry in Mataterial Science*', TMS, USA (1991).

[Du, 2001] K. Du, Y. Rau, N. Y. Jin-Phillipp, and F. Phillip, J. Mater. Sci. Technol., Vol. 18, No. 2, 135 (2001).

[Dulub, 2003] O. Dulub, U. Diebold, and G. Kresse, Phys. Rev. Lett., V90, N1, 016102 (2003).

[Eastman, 1989] J. A. Eastman and M. Rühle, Ceram. Eng. Sci. Proc., (1989) 10, 1515.

[Ernst, 1991] F. Ernst, P. Pirouz, and A. H. Heuer, Phil. Mag., A63 (1991) 259.

[Ernst, 1995] F. Ernst, Materials Science and Engineering, R14, No.3, Apr 1 (1995).

[Ernst, 1996] F. Ernst, Z. Metalkd, (1996).

[Evans, 1990] A. G. Evans and M. Rühle, MRS. Bull., October 1990.

[Evans, 1990] A. G. Evans, D. R. Mumm, J. W. Hutchinson, G. H. Meier, and F. S. Pettit, Prog. Mater. Sci. 46 (2001) 505.

[Fecht, 1985] H. J. Fecht and H. Gleiter, Acta Metall., 33 (1985) p. 557.

[Fecht, 1989] H. J. Fecht, Phil. Mag. Let., Vol. 60 (1989) p. 81.

[Fecht, 1992] H. J. Fecht, Acta Metall. Mat., 40 (1992) S39.

[Finnis, 1990] M. Finnis, A. M. Stoneham, and P. W. Tasker, in '*Metal-Ceramic Interfaces*', Acta-Scripta Metall. Proc. Series 4 (1990) 35.

[Finnis, 1996] M. W. Finnis, J. Phys. Condens. Matter, 8, 5811 (1996).

[Fischmeister, 1988] H. F. Fischmeister, W. Mader, B. Gibbesch, and G. Elssner, in '*Interfacial Structure, Properties and Design*', Mat. Res. Soc. Symp. Proc., 12 (1988) 529.

[Fischmeister, 1992] H. F. Fischmeister, W. Mader, B. Gibbsch, and G. Elssner, Mat. Res. Soc. Symp. Proc., 122 (1992).

[Florjancic, 1985] M. Florjancic, W. Mader, M. Rühle, and M. Turwitt, Journal de Physique, C4-129 (1985).

[Frank] F. C. Frank, Report of the Symposium on the Plastic Deformation of Crystalline Solids, Carnegie Institute of Technology, Pittsburg, USA.

[Friedel, 1926] G. Friedel, Lecons de Cristallographie, Paris, Berger Lerrault (1926).

[Gao, 1990] Y. Gao and K. L. Merkle, J. Mater. Res., 5 (1990) 1995.

[Gleiter, 1971] H. Gleiter, Phys. Stat. Sol. (b) 45 (1971) 9.

[Groen, 1998] H. B. Groen and J. T. M. De Hosson, Scri. Mat. Vol38, 5 (1998) pp. 769-773.

[Guterkunst, 1994] G. Guterkunst, J. Mayer, and M. Rühle, MRS. Symp. Proc., Vol319 (1994) 3.

[Han, 2002] J. Han, J. European Ceram. Soc., 22, 49-59 (2002).

[Hansen, 1958] Hansen, '*Binary Phase Diagram*', p. 1131 (1958).

[Hargreaves, 1929] F. Hargreaves and R. J. Hills, J. Inst. Met. 41 (1929) 257.

[Heiland, 1963] G. Heiland, P. Kunstmann, and H. Pfister, Zeitschrift für Physik, 176, 485-497 (1963).

[Henke, 1993] B. L. Henke, E. M. Gullikson, and J. C. Davis. '*X-ray interactions*', Atomic Data and Nuclear Data Tables Vol. 54 (no.2), 181-342 (July 1993).

[Hila, 1982] F. Hila and M. Gillet, Thin Solid Films, 98 (1982) 23.

[Hirsch, 1965] P. B. Hirsch, A. Howie, R. B. Nicholson, D. W. Pashley, and M. J. Whelan, '*Electron Microscopy of Thin Crystals*', Butterworths (1965).

[Hoekstra, 1998] J. Hoekstra and M. Kohyama, Phys. Rev., B57, 2334 (1998).

[Hong, 1994] T. Hong, J. R. Smith and D. J. Srolovitz, Acta Met. Mater., 43, 7, 2721 (1995).

[Horiuchi, 1978] S. Horiuchi, Y. Matsui, Y. Bando, T. Katsuta, and I. Matsui, J. Electron Microsc., 27, 39 (1978).

[Horiuchi, 1988] S. Horiuchi, '*High Resolution Electron Microscopy*', Kyoritsushuppan, Tokyo, Japan (1988).

[Howie, 1961] A. Howie and W. J. Whelan, Proc. Roy. Soc., A263, 217

(1961).

[Huang, 1988] X. Y. Huang, W. Mader, J. A. Eastman, and R. Kirchheim, Scripta metall., 22 (1988) 1109.

[Ichimori, 1996a] T. Ichimori, T. Katoh, H. Ichinose, K. Ito, and Y. Ishida, Proc.of JIMIS-8 (1996) pp. 359-362.

[Ichimori, 1996b] T. Ichimori, '*Investigation of Metal/Ceramics Interfaces by UHRTEM*', PhD thesis, the University of Tokyo, Tokyo, Japan (1996).

[Ichinose, 1981] H. Ichinose and Y. Ishida, Philo. Mag., A43, 1253 (1981).

[Ichinose, 1985] H. Ichinose and Y. Ishida, J. Phys., C4-39 (1985).

[Ichinose, 1994] H. Ichinose, T. Ichimori, H. Ishii, Y. Ishida and W. Mader, C. Physique, Colloque C1 (1994) No. 1.

[Ichinose, 1994b] H. Ichinose, H. Ishii, T. Ichimori, and Y. Ishida, Proc. 13th Int. Congr. EM, Paris, 3 (1994) 335.

[Ichinose, 1998] H. Ichinose and M. Nakanose, Thin Solid Films, 319, 87 (1998).

[Ikuhara, 1994] Y. Ikuhara, P. Pirouz, A. H. Heuer, S. Vadavalli, and C. P. Flynn, Phil. Mag. A, Vol. 70 (1994) 75.

[Ikuhara, 1995] Y. Ikuhara, P. Pirouz, A. H. Heuer, S. Yadavalli, and C. P. Flynn, Phil. Mag. A, Vol. 72 (1995) 179.

[International Tables, 1974] '*International Tables for X-ray Crystallography*', Vol. IV, the Kynoch Press, UK (1974).

[Ishida, 1969] Y. Ishida, T. Hasegawa and F. Nagata, J. Appl. Phys., 40 (1969) 2182.

[Ishida, 1987] Y. Ishida, '*Fundamentals of Diffusion Bonding, Studies in Physical and Theoretical Chemistry 48*', Elsevier, Amsterdam (1987).

[Ishida, 1990] Y. Ishida, Annual Report of Japan Institute of Metal, 11, 29 (1990).

[Ishida, 1990b] Y. Ishida, J. Wang, and T. Suga, ISIJ. Inter. 30 (1990) 1041.

[Ishida, 1992] Y. Ishida, J. Wang, and T. Suga, Acta. Metall. Mat., 40 (1992) S289.

[Ishizuka, 1977] K. Ishizuka and N. Uyeda, Acta Cryst., A33, 740 (1977).

[Ishizuka, 1980] K. Ishizuka, Ultramicroscopy, 5, 55 (1980).

[Ishizuka, 1987] K. Ishizuka, Annual Report of Japan Cryst. Soc., 29, 209 (1987).

[Jackson, 1974] K. A. Jackson, J. Cryst. Growth, 24/25, 130 (1974).

[Jedrecy, 2000] N. Jedrecy, M. Sauvage-Simkin, and R. Pinchaux, Appl. Surf. Sci., 162/163, 69-73 (2000).

[Johnson, 1982] K. H. Johnson and S. V. Pepper, J. Appl. Phys. 53 (1982) 6634.

[Kamet, 1988] S. V. Kamet, J. P. Hirth, and B. Carnahan, Mater. Res. Soc. Symp. Proc. 102, 55 (1988).

[Kawasaki, 1994] M. Kawasaki, K. Takahashi, T. Maeda, R. Tsuchiya, M. Shinohara, O. Ishiyama, T. Yonezawa, M. Yoshimoto, and H. Koinuma, Science, 266, 1540 (1994).

[Kirchheim, 1980] R. Kirchheim and R. B. McLellan, J. EIectrochem. Soc., 127 (1980) 2419.

[Klomp, 1984] J. T. Klomp, British Ceram. Proc., No. 34 (1984) 249.

[Klomp, 1987] J. T. Klomp, '*in Fundermentals of Diffusion Bonding*', Y. Ishida (ed.), Elsevier, Amsterdam (1987) 3.

[Knauss, 1991] D. Knauss and W. Mader, Ultramicroscopy 37 (1991) 247.

[Kohyama, 1999] M. Kohyama, in '*Electronic Structure in GB and Interface of Physics of Ceramics Material*', Y. Ikuhara (ed.), Nikkankogyoshinbun, Tokyo, Japan (1999).

[Kröger, 1974] F. A. Kröger, '*The chemistry of imperfect crystals*', Vol. 2, pp. 743-752 (1974).

[Kronberg, 1964] M. L. Kronberg and F. M. Wilson, Trans. AIME 85 (1964) 26.

[Kruse, 1996] C. Kruse, M. W. Finnis, J. S. Lin, M. C. Payne, V. Y. Milman, A. D. Vita, and M. J. Gillan, Phil. Mag. Lett., 73, 377 (1996).

[Kurata, 2000] H. Kurata, '*Electron Microscopy Seminar Text*', The University of Tokyo, Tokyo, Japan (2000).

[Levy, 1969] J. Levy, Phys. Stat. Sol., 31 (1969) 193.

[Lu, 1992] P. Lu and F. Cosandey, Acta Metall. Mater. 40 (1992) S259.

[Mader, 1989] W. Mader, Z. Metallkd., 80 (1989) 139.

[Mader, 1992] W. Mader, Z. Metallkd. 83 (1992) 7, 47.

[Maki, 2001] H. Maki, N. Ichinose, N. Ohashi, H. Haneda, and J. Tanaka, J. Cryst. Growth, 229, 114-118 (2001).

[Matthews, 1970] J. W. Matthews, S. Mader, and T. B. Light, J. Apply. Phys 42 (1970) 3800.

[Matthews, 1974] J. W. Matthews and A. E. Blakeslee, J. Cryst. Growth, 27, 118 (1974).

[Mayer, 1990] J. Mayer, W. Mader, D. Knauss, F. Ernst ,and M. Rühle, Mat. Res. Soc. Symp. Proc., 183 (1990).

[Mayer, 1990] J. Mayer, J. A. Dura, C. P. Flynn, M. Rühle, Surf. Coatings Techn., 43/44 (1990) 199.

[Mayer, 1992] J. Mayer, G. Gutekunst, G. Möbus, J. Dura, C. P. Flynn, M. Rühle, Acta Met. Mater., 40, S217 (1992).

[McDonald, 1965] J. E. McDonald and J. G. Eberhart, Trans. AIME., 233 (1965) 512.

[Merkle, 1990] K. L. Merkle, '*in Metal-Cermic Interfaces*', Acta-Scripta Metall. Proc. Series 4 (1990) 242.

[Merkle, 1992] K. L. Merkle, M. I. Bukket, and Y. Gao, Acta metall., Vol. 40 (1992) S249.

[Möbus, 1996] G. Möbus, Ultramicroscopy, 65, 205 (1996).

[Möbus, 1997] G. Möbus, '*IDIM user guide*', MPI-MF, Stuttgart, Germinay (1997).

[Murakami, 2003] K. Murakami, M. Saito, E. Takuma, and H. Ichinose, J. Electron Microscopy, 52 (1), 27-32 (2003).

[Muschik, 1992] T. Muschik and M. Rühle, Phil. Mag., A, 65 (1992) 363.

[Nakajima, 1980] K. Nakajima, S. Komiya, K. Akita, T. Yamaoka and O. Ryuzan, J. Electrochem. Soc., 127, 1568 (1980).

[Nakajima, 1982] K. Nakajima, S. Yamaguchi, and K. Akita, Jpn. J. Appl. Phys., 21, L237 (1982).

[Nakajima, 1985] K. Nakajima and J. Okazaki, J. Electrochem. Soc., 132, 1424 (1985).

[Nakajima, 2002] K. Nakajima, '*Mechanism of Epitaxial Growth*', Kyoritsushuppan Tokyo, Japan (2002).

[Necker, 1988] G. Necker and W. Mader, Phil. Mag. Lett., 58 (1988) 205.

[Noguera, 2000] C. Noguera, J. Phys., Condens. Matter, 12 (2000) R367-

410.

[Ochs, 2000] T. Ochs, '*Theoretische Untersuchungen der atomaren und elektronischen Struktur an Korngrenzen in kubisch raumzetrierten Übergangsmetallen und an Metall/Keramik-Grenzflächen*', PhD thesis, Universität Stuttgart, Stuttgart, Germany (2000).

[Oh, 2004] S. H. Oh, private communication (2004).

[Ohuchi, 1987] F. S. Ohuchi, R. H. French, and R. V. Kasowski, J. Appl. Phys., 62 (1987) 2286.

[Ohuchi, 1991] F. S. Ohuchi and M. Kohyama, J. Am. Ceram. Soc. 74, 1163 (1991).

[Parker, 1998] T. M. Parker, N. G. Condon, R. Lindsay, F. M. Leibsle, and G. Thornton, Surf. Sci., 415, L1046 (1998).

[Pennycook, 1991] S. J. Pennycook and D. E. Jesson, Ultramicroscopy, 37, 14 (1991).

[People, 1985] R. People and J. C. Bean, Appl. Phys. Lett., 47, 322 (1985).

[Phillipp, 1994] F. Phillipp, R. Höschen, M. Osaki, G. Möbus, and M. Rühle, Ultramicroscopy 56, 1 (1994).

[Ranganathan, 1966] S. Ranganathan, Acta Cryst. 21 (1966) 197.

[Read, 1950] W. T. Read and W. Schockley, Phys. Rev. 78 (1950) 275.

[Richter, 2000] G. Richter, '*Characterisierung der Keimbildung und des Wachstumsdünner Pd-Schichten auf $SrTiO_3$(001)-Oberfläche*', PhD thesis, Universität Stuttgart, Stuttgart, Germany (2000).

[Robinson, 1985] I. K. Robinson, Phys. Rev., B33, 6, March (1986).

[Rodrigues, 1983] J. A. Rodrigues and R. Kirchheim, Scripta Metal., 18 (1983) 347.

[Romanov, 1998] A. E. Romanov, T. Wagner, and M. Rühle, Scripta Materialia 38, 869 (1998).

[Rosenhain, 1913] W. Rosenhain and J. C. W. Humphrey, J. Iron Steel Inst. 41 (1913) 257.

[Rühle, 1989] M. Rühle and A. G. Evans, Mat. Sci. Eng. A107 (1989) 187.

[Rühle, 1989b] M. Rühle, A. G. Evans, M. F. Ashby, and J. P. Hirth, '*Metal-Ceramics Interface*s', 4. Acta-Scripta Metallurgica

Proc., Pergamon, (1990).

[Rühle, 1996] M. Rühle, J. European Ceram. Soc., 16, 353 (1996).

[Saito, 2001] M. Saito, Master thesis, The University of Tokyo, Tokyo, Japan (2001).

[Saito, 2004] M. Saito, T. Wagner, N. Kasper, A. Stierle, and M. Rühle, Proc. APEM-8 Int. Conf., p. 446, Kanazawa, Japan (2004).

[Sakamoto, 1986] T. Sakamoto and G. Hashiguchi, Jpn. J. Appl. Phys., 25, L78 (1986).

[Scherzer, 1949] O. Scherzer, J. Appl. Phys., 20, 119 (1949).

[Scheu, 2000] C. Scheu, W. Stein, and M. Rühle, Phys. Stat. Sol., (b) 222, 199 (2000).

[Scheu, 2002] C. Scheu, J. Microscopy, Vol. 207, Pt 1, 52, July (2002).

[Schönberger, 1992] U. Schönberger, O. K. Anderson, and M. Methfessel, Acta metall. Mater., 40 (1992) S1.

[Schweinfest, 1998] R. Schweinfest, F. Ernst, T. Wagner, and M. Rühle, J. of Microsc., 194, p. 142 (1998).

[Seifert, 1996] W. Seifert, N. Carlsson, M. Miller, M-E. Pistol, L. Samuelson, and L. R. Wallenberg, Prog. Cryst. Growth and Charact., 33, 423 (1996).

[Shashkov, 1995] D. A. Shashkov and D. N. Seidman, Phys. Rev. Lett., 75, 268 (1995).

[Shashkov, 1996] D. A. Shashkov, D. K. Chan, R. Benedek, and D. N. Seidman, Proc. JIMIS-8, (1996) 85.

[Shieu, 1990] F. S. Shieu and S. L. Sass, Acta Metall. Mater., 38 (1990) 1653.

[Shindo, 1996] D. Shindo and K. Hiraga, '*High Resolution Microscopy for Material Evaluation*', Kyoritushuppan, Tokyo, Japan (1996).

[Shindo, 1999] D. Shindo and T. Oikawa, '*Analytical Electron Microscopy for Material Evaluation*', Kyoritushuppan, Tokyo, Japan (1999).

[Sinnott, 2003] S. B. Sinnott and E. C. Dickey, Mat. Sci. and Eng., R43 (2003) 1-59.

[Smith, 1976] D. A. Smith and R. C. Pond, Int. Metal Rev. 205 (1976) 61.

[Smith, 1994] J. R. Smith, T. Hong, and D. J. Srolovitz, Phys. Rev. Lett., 72, 4021 (1994).

[Smith, 2000] J. R. Smith and W. Zhang, Acta Mater., 48, 4395 (2000).

[Stadelmann, 1987] P. A. Stadelmann, Ultramicroscopy, 21, 131 (1987).

[Stierle, 2005] A. Stierle, A. Steinhäuser, A. Rühm, F. U. Renner, R. Weigel, N. Kasper, and H. Dosch, Review of Scientific Instruments, *in print*.

[Stoneham, 1985] A. M. Stoneham and P. W. Tasker, Oxide Interfaces: Theory of Oxide-Oxide and Oxide-Metal Interfaces, (1985) 155.

[Stoneham, 1987] A. M. Stoneham and P. W. Tasker, Ceramic Microstructures 1987 J. A. Pask and A. G.Evans(ed.), NewYork Plenum.

[Strecker, 1993] A. Strecker, U. Salzberger, and J. Mayer, Praktische Metallographie, 30, 482 (1993).

[Sutton, 1995] A. P. Sutton and R. W. Balluffi, '*Interfaces in Crystalline Materials*', Clarandon Press, Oxford (1995).

[Takeda, 1978] Y. Takeda and A. Sasaki, J. Cryst. Growth, 45, 257 (1978).

[Tanaka, 2000] N. Tanaka, Electron Microscopy Seminar Text, The University of Tokyo, Tokyo, Japan (2000).

[Tasker, 1987] P. W. Tasker and A. M. Stoneham, J. Chimie Phys., 84, 149 (1987).

[Tchernychova, 2004] E. Tchernychova, '*Transmission Electron Microscopy Investigations of Thin Mo and Pd Films Grown on $SrTiO_3$ Substrates*', PhD thesis, Universität Stuttgart, Stuttgart, Germany (2004).

[Tchernychova, 2003] E. Tchernychova, C. Scheu, T. Wagner, Q. Fu, and M. Rühle, Surf. Sci. 542 (2003) 33-44.

[Trampert, 1992] A. Trampert, F. Ernst, C. P. Flynn, H. F. Fischmeister, and M.Rühle, Acta Metall. Mater., 40 (1992) S227.

[Tricker, 1995a] D. M. Tricker and W. M. Stobb, Phil. Mag. A, Vol. 71 (1995) 1037.

[Tricker, 1995b] D. M. Tricker and W. M. Stobb, Phil. Mag. A, Vol. 71 (1995) 1051.

[Trumble, 1989] K. P. Trumble and M. Rühle, Acta Metal., 37 (1989) 853.

[Uemura, 1987] Y. Uemura, Y. Inomata, and H. Ichinose, J. Cera,. Soc. Japan, 95, 788 (1987).

[van Benthem, 2002] K. van Benthem, '*Electron Microscopic Investigations of the Bonding Behaviour of Metals on $SrTiO_3$ Substrates*', PhD thesis, Universität Stuttgart, Stuttgart, Germany (2002).

[Van der Merwe, 1962] J. H. Van der Merwe, J. Appl. Phys., 34, 123 (1962).

[Vlieg, 2000] E. Vlieg, J. Appl. Cryst. 33, 401 (2000).

[Vlieg, 2001] E. Vlieg, '*A concise ROD manual*', Nijmegen, the Netherlands, June (2001).

[Wagner, 2001] T. Wagner, A. D. Polli, G. Richter, and H. Stanzick, Z. Metallkd., 92, 7 (2001).

[Wagner, 2001b] T. Wagner, G. Richter, and M. Rühle, J. Appl. Phys., V89, N5, 2606 (2001).

[Wander, 2001] A. Wander, F. Schedin, P. Steadman, A. Norris, R. McGrath, T. S. Turner, G. Thornton, and N. M. Harrison, Phys. Rev. Lett., V86, 3811 (2001).

[Weins, 1969] M. Weins, B. Chalmers, H. Gleiter and M. Ashby, Scripta Met. 3 (1969) 602.

[Weins, 1970] M. Weins, H. Geiter and B. Chalmers, Scripta Met. 4 (1970) 235.

[Wulff, 1901] G. Wulff, Z. Kristallogr., 34, 449 (1901).

[Zaoui, 2004] A. Zaoui, Phys. Rev. B69, 115403 (2004).

[Zhang, 1999] Y. Zhang, H. Ichinose, M. Nakanose, K. Ito, and Y. Ishida, J. Electron Microsc., 48, 245 (1999).

Publications

K. Murakami, M. Saito, E. Takuma, and H. Ichinose, J. Electron Microscope (Tokyo) **52**, p. 27-32 (2003)
"ARHVTEM of the Pd/ZnO heterointerface chemical structure"

M. Saito, T. Wagner, N. Kasper, A. Stierle, and M. Rühle, 8th Asia Pacific Electron Microscope Conference, Conference Paper, p. 446 (2004)
"Atomic structure of ZnO(0001) surface and Pd/ZnO(0001) interface"

S. B. Lee, M. Saito, and F. Phillipp, Zeitschrift für Metallkunde, **96**, p. 452, May (2005)
"Dynamic observation of nanometer-sized island formation on the $SrTiO_3$(001) and (011) surfaces by in situ high-resolution transmission electron microscopy"

T. A. Schaedler, A. S. Gandhi, M. Saito, M. Rühle, R. Gambino, C. G. Levi, J. Materials Research, Vol. **21**, No. 3, 791, Mar (2006)
"Extended solubility of CoO in ZnO and effects on magnetic properties"

Curriculum Vitae

Name:	Mitsuhiro Saito
Date of Birth:	30. January 1971
Place of Birth:	Tokyo, Japan
Nationality:	Japan
Marital Status	married

2001 - 2005: Ph.D. Student in the group of Prof. Dr. Dr. h.c. Manfred Rühle
at the Max-Planck-Institut für Metallforchung Stuttgart

2001 - 2001: Ph.D. Student, Department of Advanced Materials,
The University of Tokyo (Japan)

1999 - 2001: Department of Advanced Materials, the University of Tokyo (Japan)
Master of Science (2001)
The title of thesis: "*HRTEM study of Metal/Ceramic Interfaces*"

1993 - 1999: Department of Physics, Gakushuin University (Japan)
Bachelor of Science (1999)
The title of thesis: "*Analysis of magnetizing process of Fe quantum lines with Magneto Optical KERR Effect*"

Acknowledgements

This work was performed at the Max-Planck-Institut für Metallforschung Stuttgart, Stuttgart, Germany, in the time between August of 2001 and September of 2005 under financial supports by the Max Planck Society and the German Science Foundation through the Graduirtenkolleg ‘Innere Grenzflächen in kristallinen Materialien’.

I gratefully acknowledge Prof. Dr. Dr. h.c. M. Rühle who gave me the opportunity to prepare this study in his laboratory and in Germany. I am also thankful for his constant support and for his interest.

I thank Prof. Dr. F. Aldinger for taking over the *Mitbericht*.

I gratefully appreciate my advisor Dr. T. Wagner for his continuous support and many fruitful discussions during the past four years. I am also thankful for correcting my Japanese English.

Dr. G. Richter and Dr. F. Phillipp are acknowledged for the extensive introduction into and constant help with the quantitative HRTEM image analysis and many scientific discussions.

I acknowledge Dr. A. Stierle and Dr. N. Kasper for introducing me into the field of surface science, their co-operation, and much help at ANKA in Karlsruhe.

Special thanks are due to Dr. A. Zaoui for his support and for many fruitful discussions regarding his important theoretical results.

Thanks to Dr. C. Scheu and Dr. W. Sigle for their introduction into EELS measurement and for their supports.

I appreciate the TEM specimen preparation team, especially U. Salzberger and M. Kelsch for their continuous supports and for introducing me into TEM specimen preparation technique.

I am grateful to Dr. Q. Fu and M. Pudleiner for the MBE experiment of Pd/ZnO, many scientific discussions, and technical support.

Thanks to R. Höchen for the introduction to the ARM and U. Täffner for technical supports regarding AFM.

I strongly acknowledge H. Opielka and his family for continuous encouragement and for many supports.

Special thanks are also due to all members of the group of Prof. Rühle and L. Cha, Dr. E. Tchernychova, I. Swoboda, Dr. N. Rauch, Dr. S. H. Oh, Dr. S. Krämer, Dr. S. B. Lee, Dr. W. Kurtz, A. Schneider, and A. Huber, for warm working atmosphere, private discussions, and supports with all kind of problems.

I acknowledge Prof. Dr. H. Ichinose, Dr. C. Iwamoto, Dr. H. Sawada, and Dr. E. Takuma in the Univ. of Tokyo for introducing me into the field of HRTEM.

I am grateful to Dr. A. Yamazaki of Andersen group in MPI-FKF and Dr. T. Mizoguchi in Kyoto Univ. for advice in *ab-initio* calculation and scientific discussions.

Special thanks to my wife, my grandmothers, and my parents in Japan for their continuous encouragement and supports.

Stuttgart, Sep 2005